Additive Manufacturing of Nickel-Base Superalloy IN939 by Powder Bed Fusion-Laser Beam

By

Merve Nur Doğu

B.Sc., M.Sc.

A thesis submitted in fulfilment of the requirements for the degree of

Doctor of Philosophy (PhD)

from

Dublin City University

School of Mechanical and Manufacturing Engineering

Supervisor: Prof. Dermot Brabazon

Co-supervisor: Dr. John Geraghty

August 2024

Declaration

I hereby certify that this material, which I now submit for assessment on the programme of study leading to the award of PhD is entirely my own work, that I have exercised reasonable care to ensure that the work is original, and does not to the best of my knowledge breach any law of copyright, and has not been taken from the work of others save and to the extent that such work has been cited and acknowledged within the text of my work.

Signed:  ID No.: 20214792 Date: 20-August-2024

Acknowledgements

I would like to express my most sincere gratitude to my remarkable supervisor, Prof. Dermot Brabazon, for his kind attitude, guidance, endless support and belief in me. I thank him for being an exemplary mentor and role model. His boundless support, vast knowledge and encouragement are what made this PhD possible.

I would like to thank Hengfeng Gu, Jon Ginn, Thaddeus Song En Low, Chong Teng and ANSYS Inc. for their support and guidance.

I would also like to express my deepest gratitude to Dr. Muhannad Obeidi for sharing his unparalleled technical knowledge and constructive feedback, and for his counsel and guidance.

I also would like to thank my former labmate, Dr. Andre Mussatto, for sharing his insights on the PhD scheme, critical thinking skills and the lab environment.

I would additionally like to express my sincere gratitude to Prof. Ziya Esen, Prof. Arcan Dericioğlu and Dr. Kemal Davut for all the knowledge they shared, and for being superb mentors and laudable examples for my academic life. I also wish to express my deepest appreciation to Dr. Ezgi Bütev and Dr. Güney Mert Bilgin for all the expertise they have shared and their never-ending support. Furthermore, I would like to thank Seren Özer, who consistently offered me strength, encouragement and friendship throughout the entire period of study.

I would also like to express my sincere gratitude to Ms. Joan Kelly and all the technical staff at the Nano Research Facility and the School of Mechanical and Manufacturing Engineering. I would also like to acknowledge Science Foundation Ireland and Dublin City University for their generous support.

I would especially like to thank my lovely friends who have supported me throughout my life, and whose encouragement gave me the strength I needed to complete this PhD.

I would like to express my sincere appreciation to my partner and best friend, Rowan, for the endless support and encouragement. Rowan has always motivated me to overcome difficulties and brightened up my darkest days with humour, love and support. Go raibh maith agat, mo chroí. I would also like to thank Rowan's lovely parents, Evelyn and Ian, for their love and support.

As a female Turkish scientist, I would like to express my thanks to Mustafa Kemal Atatürk, founder of the Republic of Türkiye and champion for the rights of women. Thanks to him, I am here.

Furthermore, I would like to thank the innumerable cups of Turkish coffee, for giving me the strength to endure the sleepless nights.

Despite there being more than three thousand kilometers between us, I could always feel the love and support of my parents, Meryem and Satılmış, my sister, Nur Banu, and our chubby cat Mardin. I feel extremely lucky to have such a kind and nurturing family, and we have missed each other dearly over these past four years. Therefore, I would like to dedicate my thesis to my beloved family, in gratitude for the care they have provided me throughout my life.

Aramızda üç bin kilometreden fazla mesafe olmasına rağmen annem Meryem, babam Satılmış, kız kardeşim Nur Banu ve tombul kedimiz Mardin'in sevgisini ve desteğini her zaman hissettim. Böyle nazik ve anlayışlı bir aileye sahip olduğum için kendimi son derece şanslı hissediyorum ve geçtiğimiz dört yılda birbirimizi çok özledik. Bu nedenle tezimi, hayatım boyunca bana gösterdikleri ilgiden dolayı şükranlarımı sunarak sevgili aileme ithaf etmek istiyorum.

Table of Contents

List of Figures

List of Tables

List of Abbreviations

AM	: Additive manufacturing
APB	: Antiphase boundary
BCC	: Body-centered cubic
BCT	: Body-centered tetragonal
CAD	: Computer-aided design
Co	: Cobalt
CTE	: Low-coefficient-of-thermal-expansion
DDC	: Ductility-dip cracking
DRX	: Dynamic recrystallization
EBSD	: Electron backscatter diffraction
EDS	: Energy dispersive X-ray spectroscopy
FCC	: Face-centered cubic
Fe	: Iron
GCP	: Geometrically close-packed
GND	: Geometrically necessary dislocation
GOS	: Grain orientation spread
GP	: Guinier-Preston
GTE	: Gas turbine engine
HAGB	: High-angle grain boundaries
HAZ	: Heat affected zone
HCP	: Hexagonal close-packed
HIP	: Hot isostatic pressing
IPF	: Inverse pole figure
IQ&GB	: Image quality & grain boundaries
KAM	: Kernel average misorientation
LAGB	: Low-angle grain boundary
LED	: Linear energy density
LOF	: Lack-of-fusion
L-PBF	: Laser powder bed fusion
MAGB	: Medium angle grain boundary

MRD : Multiple random distribution

Ni : Nickel

PBF-LB : Powder bed fusion-laser beam

PF : Pole figure

PMZ : Partially melted zone

RSM : Response surface method

SEM : Scanning electron microscope

SFE : Stacking fault energy

SHT : Solution heat treatment

SLM : Selective laser melting

SSD : Statistically stored dislocation

SSS : Solid-solution strengthening

TCP : Topologically close-packed

TEM : Transmission electron microscopy

TIG : Tungsten inert gas

UTS : Ultimate tensile strength

VED : Volumetric energy density

XRD : X-ray diffraction

YS : Yield Strength

List of Publications

1. M.N. Doğu, M.A. Obeidi, H. Gu, C. Teng, D. Brabazon, **Powder Bed Fusion–Laser Beam of IN939: The Effect of Process Parameters on the Relative Density, Defect Formation, Surface Roughness and Microstructure**, Materials 17 (2024). https://doi.org/10.3390/ma17133324.

2. M.N. Doğu, A. Mussatto, M.A. Yalçın, S. Ozer, K. Davut, M.A. Obeidi, A. Kumar, S. Hudson, D. O'Neill, R. O'Connor, H. Gu, D. Brabazon**, A comprehensive characterization of the effect of spatter powder on IN939 parts fabricated by laser powder bed fusion**, Mater Des 235 (2023). https://doi.org/10.1016/j.matdes.2023.112406

3. M.N. Doğu, S. Ozer, M.A. Yalçın, K. Davut, G.M. Bilgin, M.A. Obeidi, H. Brodin, H. Gu, D. Brabazon, **Effect of solution heat treatment on the microstructure and crystallographic texture of IN939 fabricated by powder bed fusion-laser beam**, Journal of Materials Research and Technology 24 (2023). https://doi.org/10.1016/j.jmrt.2023.05.152.

4. M.N. Dogu, E. McCarthy, R. McCann, V. Mahato, A. Caputo, M. Bambach, I.U. Ahad, D. Brabazon, **Digitisation of metal AM for part microstructure and property control**, International Journal of Material Forming 15 (2022). https://doi.org/10.1007/s12289-022-01686-4.

5. M.N. Doğu, K. Davut, M.A. Obeidi, M.A. Yalçın, H. Gu, T.S.E. Low, J. Ginn, D. Brabazon, **Recrystallization and grain growth kinetics of IN718 manufactured by laser powder bed fusion**, Journal of Materials Research and Technology 19 (2022) 4242–4257. https://doi.org/10.1016/j.jmrt.2022.06.157.

6. A. Mussatto, M.N. Doğu, R.K. Vijayaraghavan, R. Groarke, M.A. Obeidi, G.B. McGuinness, **High strength bioinspired calcium phosphate-based material for bone repair applications**, Mater Today Commun 33 (2022). https://doi.org/10.1016/j.mtcomm.2022.104693.

7. M.A. Obeidi, A. Mussatto, M.N. Dogu, S.P. Sreenilayam, E. McCarthy, I.U. Ahad, S. Keaveney, D. Brabazon, **Laser surface polishing of Ti-6Al-4V parts manufactured by laser powder bed fusion**, Surf Coat Technol 434 (2022). https://doi.org/10.1016/j.surfcoat.2022.128179.

8. M.A. Obeidi, A. Conway, A. Mussatto, M.N. Dogu, S.P. Sreenilayam, H. Ayub, I.U. Ahad, D. Brabazon, **Effects of powder compression and laser re-melting on the microstructure and mechanical properties of additively manufactured parts in laser-powder bed fusion**, Results in Materials 13 (2022) 100264. https://doi.org/10.1016/j.rinma.2022.100264.

9. A. Mussatto, R. Groarke, R.K. Vijayaraghavan, C. Hughes, P.J. Mcnally, Y. Delaure, D. Brabazon, **Assessing dependency of part properties on the printing location in laser-powder bed fusion metal additive manufacturing**, 30 (2022). https://doi.org/10.1016/j.mtcomm.2022.103209.

10. M.A. Obeidi, M. Monu, C. Hughes, D. Bourke, M.N. Dogu, J. Francis, M. Zhang, I.U. Ahad, D. Brabazon, **Laser beam powder bed fusion of nitinol shape memory alloy (SMA)**, Journal of Materials Research and Technology 14 (2021). https://doi.org/10.1016/j.jmrt.2021.07.126.

List of Oral Presentations

1. V. Mahato, C. Hughes, M. Monu, J. Chekotu, **M.N. Doğu**, M. Samimi, **Process Parameters for Optimized AM**, I-Form Gathering (Virtual Evenet), December 2021, Ireland (Researcher Challenge Communications Award).

2. M.N. Doğu, D. Brabazon, **Influence of Solution Heat Treatment Temperature and Holding Time on the Microstructure, Texture and Hardness of IN718 produced by the L-PBF**, International Student Conference in Metallic Materials, July 2022, Dublin City University, Ireland.

3. M.N. Doğu, S. Ozer, M. A. Yalçın, K. Davut, G. M. Bilgin, M. A. Obeidi, H. Brodin, H. Gu, J. Ginn, D. Brabazon, **Influence of solution heat treatment on microstructure of IN939 fabricated by laser powder bed fusion,** International Conference on Material Forming (ESAFORM 2023), April 2023, Krakow, Poland.

4. M.N. Doğu, S. Ozer, M. A. Yalçın, K. Davut, H. Gu, D. Brabazon, **Influence of spatter powder on IN939 parts produced by laser powder bed fusion,** International Conference on Material Forming (ESAFORM 2024), April 2024, Toulouse, France.

List of Poster Presentations

1. M.N. Doğu, K. Davut, M.A. Obeidi, M.A. Yalçın, H. Gu, T.S.E. Low, J. Ginn, D. Brabazon, **Recrystallization and grain growth kinetics of IN718 manufactured by laser powder bed fusion**, I-Form Gathering, December 2022, Athlone, Ireland.

2. M.N. Doğu, M.A. Obeidi, H. Gu, D. Brabazon, **IN939 fabricated by the Laser Powder Bed Fusion: The effect of process parameters on the density, surface roughness, microstructural and mechanical properties**, 152nd Annual Meeting and Exhibition (TMS 2023), March 2023, San Diego, California, USA.

Abstract

Merve Nur Doğu

Additive Manufacturing of Nickel-Base Superalloy IN939 by Powder Bed Fusion-Laser Beam

IN939 is a precipitation-hardenable Ni-base superalloy. It has been widely used for blades and vanes in gas turbines, and aircraft engines due to its outstanding properties such as high microstructural stability up to 850 ^{o}C, high corrosion, oxidation and creep resistance. Recently, a growing interest in the fabrication of IN939 parts with the PBF-LB process has emerged due to its significant advantages such as intricate geometric complexity in a single step, design freedom, as well as reductions in material waste and tooling costs. IN939 is considered reasonably weldable yet it is crack-susceptible.

There is a significant gap in the literature concerning the influence of PBF-LB process parameters and subsequent heat treatments on the material characteristics of IN939 compared to established Ni-base superalloys like IN718 and IN625. For this reason, investigation of the effects of PBF-LB process parameters and post-heat treatment on the material properties of IN939 is crucial to obtain crack- and defect-free components.

This thesis investigates the effects of PBF-LB process parameters and post-heat treatments on IN939. Through a systematic approach, the research evaluates the characteristics of IN939 powders, including virgin and spatter powders, and their impact on part quality and process efficiency. Furthermore, the influence of PBF-LB process parameters such as laser power, scanning speed, and hatch distance on material properties is comprehensively analyzed, emphasizing parameter optimization for defect mitigation and surface quality improvement. Additionally, the investigation delves into the effects of different scanning strategies on the material properties of IN939, providing valuable insights into optimizing scanning parameters to achieve desired performance. Moreover, this study explores the impact of various solution heat treatment temperatures on the material properties of IN718 and IN939, offering practical recommendations for heat treatment parameter optimization.

Chapter 1: Introduction

1.1 Background and Motivation

Nickel-base (Ni-base) superalloys, which are a unique class of metallic materials, have been widely used in gas turbine engines thanks to their outstanding properties such as high-temperature strength and toughness, as well as corrosion and oxidation resistance, for over seven decades. Since their initial development, they have undergone continuous refinement and optimization, leading to the creation of increasingly advanced materials with improved properties and performance characteristics. They have become essential materials in aerospace, power generation, and other industries where high-temperature and corrosive environments are encountered [1–3]. Although several decades have elapsed since their introduction, comprehension of the metallurgical behaviour of Ni-base superalloys remains an ongoing work. Weldability and the underlying mechanisms of accountability for crack initiation in these alloys remain some of the significant research areas [4].

Across a range of industries, the production of alloy components typically involves the utilization of various conventional fabrication methods, including powder metallurgy, casting, welding/joining, and machining, to manufacture a single part. However, these conventional techniques often face limitations in fabricating highly intricate geometries and may not be cost-effective for small-batch productions or frequent design changes. In contrast, additive manufacturing (AM) technologies offer the ability to produce complex-shaped parts in a single step, thereby reducing raw material waste and saving time and energy, particularly for the production of a limited quantity of alloy parts [5].

The powder bed fusion-laser beam (PBF-LB) process, which is a metal AM process, uses a focused laser beam to selectively melt the metal powder. It has been used in diverse industries such as aerospace, defense, energy, automotive and biomedical industries. This process provides greater design flexibility compared to conventional manufacturing methods by enabling the creation of intricate parts while minimizing material wastage, production costs and time. Moreover, the PBF-LB process allows for precise control over microstructure, facilitating the fabrication of materials with distinctive microstructural characteristics and enhanced mechanical properties compared to those produced through casting processes. As a result of these advantages, the PBF-LB process

is increasingly being explored for the fabrication of high-temperature components in aerospace and nuclear applications [5–8].

Despite its numerous advantages, the PBF-LB process of precipitation-hardenable Ni-base superalloys presents significant challenges. The rapid heating and cooling cycles experienced during fabrication lead to high residual stresses in the final parts. When combined with the inherent cracking susceptibility of Ni-base superalloys, these residual stresses limit the processing and applications of such materials. As a result, successful application of the PBF-LB process to precipitation-hardenable Ni-base superalloys is currently restricted to a few specific alloys, with many others possessing superior elevated temperature properties being overlooked. Furthermore, even for extensively studied alloys, there remains a knowledge gap concerning their microstructural and mechanical responses to post-processing heat treatments [6,9,10].

Inconel 939 (IN939), which is a precipitation-hardenable Ni-base superalloy, has been extensively used for blades and vanes in gas turbines, fuel nozzles, diffusers, turbine airfoils and aircraft engines due to its outstanding properties such as microstructural stability of elevated temperatures up to approximately 850 ºC as well as high-temperature corrosion, oxidation, and creep resistance [11–15]. It is in the "fairly weldable" region of the weldability assessment plot of Ni-base superalloys yet remains "crack-susceptible". Although it has been produced with conventional manufacturing techniques and used since the 1960s in various application areas, the application of the PBF-LB process appears to be in the initial stages of development when compared to other Ni-base superalloys such as IN718. However, it is highly valued for additive manufacturing due to its outstanding performance in hot-gas path applications. As a result, there is a growing interest in the IN939 fabricated by PBF-LB. Additionally, there is a significant gap in the literature regarding the effects of PBF-LB process parameters and post-heat treatments on the material properties of IN939 compared to well-known Ni-base superalloys (i.e., IN718 and IN625) [4,7,14–18].

In the PBF-LB process, the interaction between the high-energy laser and metal powder generates a melt pool and spatter, with occasional vapor plumes or plasma. While the melt pool's behaviour is relatively predictable, the spatter is more difficult-to-predict behaviour, influenced by factors such as recoil pressure, the Marangoni effect, and heat transfer. Spatter, which can be classified as a hot droplet or cold powder spatter, negatively affects process stability, energy efficiency, and product quality by disrupting powder re-

coating, reducing laser efficiency, and contaminating both the parts and equipment. To enhance part quality and equipment longevity, effective spatter control through optimized laser parameters and protective gas flows is crucial [19]. While considerable research has been conducted on the spatter effects in Ni-base superalloys like IN718 [20–24] and Hastelloy X [25–27], there is still a lack of understanding regarding its impact on IN939 parts built using PBF-LB. Despite the current challenges discussed above and the importance of ensuring the structural properties of additively manufactured parts, there have been no systematic studies on spatter's effect on IN939 fabricated by the PBF-LB.

In the PBF-LB process, the scanning strategy plays a pivotal role in determining the microstructure, mechanical properties, and overall performance of fabricated parts. Among the numerous process parameters, the scanning strategy, which includes factors such as scanning directions, sequence, vector length, and rotation angle, directly influences the thermal history and melt track formation. Common strategies such as uni-directional, bi-directional, and chessboard scanning each offer distinct advantages in controlling residual stresses, enhancing material density, and refining grain structures. Although much research has focused on various Ni-base superalloys such as IN718, IN738, and Hastelloy X, there remains a significant gap in understanding the effects of scanning strategies on the material properties of IN939, underscoring the need for further investigation in this area [28–32].

Solution heat treatment (SHT) is a crucial step in optimizing the microstructure and mechanical properties of IN939 fabricated by the PBF-LB. As a precipitation-hardenable Ni-base superalloy, IN939 undergoes SHT to dissolve undesirable phases formed during solidification, followed by rapid cooling to prevent further precipitation. This process not only changes the microstructure but also prepares the alloy for subsequent aging treatments, which promote the nucleation and growth of the strengthening γ' phase. Moreover, the optimization of SHT is vital, as the initial microstructure resulting from different fabrication methods and process parameters can vary significantly. Therefore, tailored SHT procedure are essential for ensuring the desired material performance, particularly in critical applications like aerospace, where eliminating defects and achieving consistent properties are significant [33,34].

1.2 Thesis Aim and Objectives

The thesis aimed to investigate the effects of PBF-LB process parameters and post-heat treatments on the material properties of IN939. Additionally, it sought to enhance and develop scientific knowledge about the processing of IN939 using the PBF-LB process by understanding its material properties, physical metallurgy, and process characteristics necessary to achieve optimal and reliable properties. This aim was achieved by focusing on the following specific objectives:

1. Investigation of the effect of virgin and spatter IN939 powders on the PBF-LB process.
2. Investigation of the effect of PBF-LB process parameters (laser power, laser scanning speed, and hatch distance) on the relative density, defect formation (such as porosity and crack), surface roughness and microstructure of IN939.
3. Investigation of the effect of laser scanning strategy on the relative density, defect formation (such as porosity and crack), surface roughness, microstructure, crystallographic texture, microhardness and residual stress of IN939.
4. Investigation of the effect of various solution heat treatment temperatures on the microstructure, crystallographic texture and microhardness of IN939.

1.3 Thesis Format and Outline

The thesis is presented as a compilation of published research papers and submitted manuscripts containing original contributions. The contribution of the candidate to the publications are as following:

Chapter	Publication Title	Status	Candidate contribution
3	A comprehensive characterization of the effect of spatter powder on IN939 parts fabricated by laser powder bed fusion	Published, Materials & Design, 2023	First author, corresponding author, project administration, conceptualisation, methodology, investigation, data curation, formal analysis, visualisation, writing - original draft, writing - review & editing

4	Powder bed fusion-laser beam of IN939: Effect of process parameters on the relative density, defect formation, surface roughness, and microstructure	Published, Materials, 2024	First author, corresponding author, project administration, conceptualisation, methodology, investigation, data curation, formal analysis, visualisation, writing - original draft, writing - review & editing
5	A comprehensive characterization of the effect of scanning strategy on IN939 fabricated by powder bed fusion-laser beam	Journal review completed; Revised manuscript submitted, Journal of Materials Research & Technology, 2024	First author, corresponding author, project administration, conceptualisation, methodology, investigation, data curation, formal analysis, visualisation, writing - original draft, writing - review & editing
6	Effect of solution heat treatment on the microstructure and crystallographic texture of IN939 fabricated by powder bed fusion-laser beam	Published, Journal of Materials Research & Technology, 2023	First author, corresponding author, project administration, conceptualisation, methodology, investigation, data curation, formal analysis, visualisation, writing - original draft, writing - review & editing
7	Recrystallization and Grain Growth Kinetics of IN718 Manufactured by Laser Powder Bed Fusion	Published, Journal of Materials Research & Technology, 2022	First author, corresponding author, project administration, conceptualisation, methodology, investigation, data curation, formal analysis, visualisation, writing - original draft, writing - review & editing

This thesis comprises seven chapters, arranged progressively. Moreover, the following is a brief description of the work performed and/or contents included in each chapter:

Chapter 1 introduces several subjects the thesis encompasses including the thesis structure and summarises the aims and objectives of the thesis.

Chapter 2 provides a comprehensive review of the background information essential to the topic and discusses prior research conducted in the field. It emphasizes the challenges, limitations, and gaps in existing studies, thereby underscoring the necessity for additional research efforts.

Chapter 3 presents a thorough investigation into the impact of IN939 powder on the PBF-LB process. It includes a detailed characterization of both virgin and spatter powders and examines how spatter powder affects the porosity, microstructure, hardness, surface roughness, and crystallographic texture of the fabricated parts.

Chapter 4 shows an in-depth investigation into the effects of PBF-LB process parameters, including laser power, laser scanning speed, and hatch distance, on the relative density, defect formation, surface roughness, and microstructure of IN939 fabricated by the PBF-LB process.

Chapter 5 offers a detailed characterization of how the laser scanning strategy affects the relative density, defect formation, surface roughness, microstructure, crystallographic texture, microhardness, and residual stress of IN939 fabricated by the PBF-LB process.

Chapter 6 gives a detailed investigation of the effects of various solution heat treatment temperatures (1120 ^{o}C, 1160 ^{o}C, 1200 ^{o}C, and 1240 ^{o}C) on the microstructure, crystallographic texture, and microhardness of IN939 fabricated by the PBF-LB process.

Chapter 7 investigates the recrystallization and grain growth behaviour of IN718 fabricated by the PBF-LB process under varying temperatures (1050 ^{o}C, 1150 ^{o}C, and 1250 ^{o}C) and holding times (15, 45, and 90 minutes). This study was conducted as an initial investigation to gain familiarity with Ni-base superalloys fabricated using the PBF-LB process.

Chapter 8 presents a summary of the key findings from this research and provides recommendations for further research work.

The flow diagram of Figure 1.1 provides a graphical visualization of the evolution of this PhD thesis and how each chapter fits together and was integrated to impact the state-of-the-art of additive manufacturing of Ni-base superalloy IN939 by PBF-LB.

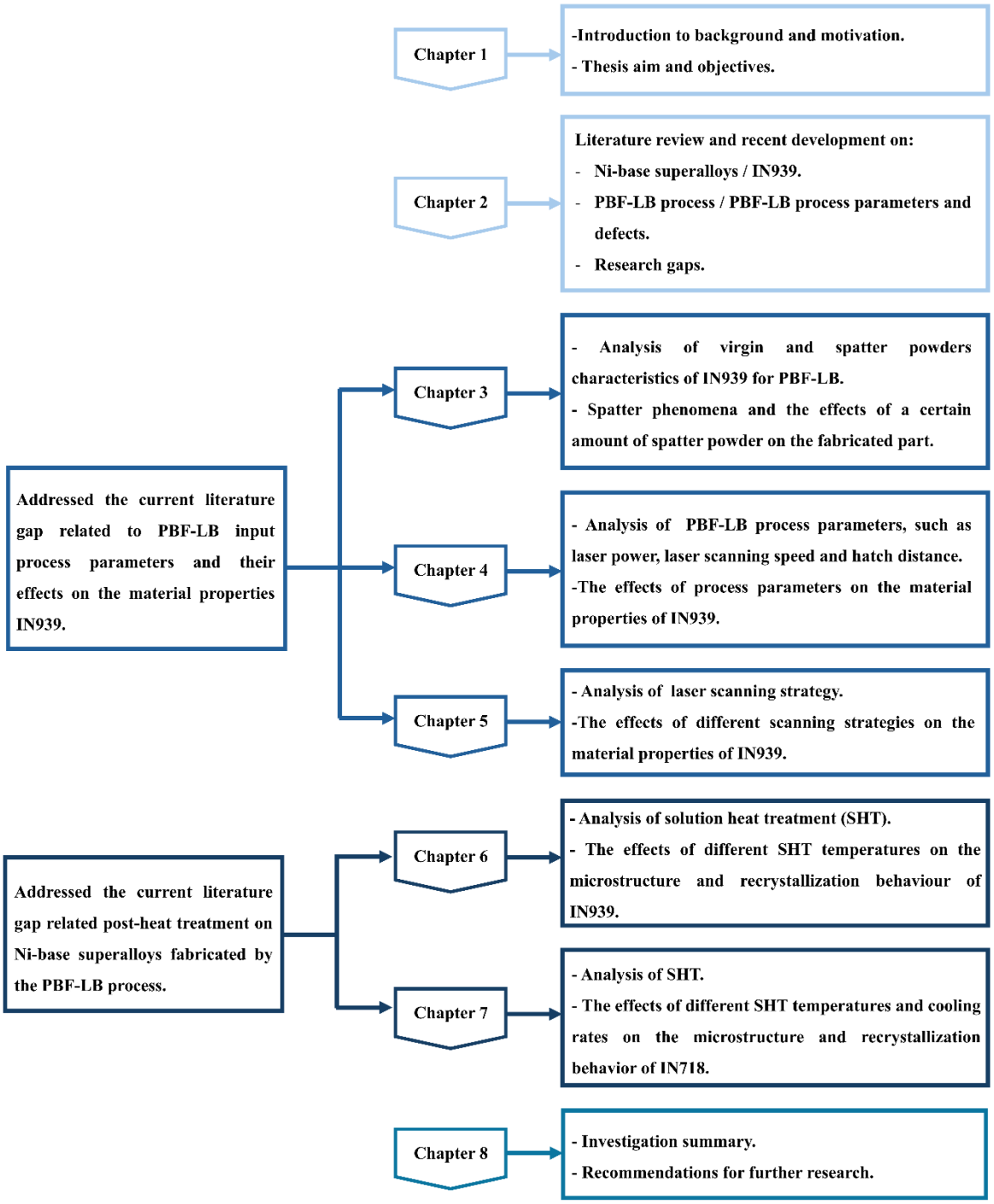

Figure 1.1 Graphical illustration of the flow and connectivity of the research conducted in the current thesis.

Chapter 2: Literature Review

2.1 High-Temperature Materials

High-temperature materials are primarily used for gas turbines, rockets and heat exchangers due to their remarkable ability to maintain their properties at elevated temperatures. The desirable characteristics of a high-temperature material can be classified as [35]:

- an ability to withstand loading at an operating temperature close to its melting temperature ($T_{operating}/T_m$ should be greater than 0.6 for high-temperature materials).
- a significant durability against mechanical deterioration for prolonged durations.
- an ability to withstand severe operating environments.

Figure 2.1(a) shows a simplified illustration of the main sections and temperature distributions of a gas turbine engine (GTE). Basically, air undergoes compression in the compressor section, raising its pressure and temperature to approximately 400 ^{o}C. Subsequently, fuel is introduced and mixed with the compressed and heated air before being ignited by a flame in the combustion section (reaching temperatures exceeding 2000 ^{o}C) which is the hottest part of the engine. The resulting expanding gases pass through the turbine section, where temperatures can reach up to 1600°C, extracting power to drive the compressor, before being expelled through the exhaust [4]. The material types used in different sections of a GTE are depicted in Figure 2.1(b). High-temperature materials employed in GTEs operate under severe conditions and therefore require superior properties. These include high yield stress and ultimate strength to prevent yielding and failure, high ductility and fracture toughness to enhance impact resistance and damage tolerance, high resistance to fatigue crack initiation and propagation to ensure prolonged operating life, low thermal expansion to maintain precise tolerances between rotating components, high creep resistance and stress rupture strength, as well as high corrosion and oxidation resistance [36].

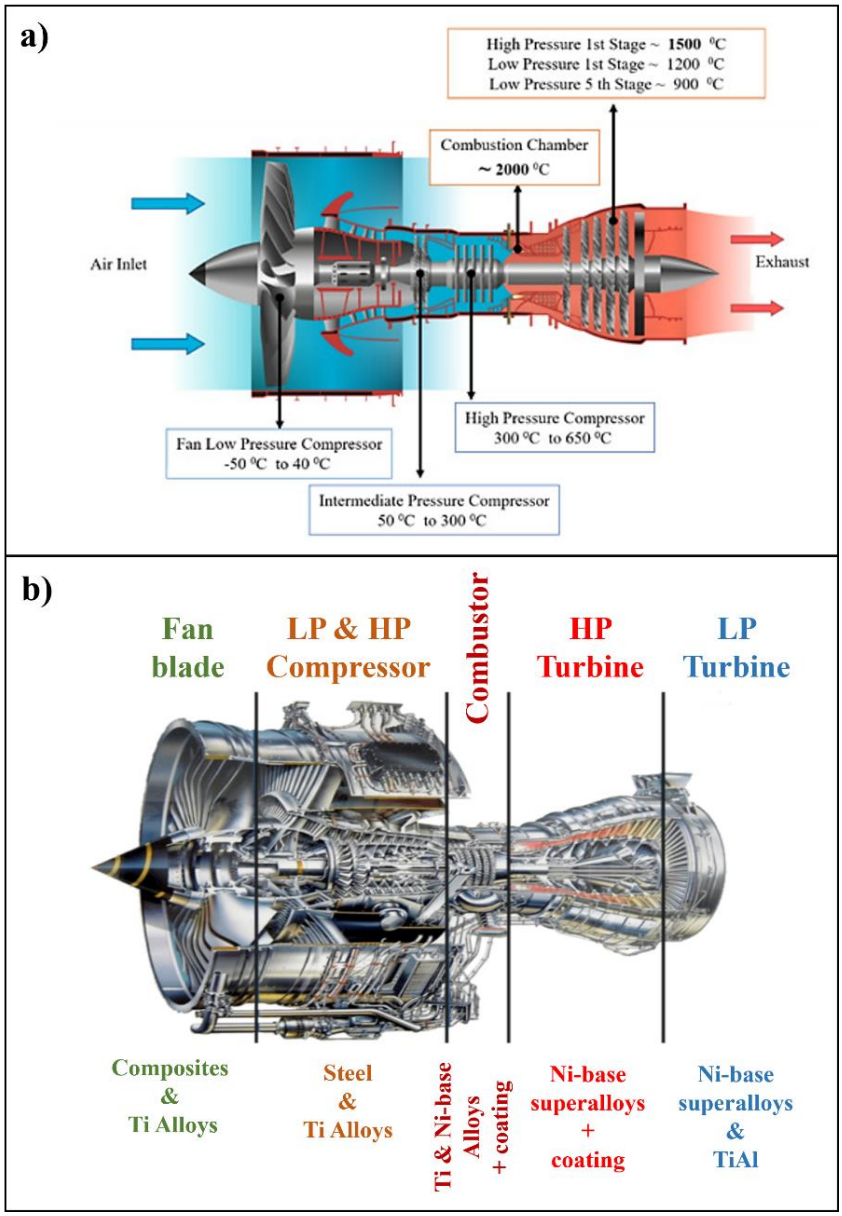

Figure 2.1 (a) Main sections and temperature distributions of a GTE [37] and (b) material types used in different sections of a GTE. Re-drawn from [38].

2.2 Superalloys

Superalloys were initially developed during World War II to meet the demand for high-temperature materials in military gas turbine applications. Since then, research and development in the field of superalloys have continued, leading to the creation of more advanced alloys with improved performance and material properties [1]. The most notable aspect of these materials is their ability to maintain high mechanical strength at elevated temperatures (typically up to 80% of their absolute melting temperature). They are used in a wide range of applications thanks to their superior properties [39].

Superalloy applications in GTEs can be categorized as stationary parts (combustor cans, nozzles, guide vanes, seals, and casings) and rotating parts (discs, shafts, blades, and spacers). The combustor having an intricate design undergoes extreme temperatures, but it is subjected to limited structural loads. Therefore, creep and oxidation resistance, along with excellent formability and weldability are significant when selecting the material. The subsequent crucial components in the GTE are the turbine vanes which encounter slightly lower temperatures than the combustor. However, maintaining oxidation resistance remains significant. The variation in pressure on the airfoil surfaces induces stress, making resistance to creep a vital factor in the selection of the materials. One of the most common phenomena observed is the "bowing" of the airfoil due to creep deformation. Moreover, turbine blades are directly exposed to the intense heat of the gas stream, facing similar challenges of hot corrosion and oxidation as observed in the combustor and vane surfaces. Beyond these concerns, the blades must endure substantial structural loads arising from both centrifugal and thermal stresses. Additionally, the rotating blade tips must maintain extremely tight clearances with stationary components to enhance engine efficiency, demanding a high resistance to creep deformation in the alloy. Furthermore, turbine disks are designed to possess high tensile strength, fatigue resistance and toughness. Unlike turbine blades, they do not encounter extremely high temperatures [40].

2.2.1 Classification of Superalloys

Superalloys are classified as iron-nickel-base superalloys, nickel-base superalloys, and cobalt-base superalloys according to the base alloying element in the chemical composition. All of these superalloys share a common basic microstructure characterized by the austenitic face-centered cubic (FCC) matrix phase, also called the gamma (γ) phase, and several dispersed secondary strengthening phases [41]. In elemental form, cobalt (Co) has a hexagonal close-packed (HCP) crystal structure (transforming into an FCC crystal structure at 417 ^{o}C) and iron (Fe) has a body-centered cubic (BCC) crystal structure (transforming into an FCC austenite at 912 ^{o}C) at room temperature. Among them, nickel (Ni) is the only superalloy base metal having an FCC crystal structure at room temperature. For this reason, Ni addition stabilizes both Fe and Co in superalloys to retain an FCC crystal structure throughout the temperature range encountered in GTE [40].

Iron-nickel-base (Fe-Ni-base) superalloys, also called iron-base superalloys, are used mostly for turbine discs or forged rotors thanks to their superior properties such as high toughness and ductility, along with low cost due to the substantial amount of Fe

addition. They have 15-60 wt.% Fe, along with at least 25 wt.% Ni to stabilize the matrix [41]. Fe-Ni-base superalloys can be divided into three groups such as precipitation-hardened superalloys (γ'-Ni_3(Al, Ti) and/or, γ''-Ni_3Nb precipitates form in the FCC γ matrix), low-coefficient-of-thermal-expansion (CTE) group of superalloys, and superalloys modified from stainless steel (primarily strengthened by solid-solution hardening and minor carbide precipitation) [40].

Cobalt-base (Co-base) superalloys are mostly used when the primary concern is hot corrosion or in structural applications with low stress operating at moderate-to-high temperatures. For this reason, they are preferred for the vanes and other stationary parts of the GTE due to their hot corrosion resistance and superior stress-rupture properties. Although their microstructure consists of an FCC γ matrix, along with several strengthening phases, they are strengthened by carbide formation and solid-solution strengthening. The advantages of Co-base superalloys can be classified as higher melting temperatures, superior hot corrosion resistance due to a higher chromium (Cr) content, and superior thermal fatigue and weldability (compared to Ni-base superalloys) [1,40].

The following section provides extensive details on Ni-base superalloys.

2.3 Nickel-base Superalloys

Nickel-base (Ni-base) superalloys were first designed in the 1940s for high-temperature applications in jet engines, including Nimonic 75, developed by Henry Wiggin Ltd, UK. Research and development of Ni-base superalloys have continued since then [7]. Thanks to their superior properties such as high-temperature strength, toughness, and corrosion and oxidation resistance, they are a unique class of metallic materials and are widely used in GTEs. Additionally, 40–50% of the total weight of an aircraft engine contains Ni-base superalloys, used mostly in turbine and combustor sections of the engine, which are subjected to elevated temperatures during operation [42]. Wrought Ni-base superalloys are mostly used when high toughness is required for applications, such as turbine discs and forged blades. On the other hand, castings are preferred for high strength and creep resistance in high-temperature applications, such as investment-cast turbine blades and wheels [40]. The detailed application areas of Ni-base superalloys are shown in Figure 2.2.

Ni-base superalloys can be primarily classified as solid-solution strengthened and precipitation hardened according to the type and content of the elements. Additionally,

oxide dispersion strengthened Ni-base superalloys, whose properties are determined by the fine oxide particles dispersed in the γ matrix, can be another sub-category [6].

2.3.1 Microstructure and Phases of Ni-base Superalloys

Ni (the atomic number is 28, and the fifth most abundant element on earth) is in the first row of the d block of transition metals, alongside Fe and Co and its crystal structure is FCC. Under ambient conditions, the density is 8.907 g/cm^3 (denser than the other metals such as titanium, Ti, and aluminium, Al, used for aerospace applications) and the melting temperature is 1455 ^{o}C [35].

Aerospace industry	**Pulp and paper mills**
Aircraft gas turbines: disks, combustion chambers, bolts, casings, shafts, exhaust systems, blades, vanes, burner cans, afterburners, thrust reversers. Space vehicles: aerodynamically heated skins, rocket engine parts.	tubing, doctor blades, bleaching circuit equipment, scrubbers.
	Nuclear power systems
	control rod drive mechanisms, valve stems, springs, ducting.
Chemical and petrochemical industries	**Marine architecture**
	ships, submarines.
bolts, fans valves, reaction vessels, tubing, transfer piping, pumps.	**Electronic parts**
	resistors.
Pollution control equipment	**Medical applications**
scrubbers, flue gas desulfurization equipment (liners, fans, stack gas reheaters, ducting).	dentistry uses, prosthetic devices.
Steam turbine power plants	**Automotive industry**
bolts, blades, stack gas reheaters.	spark plugs, glow plugs (in diesel engines), catalytic converters, combustion systems. Reciprocating engines: turbochargers, exhaust valves, hot plugs, valve seat inserts.
Metals processing mills	
ovens, furnace, afterburners, exhaust fans.	
Heat-treating equipment and metal processing	**Coal gasification and liquefaction systems**
trays, fixtures, conveyor belts, baskets, fans, furnace mufflers, hot-work tools and dies.	heat exchangers, repeaters, piping.

Figure 2.2 Examples of application areas of Ni-base superalloys. Re-drawn from [7].

The microstructure of a superalloy contains a γ (gamma) phase matrix (FCC), along with several secondary phases such as γ' (gamma prime) phase (ordered FCC), γ" (gamma double prime) phase (ordered body-centered tetragonal (BCT)), η (eta) phase (ordered hexagonal), carbides, intermetallic compounds, and many others. It is important to note that not all phases are present in every superalloy. Table 2.1 provides a comprehensive

overview of the phases in superalloys [40]. Additionally, the schematic evolution of microstructure showing both useful and deleterious phases and crystal structures of some phases in Ni-base superalloys are shown in Figure 2.3.

Table 2.1 Phases in superalloys (adapted from [40]).

Phase	Crystal Structure	Formula
γ (gamma)	FCC	Ni (solid solution)
γ' (gamma prime)	ordered $L1_2$	Ni_3Al $Ni_3(Al, Ti)$
η (eta)	HCP ($D0_{24}$)	Ni_3Ti (no solubility for other elements)
γ'' (gamma double prime)	ordered $D0_{22}$	Ni_3Nb
δ (delta)	Orthorhombic (ordered Cu_3Ti)	Ni_3Nb
MC	FCC	TiC NbC HfC
$M_{23}C_6$	FCC	$Cr_{23}C_6$ $(Cr, Fe, W, Mo)_{23}C_6$
M_6C	FCC	Fe_3Mo_3C Fe_3W_3C-Fe_4W_2C Fe_3Nb_3C Nb_3Co_3C Ta_3Co_3C
M_7C_3	Hexagonal	Cr_7C_3
M_3B_2	Tetragonal	Ta_3B_2 V_3B_2 $Nb_3B_2(Mo, Ti, Cr, Ni, Fe)_3B_2$ Mo_2FeB_2
MN	FCC	TiN (Ti, Nb, Zr)N (Ti, Nb, Zr)(C, N) ZrN NbN
μ	Rhombohedral	Co_2W_6 $(Fe, Co)_7(Mo, W)_6$
Laves	Hexagonal	Fe_2Nb Fe_2Ti Fe_2Mo Co_2Ta Co_2Ti
σ (sigma)	Tetragonal	FeCr FeCrMo CrFeMoNi CrCo CrNiMo
M_2SC	HCP	$(Zr, Ti, Nb)_2SC$

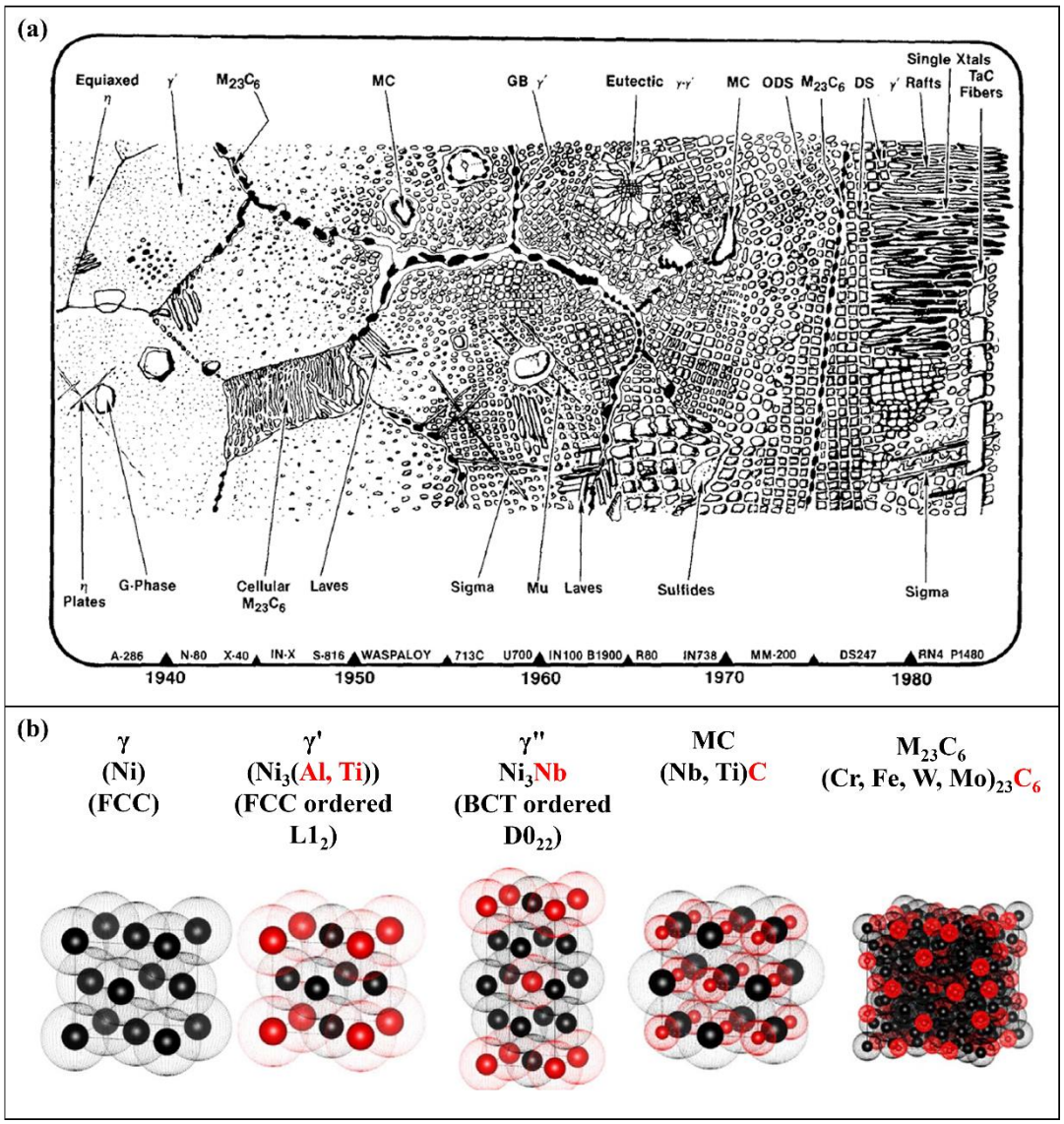

Figure 2.3 The schematic evolution of (a) microstructure showing useful and deleterious phases and (b) crystal structures of some phases in Ni-base superalloys. Re-drawn from [17,43].

2.3.1.1 γ (Gamma) Phase

The FCC γ (gamma) phase creates the matrix of the superalloy and contains the base metal of the superalloy (Ni for Ni-base superalloys), along with a high percentage of solid-solution elements such as Co, Cr, Mo, Fe, W, Re [6]. The FCC γ phase has optimal mechanical properties due to its high modulus and multiple slip systems. Additionally, it is suitable for relatively high-temperature applications due to the low diffusivity of alloying elements. For these reasons, the FCC γ phase is ideal for the matrix of high-temperature materials [40].

2.3.1.2 Geometrically Close-Packed Phases

Geometrically close-packed (GCP) phases represent intermetallic compounds with the chemical formula A_3B. Within this category, notable phases include the principal strengthening components γ' (Ni_3Al and Ni_3Ti)) and γ″ (Ni_3Nb). Additionally, closely related phases such as η (Ni_3Ti) and δ (Ni_3Nb) are included. Notably, the γ' phase stands out as the most thermodynamically stable among the GCP phases and serves as the predominant strengthening constituent in superalloys. Conversely, the γ'' phase finds application in enhancing the strength of specific alloys, such as IN718 [41,44–46].

2.3.1.2.1 γ' (Gamma Prime) Phase

γ' (gamma prime) phase, classified as a GCP phase, exhibits an ordered Ll_2 crystal structure, commonly represented as Ni_3Al or Ni_3(Al, Ti). However, notable elemental substitution is observed within this phase. For instance, Co and Cr may substitute for Ni, and Ti can replace Al. Additionally, Fe can replace either Ni or Al within the structure [47]. Pure Ni_3Al is a superlattice characterized by the Cu_3Au ($L1_2$)-type structure that possesses a long-range order structure up to its melting point of 1385 ^oC. It is stable over a relatively narrow range of compositions. However, alloying elements possess the capacity for extensive substitution in either of its constituents to a considerable degree, consequently effecting substantial alterations in the phase properties. The γ' phase is the main strengthening precipitate (in which up to 60% of the Al can be substituted by Ti and/or Nb) for most of the Ni-base superalloys [2].

The lattice parameters of γ and γ' phases are close to each other (the crystal lattice of the γ' phase varies slightly (0-0.5%) from that of the γ FCC matrix). For this reason, the γ' phase forms as a coherent precipitate within the austenitic γ matrix phase (cube to cube relationship: $\{100\}_\gamma \parallel \{100\}_{\gamma'}$ (crystal planes are parallel) and $<010>_\gamma \parallel <010>_{\gamma'}$ (crystal directions are parallel)) and it is the main strengthening phase in most of the Ni-base superalloys. Additionally, the morphology of the γ' is dependent on the exact composition and heat treatment [3,48]. Moreover, γ' phase mismatch with the γ matrix phase, γ' phase antiphase boundary (APB) energy (which is the energy associated with the disruption of the atomic ordering across an antiphase boundary in an ordered crystal structure), γ' phase morphology, and γ' phase stability are affected by the alloying elements [1]. The lattice mismatch (δ), which quantifies the compatibility between γ and γ' phases, is a significant factor in determining the morphology of the γ' phase. The lattice mismatch is defined

according to Equation 2.1 (where α_γ and $\alpha_{\gamma'}$ are lattice parameters of the γ and γ' phases) [35]:

$$\delta = 2\left[\frac{\alpha_{\gamma'}-\alpha_\gamma}{\alpha_{\gamma'}+\alpha_\gamma}\right] \quad (2.1)$$

The γ' phase morphologies change according to the lattice mismatch and tend to be spherical (lattice mismatches are between 0 and ± 0.2%), cuboidal (lattice mismatches are between ± 0.5 and ± 1%) and platelike (lattice mismatches are above about ± 1.25%) [1]. Moreover, Ricks et al. [49] reported that the critical particle size of the γ' phase to change the morphology of the γ' phase from spherical to cuboidal during the precipitation hardening (aging) heat treatment is dependent on the lattice mismatch and is different for individual alloys. Additionally, a larger lattice mismatch leads to the transition occurring at a smaller critical particle size of the γ' phase. However, the sign of the mismatch is not strongly effective in this transition [50]. Moreover, Figure 2.4 displays the morphology evolution of the γ' phase with an increasing aging degree. The γ' phase has spherical morphology in the initial stage of the aging (to minimize the surface energy), then it continues to grow on the corners until it transforms into the cuboidal morphology which mostly observed in the overaged alloys [6].

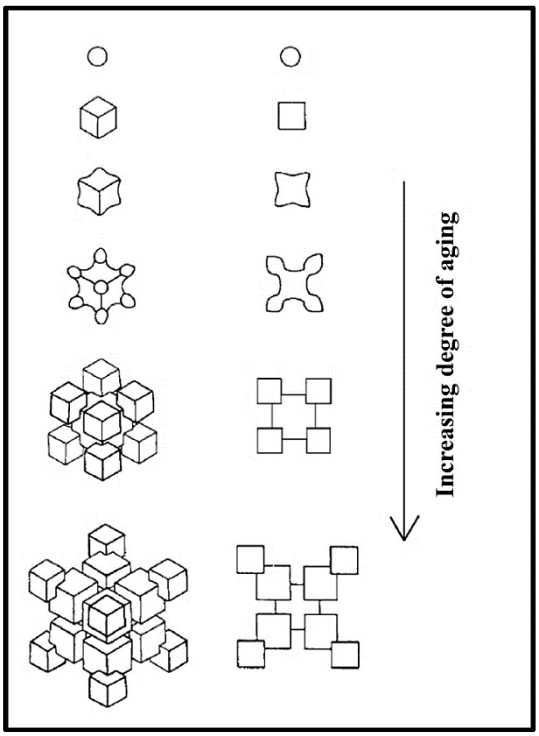

Figure 2.4 Schematic diagram of the γ' phase morphology development during aging. Re-drawn from [35].

The cooling rate during the production process and applied heat treatment affects the γ' phase's morphology, size and distribution. Thus, it significantly impacts the final properties of the superalloys. Moreover, the monomodal and multimodal γ' phase morphologies occur with high and slow cooling rates, respectively. The cooling rate effect on the γ' phase morphology in AD730^{TM} wrought Ni-base superalloy is shown in Figure 2.5 [51]. Furthermore, the volume fraction of the γ' phase plays a crucial role in the controlling of the properties (i.e., strength and creep) of the superalloys. The addition of Al and Ti elements into the superalloys provides an increase in the volume fraction of the γ' phase, but careful control of the amounts of each element is essential. When the Al/Ti ratio equals or exceeds 1, prolonged exposure to high temperatures leads to the transformation of γ' phase by Ni_2AlTi, NiAl, or Ni(Al, Ti). These phases undergo rapid overaging at moderately high temperatures, resulting in the formation of substantial platelike precipitates. Additionally, when the γ' phase volume fraction exceeds approximately 45%, the superalloy becomes challenging to deform through hot or cold working. Most wrought Ni-base superalloys possess between 20 and 45% γ' phase volume fraction, whereas cast Ni-base superalloys contain about 60% or more γ' phase volume fraction according to the composition and application. Additionally, an improvement in the creep strength can be obtained with the increase of γ' phase volume fraction [1–3,40].

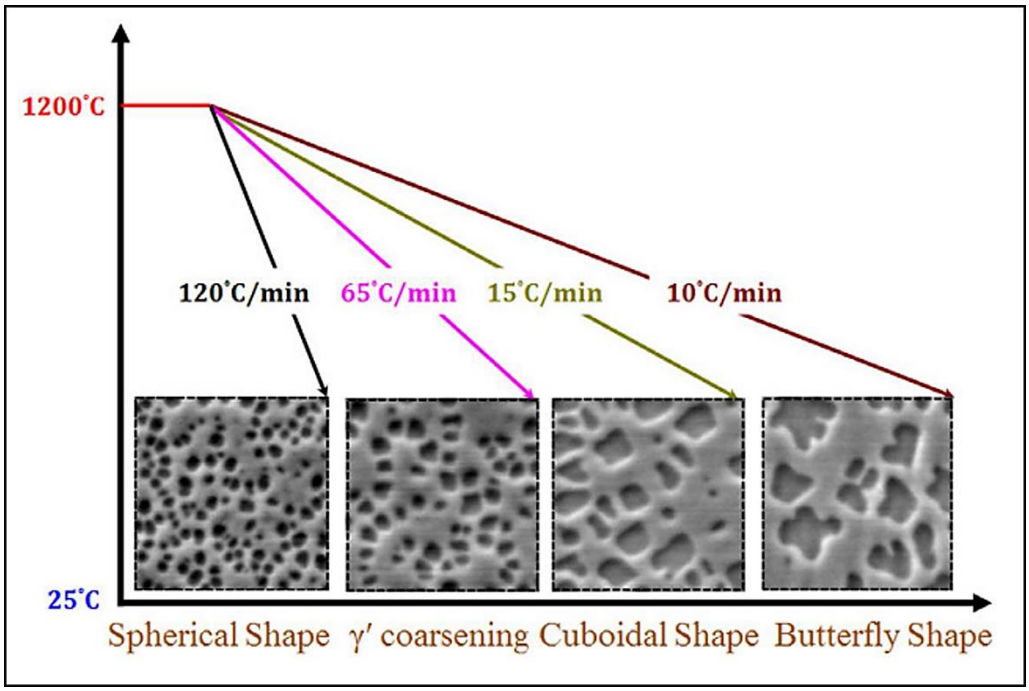

Figure 2.5 The evolution of the γ′ phase morphologies (in AD730^{TM} wrought Ni-base superalloy) during the various cooling rates [51].

2.3.1.2.2 γ" (Gamma Double Prime) Phase

The γ" (gamma double prime) phase, classified as a GCP phase, shows an ordered BCT $D0_{22}$ crystal structure, commonly represented as Ni_3Nb. Although it is not as common as the γ' phase, it is the main strengthening phase in IN718. It has a coherent disc-like morphology with {100} habit plane and has higher coherency strain and APB energy. The metastable γ" phase can transform into the stable orthorhombic δ phase (Ni_3Nb, $D0_a$), which requires 6-10 wt.% Nb concentration over a long period of exposure to high temperatures (above 700 ^oC) [44,45].

2.3.1.2.3 δ (Delta) Phase

The δ (delta) phase, classified as a GCP phase, has an ordered BCT $D0_{22}$ crystal structure, commonly represented as Ni_3Nb. It is incoherent with the γ phase matrix and can be detrimental to the mechanical properties when it is extremely coarse and acicular. On the other hand, the δ phase can also lead to grain refinement [45,52,53]. The formation of the δ phase occurs within the temperature range of 650 to 980 ^oC, and its characteristics during formation are significantly influenced by temperature. Below 700 ^oC, nucleation of the δ phase is observed at the γ phase grain boundaries, and its growth takes place at the expense of γ" phase. When the temperature is between 700 and 885 ^oC, formation of the δ phase is accompanied by rapid coarsening of the γ" phase. The rapid formation of the δ phase in less than 24 h occurs at temperatures between 840 and 950 ^oC [35].

2.3.1.2.4 η (Eta) Phase

The η (eta) phase, classified as a GCP phase, has a hexagonal $D0_{24}$ crystal structure, commonly represented as Ni_3Ti. The η phase can develop in Fe-Ni-base, Ni-base, and Co-base superalloys, particularly in grades featuring high Ti/Al ratios that have undergone prolonged exposure to high temperatures. Moreover, the η phase which is incoherent with the γ phase matrix exhibits limited solubility for other elements [3]. Although it has a slower precipitation rate, it tends to grow more rapidly, along with forming larger particles (which can extend across grains) compared to the γ' phase. Two distinct forms of the η phase may be observed. They can be classified as a cellular constituent, resembling pearlite, with alternate lamellae of γ and η (at grain boundaries) and platelets with a Widmanstätten pattern (intragranular). The cellular form has a detrimental effect on notched stress-rupture strength and creep ductility, while the Widmanstätten pattern impairs stress-rupture strength without affecting ductility [3]. The η phase is relatively easy

to identify due to its characteristic appearance. Furthermore, the η phase occurs at elevated temperatures, but a solid-state transformation to the γ' phase is also possible at lower temperatures [33,54].

2.3.1.3 Carbides, Nitrides, and Borides

Carbides affect the superalloy properties either improving or reducing according to their location, composition and morphology. They tend to be located at the grain boundaries in Ni-base superalloys. On the other hand, they are commonly observed intragranular in Co- and Fe-Ni-base superalloys. Generally, they contribute positively to rupture strength at high temperatures according to their composition and morphology. For example, fine blocky dispersed particles located on grain boundaries can provide a strengthening effect by impeding grain boundary sliding, consequently enhancing creep and rupture strength. However, if these elements are present in the form of continuous films along the grain boundaries, they can have a detrimental impact on ductility and impact resistance by providing easy crack initiation and propagation. Additionally, the chemical stability of the superalloy matrix can be adversely affected by carbides due to the locally depleting carbide-forming elements [40,41,47].

There are some significant types of carbides such as MC, M_6C, $M_{23}C_6$, and M_7C_3 (M represents a metal atom such as Cr, Mo, Ti, Ta, Nb or Hf). The MC carbides, which are primary carbides and commonly have an FCC crystal structure, form as eutectic phase or discrete blocky particles during the solidification. They are generated through either direct reactions or precipitation from supersaturated solid-solutions at high temperatures (about 1038 ^{o}C) [1]. These carbides occur as discrete particles that are heterogeneously distributed throughout the superalloy in different locations such as intragranular, intergranular, and often between dendrites [1,35]. In superalloys, MC carbide formation follows the preferred order: HfC, TaC, NbC, and TiC (in order from high to low stability). It should be noted that this order differs from the thermodynamic order, which is HfC, TiC, TaC, and NbC [2]. Moreover, they can possess coarse cubic, random, globular, blocky, or script morphologies (Figure 2.6). Although they are stable at low temperatures, they can degenerate into secondary carbides at higher temperatures [1,47].

The $M_{23}C_6$ and M_7C_3 carbides, which are secondary carbides, primarily form along the grain boundaries in different morphologies such as irregular, discontinuous blocky particles, plates, cells, regular geometric or discrete globular (the most desirable). $M_{23}C_6$ carbides (while Cr is the primary "M" element, other metallic elements such as Ni, Co, Fe,

Mo, and W can act as substitutes, i.e., $Cr_{23}C_6$) readily precipitate in superalloys featuring a moderate-to-high Cr content during lower-temperature heat treatment and service (typically within the range of 760 to 816 °C, with the possibility of formation extending up 982 °C). The formation of $M_{23}C_6$ carbides can be attributed to both the degeneration of MC carbides and the utilization of available soluble residual carbon within the alloy matrix. Although they commonly precipitate at the grain boundaries, they may form along the twin bands, stacking faults, and at twin ends. Moreover, globular, or discontinuous blocky $M_{23}C_6$ carbides at the grain boundaries can enhance ductility and creep resistance by inhibiting grain boundary sliding [1,3,41].

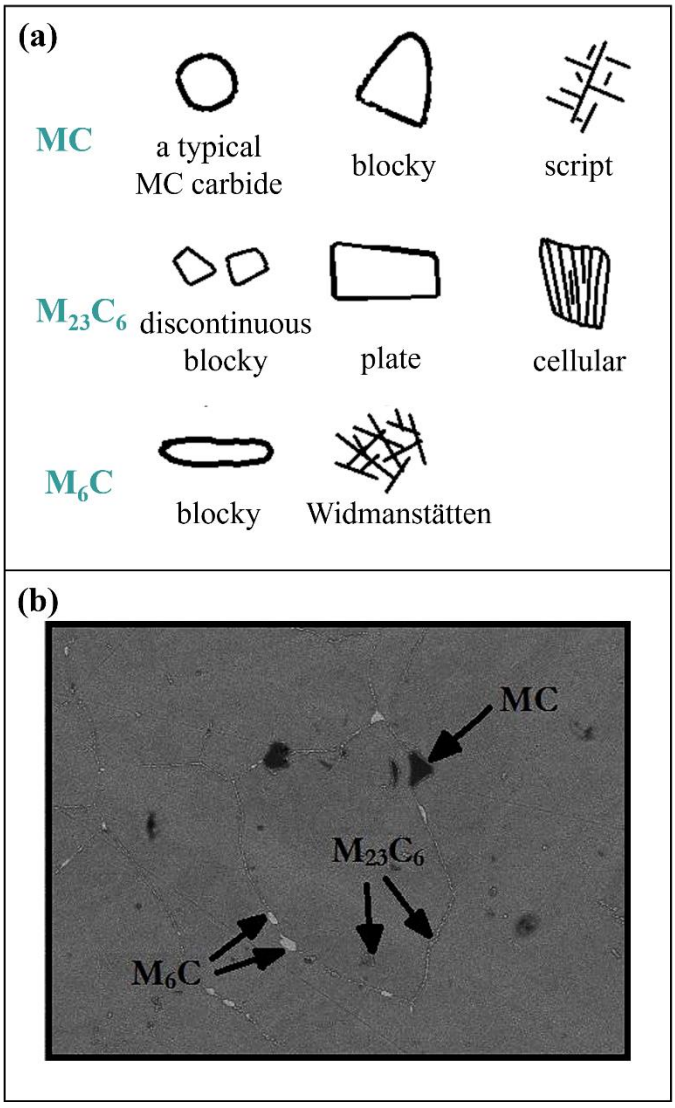

Figure 2.6 The carbide morphologies: (a) schematic image, and (b) SEM image for MC, $M_{23}C_6$ and M_6C carbides. Re-drawn from [47].

The formation of $M_{23}C_6$ carbides may form according to the following equations [47,55]:

$$\gamma \rightarrow M_{23}C_6 + \gamma \quad (2.2)$$

and/or

$$MC + \gamma \rightarrow M_{23}C_6 + \gamma' \ (760\text{-}980\ ^oC) \quad (2.3)$$

The M_6C carbides, which have complex cubic structures, form at slightly higher temperatures (815 to 980 ^oC) than $M_{23}C_6$ carbides. They are like $M_{23}C_6$ carbides and rich in such refractory elements (Mo and W) and more thermodynamically stable than them. However, higher Mo + W content (6 to 8 at.%) is required to form them in Ni-base superalloys. The decomposition of MC carbides or soluble residual carbon in the matrix can form the M_6C carbides [40]. They tend to precipitate at the grain boundaries in a blocky form and intragranular in an acicular morphology [47]. The M_6C carbides can form according to the following equations [55]:

$$MC + \gamma \rightarrow M_6C + \gamma' \ (815\text{-}980\ ^oC) \quad (2.4)$$

and/or

$$M_6C + M' \leftrightarrow M_{23}C_6 + M'' \quad (2.5)$$

Superalloys have TiN (the most common nitride), HfN, and NbN nitrides, which appear as small particles (yellow to orange colour). They are not affected by the heat treatments and are not soluble in the melting point of the superalloy. Additionally, they do not have any major effect on the mechanical properties [3].

Boron is added in small amounts to some superalloys to enhance stress-rupture and creep properties, or to retard η phase formation. Borides having blocky to half-moon shapes, are found mainly at the grain boundaries. Additionally, they can be used to improve the strength of Fe-Ni-base and Ni-base superalloys, similar to carbides [40].

2.3.1.4 Topologically Close Packed Phases (TCP)

Topologically close-packed (TCP) phases, which can form platelike or needle-like, are considered undesirable in superalloys due to the adverse effects on the rupture strength and ductility. The TCP phases can occur during the heat treatment or more commonly in service and are composed of close-packed layers of atoms. In superalloys, the TCP phases include σ (A_xB_y), μ ($A_{x'}B_{y'}$), and Laves (A_2B) phases (A is Fe, Ni, or Co, and B is Nb, Mo, Ta, or Cr). Moreover, the presence of high levels of BCC transition metals, such as Cr, W, Ta, Mo, and Nb, contributes to the formation of TCP phases [40,56,57]. Among the TCP phases, the σ phase (a composition of ($Cr_{46}Fe54$) or $(Ni)_8(Cr, Mo)_4(Cr, Mo, Ni)_{18}$) is the

most detrimental phase because it can cause brittleness and crack initiation and propagation sites. Furthermore, it comprises a high percentage of refractory elements. Therefore, the σ phase precipitation can deplete refractory metals in the γ matrix. Thus, a reduction of strength in the γ phase matrix can occur. Additionally, it can form at the grain boundaries (where high Mo and Cr concentrations) in superalloys with high γ' phase volume fractions [2,40].

2.3.2 Alloying Elements in Ni-base Superalloys

Mechanical properties (such as yield strength, toughness, ductility, low-cycle fatigue life and creep), various microstructural features (i.e., the γ/γ′ lattice mismatch, γ′ phase volume fraction, diffusion rates, APB energy and stacking fault energy (SFE)) or cost can be tailored by adjusting the composition and in superalloys. Additionally, surface stability improvement is achieved by forming a protective surface oxide scale, primarily composed of Cr and/or Al oxides [1]. The role of alloying elements in Ni-base superalloys are given in Table 2.2.

Table 2.2 Role of alloying elements in Ni-base superalloys (adapted from [1,40]).

Elements in Ni-base Superalloys	Effect
Co, Cr, Fe, Mo, W, Re	Solid-solution strengtheners
Ta, Ti, Nb, Hf Cr Cr, Mo, W Mo, W, Nb	Carbide formation: MC M_7C_3 $M_{23}C_6$ M_6C
C, N	Carbonitrides: M(CN)
Al, Ti	γ' phase (Ni_3(Al, Ti)) formation
Co	Raises solvus temperature of the γ' phase
Al, Ti, Nb, Ta	Hardening precipitates and/or intermetallics
Al, Cr, Y, La, Ce	Oxidation resistance
La, Th	Improves hot corrosion resistance
Cr, Co, Si	Sulfidation resistance
B, Ta, Re	Improves creep properties
B	Increases rupture strength
B, C, Zr, Hf	Grain-boundary strengtheners
Re	Retards the γ' phase coarsening

2.3.3 Strengthening Mechanisms for Ni-base Superalloys

Aerospace metals must possess the ability to endure high stress without undergoing plastic deformation. The enhancement of metal strength involves impeding the movement of dislocations under an externally applied load. The strength properties can be increased by stopping or slowing dislocation slip. Several methods such as strain (work) hardening, solid-solution strengthening, dispersion strengthening, precipitation (or age) strengthening, and grain refinement strengthening can be employed to enhance resistance against dislocation slip [36].

2.3.3.1 Grain boundary strengthening

Grain boundary strengthening occurs as dislocations move through a crystal lattice and encounter grain boundaries. The mismatch in lattice orientation and the repulsive strain field at the boundary stop dislocations, causing them to accumulate and form a pile-up. The increasing repulsive stress from successive pile-ups eventually forces dislocations to move into the adjacent grain, thus strengthening the material [36].

Increasing the number of neighbouring grains by decreasing grain size results in more grain boundaries creating more barriers against dislocation movement, along with increasing the amount of stress necessary to move dislocation across a grain boundary [58]. The reduction in grain size has additional beneficial effects, such as an increment in strength, fracture toughness and fatigue life [36].

The Hall-Petch relationship given by Equation 2.6 (D is the mean grain size, σ_y is the yield strength, σ_0 is the friction stress of the matrix, a material constant defining the stress required to move dislocations in a single crystal without a grain boundary ($D^{-1/2}=0$), and k_y is a material constant representing the slope of the σ_y vs $D^{-1/2}$, that has been determined to be 750 MPa $\mu m^{-1/2}$ for superalloys,) explains the inverse relationship between yield strength and grain size [36,58,59].

$$\sigma_y = \sigma_0 + \frac{ky}{\sqrt{D}} \tag{2.6}$$

The Hall–Petch relationship is applicable for metals with a grain size between about 1 mm and 1 μm. However, it is not valid for materials with grains that are larger than 1 mm and smaller than 1 μm [36].

2.3.3.2 Solid-Solution Strengthening

Solid-solution strengthening increases the matrix strength by adding alloying elements that integrate into the crystal structure of the base metal, forming a solid solution by occupying either interstitial or substitutional lattice sites. The size, crystal structure, and electronegativity of the alloying element, according to the Hume–Rothery rules, determine its location in the lattice. If the atomic size of the alloying element is much smaller (typically less than 60%) compared to the base metal atoms, it occupies an international site; if the size difference is within about 15%, it occupies a substitutional site [1,36,60]. Moreover, solute atoms affect the gamma matrix by altering the local modulus and atom arrangements, limiting atom diffusion, and changing the stacking fault energy (SFE) of the matrix, thereby achieving significant hardening [1].

The lattice strain provides a barrier to dislocation movement. Thus solid-solution strengthening takes place and the easy movement of dislocation through the strained region of the crystal lattice determines the strengthening degree. The dislocations are attracted or repelled by the interstitial or substitutional atoms (which create the local strain) and this impedes their motion. To move the dislocation against the strain field, applied stress must be increased. Hence, this increases the yield strength. To have an effective hardening process with solid-solution strengthening, the alloying elements should have a high degree of solid solubility in the host metal. The insoluble alloying elements form second-phase particles. This does not provide solid-solution strengthening [36]. Moreover, the yield strength, ultimate tensile strength, and hardness of aerospace alloys can be increased by solid-solution strengthening. However, the effectiveness of solid-solution strengthening reduces above approximately 60% of the absolute melting temperature (0.6Tm) due to increased diffusion [40].

2.3.3.3 Precipitation Strengthening

Precipitation strengthening is a strengthening process that involves the formation of hard precipitate particles within the host alloy, thereby restricting dislocation slip. This can be achieved by the addition of elements such as Ti, Al, and Nb (in the case of Ni-base superalloys) which have limited solubility (drastically decreasing with a reduction in temperature) in the alloy matrix. The host matrix rejects the alloying elements from the lattice sites when the solubility decreases with temperature reduction, and the rejected atoms create small precipitates that induce high lattice strains. Thus, the high lattice strains resist dislocation slip which increases strength. These precipitates which are the γ'-Ni_3(Al,

Ti) or γ"-Ni_3Nb phase (generally coherent intermetallic compounds) can be generated during heat treatment from the supersaturated solid solution and inhibit the dislocation movement. Moreover, dislocation movement within a matrix containing precipitates can only occur by either cutting through the particles or bypassing them. Precipitation strengthening can provide a significant increase in the creep strength of alloys for high-temperature applications [1,36,40].

Precipitation strengthening is achieved via age hardening heat treatment by forming a fine dispersion of precipitates which impede the dislocation movement. Precipitation strengthening takes place in the following steps [60]:

- Solution heat treatment (SHT) step: the alloy is heated at a high temperature (within the single-phase region) to dissolve and disperse the alloying elements in the host metal matrix.

- Quenching: after the SHT step, the alloy is rapidly cooled down from the SHT temperature to achieve a supersaturated solid solution of alloying elements in the host metal.

- Aging or age hardening step: the alloy is reheated to an intermediate temperature to obtain finely dispersed precipitate particles.

The effectiveness of precipitation strengthening can be controlled by the following factors [1,40,58]:

- Coherency strains between the γ matrix phase and the precipitate phases (γ' and γ" phases). The difference in their lattice parameters creates coherency strains.

- APB energy (representing the energy required for the dislocation to cut through the ordered precipitate) in the presence of an ordered precipitate phase (γ' and γ" phases). The dislocation cutting could create disordering between the precipitate phases and matrix.

- Volume fraction of the precipitate phases (γ' and γ" phases).

- The particle size, morphology, and distribution of the γ' and γ" phases.

Precipitation strengthening contains different strengthening mechanisms which are solid-solution strengthening (SSS), Guinier-Preston (GP) strengthening, coherent precipitate strengthening and incoherent precipitate strengthening (shown in Figure 2.7) [36].

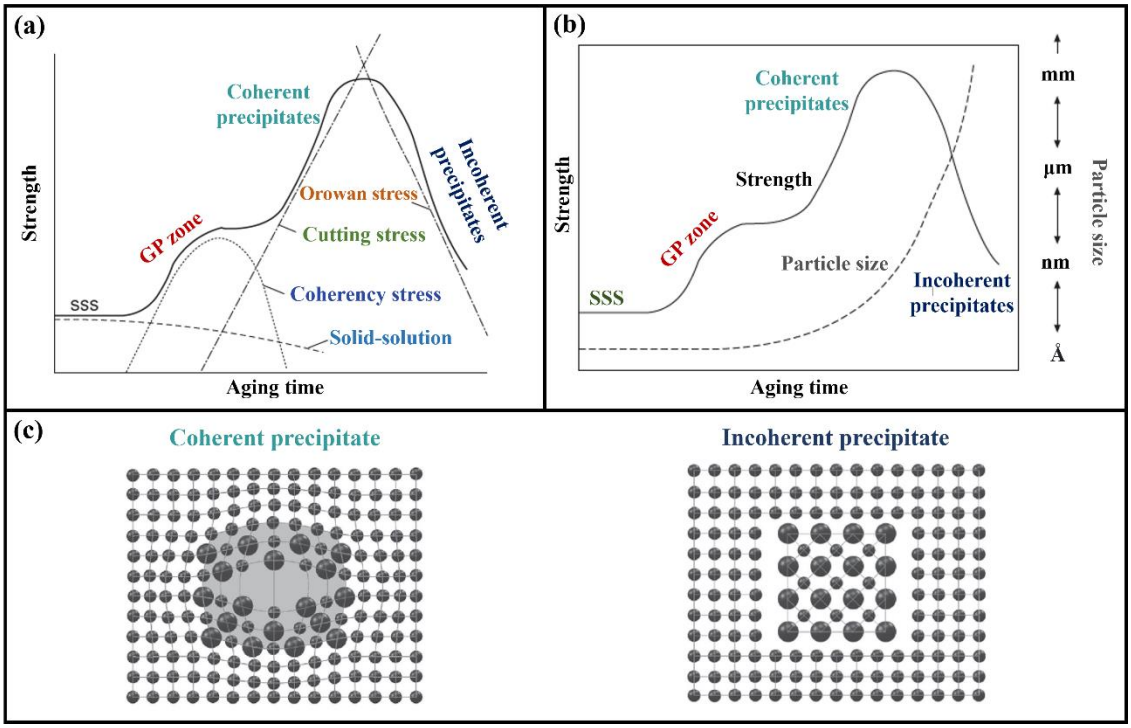

Figure 2.7 (a) Precipitation strengthening mechanism, (b) the effect of aging time on strength and particle size during aging heat treatment, and (c) a schematic drawing of coherent and incoherent precipitates. Re-drawn from [36].

When the γ' phase particles are larger than the critical size and too strong to be cut through, dislocations bend and loop around the particles which is called dislocation bowing (Orowan strengthening). Incoherent precipitate strengthening occurs by the Orowan hardening mechanism. Conversely, if the γ' phase particles are smaller than the critical size, dislocations can traverse them, a process referred to as dislocation cutting (Figure 2.8).

Incoherent precipitates generate higher lattice strains, promoting Orowan strengthening and increasing resistance to dislocation slip compared to coherent precipitates. Maximum strengthening occurs with closely spaced incoherent precipitates and during the transformation of coherent to incoherent precipitates. Over-aging leads to the coarsening of precipitate phases, resulting in a reduction in strength [36,58,61] .

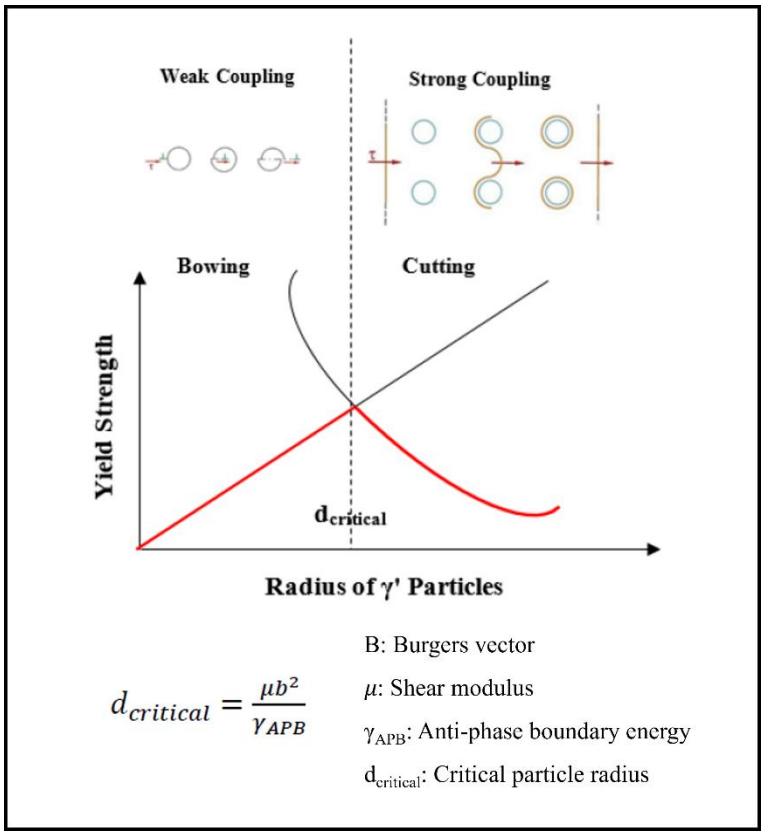

Figure 2.8 The interaction between dislocations and particles depends on the size of the precipitates. Re-drawn from [58].

Carbides can provide **carbide hardening** by inhibiting grain-boundary slip when they preferentially precipitate at the grain boundaries. Grain boundaries can be mainly stabilized with small globular and noncohesive carbides. When carbides precipitate within the grains, they can also provide strengthening (in the same way as precipitates, but less effective than that of the typical gamma phase precipitate). However, they are more effective when they precipitate at the grain boundaries, and they improve creep resistance by preventing grain-boundary sliding and pinning and avoiding grain growth [1,3,40].

Oxide dispersion strengthening (ODS) is another mechanism that is similar to precipitation hardening. However, strengthening agents (such as oxides which are always incoherent within the alloy) are not precipitated from the matrix but rather added to the alloy separately. ODS alloys are very suitable for elevated-temperature applications because the oxide dispersion contributes to strengthening, and this strengthening effect remains effective up to temperatures as high as 1300 °C [3,40].

2.3.4 An Overview of the Chemistry, Physical, and Materials Properties of IN939

2.3.4.1 Chemical Composition and Microstructure of IN939

IN939, which is also known as Nimocast 739, was developed in the late 1960s by the International Nickel Company to meet the demand for a robust, highly corrosion-resistant alloy, capable of prolonged operation at temperatures up to 850°C, as a cast alloy with an increased precipitation-hardening phase volume fraction and improved corrosion resistance when compared to the existing IN738LC alloy [4,62–65]. It is a precipitation-hardenable Ni-base superalloy, which is strengthened mainly by the formation of $L1_2$-ordered γ' phase (Ni_3(Al, Ti)) and has been widely used for land-based and marine gas turbines, fuel nozzles, diffusers, turbine airfoils and aircraft engines, due to its outstanding properties such as microstructural stability of elevated temperatures up to approximately 850 ˚C, as well as high-temperature corrosion, oxidation and creep resistance [11–15].

The specific chemical composition of IN939 can vary according to different manufacturers. The nominal chemical compositions determined by the International Nickel Company (INCO), EOS Inc., Siemens Energy Inc., and SLM Solutions Inc. are shown in Table 2.3. IN939 has Ni as a base element providing FCC crystal structure matrix. Additionally, it comprises high amounts of Cr and Co, in addition to various other significant major and minor alloying elements. Alloys high in Cr (>15 wt.%) and low in Al (<3 wt.%) form a Cr_2O_3 scale and an Al_2O_3 subscale protective oxide layer that provides hot corrosion resistance [66]. Cr is predominantly located within the γ matrix, where it acts as a potent solid-solution strengthener. Additionally, carbides and TCP phases contain Cr.

The density of IN939 is in the range of 8.1 and 8.2 g/cm^3, which varies according to the manufacturers. Some of the reported density values for IN939 in the literature are 8.1 g/cm^3 [67], 8.15 g/cm^3 [68], 8.16 g/cm^3 [62] and 8.2 g/cm^3 [69].

IN939 was developed as cast and is still produced as cast [62,64–66,70–80]. However, it can be fabricated using different fabrication methods such as wrought [77,81], and recently additive manufacturing (AM) [15,18,33,63,74,77,82–90]. The fabrication method has an important role in the final microstructure of the alloy because it affects the solidification.

Table 2.3 The nominal chemical composition of IN939 according to different manufacturers.

Element (wt.%)	**INCO** [62]	**EOS** [68]	**Siemens Energy** [67]	**SLM Solutions** [69]
Ni	Balance	Balance	Balance	Balance
C	0.15	0.15	0.15	0.15
Cr	22.5	22.5	22.0	22.0-23.0
Co	19.0	19.0	19.0	18.0-20.0
W	2.0	2.0	2.0	1.0-3.0
Nb	1.0	1.0	1.0	0.5-1.5
Ta	1.4	1.4	1.4	1.0-1.8
Ti	3.7	3.7	3.7	3.0-4.5
Al	1.9	1.9	1.9	1.0-3.0
Zr	0.1	0.1	<0.03	0.1
B	0.01	0.01		-
Si	-	-	<0.5	0.5
Mn	-	-		0.5

As-cast IN939 has a dendritic microstructure having the γ matrix phase, along with other phases such as γ' phase, carbides, and η phase (Figure 2.9). The dendritic structures have elemental segregations such as Cr, Co, and W in the dendrites and Ti, Ta, and Nb concentrated in interdendritic areas. Additionally, IN939 possesses two types of carbides which are MC and $M_{23}C_6$ carbides. MC carbides are based on Ti, Ta, and Nb, and predominantly found in intragranular locations, whereas $M_{23}C_6$ carbides are based on Cr, and formed largely at intergranular locations, particularly after degeneration of the MC phase during aging at 800 to 900 ^{o}C [62,65,77]. Although the casting parameters such as pouring and mould temperature, mould backing, and mould inoculation have no crucial effect on the degree of elemental segregation, they affect the cast microstructure (i.e., grain size and dendrite size). Recently, Jahangiri [78] investigated the effect of the solidification cooling rate on the microstructural characteristics of cast IN939. According to his study, the higher cooling rates promote more regular and polygonal MC carbides, whereas the lower cooling rates provide a Chinese script form of MC carbides. Additionally, the γ' phase was formed as coarse and cubic morphology in the dendrite cores, and very coarse and flower-like in the interdendritic regions, respectively when the cooling rates were around 0.13 ^{o}C/s. On the other hand, mainly spherical γ' phase in the dendrite cores, and a mixture of spherical and cubic γ' phase in the interdendritic regions were observed at

cooling rates around 1.1 °C/s. Moreover, the γ' phase volume fractions in as-cast IN939 are reported about 25% in the dendrite core and about 30% in the interdendritic regions.

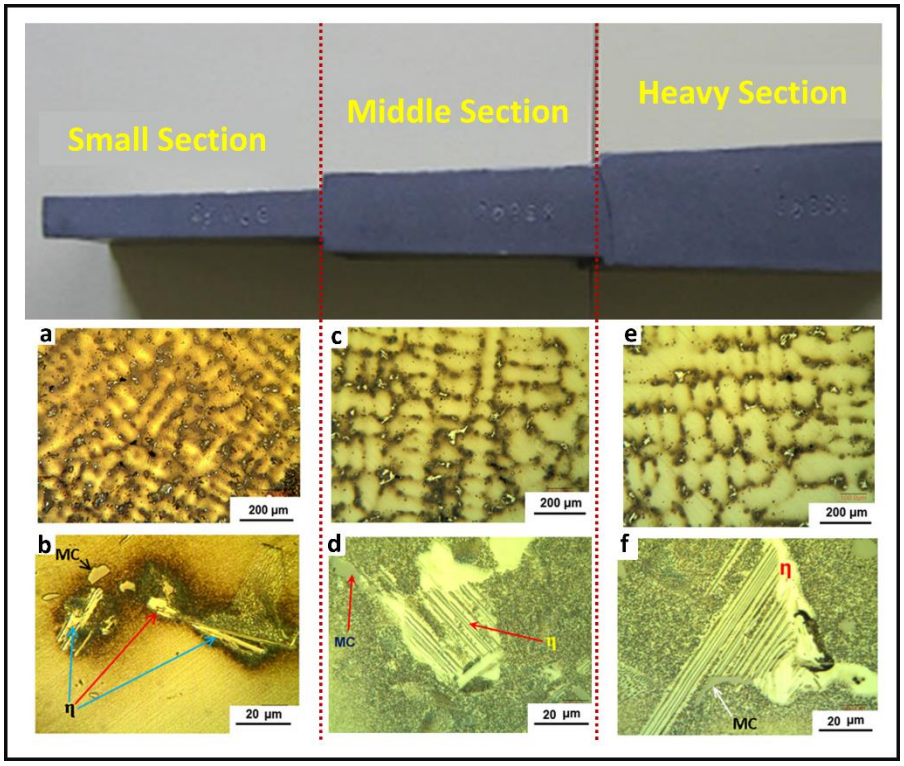

Figure 2.9 Optical micrographs of as-cast IN939 (a, b) small section (fast cooling rate), (c, d) middle section, and (e, f) heavy section (slow cooling rate). Re-drawn from [78].

As-wrought IN939 was reported by Jahangiri et al. [77,81]. In their study, IN939 ingots were cast, and then two-stage homogenization annealing was carried out at 1125 °C (for 20 h) and 1200 °C (for 10 h) to provide complete dissolution of η phase, prevent incipient melting and improve hot workability. After that, IN939 ingots were hot rolled. The microstructure after homogenization and final hot rolling is shown in Figure 2.10. Recrystallization and twins were observed in the wrought IN939 microstructure. These twins point out that twinning serves as a significant deformation mechanism for this alloy at elevated temperatures. Thus, these twins can affect the dynamic recrystallization of the alloy, and precipitation of the γ' phase and carbide particles, along with enhancing the alloy strength.

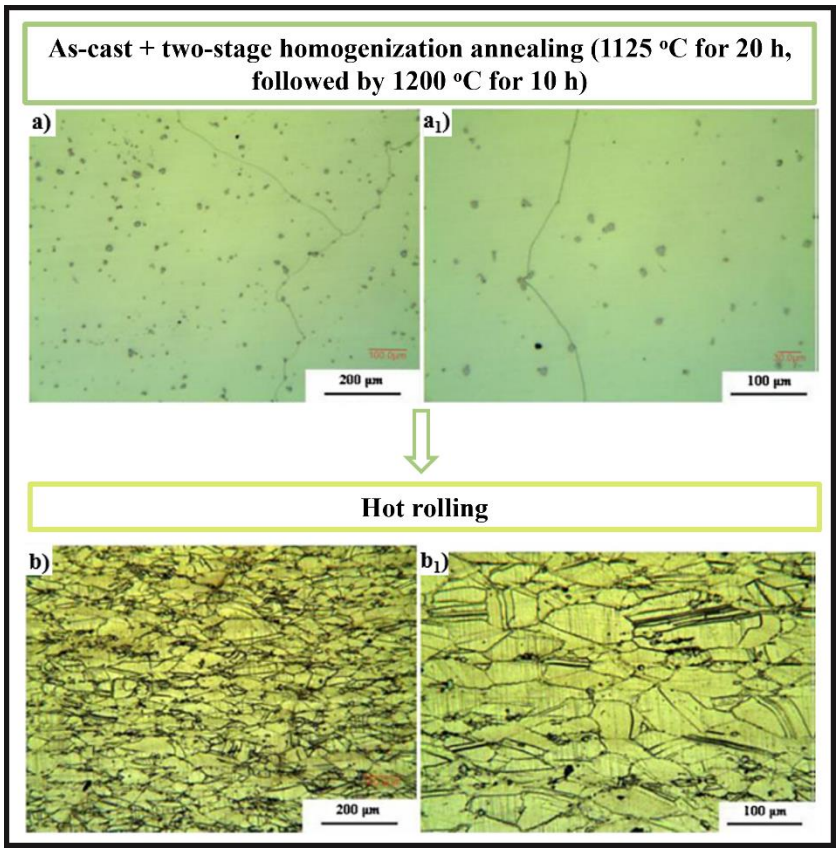

Figure 2.10 Optical micrographs of (a, a_1) as-cast + two-stage homogenized and (b, b_1) hot rolled IN939. Re-drawn from [81].

Figure 2.11 shows optical microscope and scanning electron microscope (SEM) images of IN939 sample fabricated by powder bed fusion-laser beam (PBF-LB) for both the XZ and XY planes. The XZ plane images reveal an arc-shaped melt pool morphology, resulting from the Gaussian energy distribution of the laser beam applied during the PBF-LB process. In the XY plane images, the laser beam scanning paths are evident. It is important to note that the physical and mechanical properties of as-fabricated parts are significantly influenced by the geometry of the melt pool morphology, including its shape, width, and depth, which are affected by the thermal history of the PBF-LB process. A high magnification SEM image (Figure 2.11(e)) shows the presence of cellular structures approximately 0.5 µm in size and columnar dendrites with an average dendrite arm spacing of approximately 0.7 µm within the structure [82].

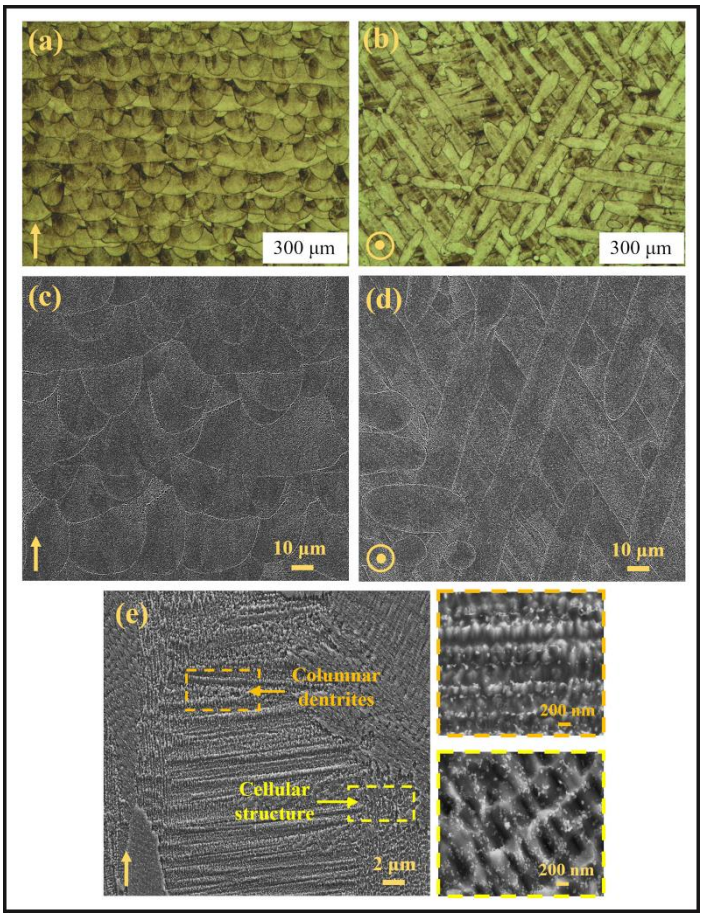

Figure 2.11 Optical microscope and SEM images of the as-fabricated IN939 sample: (a, c) the melt pool morphology in the XZ plane, (b, d) the laser beam scanning paths in the XY plane (XZ and XY planes are shown with an arrow and a dot, respectively) and (e) the high magnification image showing the cellular and columnar structures developed within the matrix. Re-drawn from [82].

The reaction temperatures have an important role in understanding the microstructure and phases of the alloys. Additionally, the stability ranges of different phases, as well as the solidus temperature of the alloy, are significant when designing the solution and precipitation hardening heat treatments. A summary of the most important reaction temperatures for IN939 are given in Table 2.4 [4]. Furthermore, phases observed in as-cast, heat-treated and service-exposed IN939 are shown in Table 2.5.

Table 2.4 A summary of the most important reaction temperatures for IN939 (adapted from [4]).

Phase reaction	**Temperature (ºC)** Gibbons and Stickler [62]	**Temperature (ºC)** Formenti et al. (from DTA) [75]	
		Heating	**Cooling**
Liquidus temperature (start of solidification)	1340	1339	1325
Formation of primary MC	1300	1276-1313	1250-1290
Solidus temperature (start of melting)	1235	1235	-
η phase solvus temperature	1145	-	1209
γ' phase solvus temperature	1080-1100	-	-
$M_{23}C_6$ carbide solvus temperature	~1000	-	-
σ phase solvus temperature	~950	-	-
Max rate of σ phase formation	~850	-	-

Table 2.5 Phases observed in as-cast, heat-treated and service-exposed IN939 (adapted from [4,62,78]).

Phase	**Composition (Elements bold are in greater concentration)**	**Observed Condition**
γ/γ' eutectic island		As-cast
γ matrix phase	Solid-solution (**Ni, Cr, Co**, Al, Ti, W, Ta, Nb)	4-stage heat treatment
γ' phase (coarse)	Ni_3Al (**Ni, Co, Al, Ti**, Cr, W, Nb, Ta)	4-stage heat treatment
γ' phase (fine)	Ni_3Al (**Ni, Al, Ti**, Co, Cr, W, Nb, Ta)	4-stage heat treatment
MC carbide	$MC_{0.88}$ (**Ti, Nb, Ta**, W)(**C**, N, Si, S, Zr)	As-cast 4-stage heat treatment
MC carbide	Nb rich Ti rich	As-cast 4-stage heat treatment
$M_{23}C_6$ carbide	Cr_{21}(**Mo, W**, Ni, Co, Ti, $Zr)_2$(**C**, $B)_6$	4-stage heat treatment + service exposed
σ phase	(**Ni, Co, Cr**, Al, Ti, W, Ta, Nb)	4-stage heat treatment + service exposed
η phase	Ni_3(**Ti**, Ta, Nb, Al)	As-cast
ε phase	Elemental Cr (Ni, Co, **Cr**, Ti, W, Ta, Nb)	4-stage heat treatment + service exposed
H phase	$(Zr, Ti)_2(C, S)$	All conditions

2.3.4.2 Heat Treatments of IN939

The properties of superalloys can be enhanced through the optimization of the manufacturing process and/or the application of heat treatments. Heat treatments are carried out to obtain optimal material performance, depending on alterations in the solubility of elements through heating and cooling processes [41]. Moreover, different post-heat treatments provide different microstructure and mechanical properties. These post-heat treatments can be categorized as SHT improving mechanical properties by dissolving detrimental phases, stress-relieve heat treatment reducing residual stress and texture, aging (single or more) providing precipitation of strengthening phases, homogenization reorienting columnar grains, and hot isostatic pressing (HIP) increasing density by decreasing defects [7,34,45,46]. Thus, optimization of the post-heat treatments is a significant step in obtaining the desired properties.

As mentioned before, IN939 is a precipitation-hardenable Ni-base superalloy. The objective of the precipitation hardening heat treatment is to obtain an optimal size and distribution of strengthening phases leading to the desired mechanical properties. However, it can be challenging to develop a heat treatment regime that provides both desired mechanical properties and efficiency in time and cost because of the complex microstructure in superalloys. Precipitation-hardening heat treatment has two main steps: SHT and aging steps. SHT is predominantly carried out by heating the alloy to a temperature between 1040-1230 °C to dissolve the precipitates formed during solidification, followed by rapid cooling of the part to ambient temperature, to prevent further precipitation. After that, the aging process is applied at a specific range of temperatures below the solvus temperature of the γ' phase and holding it at that temperature for a defined duration. The aim is to promote the nucleation and growth of the γ' phase, which contributes to strengthening the material [6,41,91].

A 4-stage heat treatment, also called standard heat treatment, for IN939 was developed by Shaw [64] to achieve the best tensile ductility, yield strength, and stress rupture life. The details of this heat treatment are given in Table 2.6. Furthermore, Gibbons and Stickler [62] reported microstructural development in every stage of this heat treatment (Table 2.7). Nevertheless, the prolonged duration associated with this heat treatment (50 h, including heating and cooling times) was considered economically impractical. Consequently, more time-efficient processing routes were actively sought.

Table 2.6 Different heat treatment routes for IN939 (adapted from [4,68]).

Heat treatment	Temperature (ºC)		Time (h)	Cooling	Remark
4-stage heat treatment	SHT	1160	4	FAC	Produces best overall mechanical properties.
	Aging 1	1000	6	FAC	
	Aging 2	900	24	AC	
	Aging 3	700	16	AC	
2-stage heat treatment	SHT	1160	4	FAC	Suitable for less demanding applications such as stationary vanes.
	Aging 1	1000	6	AC	
3-stage heat treatment	SHT	1190	4	FAC	Developed by EOS for additively manufactured IN939. 3-stage heat treatment results in similar or better properties than commonly used 4-stage heat treatment.
	Aging 1	1000	6	AC	
	Aging 2	800	4	AC	
FAC: Fast air cooling and AC: Air cooling					

Table 2.7 Standard heat treatment effects on IN939 microstructure (adapted from [62]).

Heat Treatment	Microstructure (affected by casting conditions, section size, cooling rates)
As-cast	Cored dendritic (dendrite core (Co-Cr-W-rich) and interdendritic regions (Ti-Ta-Nb-rich)) Primary MC carbide Plates of η phase (clusters in interdendritic regions) γ/γ' eutectic island (some primary γ' phase formed on cooling) Shrinkage pores (up to 0.3%)
Stage 1: SHT (1160 ºC / 4 h / FAC)	Homogenization of γ matrix Dissolution of γ' phase η phase rounded or dissolve Primary MC carbide unchanged, secondary MC carbide formed on cooling Fine γ' formed on cooling (20 nm)
Stage 2: Aging 1 (1000 ºC / 6 h / FAC)	Precipitation of primary γ' phase (70-150 nm) Precipitation of MC carbide at grain boundaries
Stage 3: Aging 2 (900 ºC / 24 h / AC)	Growth of primary γ' phase Precipitation of $M_{23}C_6$ carbide on grain boundaries in form of strings of discrete particles
Stage 4: Aging 3 (700 ºC / 16 h / AC)	Precipitation of fine γ' phase (redissolves at temperature above 820 ºC) to result in bimodal particle size distribution (150 nm + 20 nm) Slight increase in amount of $M_{23}C_6$ carbide

Moreover, research remains ongoing on the optimization of heat treatments for IN939 because different fabrication methods and process parameters affect the initial microstructure, along with phases and elemental segregations. Thus, heat treatments should be optimized according to the fabrication methods. In critical applications (particularly the aerospace industry), risks must be minimized by subjecting all components to the HIP process providing the elimination of pores [4].

A comprehensive study was conducted by Jahangiri et al. [77] regarding the microstructural stability of cast and wrought IN939 after applying 4-stage and 2-stage heat treatments during long-term aging. They concluded that a 2-stage heat treatment provides a more stable microstructure between 790-827 ^{o}C long-time aging, whereas a 4-stage heat treatment possesses a more stable microstructure in a temperature range of 827-910 ^{o}C.

Kazempour-Liasi et al. [92] studied the effects of pre- and post-weld heat treatments on the cracking of IN939 during welding. They performed 2-, 3-, and 4- stage heat treatments as a post-weld heat treatment cycle in addition to various pre-weld heat treatments. Additionally, they observed that heat treatments reduced the liquation and strain-age cracking in the heat-affected zone (HAZ).

Philpott et al. [74] compared the conventional heat treatment on the cast and additively manufactured IN939. The investigation assessed the impact of HIP, a standard 4-stage heat treatment and a modified 2-stage heat treatment on both cast and additively manufactured IN939. The findings indicated that additively manufactured IN939 underwent recrystallization and grain growth yet maintained a much smaller grain size compared to cast IN939. Notably, there was a significant difference in the precipitation and growth behaviour of carbides, with additively manufactured IN939 exhibiting networks of much finer carbide particles in the microstructure after heat treatment. Despite studying the γ' phase precipitation, no notable difference was observed between the cast and additively manufactured IN939.

Shaikh et al. [33] investigated the necessity of the solution heat treatment step for IN939 fabricated by PBF-LB by conducting direct aging and solution heat treatment with double aging. They reported that as-built IN939 contains sub-micron-sized platelet precipitates, which can be η phase according to transmission electron microscopy (TEM) compositional analysis in the interdendritic regions. Rapid growth was observed for this phase during direct aging (without SHT) and had a detrimental effect on ductility. Drawing from the outcomes of this study, it can be deduced that although a SHT may not be

mandatory for the dissolution of γ′ phase, it is still required to obtain a stable, eta phase-free microstructure.

2.3.4.3 Mechanical Properties of IN939

The mechanical properties of precipitation-hardenable Ni-base superalloys change according to the manufacturing method, applied heat treatment and exposure to high temperatures, as the gamma prime phase becomes coarse and thermodynamically stable phases form. IN939 is a highly corrosion-resistant alloy capable of prolonged operation at temperatures of up to 850 °C. For this reason, microstructural stability at elevated temperatures, as well as high-temperature corrosion, oxidation and creep resistance, are significant properties for IN939 [3]. Table 2.8 summarizes the mechanical properties of IN939.

Table 2.8 A summary of the mechanical properties of IN939 [4].

	21 ºC	**650 ºC**	**760 ºC**	**870 ºC**	**980 ºC**
YS 0.2% Offset (MPa)	800	695	635	400	205
UTS (MPa)	1050	985	915	640	325
Tensile Elongation (%)	5	7	7	18	25
1000 h–Rupture Strength (MPa)	425	195	60		
Youngs Modulus (GPa)	195 to 205				
Compressive Strength (MPa)	700 to 880				
Flexural Modulus	195 to 205				
Modulus of Rupture (MPa)	700 to 880				
Shear Modulus (GPa)	75 to 85				
Bulk Modulus (GPa)	140 to 165				
Poisson's Ratio	0.27 to 0.29				
Fatigue Strength at 10^7 cycles (MPa)	340 to 535				
Fracture Toughness (MPa$\sqrt{m}$)	26 to 28.9				
Hardness (HV)	250 to 350				
YS: Yield strength and UTS: Ultimate tensile Strength All values are given for tests at room temperature (RT) unless otherwise stated. Values given in ranges account for aging condition of alloy.					

Additionally, the mechanical properties of the as-built and heat-treated IN939 fabricated by PBF-LB are given in Table 2.9. Moreover, Table 2.10 shows the comparison of the measured average room temperature tensile properties for the heat-treated cast and additively manufactured IN939. For all four heat treatments, additively manufactured

IN939 samples have higher yield strengths and elongation values higher than cast IN939. This can be explained by the smaller grain size and finer precipitates in the microstructure.

Table 2.9 Mechanical properties of IN939 fabricated by the PBF-LB [68].

Build Direction	**Tensile Test Condition**	**0.2% YS (MPa)**	**UTS (MPa)**	**Elongation (%)**	**HRC**
As-built (Vertical)	@Room temperature	740	1090	28	33
As-built (Horizontal)		880	1160	24	
Heat-treated (Vertical)	@Room temperature	1100	1500	13	48
Heat-treated (Horizontal)		1130	1520	11	
Heat Treatment: 4 h, 1190 ºC (FAC) + 6 h, 1000 ºC (FAC) + 4 h, 800 ºC (AC)					

Temperature	**25 - 100 ºC**	**25 - 200 ºC**	**25 - 400 ºC**	**25 - 600 ºC**	**25 - 800 ºC**	**25 - 900 ºC**
CTE (As-built)	$12.18*10^{-6}$/K	$12.89*10^{-6}$/K	$13.78*10^{-6}$/K	$13.49*10^{-6}$/K	$13.99*10^{-6}$/K	$15.06*10^{-6}$/K
CTE (Heat-treated)	$11.79*10^{-6}$/K	$12.64*10^{-6}$/K	$13.64*10^{-6}$/K	$14.27*10^{-6}$/K	$15.29*10^{-6}$/K	$16.32*10^{-6}$/K
CTE: Coefficient of Thermal Expansion						

Table 2.10 Comparison of the measured average room temperature tensile properties for the cast and additively manufactured IN939.

Fabrication Method	**Heat Treatment**	**0.2% YS (MPa)**	**UTS (MPa)**	**Elongation (%)**	**Reference**
As-cast	4-stage 4 h, 1150 ºC + 6 h, 1000 ºC + 24 h, 900 ºC + 16 h, 700 ºC	786	958	3.4	[80]
	3-stage 4 h, 1150 ºC + 6 h, 1000 ºC + 16 h, 700 ºC	785	978	3.6	
	2-stage 4 h, 1150 ºC + 16 h, 845 ºC	823	861	2.0	
	2-stage 4 h, 1150 ºC + 6 h, 1000 ºC	651	974	9.2	
Fabricated by PBF-LB	4-stage 4 h, 1150 ºC + 6 h, 1000 ºC + 24 h, 900 ºC + 16 h, 700 ºC	1041	-	10.0	[4]
	3-stage 4 h, 1150 ºC + 6 h, 1000 ºC + 16 h, 700 ºC	1103	-	10.9	
	2-stage 4 h, 1150 ºC + 6 h, 1000 ºC	986	-	18.2	
	2-stage 4 h, 1150 ºC + 16 h, 845 ºC	1164	-	12.2	
Room temperature tensile properties for the vertically fabricated samples.					

2.3.5 Cracking Phenomena in Ni-base Superalloys

Ni-base superalloys, especially those that have a high-volume fraction of the γ' phase (>30%), are prone to cracking during processing or heat treatment due to their complex chemistry and high-temperature strength [93]. This susceptibility is particularly pronounced in rapid solidification processes, such as welding or PBF-LB processes, rather than casting [48,94,95]. Figure 2.12 exhibits the weldability assessment plot of some Ni-base superalloys according to the composition of Al + Ti and Cr + Co. Although these assessments act as a useful guide for weldability, cracking can still occur even in "weldable" superalloys because of incompatible processing conditions [93]. The rapid melting and solidification of metal during the PBF-LB process may cause high residual stress, undesirable metastable phases and cracking according to process parameters. For this reason, it is important to note that cracking can be observed in conventionally weldable Ni-base superalloys such as Hastelloy X fabricated by the PBF-LB when incompatible process parameters are used [29,96–99].

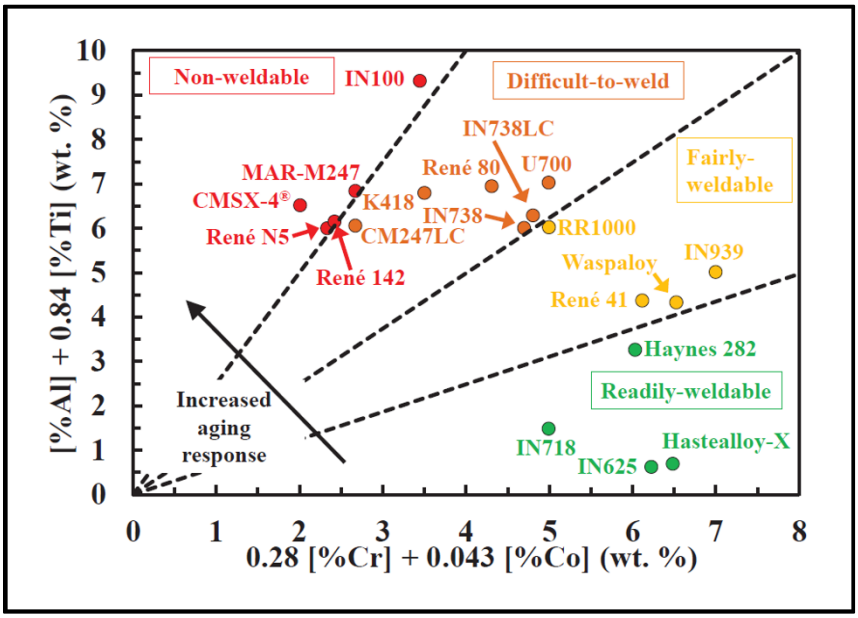

Figure 2.12 The weldability assessment plot for some Ni-base superalloys. Re-drawn from [100].

There are four cracking mechanisms which are solidification cracking, liquation cracking, strain-age cracking and ductility-dip cracking for precipitation-strengthened Ni-base superalloys. The main crack types in Ni-base superalloys, along with the comparison are given in Figure 2.13 [48,99,101,102].

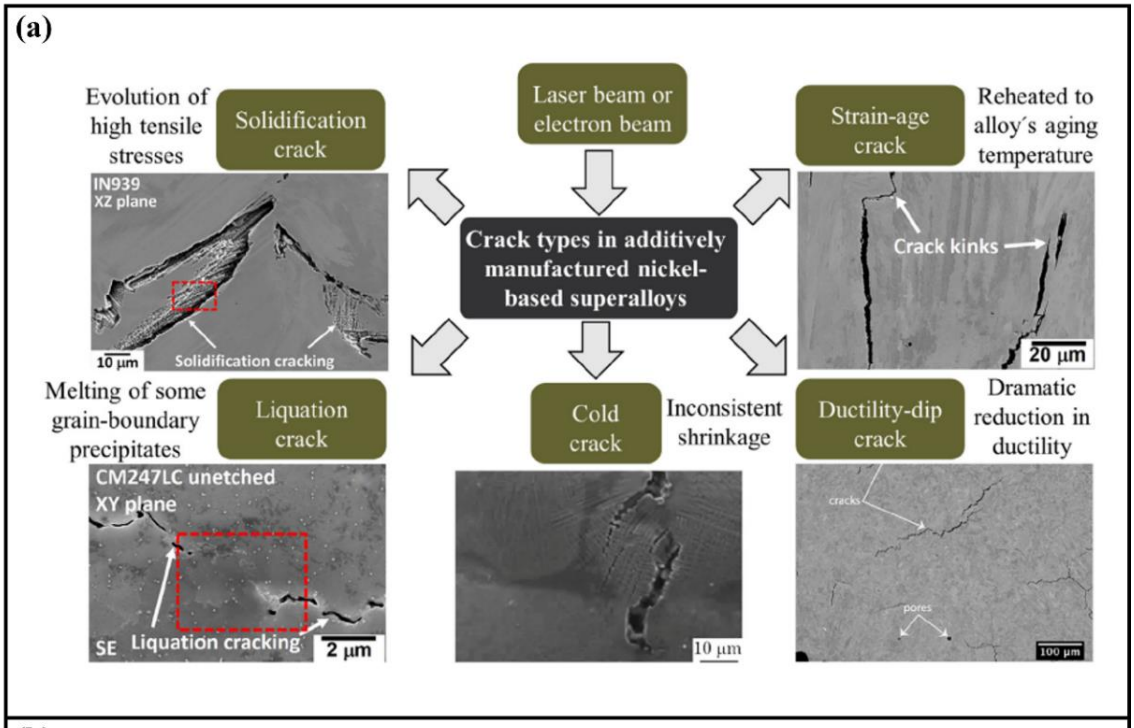

(b)

Mechanism	Solidification cracking	Liquation cracking	Ductility dip cracking	Strain age cracking
Category	Hot crack	Hot crack	Hot/cold crack	Cold crack
Time	Process	Process	Process	Process[1] / HT
Temperature	~T_{sol}	~T_{sol}	0.5-0.8 T_{liq}	γ'-precipit. range
Location	Solidification zone	GB in HAZ	GB in HAZ	GB and weak points (e.g. defects)
Origin of relevant stress	Volume shrinkage during solidification and cooling	Transient thermal stresses acting at GB	Transient thermal stresses acting primarily normal to GB	Residual stresses + volume change due to γ'-precipitation
Metallurgical condition: → influence of this condition on local: ↓	Segregation at solidification front	Low melting phases at GB	Brittle GB due to accumulated strain at GB triple points or irregularities causing strain concentrations	γ-phase oversaturated with γ'-formers
T_{sol}	▼	▼	–	–
Strength	▼	▼	–	▲
Ductility	–	–	▼	▼

Characterization of principle crack formation mechanisms in γ'-strengthened Ni-base superalloys. (GB = grain boundary, [1]Preheating temperature is in or above the temperature range for γ'-precipitation, symbols: ▼ = decrease, ▲ = increase, - = unchanged).

Figure 2.13 (a) The main crack types in Ni-base superalloys and (b) comparison of their mechanisms. Re-drawn from [48,102].

2.3.5.1 Solidification Cracking

Solidification cracking, which is also called hot cracking, is commonly observed in Ni-base superalloys fabricated by traditional manufacturing methods (such as casting), welding, and AM. Solidification cracks, also known as hot tears, occur where the material is in a semisolid state within the solidifying melt pool or the mushy zone [94,102,103]. The mechanism of solidification cracking, along with SEM images of solidification cracks in CM247LC and IN939, are shown in Figure 2.14. Moreover, high-angle grain boundary (HAGB, $\Theta > 15^{o}$) behaving as repulsive boundaries are more prone to solidification cracking than low-angle grain boundary (LAGB, $\Theta < 15^{o}$) behaving as attractive boundaries, as HAGB energy causes more stable liquid films, increasing cracking risk [104–106]. Furthermore, grain boundary strengthening elements (Zr, B, and C) segregate to the interdendritic regions upon melting and generate the low-melting liquid films. For this reason, they increase the susceptibility to solidification cracking. In addition to them, P and S which must be kept to the lowest possible point show the same effect, adding no benefit to the alloy. In general, the addition of alloying elements may promote solidification cracking when they widen the solidification range [4,94].

Solidification cracking occurs during the AM solidification process according to the following [94,102,103,107]:

- Dendrites form at the interface between molten and solid metal phases. Rapid heating and cooling cause non-equilibrium solidification, leading to solute segregation at the solidification interface. Segregated elements at grain boundaries lower the solidus temperature, creating low-melting liquid films around emerging grains.

- As dendrites grow and merge, they isolate areas of molten metal ("islands"), forming voids that serve as crack initiation sites upon solidification. The solidification of these islands results in the formation of voids (which are not fed by molten metal supply, serving as sites where cracks initiate).

- When residual stress occurs during the solidification process, this can be transmitted through solids but not by liquids. Consequently, this stress accumulates in the liquid films, surpassing their yield strength. Finally, cracking paths form within these liquid films, along which tears propagate in the final stage of solidification. Thus, the formation of cracks occurs.

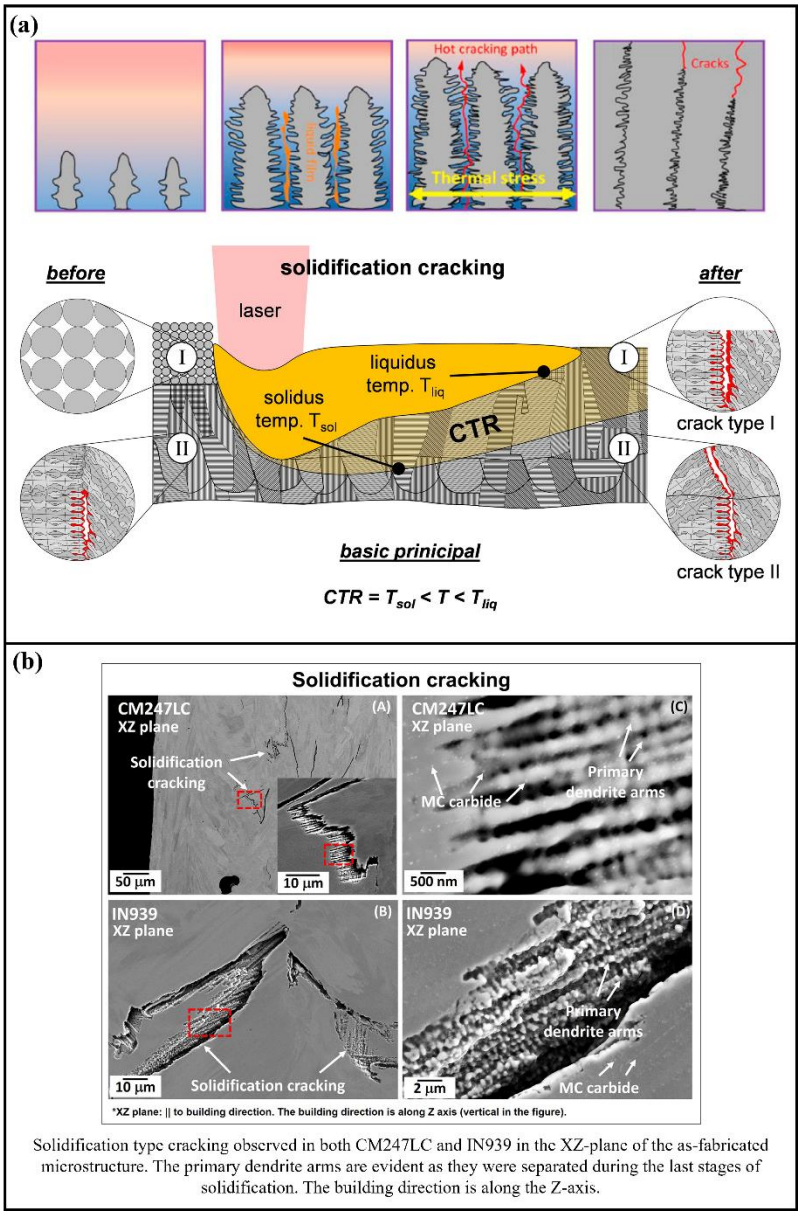

Solidification type cracking observed in both CM247LC and IN939 in the XZ-plane of the as-fabricated microstructure. The primary dendrite arms are evident as they were separated during the last stages of solidification. The building direction is along the Z-axis.

Figure 2.14 (a) The solidification cracking mechanism and (b) SEM images of solidification cracks in CM247LC and IN939. Re-drawn from [16,102,103,108].

2.3.5.2 Liquation Cracking

Liquation cracking, classified as a hot cracking, occurs in the laser-welding formation and appears as tiny tears in the HAZ of welding beads and melt pools. The heat-flow mechanics and thermal stresses, phases present, and their morphology, freezing ranges and grain boundary orientation affect this cracking. Additionally, the formation of localized liquid films and the nature of thermal stresses are two critical factors [93,103]. There are two basic mechanisms for HAZ liquation cracking:

- Segregation mechanism where solute and/or impurity elements segregate to the grain boundaries through a diffusion mechanism, thereby reducing the local melting temperature of the grain boundary. Solid solution-strengthened Ni-base superalloys show mostly the segregation mechanism because they are designed to be single-phase with all alloying elements in solution. Also, their cracking susceptibility is generally lower than that of precipitation-strengthened Ni-base superalloys [94].

- Penetration mechanism where local melting takes place within the microstructure at elevated temperatures and intersects with a mobile grain boundary. Subsequently, the liquid infiltrates and wets the grain boundary. The penetration mechanism has two conditions such as constitutional liquation and low-melting-point secondary precipitation (eutectic melting). In constitutional liquation, which occurs in Ni-base superalloys with secondary constituents (i.e., carbides, intermetallics, or TCP phases), the rapid heating during welding does not allow sufficient time for the secondary phase to dissolve completely into the matrix. When the eutectic temperature is surpassed, the secondary phase interacts with the matrix, forming an interfacial liquid film at the eutectic composition. These films can coalesce into larger areas, leading to liquation cracking [94,103,109]. In low-melting-point secondary precipitation, there is not enough time for the dissolution of the eutectic constituents such as γ'-γ eutectic precipitates [110], γ-Laves eutectic precipitates [111], and carbides [112] due to the rapid heating cycle. When the temperature exceeds the eutectic temperature, these eutectic constituents simply melt. When the superalloy surpasses its maximum solid solubility, the eutectic constituent remains insoluble regardless of the heating rate, leading to consistent localized melting [94,103]. The penetration mechanism types in liquation cracking, along with SEM images of liquation cracks in CM247LC are shown in Figure 2.15.

Liquation cracks are prone to propagating along the HAGBs like solidification cracks. Although liquation cracking is similar to solidification cracking, there is no dendritic structure on the cracked surface in liquation cracks [102,113].

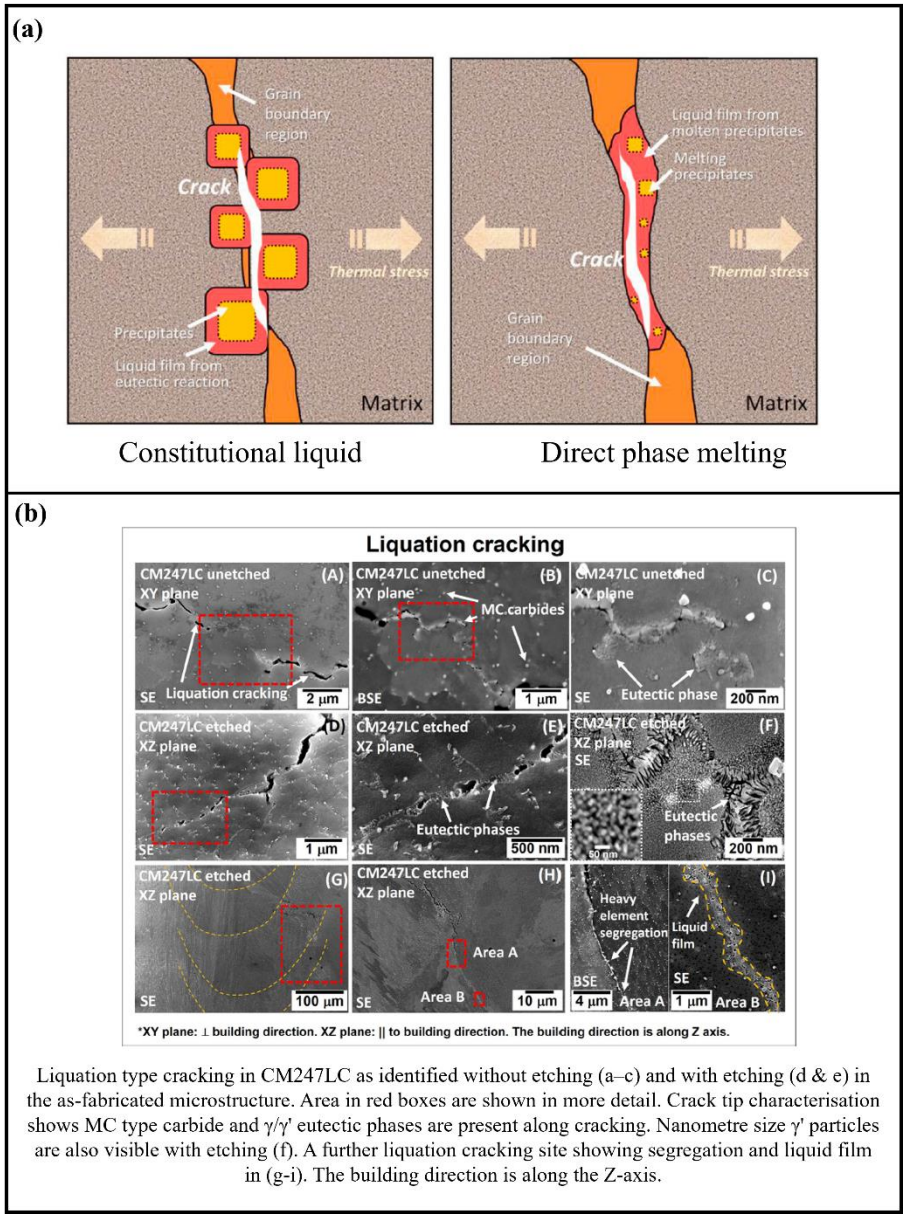

Liquation type cracking in CM247LC as identified without etching (a–c) and with etching (d & e) in the as-fabricated microstructure. Area in red boxes are shown in more detail. Crack tip characterisation shows MC type carbide and γ/γ' eutectic phases are present along cracking. Nanometre size γ' particles are also visible with etching (f). A further liquation cracking site showing segregation and liquid film in (g-i). The building direction is along the Z-axis.

Figure 2.15 (a) The penetration mechanism types in liquation cracking and SEM images of liquation cracks in CM247LC. Re-drawn from [16,103].

2.3.5.3 Solid-State Cracking

Strain-age cracking (SAC), a type of solid-state cracking or cold-cracking, is specific to the precipitation-strengthened Ni-base superalloys. It occurs mostly in the HAZ (just adjacent to the fusion boundary) during post-weld heat treatment or service, but it is also possible, albeit unlikely, to occur during reheating in multipass welds [4,48,94,102]. SAC is most common in the γ' phase strengthening superalloys and the term "unweldable" is used for many of these superalloys because of their susceptibility to SAC. The precipitation of the γ' phase from the oversaturated γ phase results in enhanced strength but reduced ductility when the material undergoes its initial heating cycle and passes the

associated temperature range (approximately 500-1100 °C). Subsequently, the process-induced stresses and additional stresses from the γ' phase precipitation (volume change) cause the formation of SAC at stress concentration points such as grain boundaries and weak points in the microstructure [4,48,94,99,114].

For SAC, the local strain and aging must occur almost simultaneously and general observations about SAC are the following [94]:

- It is always intergranular.

- Although it is most common in the HAZ (adjacent to the fusion line), it can be linked with the partially melted zone (PMZ) in some cases.

- It occurs during post-weld heating to the SHT temperature due to the simultaneous occurrence of precipitation and localized strain accumulation at grain boundaries.

Ductility-dip cracking (DDC) which is a solid-state phenomenon occurring at elevated temperatures, typically occurs in austenitic stainless steel and Ni-base superalloys (produced through multi-pass welding and laser-based AM). It is reported that these cracks are believed to be linked to a phenomenon known as a dramatic reduction in ductility (a ductility dip) in Ni-base superalloys under intermediate temperature conditions. Moreover, DDC possesses a creep-like mechanism that occurs in a temperature range that is below the threshold for dynamic recrystallization but high enough to allow grain-boundary sliding [4,102,103]. For this reason, a DDC is likely to form at a temperature ranging from 0.5Tm to 0.7Tm of the superalloy (at which temperature the superalloy suffers a quick drop of ductility). Furthermore, DDC susceptibility is affected by grain size, grain boundary segregation, grain boundary pinning by carbides and borides, impurities, alloy composition, precipitation, crystallographic orientation, relative to the applied stress and dynamic recrystallization [102,112,115,116]. Figure 2.16 shows examples of solid-state cracking.

IN939 is in the “fairly weldable” region according to Figure 2.12. Also, it is very close to the readily weldable region. There are limited studies about the cracking phenomena of IN939 in the literature. The liquation cracking (which was led due to MC carbide, γ′ phase particles, the eutectic γ–γ′ phase and the low melting phases) was reported in the HAZ of cast IN939 during tungsten inert (TIG) gas weldments [92,117–119]. On the other hand, solidification cracking and solid-state cracking were observed in IN939 fabricated by PBF-LB [16,85].

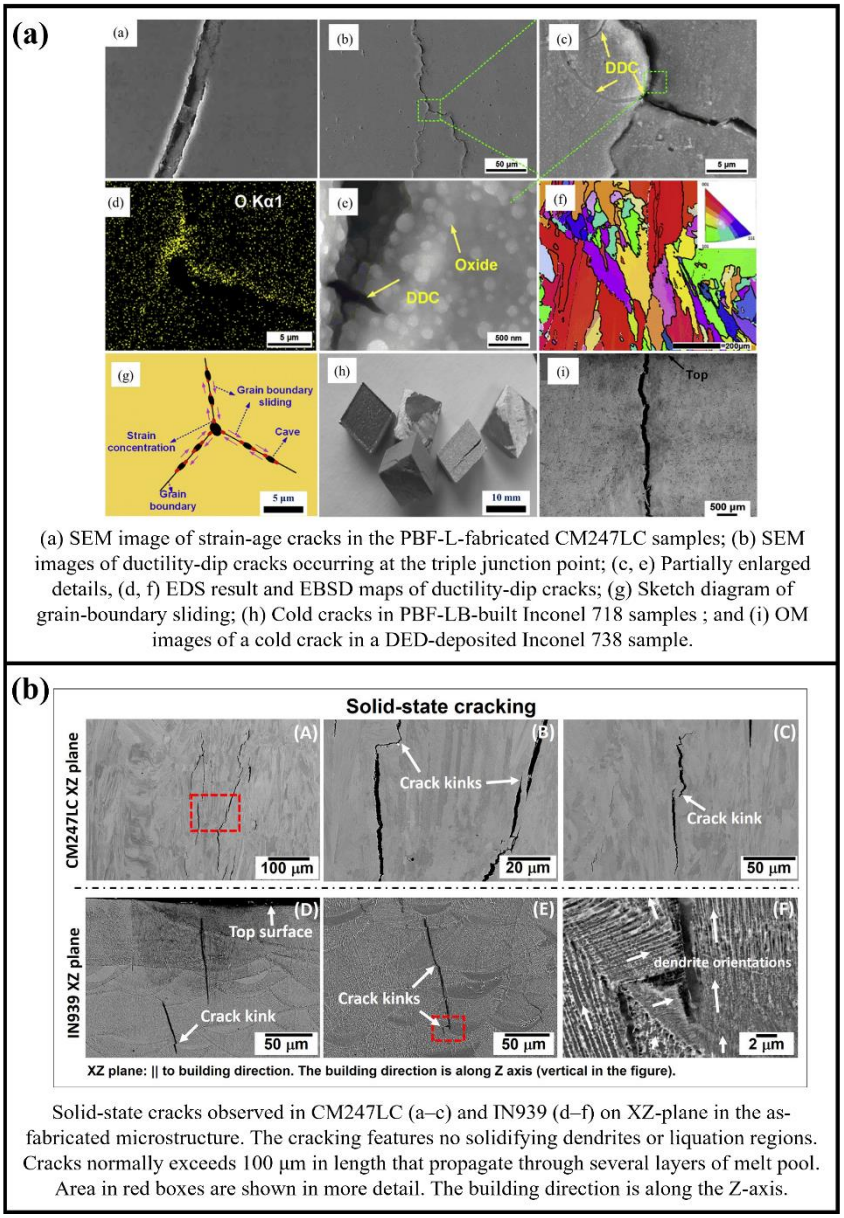

Figure 2.16 Examples of solid-state cracking. Re-drawn from [16,102].

Crack suppression has gained lots of attention and there is still much research ongoing about this worldwide. A summary of crack suppression methods and the causes of cracks is given in Figure 2.17. Basically, process parameters optimization, postprocessing and material modification are used to suppress cracks in Ni-base superalloys fabricated by high-energy beam AM [93,102,103].

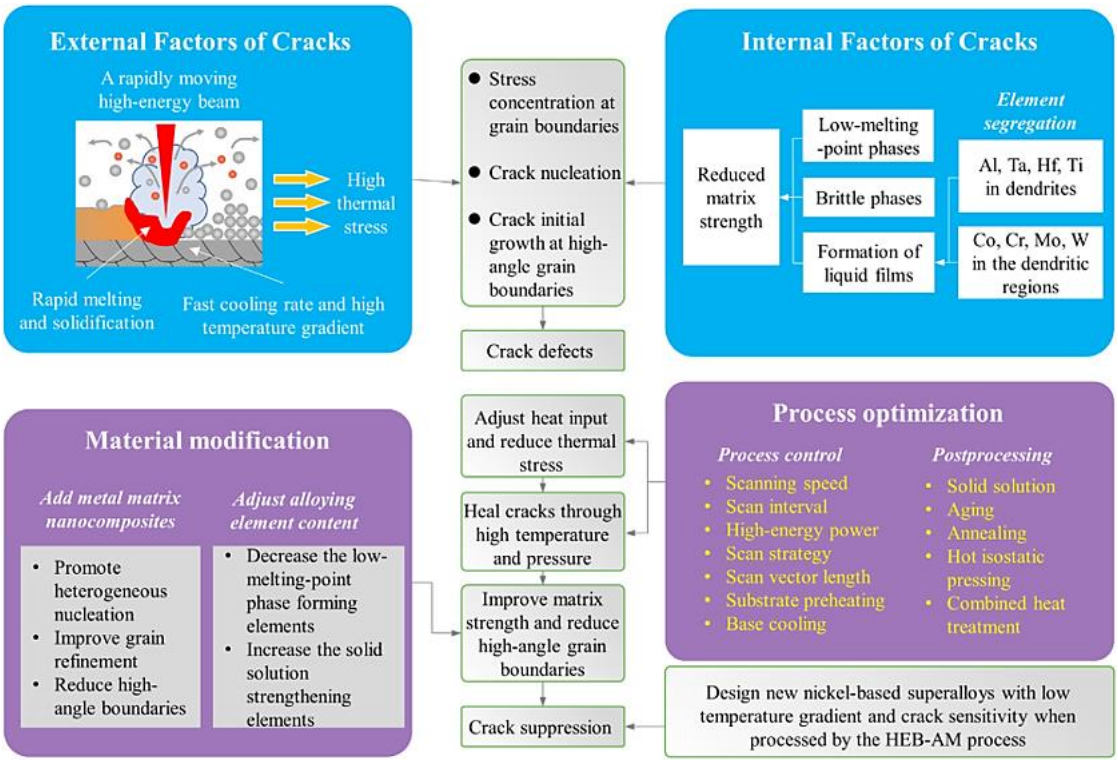

Figure 2.17 A summary of crack suppression methods and the causes of cracks [102].

2.4 Powder Bed Fusion-Laser Beam

Metal additive manufacturing (AM) processes build parts layer-by-layer. They provide numerous advantages over conventional manufacturing processes, such as the production of intricate geometries in a single step, along with design freedom, near-zero material waste and cost-efficiency compared to conventional manufacturing techniques [44,120,121]. One industry that is making increasing use of metal AM is the aerospace industry [8,122,123] where revenues are expected to be US$430 billion by the year 2025 [122].

The powder bed fusion-laser beam (PBF-LB) process, also known as selective laser melting (SLM) and laser powder bed fusion (L-PBF), is a metal AM process that uses a focused laser beam to melt metal powder. It has been used for different industries such as aerospace, defense, energy, automotive and biomedical industries. Additionally, it is particularly useful for the aerospace industry due to the aforementioned properties, high dimensional accuracy, reduced mass of components, lower cost and shorter lead times than conventional manufacturing approaches [17,124–129]. In PBF-LB process, each layer comprises a 2D cross-section of the geometry that is melted by a moving laser beam spot. The melted volume rapidly solidifies and bonds to the underlying layer. Figure 2.18 shows

the schematic diagram illustrating a typical PBF-LB arrangement, along with the process explanation.

To obtain the desired properties, the required microstructure, density, surface roughness and mechanical properties need to be attained through the optimization of process parameters. The primary microstructure in the as-built state can be controlled to a great extent by the process parameters. Moreover, the desired mechanical properties change according to the application areas. For instance, aerospace fasteners require high tensile and shear strengths, unlike turbine blades which require excellent creep and fatigue resistance [44].

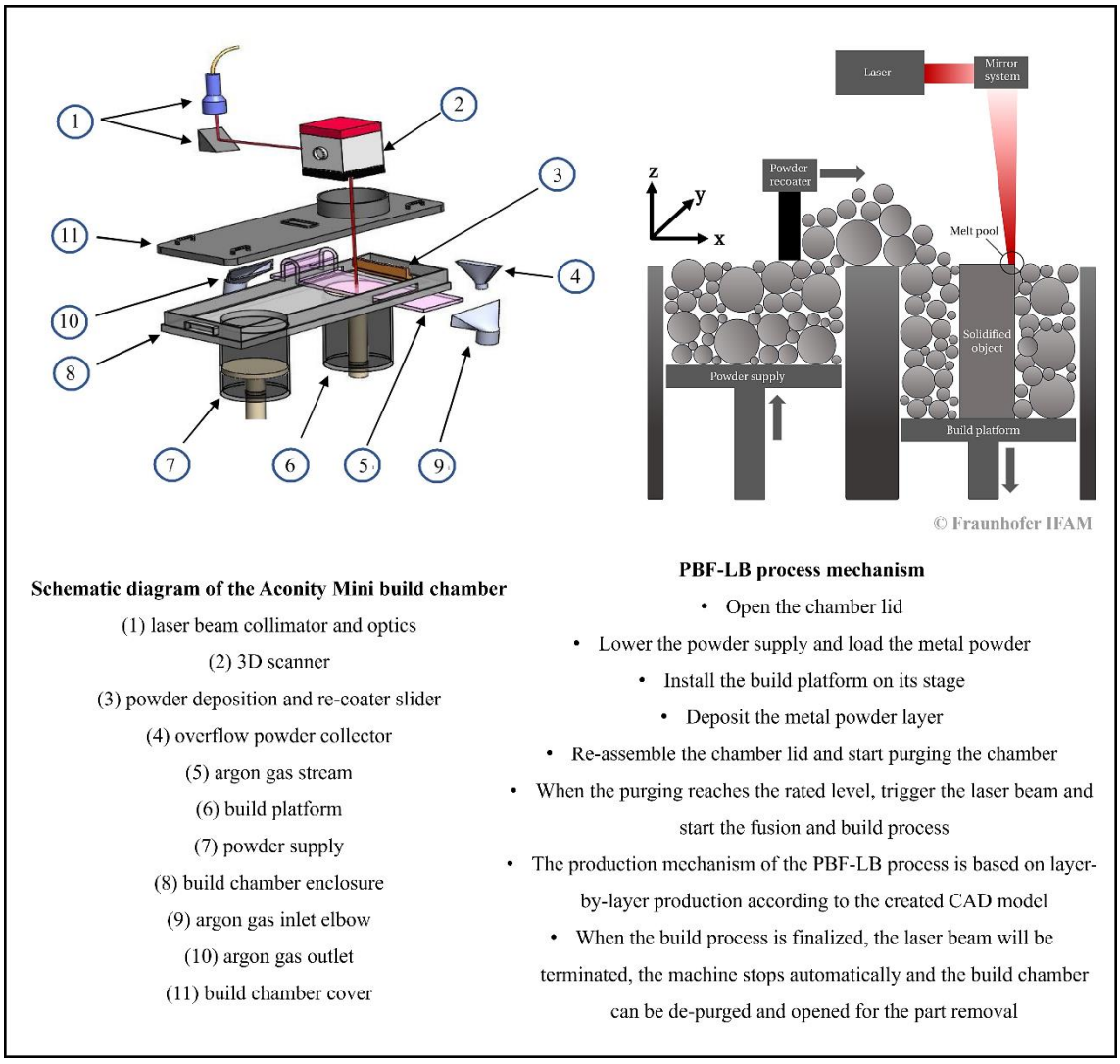

Figure 2.18 Schematic diagram illustrating a typical PBF-LB arrangement. Re-drawn from [130–132].

2.4.1 Process Parameters

Oliveira et al. [133] reviewed the processing parameters in PBF-LB and found that there are more than 100 process parameters that need to be considered. Among those, the most influential parameters are laser power, scanning speed, layer thickness, hatch distance (distance between successive layer passes) and laser scanning pattern on each layer (scanning strategies) [133]. Illustration of classified process parameters for the PBF-LB process are shown in Figure 2.19. Moreover, some process parameters can be set in advance, while others require monitoring and controlling (Table 2.11) [134].

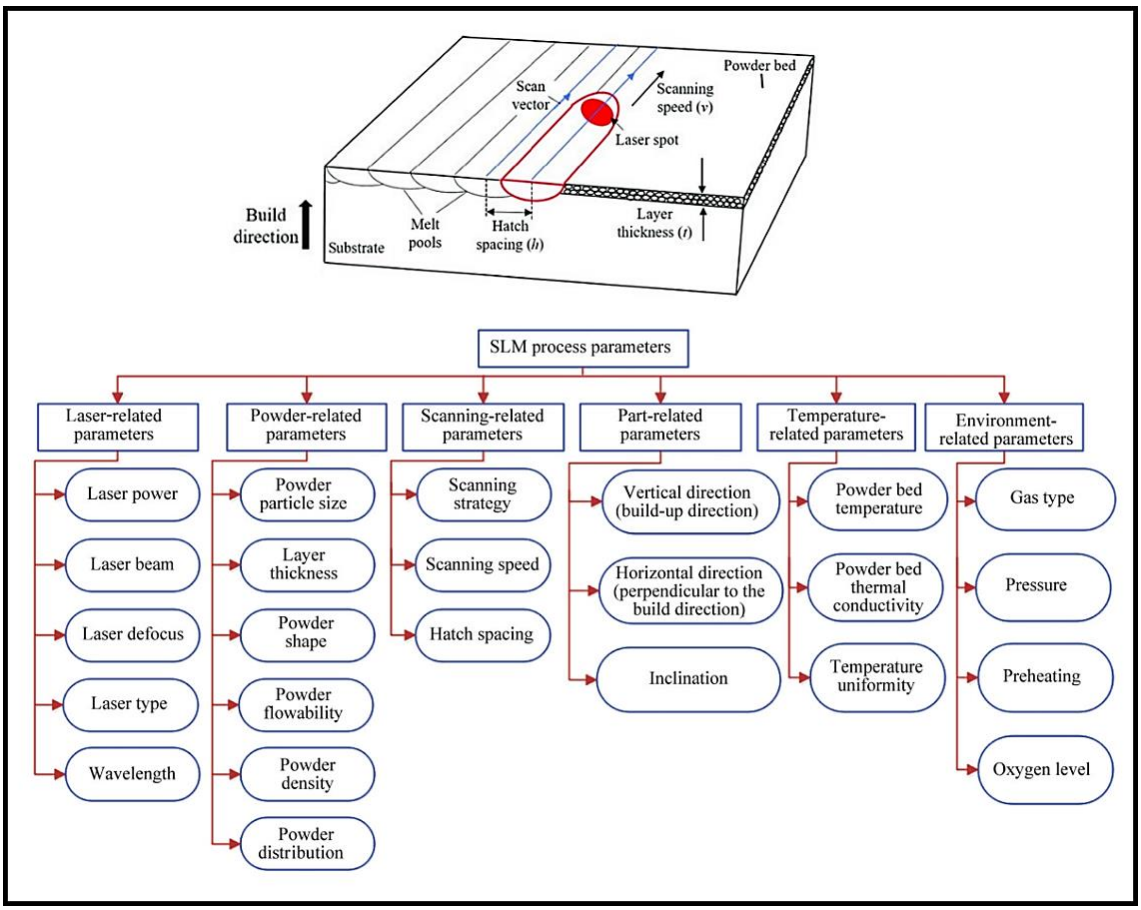

Figure 2.19 Illustration of classified process parameters for the PBF-LB process. Re-drawn from [134,135].

Table 2.11 Predefined and controllable PBF-LB process parameters (adapted from [134]).

Process Parameters	Affected Features
Controllable Parameters	
Laser Power	Distortion, part shrinkage, melt pool size and stability, depth of penetration, porosity, impurity picked-up and part functionality
Scanning Speed	Surface roughness, distortion, part shrinkage, part density, melt pool size, cracks, fracture and part functionality
Hatch Distance	Microstructural waviness, surface roughness, microstructural heterogeneity, porosity, dimension inaccuracy, shrinkage, melt pool size and part functionality
Defocus Distance	Melt pool morphology, mechanical properties, porosity and build time
Layer Thickness	Build time, staircase effect, part shrinkage, bonding, part density, porosity, surface roughness, dimensional inaccuracy and part functionality
Predefined Parameters	
Powder Shape	Flowability, impurity picked-up, packing density and porosity
Build Orientation	Anisotropy, residual stress, staircase effect, porosity, build time, dimensional inaccuracy, surface roughness, and functionality
Powder Size	Heterogeneity, packing density, porosity, impurity picked-up, functionality and balling
Gas Flow Rate & Direction	Dimensional deviation, quality of layer bonding, porosity and mechanical properties
Chamber & Powder Bed Temperature	Heterogeneity, part shrinkage and warpage

2.4.1.1 Laser Power

The laser power, a laser-related parameter, is the main parameter that transfers energy from the PBF-LB system to the powder. The aim is to melt the powder homogeneously to fabricate dense bulk components [17]. Raising the laser power is often linked with easier melting of the precursor powders, thus resulting in better densification of the as-built parts. Nevertheless, an uncontrolled increase of the laser power alone can induce porosity in the final products due to the emergence of keyhole pores and strong convective flows in the molten material [136–139]. Moreover, the melt pool dimension (generated by heating), microstructural coarsening and a higher incidence of microcracking are caused by high laser power [17,136,140–146]. For this reason, process parameters optimization is significant to eliminate defects, achieve the highest density and reduce the overall cost [137] .

2.4.1.2 Scanning Speed

The scanning speed, a scanning-related parameter, refers to the rate at which the laser beam moves across the surface of the powder bed. It has a crucial role in determining

the build rate of the produced parts. Additionally, it impacts the duration for which each section of the powder bed is exposed to the laser power, thereby affecting the energy available for melting. High scanning speeds contribute to high build rates. However, they may also result in undesirable outcomes such as a lack of fusion porosity and defects (i.e., balling) in the as-built materials. These issues are attributed to the elevated shear stresses within the melt pool when subjected to such conditions. Moreover, higher scanning speeds result in a shallower melt pool depth and narrower scanned line width due to the faster solidification rate of the melt pool. On the contrary, the amount of energy per unit of time in the melt pool can increase with a low scanning speed, thereby expanding the dimensions of the melt pool (which causes keyhole phenomenon and spattering due to turbulent melting). Furthermore, high crack density during solidification is often associated with low scanning speeds. This phenomenon occurs because low scanning speeds lead to higher maximum temperatures within the powder bed, thereby increasing the residual stresses in the solidified melt pool [17,108,137,146–150].

2.4.1.3 Hatch distance

The hatch distance or hatch spacing, a scanning-related parameter, determines the spacing between two passes of the laser beam, thereby regulating the heating of the powder bed surface. A smaller hatch distance can result in excess energy input, while a larger hatch distance may cause insufficient contact between molten regions of the powder bed. Additionally, small hatch distances lead to extensive overlap of molten material, whereas large hatch distances can lead to incomplete melting and the entrapment of unmelted powder particles. For this reason, finding an optimal distance is crucial for ensuring the quality of the final build [17,130,147]. The literature suggests that the appropriate overlap ratio varies depending on the specific case, but typically falls within the range of 40 to 60% [147,151].

2.4.1.4 Layer Thickness

The layer thickness, a powder-related parameter, determines the height of each successive powder layer that will be melted by the laser beam. Thus, it controls the build rate and total production time of individual components, which could be helpful for the industries in terms of speeding up the process, along with increasing cost efficiency [17,130,152]. Determining the layer thickness involves considering several factors. Firstly, it must align with the maximum power capacity of the laser system and whether it can adequately melt the thickness at the chosen scanning speed. Additionally, the minimum

layer thickness and the minimal feature size that can be built are constrained by the powder particle size [130]. Increasing layer thickness leads to adverse effects on the final properties of the fabricated parts. These include diminished dimensional accuracy and decreased mechanical properties such as YS, UTS, Young's modulus, Vickers microhardness and impact toughness. Moreover, thicker layers result in lower cooling rates within the powder bed and larger dendritic arm spacing in the final microstructure. On the other hand, the thinner layer thickness is associated with increased tensile strength and hardness [17,147,153–155].

2.4.1.5 Scanning Strategy

The scanning strategy, a scanning-related parameter, is a combination of several factors such as the scanning pattern (or hatch type), hatch distance, off-set (contour), hatching starting angle, scan direction, hatch rotating angle per build layer, scan vector length and up and down skin [28,130,156–162]. Schematics of different types of scanning strategies are given in Figure 2.20. The scanning strategy affects the final microstructure, surface roughness, density, crystallographic texture, anisotropy, mechanical properties and geometry-induced residual stresses [28,162–164]. In general, a shorter scan vector length is advantageous for reducing residual stress and enhancing the mechanical properties of AM parts [28]. Moreover, layer rotation can be implemented in various layer strategies, resulting in diverse outcomes. When no rotation is applied, the component tends to exhibit more heterogeneity, residual stress and shrinkage, as the laser beam consistently targets the same region of the powder bed. Furthermore, there are still considerable research gaps in scanning strategies that need to be addressed to fully leverage the benefits of additive manufacturing [17,28,163–165].

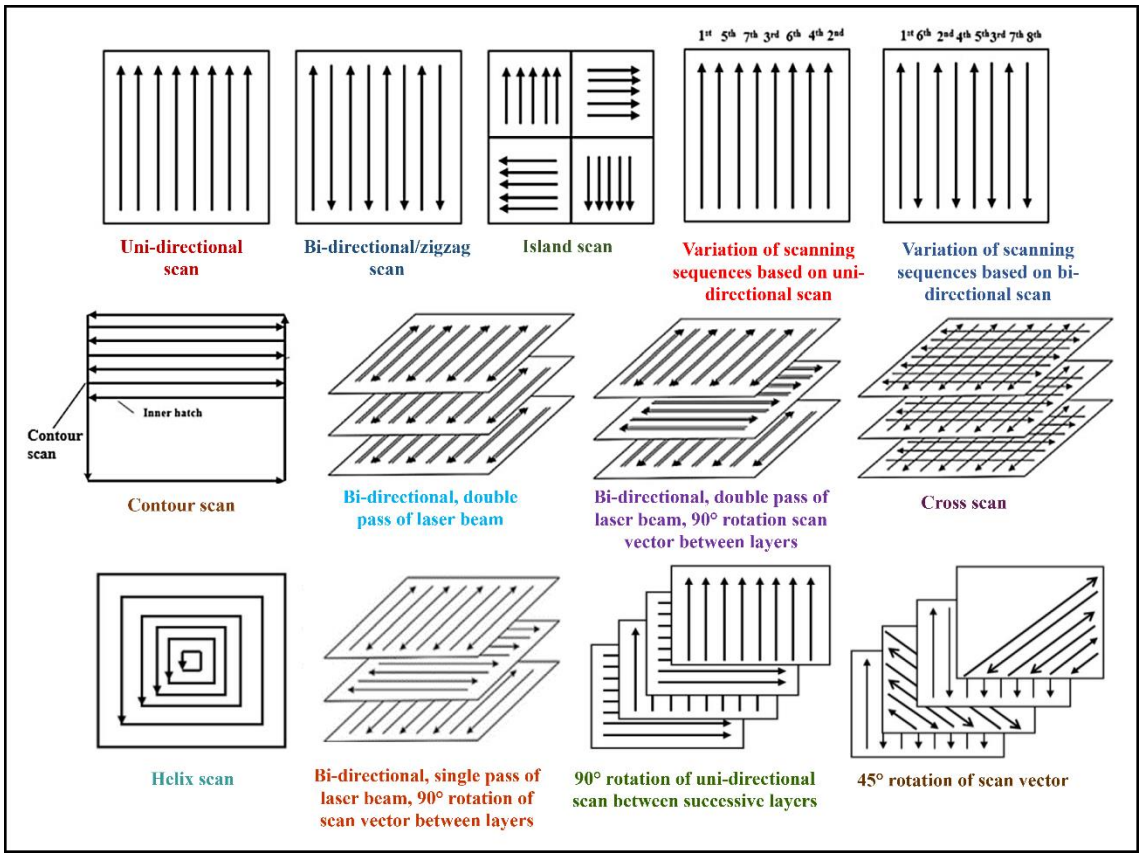

Figure 2.20 Schematics of different types of scanning strategies. Re-drawn from [28,166].

2.4.1.6 Linear and Volumetric Energy Densities

To understand the impact of various process parameters on the PBF-LB process, researchers often use the term "energy density", which integrates the combined effects of essential process parameters into a single measurable unit. The linear and volumetric energy densities (LED and VED) represent this energy unit [17,167]. Although the energy density serves as an approximate comparison term, it may not accurately transfer process parameters from one machine to another for the reproducibility of AM parts [130]. Moreover, the effects of VED on the PBF-LB process are schematically shown in Figure 2.21. The energy density equations are as follows:

$$\text{LED} = \frac{\text{Laser Power}}{\text{Scanning Speed}} \qquad \left[\frac{\text{J}}{\text{mm}}\right] \tag{2.7}$$

$$\text{VED} = \frac{\text{Laser Power}}{\text{Scanning Speed x Layer Thickness x Hatch Distance}} \qquad \left[\frac{\text{J}}{\text{mm}^3}\right] \tag{2.8}$$

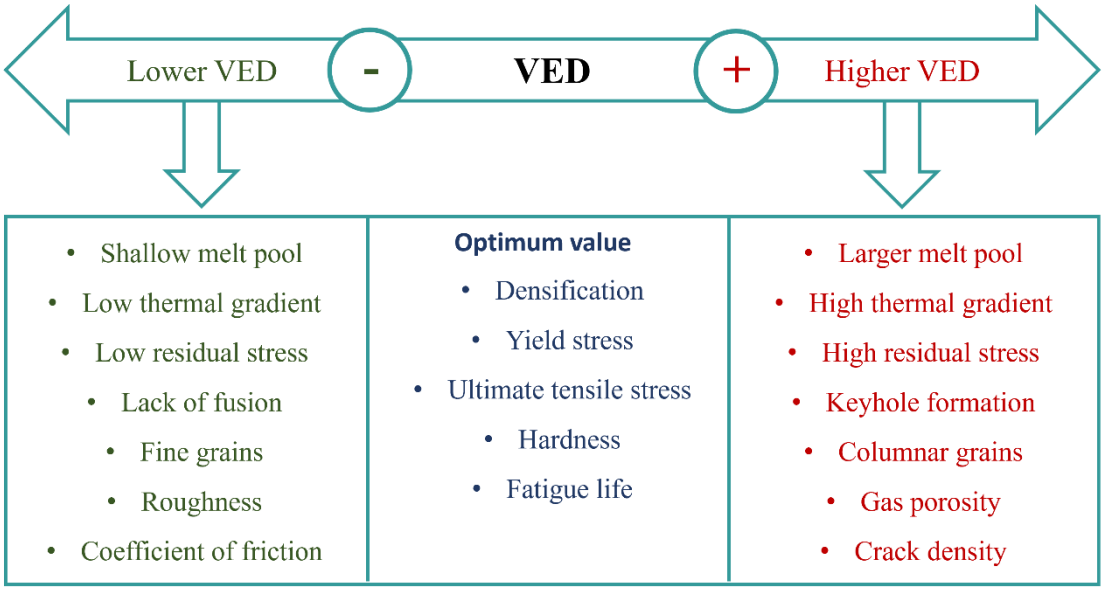

Figure 2.21 Effects of VED on the PBF-LB process. Re-drawn from [17,168].

2.4.2 Melting Modes

2.4.2.1 Conduction Mode

The conduction mode occurs when a relatively low laser power intensity is applied, resulting in the creation of a semicircular melt pool. It is typically characterized by melt pools where the presence and impact of vapor cavities are negligible because the energy density within the substrate remains low enough to prevent the substrate temperature from rising above the boiling point, thereby preventing the formation of a vapor cavity. It was reported that melt pools in the conduction mode have a small aspect ratio, typically around 0.5 (depth/width), and ideally should provide fully dense fabricated parts when there is sufficient melt pool overlap to avoid a lack of fusion porosity [169,170] .

2.4.2.2 Keyhole Mode

The keyhole mode occurs when a relatively high laser power intensity (above about 1 MW/cm^2) is applied, resulting in the creation of a deep and slender vapor depression cavity known as the keyhole within the melt pool. When laser light interacts with the material surface, it elevates the temperature, causing melting. As the temperature rises to the boiling point, metallic vapor forms, creating recoil pressure. This pressure pushes down the molten metal, forming a long and slender gas cavity called the keyhole. Moreover, it was reported that the keyhole mode has been associated with defect generation in the

fabricated parts, particularly when the depth-to-width ratio of the keyhole becomes excessively large [169] .

Figure 2.22 shows the schematic representation of the conduction and keyhole modes in the melt pool of the PBF-LB process. Additionally, these two modes have their pros and cons, and the preference for one over the other depends on the specific material type, process parameters and part requirements in each case [147].

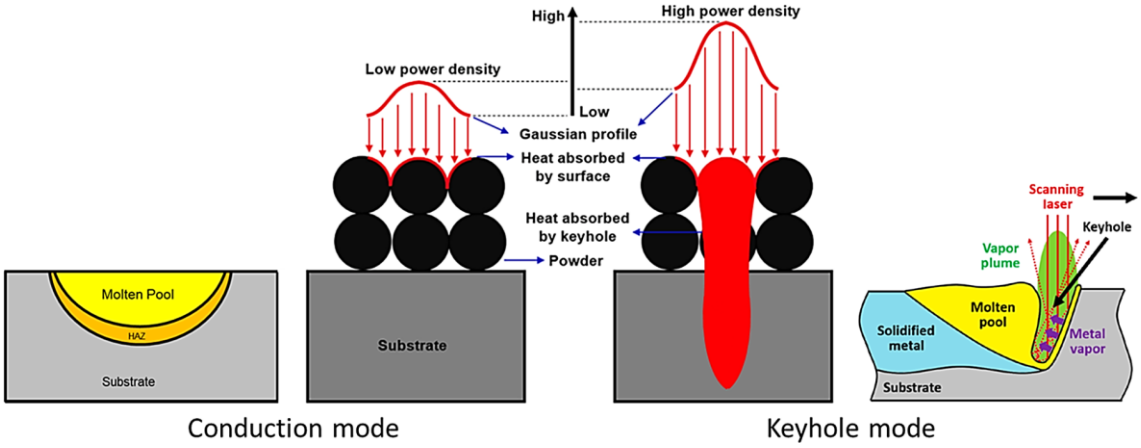

Figure 2.22 Schematic representation of conduction and keyhole modes of the melt pool in the PBF-LB process [169].

2.4.3 Defects

Defect formation is a significant problem in the PBF-LB process, frequently originating from improper parameter selection or process disruptions. It is imperative to address these issues to uphold the reproducibility, quality, and reliability of the PBF-LB parts. The origins of defects can be classified into three categories: powder-related defects (associated with the feedstock powder), processing-related defects (arising from the interaction between laser, powder and metal during melting), and post-processing-related defects (resulting from subsequent heat treatments). Commonly encountered defects in metal AM encompass various forms of porosity like lack of fusion (LOF), keyhole, balling and trapped gas. Additionally, defects may form as surface roughness, residual stress and distortion (warping) arising from the rapid solidification inherent in metal AM processes. To mitigate defect occurrence in metal AM, it is essential to understand and manage the mechanisms underlying their formation and propagation through careful selection of materials, processes and post-processing parameters [169–172]. Figure 2.23 shows a summary of the source of defects in the PBF-LB process, along with the defect-structure process map. In general, the effective process window for producing parts with nearly full

density is defined by the porosity boundaries of LOF, keyhole and balling-up. Full density, quantified as samples with over 99.9% volumetric density, is achievable within this processing window. However, it is important to note that despite operating within this window, the possibility of large defects still exists [169].

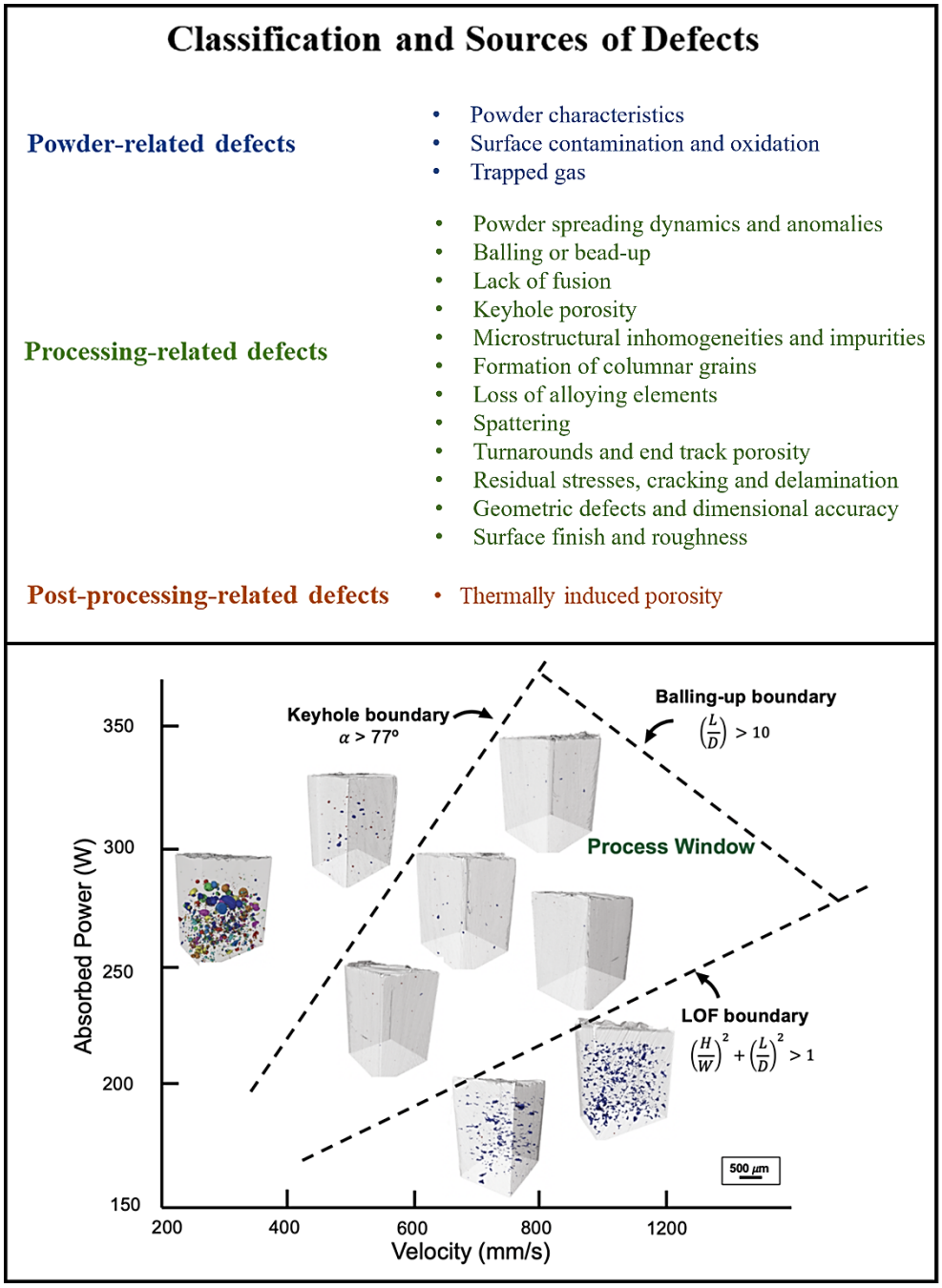

Figure 2.23 The defect structure process map (showing the variation of defect morphology across laser power-velocity space; where W is the melt pool width, D is the total depth after the melting, H is the hatch spacing, and L is the layer thickness of metal powder) for Ti6Al4V fabricated by the PBF-LB process. Re-drawn from [169,172].

2.4.3.1 Lack of Fusion

The LOF porosity, which is large, elongated or irregular, and may possess some unmelted powder particles inside, arises from inadequate penetration of the melt pool from an upper layer into the previously deposited layer or a single track into the neighbouring track on the same layer. It can play an important role as a cracking initiation point and also result in a reduction in the fatigue life of the fabricated parts [124,169]. PBF-LB parts commonly exhibit three primary types of LOF defects [169,171,173]:

- intertrack LOF, caused by the insufficient overlap of the melt pool (related to the shape and size of the melt pool, and hatch distance) during the PBF-LB process.

- inter-layer LOF, caused by incomplete bonding between the build-up layers (related to the laser energy density).

- LOF resulting from spattering (spatter powders are deposited onto the powder bed during the PBF-LB process and disrupt the uniform spread of powders).

2.4.3.2 Keyhole Porosity

Rapid vaporization of the material occurs during the keyhole mode melting, and this creates a cavity known as a keyhole or vapor depression zone. The gas bubbles pinching off from the keyhole may either escape or remain trapped inside the build as entrapped keyhole porosity after solidification. Additionally, the formation of these gas bubbles, whether they escape or remain trapped, hinges on the dynamics of the local melt pool and the subsequent solidification process. Moreover, keyhole porosities tend to be nearly spherical and the size of them may vary depending on the size and shape of the keyhole. It should be noted that not all keyhole mode melting results in keyhole porosity formation [124,133,169,171].

2.4.3.3 Balling

The balling or bead-up, also known as humping in the welding literature, causes variations in height along the length of a melted track. The area of the melt pool, particularly the area of re-melted metal, also fluctuates along the length of the track. Moreover, balling is generally considered a phenomenon to be avoided because it can cause porosity in parts produced via PBF-LB. It commonly arises at high beam powers and travel speed, imposing a constraint on the build rates achievable in PBF-LB. Moreover, other process parameters such as beam spot size, hatch distance, laser pulse frequency,

absorptivity, powder particle size and powder layer thickness also play significant roles in balling [124,169].

Some of the defects, along with causes and solutions in the PBF-LB process, are displayed in Figure 2.24. In addition to this, the effects of process parameters on combating various build defects are given in Table 2.12.

2.4.3.4 Spatter

In the PBF-LB process, the interaction between the high-energy laser and metal powder results in the formation of a melt pool, spatter, and occasionally a vapor plume or plasma. The melt pool follows the laser's path, making its behaviour relatively predictable. In contrast, spatter exhibits more complex and difficult-to-predict behaviour as it moves in three-dimensional space. Spatter can be classified into two types: hot droplet spatter, which primarily arises from melt pool instability caused by vapor-induced recoil pressure, and cold powder spatter, driven by the vapor-induced entrainment of the protective gas. These phenomena are influenced by factors such as recoil pressure, the Marangoni effect, and heat transfer within the melt pool, leading to a variety of spatter morphologies [19,147] .

Spatter is an inevitable by-product of the complex heat transfer mechanisms in PBF-LB, negatively impacting process stability, energy efficiency, and the quality of the final product. The detrimental effects of spatter are numerous: it disrupts the re-coating of powder in subsequent layers, reduces the efficiency of laser energy input, and contaminates both the manufactured parts and machine components. Furthermore, spatter contaminates recycled powder, significantly lowering its quality and leading to suboptimal part performance. Therefore, effective spatter control, through optimizing laser parameters and using protective gas flows, is essential for enhancing equipment longevity, improving part quality, and ensuring efficient powder utilization [19].

Defects		Primary causes	Potential effects	Mitigation methods
POROSITY	**Gas porosities** 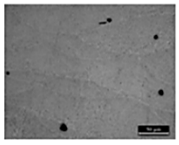 **Lack of fusion** 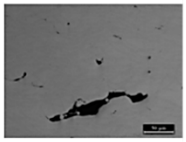 **Keyhole pores** 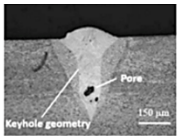	• Hollows in raw powder • Entrapment of shielding gas • High/low heat input • Selective evaporation	• Decreased performance (mainly fatigue life and creep resistance) • Anisotropy	• Dry and high-quality powders • Parameter optimization • High-purity protective gas • HIP
CRACK	**Hot tears** 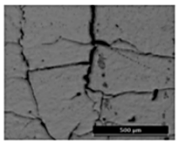 **Cracks and Delamination** 	• High level of residual stress • Natural physical and solidification features of superalloys	• Degradation of mechanical properties at different temperatures	• Parameter optimization • Compositional adjustment of superalloys • Preheating of the powder bed
SURFACE DEFECTS	**Surface roughness (balling, extensive waviness, spatter, and un-melted powders)** 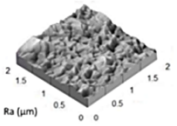	• Low heat input • Poor powder quality • High laser scanning speed • Design of part	• Decreased dimension precision and mechanical properties	• Optimization of heat input • Use of finely powdered particles • Surface post-processing treatments such as polishing
Loss of alloying elements		• Preferential evaporation of low-melting-point elements • High heat input	• Loss of strengthening phase and decreased performance	• Parameter optimization • Compositional adjustment of superalloys
Oxidation		• Residual oxygen in the powder and processing chamber	• Facilitation of crack propagation	• Clean and dry powders • High purity protective gas

Figure 2.24 Some of the defects, along with causes and solutions in the PBF-LB process. Re-drawn from [103,174].

Table 2.12 The influence of process parameters on mitigating different build defects (adapted from [133]).

Problems	Primary approach	Secondary approach
Keyhole porosity	Reduce laser power	Increase scanning speed Remelting/reheating
LOF porosity	Reduce hatch distance Reduce layer thickness	Reduce scanning speed Increase laser power Remelting/reheating
Composition change	Reduce laser power Increase scanning speed	Increase hatch distance Increase layer thickness
Residual stress and distortion	Reduce scan vector length Use heated substrate/chamber	Reduce scanning speed

2.4.4 Solidification and Grain Structure within the PBF-LB Process

When a metal AM part is produced, the process parameters and the local heat transfer conditions determine the thermal history, which drives microstructure formation processes. The temperature gradient (G), solidification rate (R) and undercooling (ΔT) at the solidification front are important parameters for the solidification microstructure. Figure 2.25 shows the solidification map based on G and R. The cellular, planar, equiaxed dendritic or columnar dendritic solidification microstructures can be obtained by tuning GxR (responsible for solidification structure size) and G/R (responsible for solidification structure morphology) values. The higher cooling rates (GxR) cause the finer structure, whereas the coarser structures can be obtained with the low cooling rates (GxR) [95,124].

The PBF-LB process is based on layer-by-layer production [175]. For this reason, the microstructure obtained with the PBF-LB process differs from the conventional manufacturing techniques (i.e., rolling, casting, or forging). During the PBF-LB process, non-equilibrium solidification occurs due to rapid cooling. Furthermore, preferential grain growth along with the heterogeneous structure can take place due to the complex heat transfer and large temperature gradients formed in a melt pool [7,176]. The material properties, process parameters and cooling conditions determine the melt pool size and shape. The downward heat flow at the melt pool boundary happens during the solidification. For this reason, a long and shallow melt pool is obtained during PBF-LB process, and the melt pool geometry affects the orientation of the grain structure [124].

The microstructure of the PBF-LB process can contain columnar grains with cellular or columnar dendritic substructures [44].

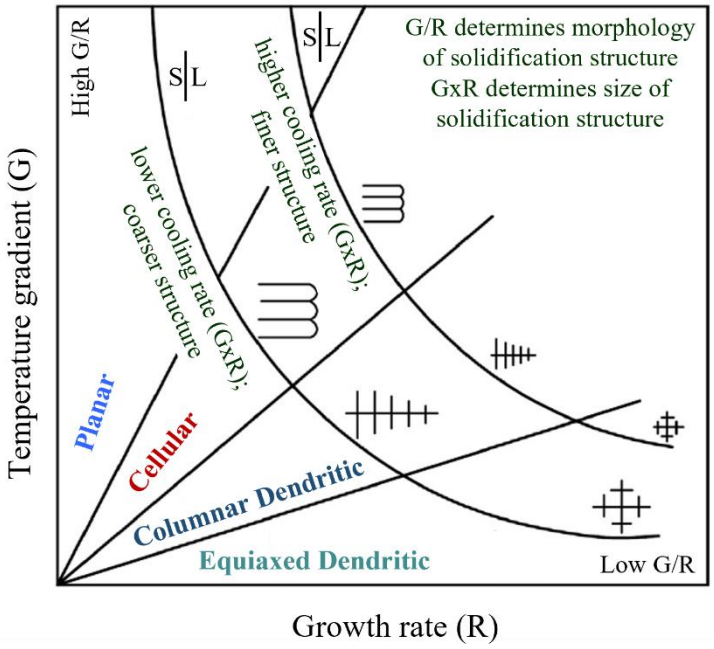

Figure 2.25 Effect of temperature gradient G and growth rate R on the morphology and size of solidification microstructure [44].

Fusion-based AM processes inherently result in an inhomogeneous grain structure and a prevalent texture, predominantly oriented along the [001] direction or with respect to the build direction. This anisotropic characteristic directly leads to adverse effects on mechanical properties in various aspects. For example, horizontal specimens (where the load direction is perpendicular to the build direction) exhibit better tensile strength and elastic modulus along the transverse direction (perpendicular to the build direction) compared to vertical specimens (where the load direction is parallel to the build direction) for Ni-base superalloys produced via AM. Additionally, Table 2.13 shows the grain structures, phases and defects of Ni-base superalloys fabricated by AM [177].

Table 2.13 The grain structures, phases, and defects of Ni-base superalloys fabricated by AM (adapted from [177]).

Grain Structures	Phases	Defects
* Generally, columnar dendrites with a strong texture along the ⟨001⟩ direction aligned with the build direction are formed * Grain refiners are often added to form small equiaxed grains to improve mechanical properties * The formation of stray grains often affects single crystallinity	* Segregation of Nb, Mo, Al, Ta, and C in the interdendritic region forms carbides and laves phases * Strengthening precipitates (γ' and γ'') are formed in as-deposited as well as heat-treated samples and affect properties	* Solidification cracking, liquation cracking, ductility dip cracking, and strain age cracking are common * Susceptible to Cr vaporization loss * Lack of fusion, gas porosities, and keyhole porosities are often found

2.5 Summary of the Existing Knowledge

The importance of Ni-base superalloys in high-temperature applications, along with the PBF-LB process was explained in the literature review section. It has been found that there are over 100 PBF-LB process parameters affecting the process and thus material properties of the fabricated parts [133]. Among them, laser power, layer thickness, scanning speed, hatch distance and scanning strategies are the most considered PBF-LB process parameters. Additionally, powder characteristics and spatter phenomena are significant for the process, reusability and properties of the fabricated parts. Moreover, the optimization of process parameters is significant to achieve desired microstructural and mechanical properties. Also, it has been found that the elimination of defects that are powder-related, processing-related and post-processing-related is crucial to achieving the desired properties.

It has been found that IN939 fabricated by PBF-LB offers significant advantages in GTEs due to their outstanding microstructural and mechanical stability up to elevated temperatures at 850 ^{o}C, corrosion and oxidation resistance, design flexibility and material efficiency. However, challenges related to microstructural defects, surface finish, weldability, cost and material availability need to be carefully addressed to ensure the successful implementation of this advanced manufacturing process. Moreover, while it is considered fairly weldable yet crack-susceptible, its fabrication using the PBF-LB process is still emerging. Despite its potential for AM, there is limited research on how process parameters and post-heat treatments affect its properties compared to the most extensively

studied Ni-base superalloys such as IN718 and IN625. Research and development concerning the PBF-LB processing of IN939 is still in its nascent phase, requiring substantial efforts to enable the effective production of IN939 parts through the PBF-LB process.

Given this context, the proposed work presented in this report to address these gaps is summarized below:

1. There have been no systematic studies on the virgin and spatter powder characteristics of IN939 for PBF-LB nor the spatter phenomena in the literature. Therefore, this work provides a comprehensive characterization of virgin and spatter IN939 powders and investigates the effects of a certain amount of spatter powder on the relative density, microstructure, hardness, surface roughness and texture of the fabricated parts, aiming to address this gap in the literature.

2. There have been only a few studies related to how the PBF-LB process parameters affect the microstructural and mechanical properties of IN939 [11,18,83,85,86,90]. This area continuous to represents a significant gap in the literature. Using different PBF-LB machines and powders from different suppliers can result in varying material properties of the fabricated parts, even when the same process parameters are used [152]. For this reason, to address this gap, the two following approaches have been examined:

- A comprehensive characterization of IN939 samples fabricated by Aconity MINI PBF-LB machine according to the full-factorial design of experiment (DoE) (examining laser power, laser scanning speed and hatch distance) to analyze the effects of process parameters on the relative density, defect formation (such as porosity and crack), surface roughness and microstructure of IN939 is presented herein.
- There have been no previous studies on the effects of scanning strategy on IN939 fabricated by PBF-LB in the literature. Therefore, a comprehensive investigation of the effects of scanning strategy on the relative density, defect formation (such as porosity and crack), microstructure, crystallographic texture, surface roughness, microhardness and residual stress of IN939 has been conducted and is presented herein to address this gap.

3. Since the microstructure of additively manufactured material differs significantly from conventionally produced material (such as casting), it becomes crucial to investigate the impact of heat treatment. This is because the influence of heat treatment on the microstructure of additively manufactured material remains relatively unknown and

inadequately explored. The standard heat treatment for conventionally produced IN939 may not adequately enhance the properties of materials produced via the PBF-LB process, due to significant differences in their microstructure and properties. The typical heat treatment regimen for IN939 involves SHT followed by aging. SHT is typically conducted above the γ' phase solvus temperature to achieve a uniform distribution of alloying elements by resolving the presence of TCP phases. Additionally, the aging step is significant to effectively enhance mechanical properties. However, existing literature indicates a lack of detailed investigation into the microstructure, grain morphology and crystallographic texture of both as-fabricated and solution heat-treated parts. Moreover, there is limited research on the recrystallization phenomena and grain growth of IN939 fabricated by the PBF-LB. This study addresses these gaps by examining the impact of solution heat treatment conducted at different SHT temperatures on the microstructure, recrystallization and texture of IN939 samples fabricated using PBF-LB.

Chapter 3: A Comprehensive Characterization of the Effect of Spatter Powder on IN939 Parts Fabricated by Powder Bed Fusion-Laser Beam

Publication Status: Published

M.N. Doğu, A. Mussatto, M.A. Yalçın, S. Ozer, K. Davut, M.A. Obeidi, A. Kumar, S. Hudson, D. O'Neill, R. O'Connor, H. Gu, D. Brabazon**, A comprehensive characterization of the effect of spatter powder on IN939 parts fabricated by laser powder bed fusion**, Materials & Design, 235 (2023).

https://doi.org/10.1016/j.matdes.2023.112406

3.1 Abstract

This study is focused on a comprehensive characterization of virgin and spatter IN939 powders and the effects of a certain amount of spatter powder on the part quality of IN939 fabricated by the PBF-LB process. A brown tint coloration formed Al_2O_3 oxide, pores, a 124.4% increase in the average particle size, a 10.2% decrease in the powder circularity, and a 7.5% decrease in the powder aspect ratio were observed in the spatter powder. Additionally, higher average grain size and lower nanohardness were obtained for the spatter powder. In order to understand the effect of a certain amount of spatter powder on the part quality, 10 wt.% spatter powder was mixed with the virgin powder. This addition was found to decrease the flowability of the powder. Moreover, this addition decreased relative density by around 0.3% and increased surface roughness by around 80.8% in the fabricated samples (termed as V and SV). On the other hand, there was no considerable microstructural, texture, microhardness, and nanohardness difference between V and SV samples, although the spatter powder addition caused a 30.2% increase in the average grain size of SV. The overall texture for both V and SV samples was (001)//BD.

3.2 Introduction

IN939, developed in the late 1960s by the International Nickel Company, is a γ'-strengthened Ni-base superalloy and has been widely used for land-based (blades and vanes) and marine gas turbines, fuel nozzles, diffusers, turbine airfoils and aircraft engines due to its outstanding properties such as high microstructural stability up to 850 ^{o}C as well as high corrosion, oxidation and creep resistance [11–13,63]. As cast IN939 microstructure contains γ solid-solution matrix, along with the γ' phase which is the main strengthening phase [33]. IN939 has been developed mainly for the conventional casting process [62], however, macro-segregation of the alloying elements and difficulty to produce intrinsic geometries such as turbine blades for the aerospace industry in a single step can be shown as some of the drawbacks of the casting process [63].

Additive manufacturing (AM) provides notable advantages over conventional manufacturing methods such as design freedom with near-net-shape production and cost reduction with minimum material waste. The powder bed fusion-laser beam (PBF-LB) process is one of the most widely used AM processes among the metal AM processes for Ni-base superalloys [120,130]. There have been very few studies for IN939 fabricated by the PBF-LB compared to other Ni-base superalloys such as IN718. However, IN939 parts are producible via PBF-LB and much more research is required for IN939 manufactured

by the PBF-LB to fill the literature gap and develop a better understanding of the material-process relationship [11,18,33,63,74,84,178]

The powder is one of the most significant process input parameters of the PBF-LB process. It is important to understand the relationship between powder properties such as powder shape, powder flow, particle size distribution, laser-material interaction and powder bed quality, and hence, the final product [179]. The high-energy laser source selectively melts metal powder according to the 3D computer-aided design (CAD) design file in a layer-wise fashion during the PBF-LB process [7,180]. During the laser-metal powder interaction, bright streaks resembling welding sparks which can contain unfused, partially melted and fully melted powder particles are ejected from a melt pool, and this is called spatter [20,131]. Spatter can have different morphologies according to different parameters. The spatter was divided into two groups as droplet spatter and powder spatter [19,181]. Additionally, Wang et al. [182] investigated the spatter formation mechanism and reported three major spatter sources (i.e., the heat effect in the melt pool, the Marangoni effect and recoil pressure) which can create different types of spatter morphologies.

The spatter may be inevitable due to the nature of the PBF-LB process, yet it creates adverse effects on the process. The spatter powder causes defects (i.e. lack of fusion, pores and oxide inclusions) by consuming significant energy when it enters the beam path. Additionally, the re-coater rubber/blade can be damaged because of the redeposited spatter powders which cause inclusions in the fabricated parts and reduce mechanical properties. Moreover, the quality and re-cycle time of the powder reduces due to the high oxygen content and irregular shapes of the spatter powder [19,182,183]. A summary of adverse effects of the spatter on the PBF-LB process is presented in Table 3.1.

Recently, the effect of spatter phenomenon of superalloys such as IN718 [20–24] and Hastelloy X [25–27] has been subject of considerable research. However, the understanding of the effect of a certain amount of spatter on IN939 built parts is still lacking. Moreover, despite the current challenges discussed above and the importance of ensuring the structural properties of additively manufactured parts, there have been no systematic studies on spatter's effect on IN939 fabricated by the PBF-LB. This study aims at closing those gaps by first characterizing the structure and properties of spatter in detail. A feedstock of virgin powder containing a certain amount of spatter powder was used to fabricate IN939 parts by the PBF-LB process. The structure and properties of the parts

produced only from virgin powder were compared to those produced from the mixture of spatter and virgin powder. This methodology was employed to ensure the findings are accurate, helpful, and applicable to the broader range of the PBF-LB process.

Table 3.1 Summary of potential reported adverse effects of spatter on the PBF-LB process (adapted from [19]).

Category	Adverse effects
Effect of spatter on printing processing	• Inefficient use of laser energy • Abrasion of the re-coater rubber/blade
Effect of spatter on structure and performance	• Spatter oxidation • Lack of fusion and pores • Surface roughness increment
Effects of spatter on powder recycling	• Porosity increment in the powder • High oxygen content • Mixture of small spatter particles

3.3 Materials and Methods

3.3.1 Powders and Characterization Techniques

The powder processed was a commercially available gas-atomized IN939 powder (Truform 939-N65, Praxair Surface Technologies) whose chemical composition is given in Table 3.2. This powder is termed virgin powder from here on. Additionally, the IN939 overflow powder of a single usage printing was sieved for six minutes using an Endecotts Octagon 200CL sieve shaker fitted with a woven wire mesh sieve. The powder left on the top mesh, having a mesh size of 63 μm, is defined as the spatter powder.

Table 3.2 The nominal chemical composition (wt.%) of the gas-atomized IN939 powder.

Elements	**Al**	**Co**	**Cr**	**Nb**	**Ta**	**Ti**	**W**	**Zr**	**Ni**	**B**	**C**	**O**	**N**
wt.%	1.9	18.9	22.8	1.0	1.4	3.8	2.0	0.028	Bal.	0.004	0.16	0.014	0.009

The particle size distribution (PSD), circularity, aspect ratio and convexity of the virgin and spatter powders were measured using Malvern Matersizer 3000 particle size analyzer with an *Aero S* dispersion unit (Malvern Panalytical Ltd, UK) and Malvern Morphologi G3. Feedstock of virgin powder containing 10 wt.% of the spatter was

prepared through ball mill mixing (in a small volume drum without any media, half full of powder, mixed for 5 minutes at 100 rpm) and the flowability properties of the virgin, as well as the mixture of virgin + 10 wt.% spatter powders were measured using a Freeman FT4 powder rheometer [184]. The definitions of flow terms for the FT4 powder rheometer are given in Table 3.3. In order to measure the reflection of white light from the powders, light spectrometry was conducted using an in-house developed system equipped with an Ocean Optics LS-1-CAL-INT Series Calibration Light Source and a Maya2000 Pro spectrometer. For light spectrometry, a flat layer of powder was illuminated by white light passing through an optical fiber at a fixed 45°. X-ray photoelectron spectroscopy (XPS) analysis was carried out using Scienta Omicron XPS with a monochromated Al K-alpha X-ray source (1486 eV) and Argus CU 128 channel detector.

Table 3.3 Definitions of flow terms for the FT4 powder rheometer [184–186].

Term	**Definition**
Basic flowability energy (BFE)	The energy needed to set up a particular flow pattern which is a downward anti-clockwise motion of the blade in a conditioned, precise volume of powder.
Stability index (SI)	Indication of the stability in the measured flow energy changes during repeated testing of powder.
Flow rate index (FRI)	The change in the flow energy when there is reduction by a factor of 10 in the flow rate (tip speed). In short, the sensitivity of a powder to flow rate change.
Specific energy (SE)	Similar to BFE with the difference being that it includes the energy required to establish an upward flow pattern.
Conditioned bulk density (CBD)	The powder density without localized stress and excess air.

3.3.2 Fabrication of IN939 Samples

In this study, IN939 samples were fabricated using an Aconity MINI (GmbH) metal 3D printer equipped with a 200 W fiber laser manufactured by IPG Photonics with a wavelength of 1068 nm. The build chamber is fitted with a rubber blade, linear motion powder re-coater mechanism and supplied with argon gas of 99.999% purity with oxygen level monitoring to ensure oxygen level to be less than 20 ppm. To investigate the effect of the spatter on part quality, a feedstock of virgin powder containing 10 wt.% of the spatter was prepared through ball mill mixing. Five cubes were fabricated with each feedstock

type to produce the V and SV samples, from the virgin and 90 wt.% virgin + 10 wt.% spatter powders, respectively, using the same PBF-LB process parameters. The sample nomenclature and the PBF-LB process parameters are shown in Table 3.4. A hatching strategy with 67° scanning rotation was applied. In order to deliver enough powder for each layer melting, a supply factor of 3 was used during the production. This indicates that the volume of new powder added is three times that required for the volume of the set build layer thickness in each layer. Excess powder, relative to that required to accommodate the build layer volume, is pushed into the overflow container during powder spreading. This level of supply factor was chosen to ensure that there was sufficient powder deposited and that there were no gaps between the powder particles on the powder bed before the laser processing step. The input volumetric thermal energy density (VED) was calculated according to the following equation:

$$VED = \frac{\text{Laser power (W)}}{\text{Scanning speed } \left(\frac{\text{mm}}{\text{s}}\right) \text{ x Layer thickness (µm) x Hatch distance (µm)}} \quad (3.1)$$

Table 3.4 The sample nomenclature and the PBF-LB process parameters of IN939 cubes.

Sample	Details	Relative Density (%)	Dimensions	PBF-LB process parameters
V	Fabricated with 100 wt.% virgin powder	99.1 ± 0.023	5 mm wide 5 mm length 7 mm height	Laser power: 190W Scanning speed: 800 mm/s Hatch distance: 60 µm Layer thickness: 60 µm Spot size: 80 µm Scanning rotation: 67° VED: 66 J/mm^3
SV	Fabricated with 90 wt.% virgin powder + 10 wt.% spatter powder	98.8 ± 0.022		

The density of the IN939 samples was measured by Archimedes principle with the help of Sartorius Entris II Essential BCE124I-1S analytical balance having accuracy and repeatability of ± 0.1 mg according to ASTM B962-13 [187]. Ethanol was used as the fluid. The surface morphology of the IN939 samples was characterized with a Bruker ContourGT over an area of 2 mm × 2 mm. S_a value, which expresses the height of each point compared to the arithmetical mean plane, was used as a direct description of the surface roughness. Also, S_z value, which represents the sum of the maximum peak height and the maximum pit depth, was calculated.

3.3.3 Microstructural and Mechanical Characterization

Both powders (virgin and spatter) and the XY and XZ planes of the fabricated samples (V and SV samples) shown schematically in Figure 3.1 were hot mounted with conductive Bakelite for the metallographic examination. Samples were automatically ground using conventional SiC grinding papers (320, 500, and 800 grit sizes) and polished with progressively finer diamond suspensions (9, 3, 1 μm). An additional final polishing step using 0.25 μm fumed silica (OP-S) was applied for electron backscatter diffraction (EBSD) analysis. Then, as-polished samples were etched with the Glyceregia reagent (15 ml HCl, 10 ml glycerol and 5 ml HNO_3) for further microstructural examination.

Nikon Eclipse LV 150 optical microscope (OM) and Carl Zeiss Merlin Field Emission Gun Scanning Electron Microscope (FEG-SEM) were used for microstructural investigation. Backscatter-electron scanning electron microscopy (BSE-SEM) and energy dispersive X-ray spectroscopy (EDS) were also used to investigate the oxide formation on the spatter powder (with acceleration voltage of 10 kV, 1.0 nA probe current, WD: 8.5 mm). EBSD analysis was carried out in the ZEISS Merlin SEM using an acceleration voltage of 15 kV, 6.0 nA probe current. EBSD maps of 54 μm x 54 μm (for powders) and 325 μm x 325 μm (for fabricated samples) were measured on a hexagonal grid with a step size of 0.075 μm (for powders) and 0.5 μm (for fabricated samples). EBSD raw data was post-processed using TSL OIM Analysis v7.3.1 software and points having CI (confidence index) below 0.1 were removed from datasets. Additionally, texture analyses were performed using the generalized spherical harmonic series expansion method of Bunge [188]. The harmonic series were expanded to a rank (L) of 34, and a Gaussian smoothing with a half-width of 5° was used.

The phase contents of the samples were determined by X-ray diffraction (XRD) analysis with a Rigaku D/Max 2200/PC using Cu-Kα radiation at 40 kV via continuous scanning between 10° and 110° 2θ angles with a scan speed of 0.5°/min.

The Vickers microhardness values of the samples were determined from the average of 10 measurements from XZ and XY planes of each fabricated sample using a Zwick/Roell ZHV10 microhardness tester with a load of 200 g and in accordance with the ASTM E92 standard [189]. Nanohardness tests were carried out on the XY planes of the fabricated samples using a nanoindenter (Bruker Hysitron TI Premier, USA) equipped with a standard Berkovich diamond indenter. An array of 10 x 10 nanoindentations was performed in the center region of each sample with a load of 10 mN (indentation depth around 300 nm) and at intervals of 50 μm between the indentations. Additionally, an array

of 8 x 8 nanoindentations was performed at the cross-section of powders with a load of 10 mN (resulting in an indentation depth of around 300 nm) and at intervals of 5 µm between indentations.

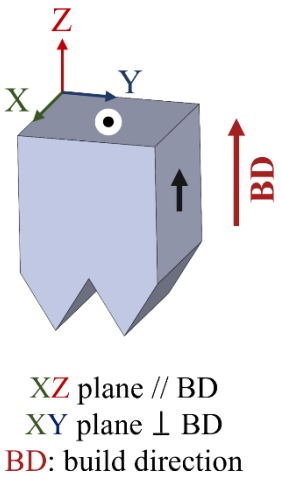

Figure 3.1 Schematic representation of the fabricated samples.

3.4 Results

3.4.1 The Characterization of the Virgin and Spatter Powders

Spatter formation during the PBF-LB process, along with the SEM and BSE-SEM images of virgin and spatter powders are shown in Figure 3.2. There is a significant difference between virgin and spatter powders in terms of morphology, particle size distribution, color and the presence of oxides. A brown tint coloration, which can be due to the interaction between the laser and virgin powder was observed on the spatter powder. The SEM images show the morphologies of virgin and spatter powders in Figure 3.2(a, c), respectively. The virgin powder has good sphericity with a few satellites which is a typical feature of gas-atomized powder production. On the other hand, a significant number of satellites as well as agglomeration is obvious on the spatter powder. The high sensitivity (HS) circularity, aspect ratio, convexity (gradations are between 0-1) and PSD graphs are given in Figure 3.3. It can be seen from both SEM images (Figure 3.2(a, c)) and HS circularity values (Figure 3.3(b)), that the spatter powder has lower sphericity (0.846 ($D_{0.5}$)) than virgin powder (0.942 ($D_{0.5}$)). Both powders have a Gaussian type of particle size distribution which is preferable for the PBF-LB process. However, the spatter powder has larger particle size and wider particle distribution (29.1µm (D_{10}), 70 µm (D_{50}), 148 µm (D_{90})) than the virgin powder (17.4 µm (D_{10}), 31.2 µm (D_{50}), 52 µm (D_{90})) shown in (Figure

3.3(a)). Additionally, PSD of the virgin + 10 wt.% spatter powder (18.0 µm (D_{10}), 34.1 µm (D_{50}), 71 µm (D_{90})) is given in Figure 3.3(a). It can be seen from the PSD graph, the addition of 10 wt.% spatter powder into the virgin powder created bimodal PSD. The large spatter powders can be redeposited by falling onto the powder bed during the PBF-LB process. Therefore, the fabricated parts can have inclusions, resulting in reduced mechanical properties [19]. Moreover, the as-polished cross-section images of the virgin and spatter powders are shown in BSE-SEM images (Figure 3.2(b, d)). A significant number of pores were observed in the large spatter powders compared to virgin powder.

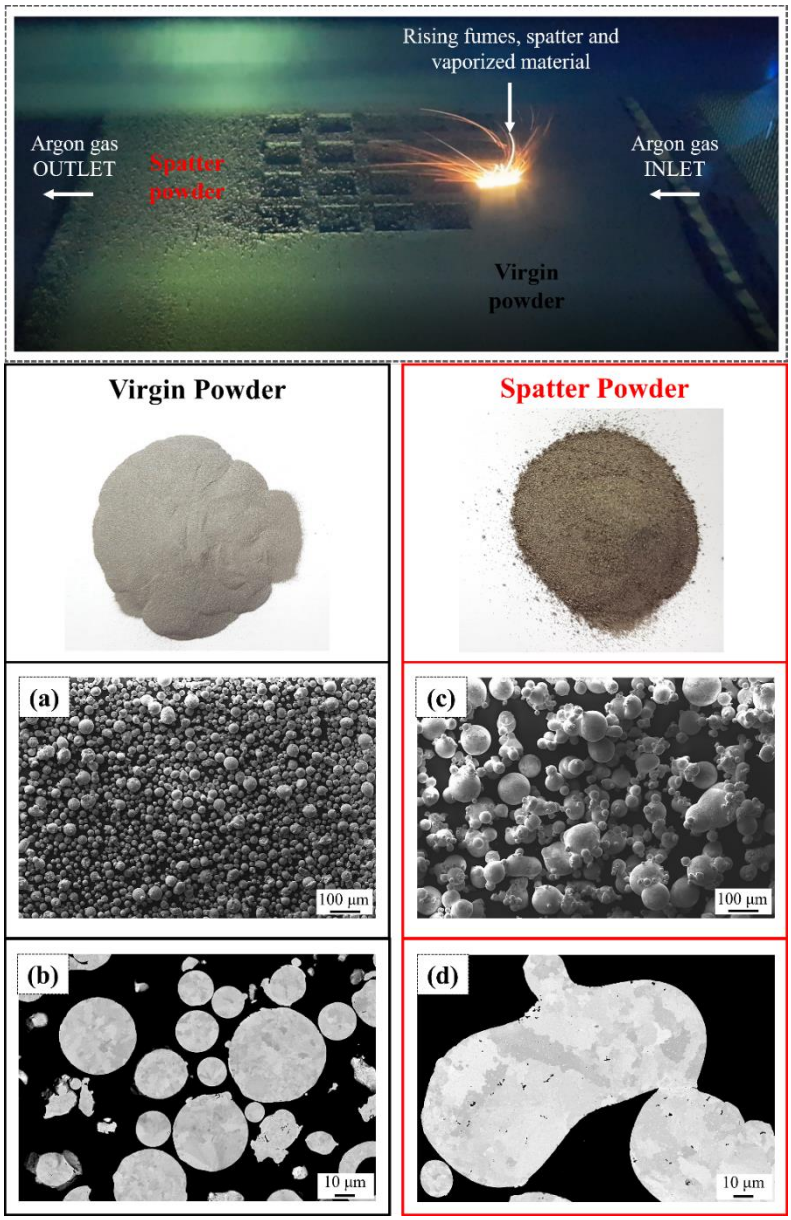

Figure 3.2 The formation of the spatter during the PBF-LB process. The SEM images show the morphology of (a) virgin and (c) spatter powders. The BSE-SEM images display the as-polished cross sections of (b) virgin and (d) spatter powders.

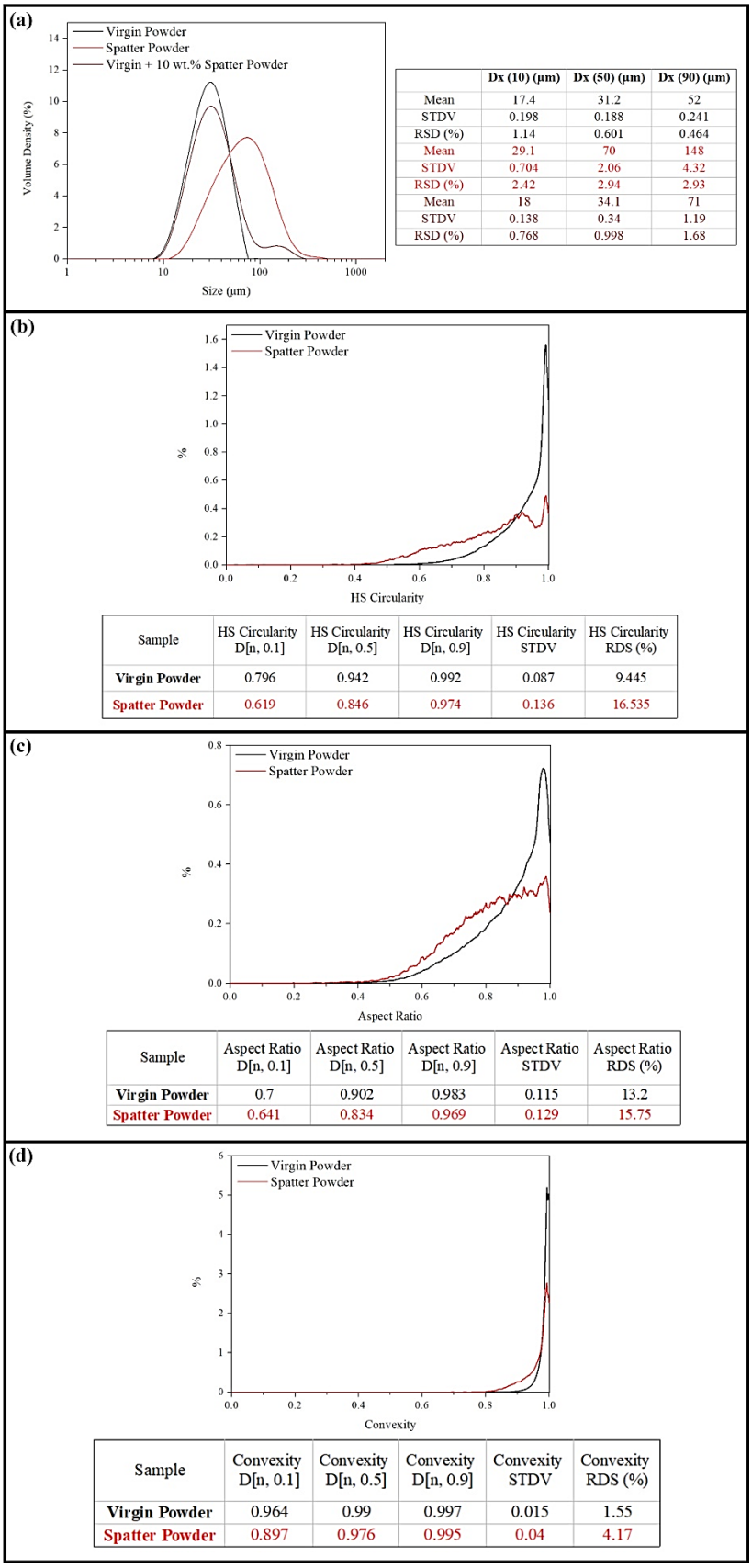

	Dx (10) (µm)	Dx (50) (µm)	Dx (90) (µm)
Mean	17.4	31.2	52
STDV	0.198	0.188	0.241
RSD (%)	1.14	0.601	0.464
Mean	29.1	70	148
STDV	0.704	2.06	4.32
RSD (%)	2.42	2.94	2.93
Mean	18	34.1	71
STDV	0.138	0.34	1.19
RSD (%)	0.768	0.998	1.68

Sample	HS Circularity D[n, 0.1]	HS Circularity D[n, 0.5]	HS Circularity D[n, 0.9]	HS Circularity STDV	HS Circularity RDS (%)
Virgin Powder	0.796	0.942	0.992	0.087	9.445
Spatter Powder	0.619	0.846	0.974	0.136	16.535

Sample	Aspect Ratio D[n, 0.1]	Aspect Ratio D[n, 0.5]	Aspect Ratio D[n, 0.9]	Aspect Ratio STDV	Aspect Ratio RDS (%)
Virgin Powder	0.7	0.902	0.983	0.115	13.2
Spatter Powder	0.641	0.834	0.969	0.129	15.75

Sample	Convexity D[n, 0.1]	Convexity D[n, 0.5]	Convexity D[n, 0.9]	Convexity STDV	Convexity RDS (%)
Virgin Powder	0.964	0.99	0.997	0.015	1.55
Spatter Powder	0.897	0.976	0.995	0.04	4.17

Figure 3.3 (a) Particle size distribution, (b) HS circularity, (c) aspect ratio and (d) convexity graphs of the powders.

In this study, 10 wt.% spatter powder was mixed with the virgin powder to better understand the effects of a certain amount of spatter powder on the flow properties as well as fabricated part properties. Figure 3.4 shows the flowability properties of these powders including the measured stability and variable flow rate of the virgin and the mixture of virgin + 10 wt.% spatter powders. The flowability is directly affected by the particle size distribution and aspect ratio of powder [26]. Better powder flowability and packing can be obtained from powders with narrower PSD and with high circularity and aspect ratio. BFE is a standard metric for powder flowability and the lower BFE represents the better flow properties [184,185,190]. The BFE values were determined as 569.05 ± 2.28 mJ and 629.03 ± 27.59 mJ for virgin and the mixture of virgin + 10 wt.% spatter powders, respectively. Additionally, low SE values (below 5) indicate low cohesion within the powder. The addition of only 10 wt.% of spatter powder to the virgin powder resulted in a 2.38% increase in BFE and an 18.21% decrease in SE. Considering the powder flow results shown in Figure 3.4, the virgin powder showed overall slightly better flowability. Despite the virgin + 10 wt.% spatter powder having inferior particle characteristics to the virgin powder, its flowability performance closely reflected that of virgin powder as the existing coarse particles impaired the overall cohesion of the powder.

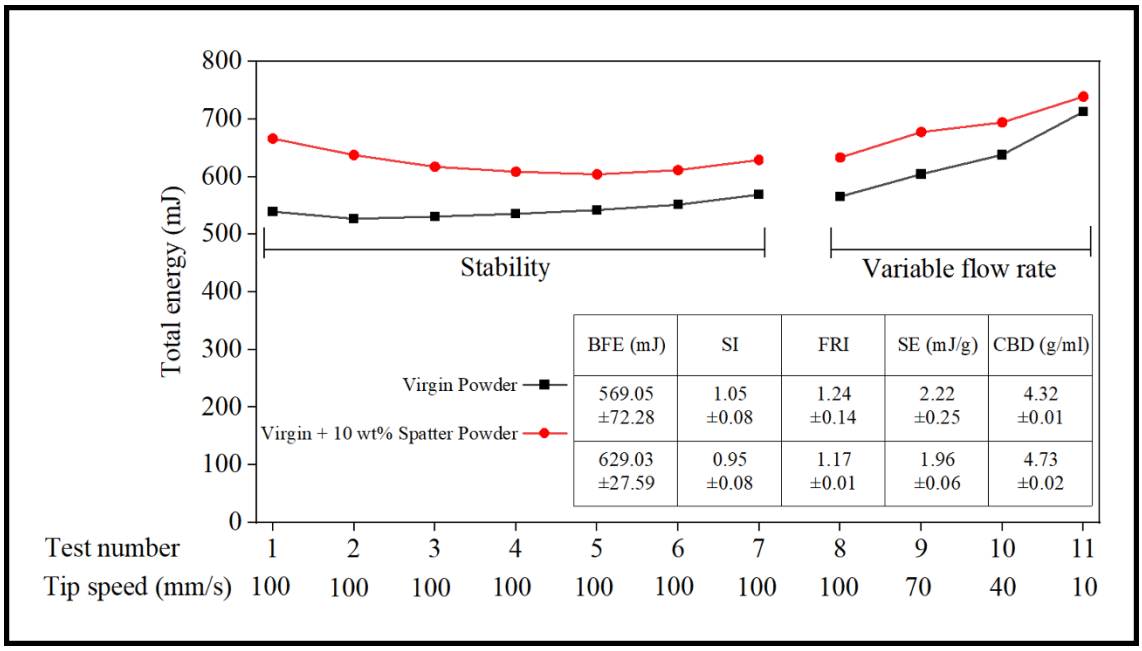

Figure 3.4 Flowability energy versus speed for the virgin and the mixture of virgin + 10 wt.% spatter powders.

Figure 3.5 displays SEM images with EDS maps of virgin and spatter powders. All elements are homogeneously distributed in the virgin powder (Figure 3.5(a)). On the other

hand, the dark spots which mostly contain Al and O elements were detected on the spatter powder surface (Figure 3.5(b)). These oxides were determined as Al_2O_3 according to EDS quantification [191]. Moreover, Figure 3.6(a) shows the light reflectivity properties of the virgin and spatter powders. A clear reduction was observed in the spatter powder reflectivity between 400 and 900 nm wavelength. The improved light absorption property of the spatter powder which has a brown tint coloration could be due to oxide formation on the surface of the spatter powder. The XRD patterns of the virgin and spatter powders are shown in Figure 3.6(b). There is no significant difference between XRD patterns attributed to γ (gamma) phase of the powders [46].

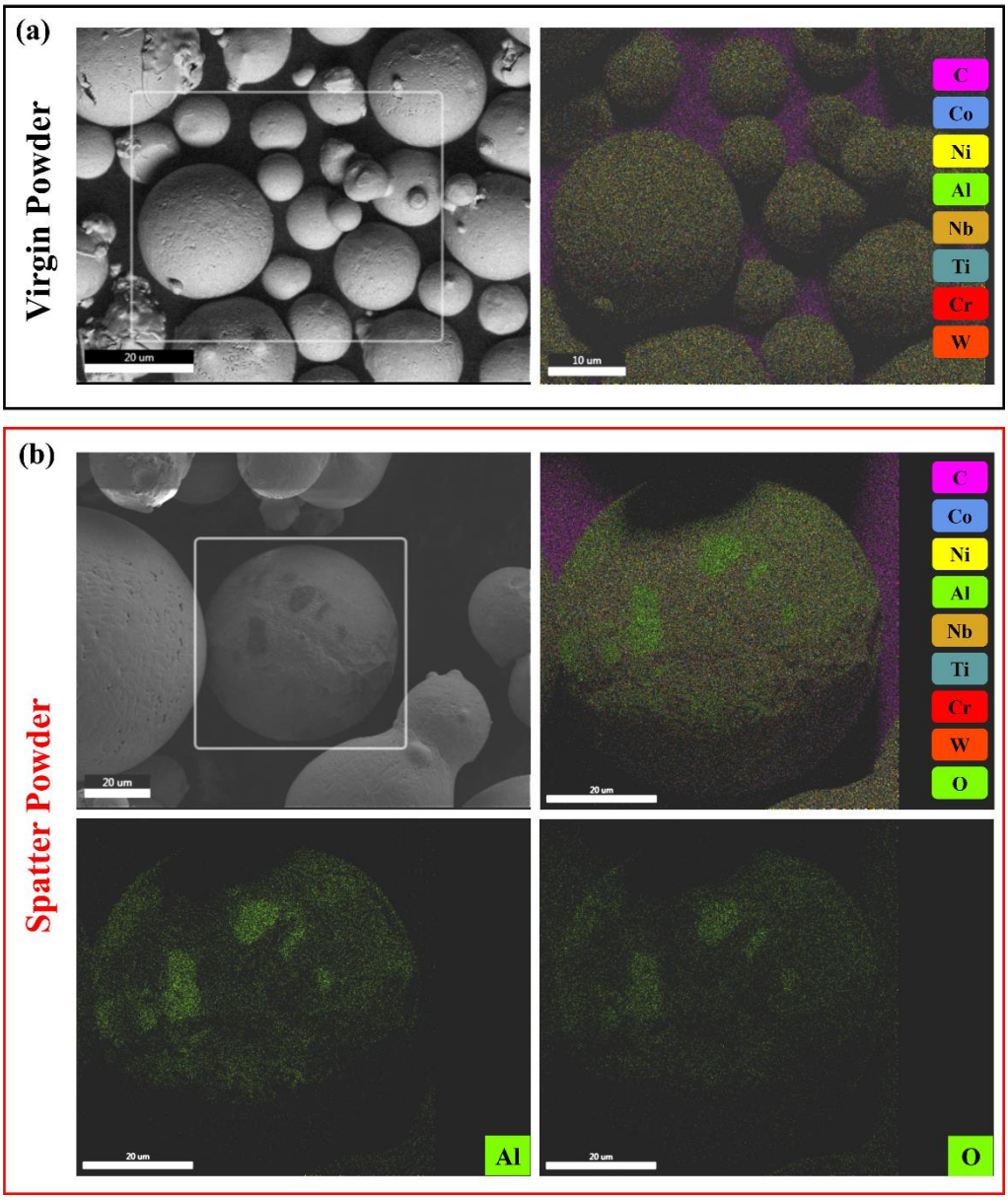

Figure 3.5 SEM images with EDS maps of the (a) virgin and (b) spatter powders.

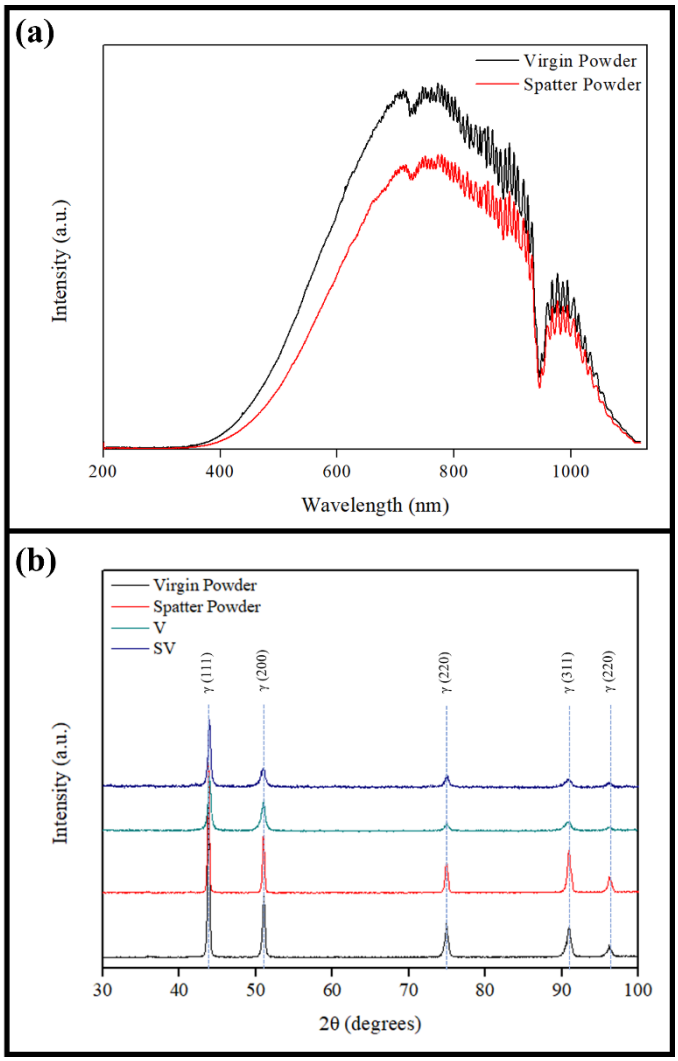

Figure 3.6 (a) Reflected spectrum graph of the virgin and spatter powders and (b) XRD patterns of the powders and fabricated samples (V and SV).

XPS survey spectra (Figure 3.7) show that a few elements are present at the surface. However, there is a clear difference in surface composition between the virgin and spatter powders. In both cases, the strongest signals are the C 1s and O 1s which are from atmospheric contamination, oxidation and the formation of carbides and carbonates with the metals in the powder. Such intense carbon and oxygen peaks are commonly observed during the XPS of powders used in additive manufacturing [131]. The surface layer has a thickness ranging from 5-10 nm and plays a crucial role as it accounts for the majority of the XPS signature. Upon analysing the high-resolution C 1s data of the spatter powder, it becomes apparent that there is a significant reduction in the carbon content at the surface. The peak profile of the virgin powder suggests the presence of metal carbides, which exhibit a binding energy below 285 eV. For spatter powder, it changes to a profile associated with adventitious carbon, commonly seen on planar surfaces, which is

dominated by C-C (284.5 eV) and C-O (286 eV) bonds. The O 1s spectrum shifts to higher binding energy, indicating an increase in water vapour and carbon on the surface, along with a reduction in metal oxidation below 531 eV.

High-resolution spectra of the cobalt, nickel, and chromium, all of which are quite noisy due to the presence of the contaminant overlayer suppressing the signal, are visible in the full survey spectra (Figure 3.7). There is a clear increase in chromium signal post-spatter, though this cannot be explained simply by the reduction in the thickness of the contaminant overlayer, as both the Co and Ni signals reduce post-spatter. This suggests that the process promotes the preferential diffusion of some elements to the surface. These three metal peaks appear more oxidized following spatter, as evidenced by a shift to the higher binding energy. Although the O 1s peak suggests less metal oxidation, this can be explained by the formation of metal hydroxides and oxyhydroxides at the surface, which typically have higher binding energy [192].

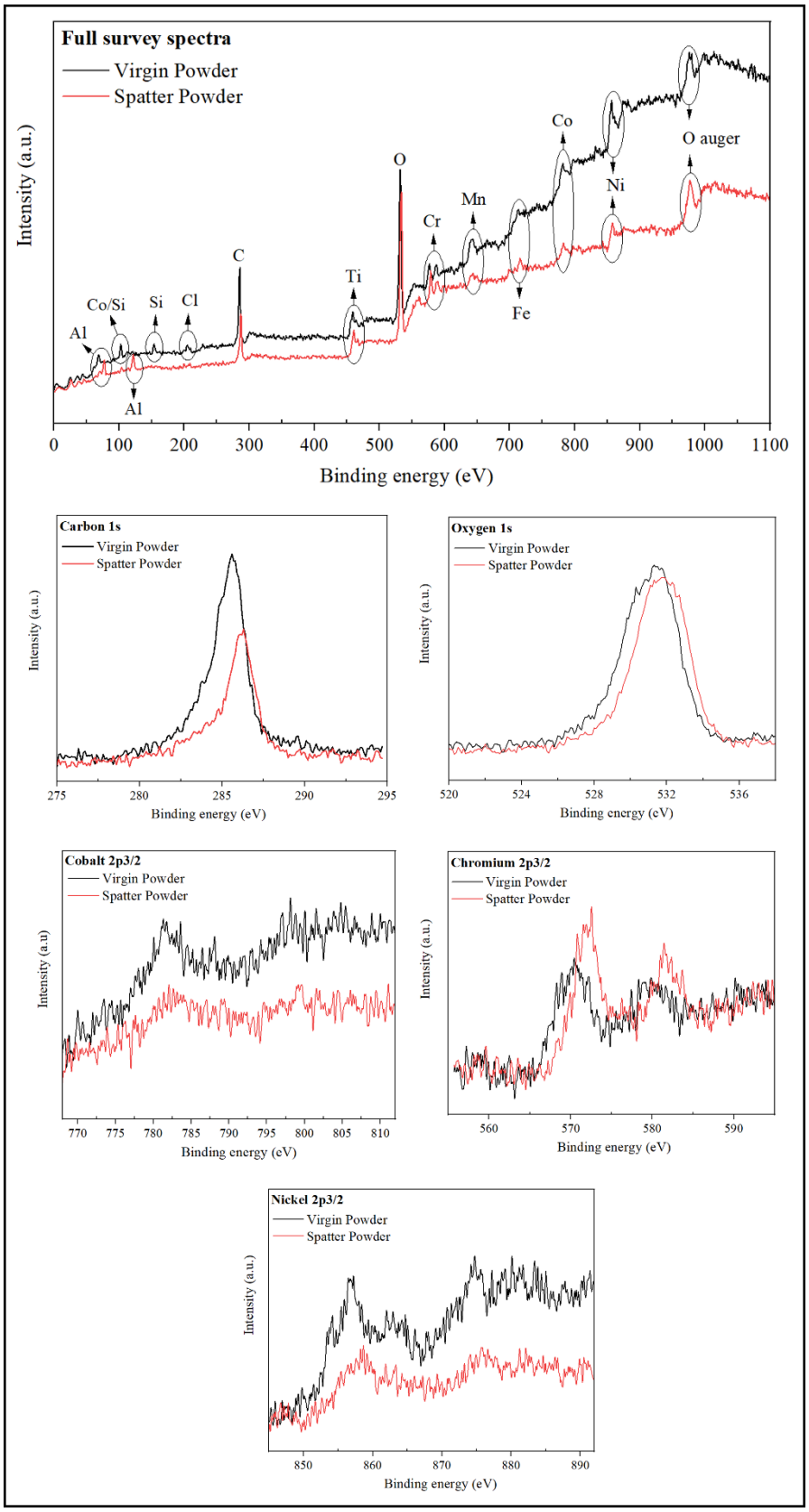

Figure 3.7 XPS survey spectra of the virgin and spatter powders.

EBSD maps including the inverse pole figure (IPF) with respect to normal direction, kernel average misorientation (KAM) and grain orientation spread (GOS) maps of the virgin and spatter powders are given in Figure 3.8. The virgin powder contains smaller grains compared to the spatter powder. The area-weighted average grain size values were measured as 1.62 ± 0.50 μm and 4.87 ± 1.68 μm for the virgin and spatter powders, respectively (Table 3.5 and Figure 3.9(a)). Kernel average misorientation (KAM) is calculated for each point in the EBSD map. First the misorientations between a certain point and points at its perimeter are determined and then the average of those misorientations give the KAM value of the center point. Moreover, misorientations exceeding 5 degrees are not included in the calculation of average misorientation, as misorientations higher than this threshold value represents grain boundaries. Also, it is a measure of local misorientations, which is also related to defect density. The high plastic strain and high dislocation density are the reason for the high KAM values. Additionally, GOS is another measure of local misorientation, however, it is a grain-based local misorientation. To calculate GOS, firstly, the average orientation of a grain is calculated. After that, the misorientation between this average orientation and the orientation of each individual measurement point within the grain is calculated. Finally, the average of these misorientations is calculated and assigned to each point within the grain. GOS value increases with high defect density and deformation, whereas recrystallization decreases GOS values. Both KAM and GOS maps are labelled with a rainbow scale (blue and red represent minimum and maximum, respectively) [45]. The virgin powder has higher KAM and GOS values compared to the spatter powder (Table 3.5). Moreover, the surface of the virgin powder has higher KAM compared to the interior (Figure 3.8(a)). On the other hand, the interface region between the spatter powder and small powder which could be satellite has higher KAM compared to the whole spatter powder (Figure 3.8(b)). A similar trend with KAM was observed for the GOS maps shown in Figure 3.8(a, b) and graphs of the virgin and spatter powders, along with the GOS graph (Figure 3.9(b)). There are two spatter powder particles on the GOS map shown in Figure 3.8(b). The particle on the left-hand side of the GOS map was partially agglomerated with two satellite powder particles which are much smaller than the other powder particles. The defect density (KAM and GOS) is higher in these satellites. Thus, this causes an increase in the bimodality of the GOS distribution of the spatter powder (Figure 3.9(b)), although the average KAM and GOS values of the spatter powder are lower than the virgin powder.

Table 3.5 Average grain size, GOS, KAM and GND values of the powders and fabricated samples.

Sample	Average grain size (µm)		GOS (°)	
Virgin Powder	1.62 ± 0.50		1.12 ± 0.85	
Spatter Powder	4.87 ± 1.68		0.59 ± 0.55	
	XZ plane	**XY plane**	**XZ plane**	**XY plane**
V	12.16 ± 3.41	12.14 ± 3.01	1.54 ± 0.53	1.66 ± 0.60
SV	16.52 ± 4.22	11.08 ± 3.12	1.74 ± 0.56	1.54 ± 0.56
Sample	**KAM (°)**		**GND (10^{12} m/m^3)**	
Virgin Powder	0.43 ± 0.39		130.14	
Spatter Powder	0.27 ± 0.17		68.30	
	XZ plane	**XY plane**	**XZ plane**	**XY plane**
V	0.71 ± 0.50	0.73 ± 0.51	38.90	42.76
SV	0.67 ± 0.45	0.69 ± 0.47	38.51	38.25

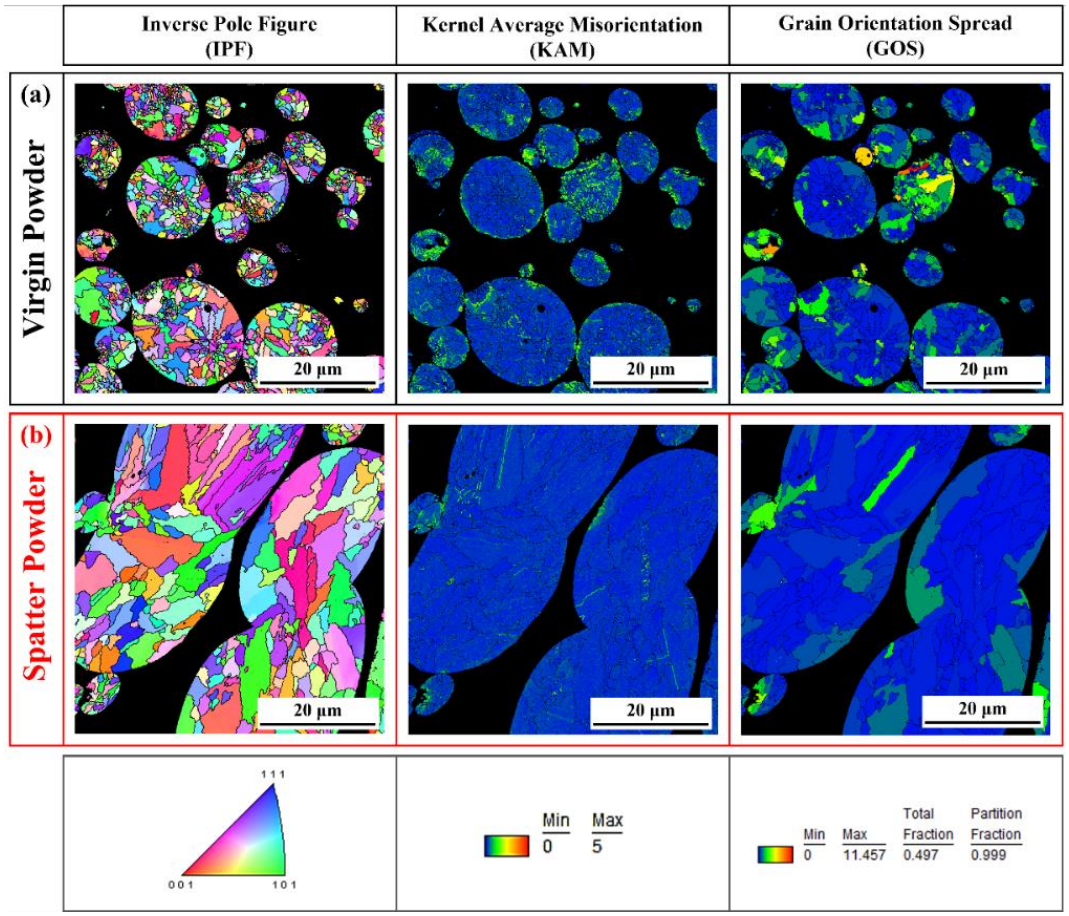

Figure 3.8 EBSD maps: IPF (with respect to sample normal), KAM and GOS maps of the (a) virgin and (b) spatter powders.

Figure 3.9(c) shows the geometrically necessary dislocation (GND) density distributions of samples, and the average GND density values are given in Table 3.5. The dislocation density in metallic materials includes GND and statistically stored dislocations. It is reported that GNDs account for most dislocations in total FCC cubic metals [193]. The virgin powder has a higher GND value (130.14 x 10^{12} m/m^3) compared to the spatter powder (68.30 x 10^{12} m/m^3), which is a similar trend to KAM and GOS. The virgin powder was produced with the gas-atomization process and the higher KAM, GOS and GND values can be explained with the higher cooling rates due to the gas atomization process (a high-speed inert gas goes through the melt stream and causes high cooling rates) [26,194]. On the other hand, the spatter powder has laser interaction causing local reheating, melting, solidification and a shorter interaction with the inert gas compared to the gas-atomized virgin powder. Thus, this interaction can decrease the dislocation density.

The misorientation angle graph is displayed in Figure 3.9(d) and the dashed purple line represents the Mackenzie distribution for completely random oriented cubic polycrystals. The calculation for the misorientation angle is done between 5^o and 65^o as a default. The misorientation angle distributions of the virgin and spatter powders show the predominance of low-angle grain boundaries ($<15^o$) indicating more substructure regions and higher dislocation density. On the other hand, the spatter powder approaches to the Mackenzie distribution compared to the virgin powder.

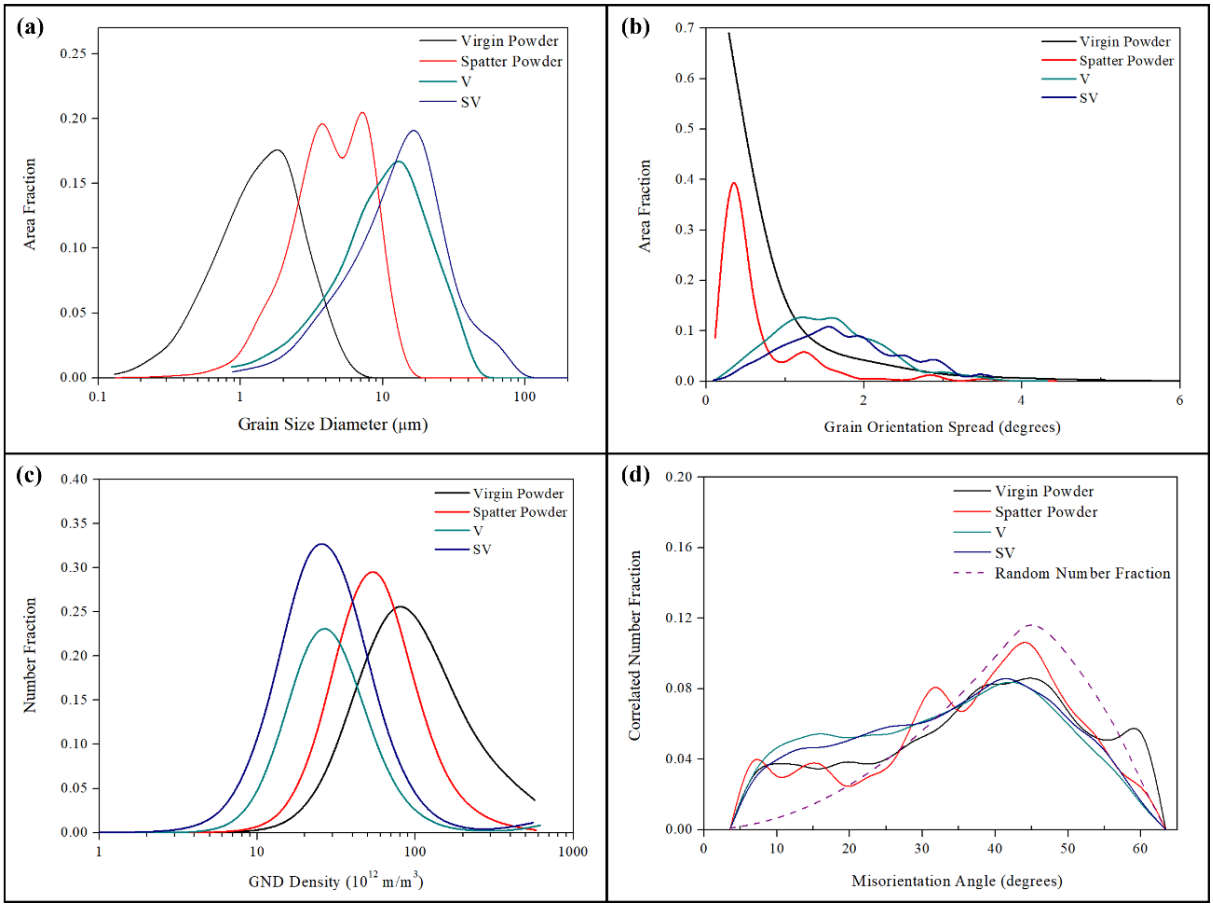

Figure 3.9 Analysis of the EBSD data for the powders and fabricated samples showing (a) grain size distribution, (b) GOS, (c) GND density and (d) misorientation angle.

Figure 3.10(a, b) shows the nanohardness contour maps of the virgin and spatter powders. The measured nanohardness (GPa) and reduced modules (GPa) values are given in Figure 3.10(e). The spatter powder has a lower nanohardness value (2.2 ± 0.2 GPa) compared to the virgin powder (3.8 ± 0.3 GPa).

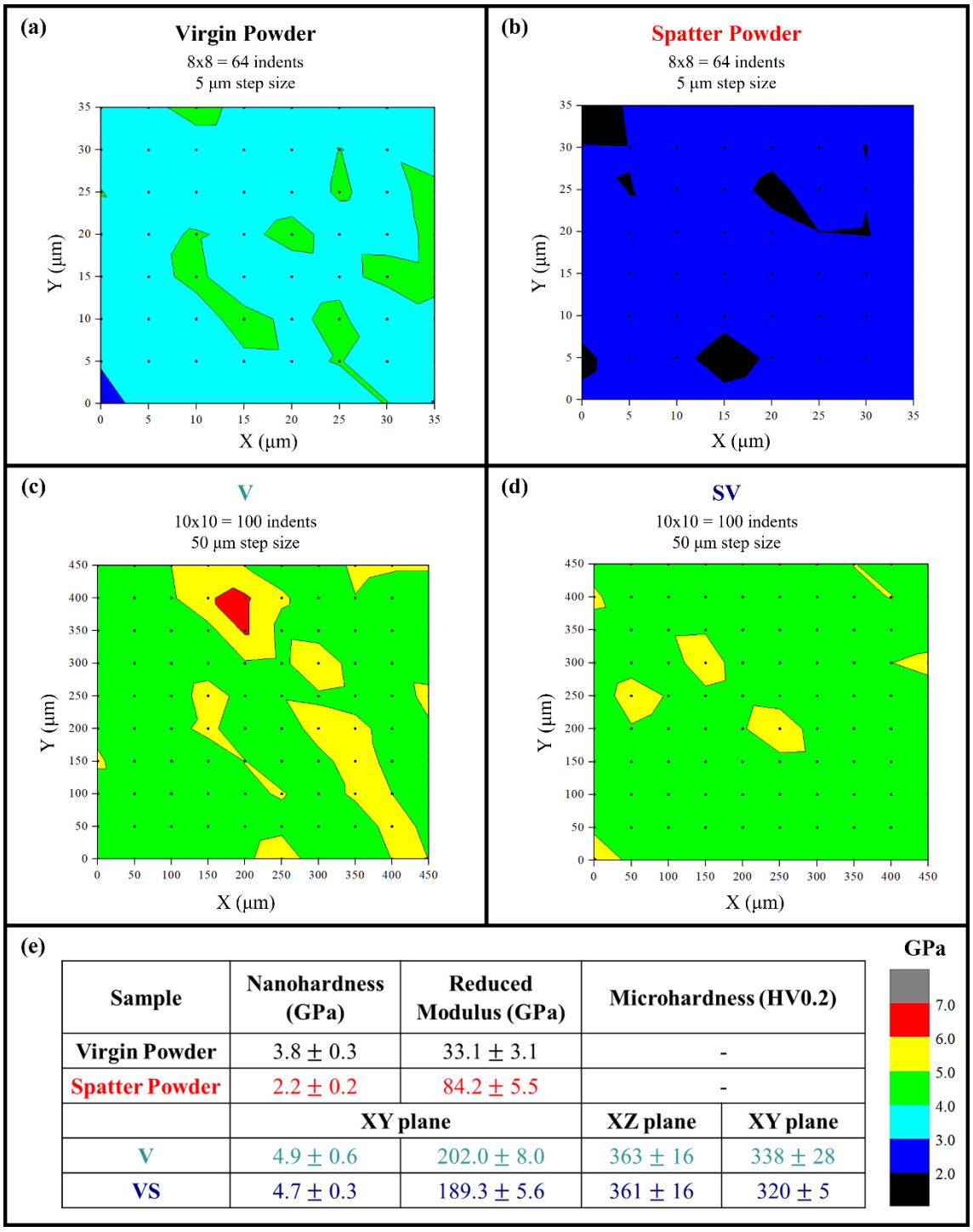

(e)

Sample	Nanohardness (GPa)	Reduced Modulus (GPa)	Microhardness (HV0.2)	
Virgin Powder	3.8 ± 0.3	33.1 ± 3.1	-	
Spatter Powder	2.2 ± 0.2	84.2 ± 5.5	-	
	XY plane		XZ plane	XY plane
V	4.9 ± 0.6	202.0 ± 8.0	363 ± 16	338 ± 28
VS	4.7 ± 0.3	189.3 ± 5.6	361 ± 16	320 ± 5

Figure 3.10 Nanohardness contour maps of (a) virgin powder, (b) spatter powder, (c) V sample and (d) SV sample, along with (e) the tabulated nanohardness (GPA), reduced modules (GPa) and Microhardness (HV0.2) values.

3.4.2 The Characterization of the Fabricated Samples

In the second part of the study, cube shaped samples produced from only virgin powder and from mixture of virgin and spatter powder were characterized. The addition of only 10 wt.% spatter powder resulted in a 0.3% relative density reduction (from 99.1% to 98.8%). This was an expected result since the spatter powder has a larger particle size, and this can affect each layer as well as the part density [26].

Figure 3.10(c, d) shows the nanohardness contour maps of the V and SV. There is no significant difference between the V and SV samples in terms of the measured nanohardness (GPa), reduced modulus (GPa) and microhardness (HV0.2) values (Figure 3.10(e)).

The surface roughness profiles for the XZ planes with the pictures of the V and SV samples are shown in Figure 3.11. The effect of adding only 10 wt.% spatter powder on the surface roughness can be seen even by the eye (Figure 3.11(b)) when it is compared with the sample fabricated using only 100 wt.% virgin powder (Figure 3.11(a)). Addition of 10 wt.% spatter powder increased the surface roughness around 80% as the measurements showed average surface roughness (S_a) values of 5.12 μm and 9.27 μm for the V and SV samples, respectively. Moreover, the S_z values (the maximum height) within the measured area are 76.61 μm and 140.12 μm for the V and SV samples, respectively.

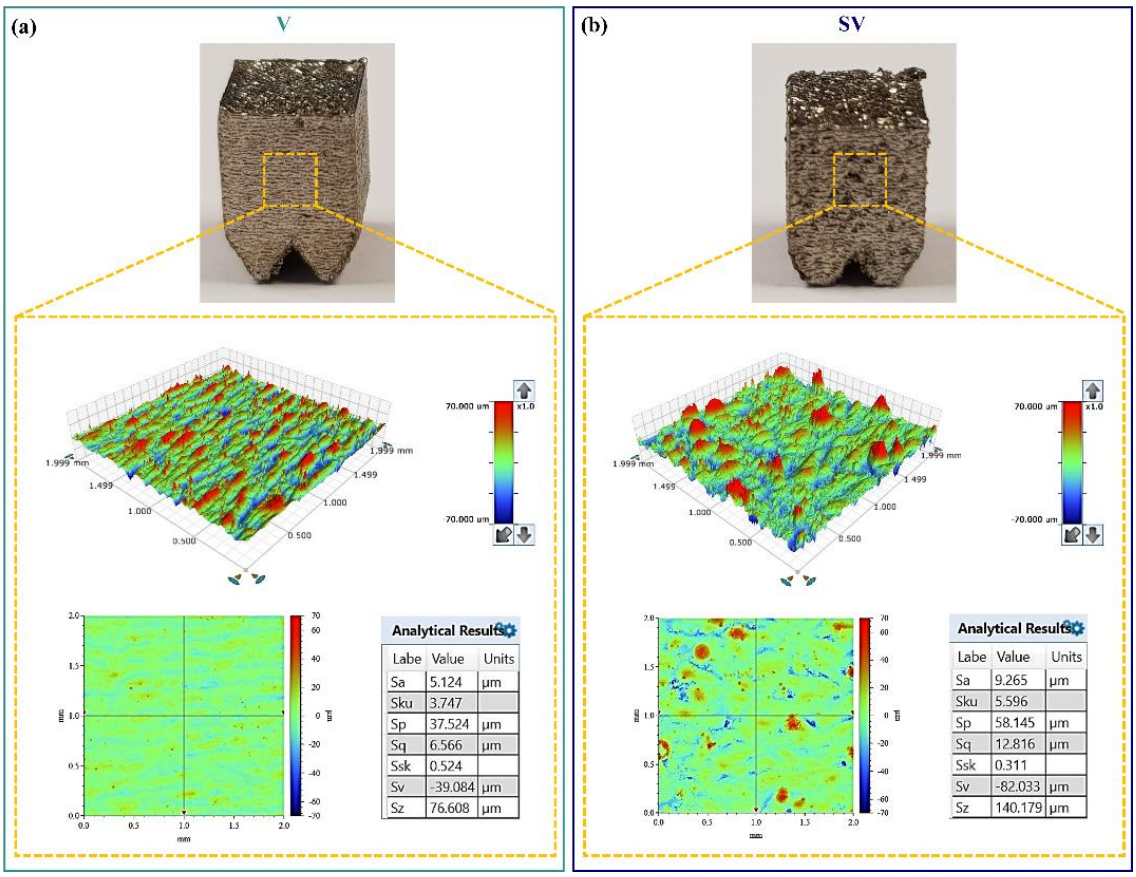

Figure 3.11 The surface roughness profiles for the XZ planes of the pictured 5 mm^3 cube of the (a) V and (b) SV samples.

The optical micrographs and BSE-SEM images of the fabricated samples (V and SV samples) are shown in Figure 3.12. The nature of the PBF-LB process causes arc-shaped melt pools on the XZ planes (parallel to build direction) due to the Gaussian energy distribution of the laser beam [45]. Figure 3.12 suggests that a combination of the conductive stable keyhole mode was the predominated mode of melting. The micrographs also show evidence of the existence of possibly unstable melt pools. This appears slightly more prominent in the SV sample, which also shows that melt pools with a slightly high depth/width aspect ratio were formed in the SV sample when contrasted with the V sample. As seen in Figure 3.12, it is evident that melt pool fluctuations took place during the melting. This was due to many obvious factors, but primarily due to the slightly high applied energy density. This transient unstable keyhole mode of melting then introduced porosity in the solidified samples, which a good agreement is observed when correlating the micrographs of Figure 3.12(b, e) with the density values of Table 3.4 for the V versus the SV samples. Additionally, pores can be generated due to the large spatter powders hindering homogenous powder melting and bonding. These irregular pores are the reason for lower relative density that were observed in the SV sample (Figure 3.12(c)).

Furthermore, there is no significant difference between XRD patterns attributed to γ (gamma) phase of the V and SV samples (Figure 3.6(b)).

EBSD maps of the XZ and XY planes of the V and SV samples are shown in Figure 3.13. As it was observed in the optical micrographs (Figure 3.12(a, d)), similar grain morphologies were observed for the V and SV samples, and it can especially be seen in both IPF maps and image quality and grain boundaries (IQ & GBs) maps. The V and SV samples showed a microstructure composed of columnar elongated grains along the build direction (on the XZ plane). In contrast, equiaxed grains were observed on the XY planes. Additionally, the area-weighted average grain size values of the V and SV samples were measured as 12.16 ± 3.41 μm and 16.52 ± 4.22 μm on the XZ plane, respectively (Table 3.5). However, the average grain size values are similar on the XY planes of the V (12.14 ± 3.01 μm) and SV (11.08 ± 3.12 μm) samples. On the other hand, the KAM and GOS maps of the V and SV samples as well as their values didn't show significant difference (Figure 3.13(a, b) and Table 3.5). The overlapping regions have a higher KAM value compared to the inside of the melt pools on the XZ planes. Moreover, the borders have a higher KAM value compared to the center of the chessboard-like pattern on the XY planes [45].

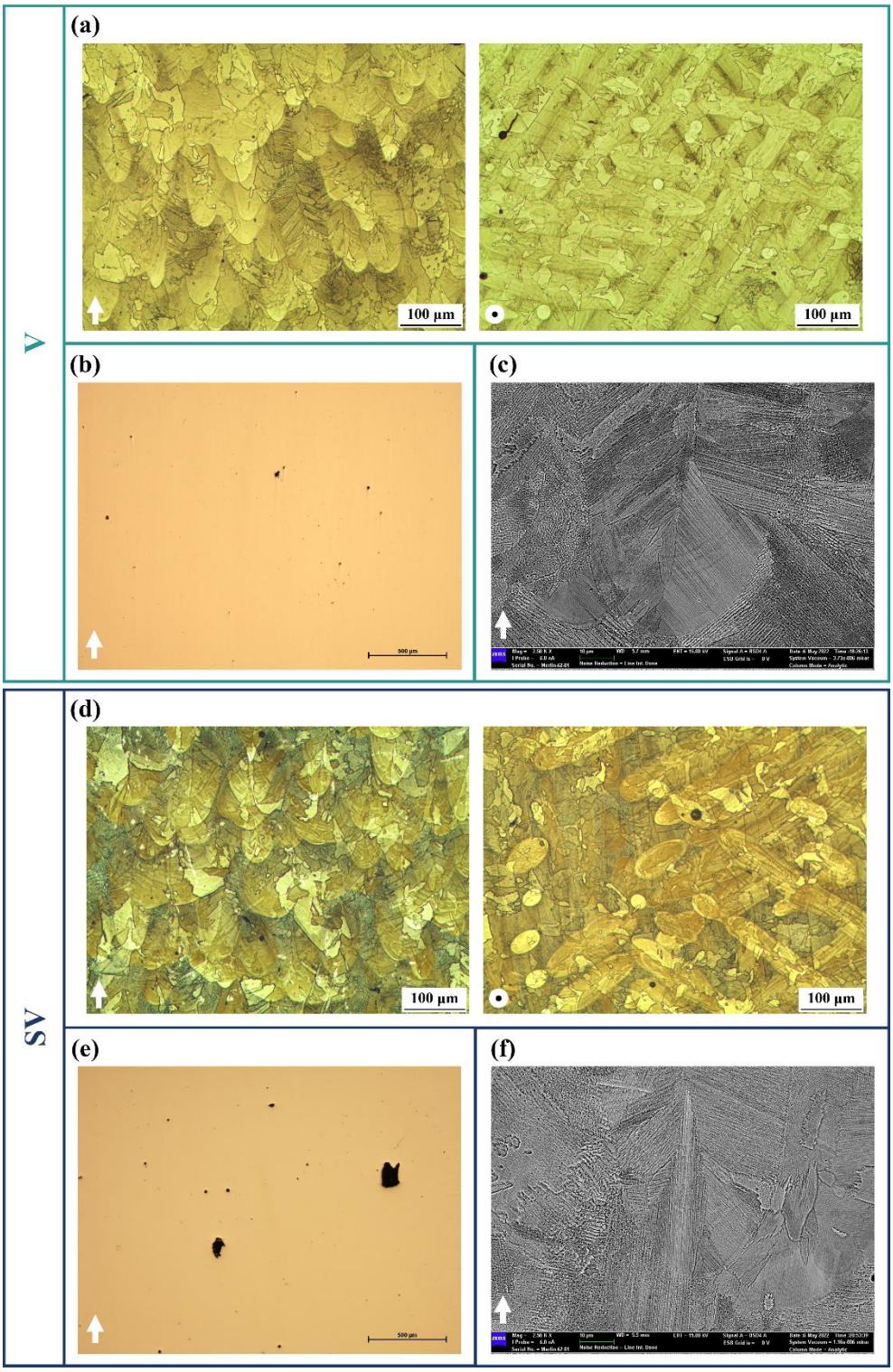

Figure 3.12 Microstructures of the V and SV samples: (a, b, d, e) optical micrographs and (c, f) back-scattered electron (BSE-SEM) images. XZ planes (parallel to the build direction) and XY planes (perpendicular to the build direction) are indicated with arrows and dots, respectively.

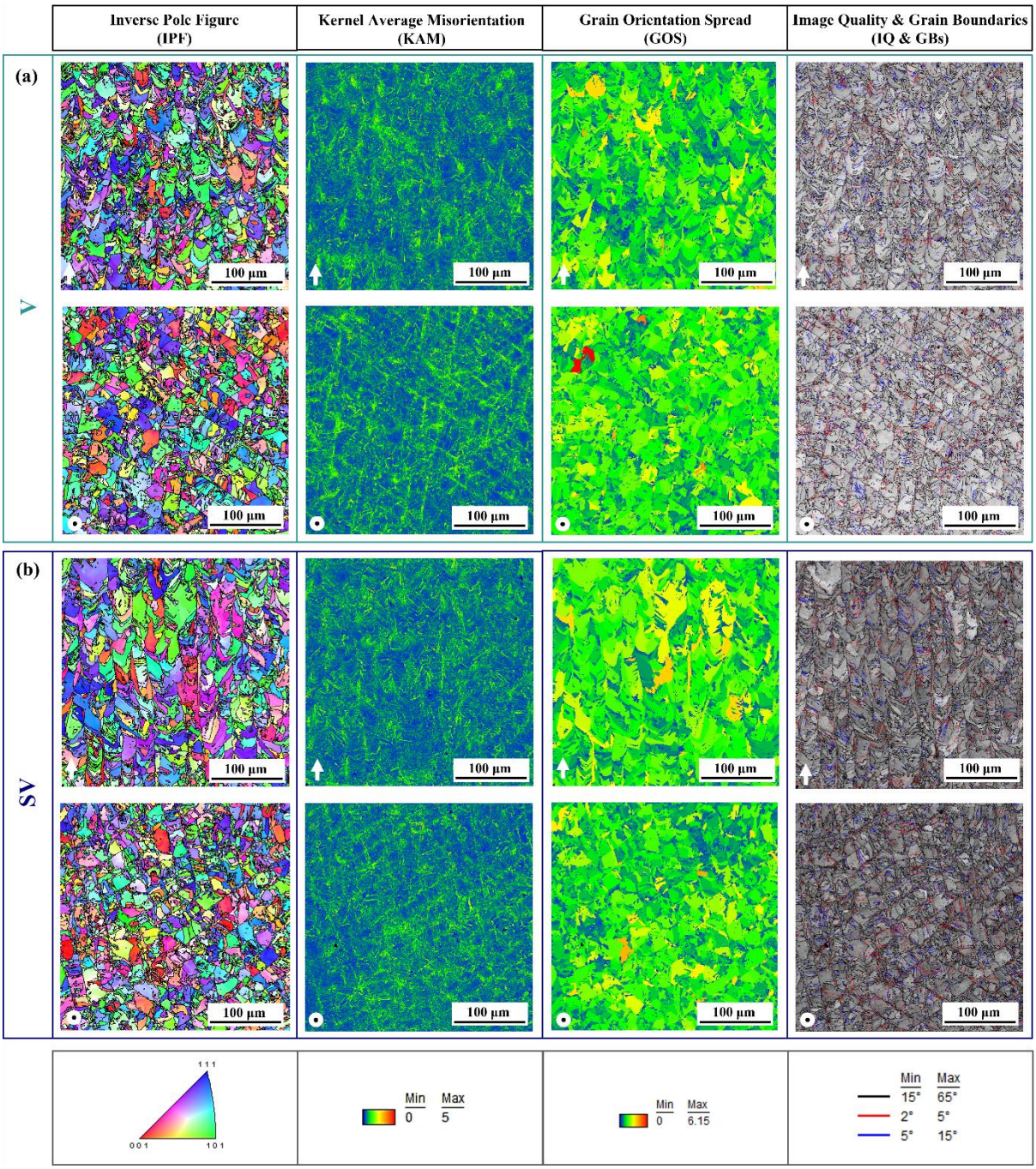

Figure 3.13 EBSD maps of the (a) V and (b) SV samples. XZ planes (parallel to the build direction) and XY planes (perpendicular to the build direction) are indicated with arrows and dots, respectively.

3.4.3 Crystallographic Texture in the Powders and Fabricated Samples

Figure 3.14 shows the pole figures (PFs) and inverse pole figures (IPFs) with respect to the normal direction were presented for the texture analyses. The maximum intensity values belonging to the spatter powder among the powders and fabricated samples were determined as 2.934 for IPFs and 5.217 for PFs. The intensity values are given in

units of multiple of random distribution (MRD). The intensity value equals to 1, for totally random distribution of crystallographic texture [195].

Both powders exhibit slightly preferred (101)//ND (normal direction) texture with intensities of 1.460 for the virgin powder, 2.934 for the spatter powder. The fabricated samples exhibit cube texture with intensities of 1.386 for the V sample and 1.837 for the SV sample. The SV sample exhibits slightly more intense (001)//BD (build direction) texture than the V sample. It should be noted that for V and SV samples surface normal direction of XY plane is also the build direction.

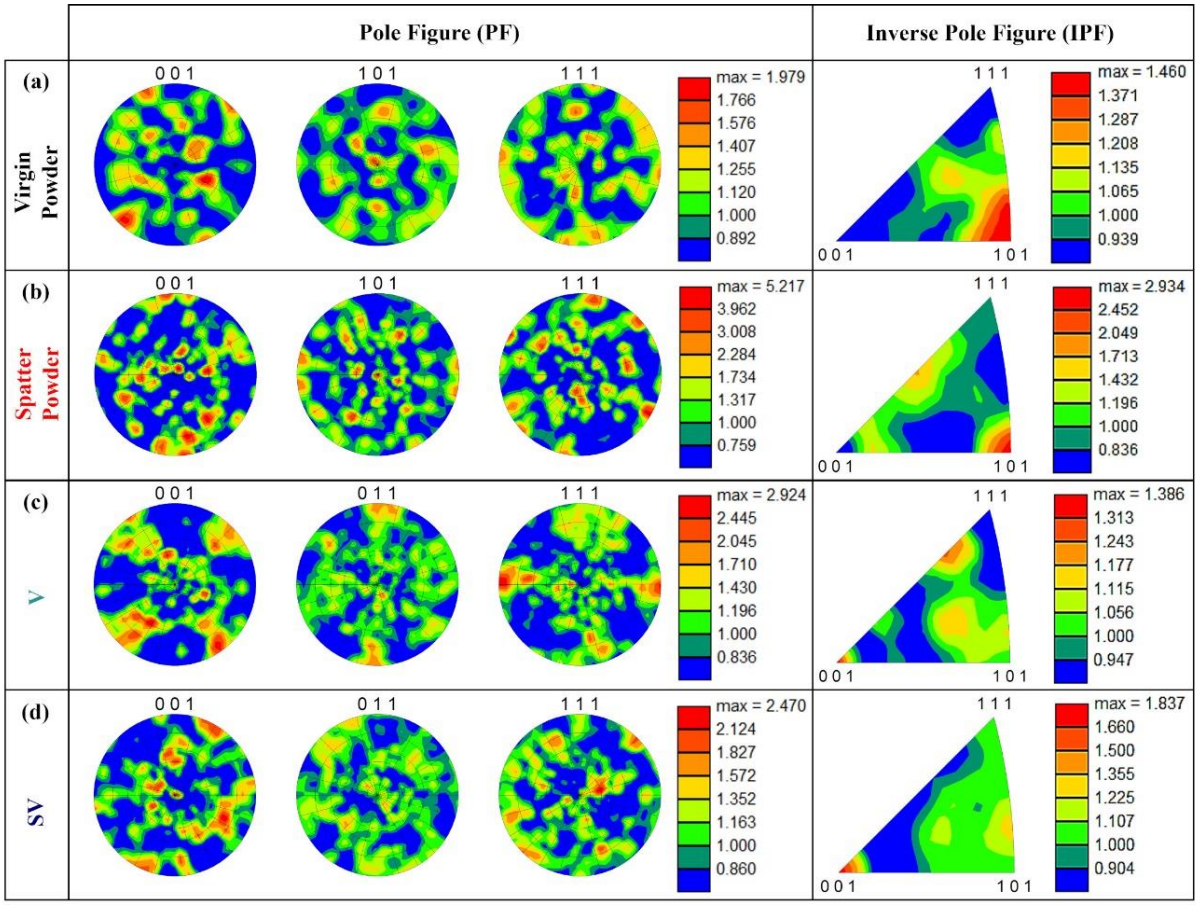

Figure 3.14 Pole figures (PFs) and inverse pole figures (IPFs) with respect to the build direction of the (a) virgin powder, (b) spatter powder, (c) V sample and (d) SV sample.

3.5 Discussion

Spatter formation may be inherent due to the nature of the PBF-LB process. It is challenging to alleviate defects caused by the spatter powder because it is unpredictable where it will land during the PBF-LB process [20]. However, it is possible to reduce the adverse effects (Table 3.1) of spatter powder with some countermeasures such as optimization of the laser volumetric energy, laser beam mode, and build chamber pressure

[19]. Gasper et al. [24,180] worked on spatter formation in IN718 and Hastelloy X fabricated by the PBF-LB, and they reported that the spatter creates a secondary powder system that is dissimilar to the virgin powder. Our findings for IN939 fabricated by the PBF-LB are consistent with their findings. Spatter caused color change and pore formation, along with a 124.4% increase in the average particle size, a 10.2% decrease in the powder circularity, and a 7.5% decrease in the powder aspect ratio. Also, the addition of only 10 wt.% of spatter powder to the virgin powder caused a reduction in flowability. The PBF-LB process required good powder packing and flowability and it has been indicated that spherical powders are the best for these properties. Additionally, the larger average particle size, along with wider particle size distribution of spatter powder can affect the actual layer thickness by creating an extra material within the interaction zone. Thus, the surface roughness increases [26]. For the above-mentioned reasons, a 0.3% relative density reduction and an 80.8% surface roughness increment were observed in the SV sample.

The oxide formation on the spatter powder is shown in Figure 3.5(b). EDS mapping displayed Al_2O_3 oxide spots on the spatter powder. Gasper et al. [20,25] also observed Al_2O_3 oxide spots on the spatter IN718 [20] and Hastelloy X [25] powders. The nominal chemical composition of the IN939 powder was given in Table 3.2 and the main alloying elements are Ni, Cr, Co, Ti and Al. According to the Ellingham diagram [196], these elements have a strong tendency to oxidize in possible forms such as NiO, TiO_2, Cr_2O_3 and Al_2O_3 (ordered from the least stable to most stable oxides) in Ni-base superalloys. Among them, the most stable oxide is Al_2O_3 with respect to the Gibbs free energy. Therefore, it can be said that the most likely oxide to form and exist in Ni-base superalloys is Al_2O_3 in the presence of O_2. The oxidation of some elements in Ni-base superalloys cannot be completely eliminated and the reasons were well explained in the study of Zhang et al. [196]. In order to avoid the oxidation of some elements in Ni-base superalloys completely, the equilibrium partial pressure of oxygen at the melting point of each element must be lower than certain values (can be seen in the Ellingham diagram). For example, the equilibrium partial pressure of oxygen for grade 1 argon is around 0.2 ppm (2×10^{-7} atm) and it is still higher than the oxidation threshold of Al (10^{-58} atm) [20,196]. For this reason, oxidation of Al can only be mitigated but cannot be completely eliminated, although the PBF-LB process was performed under argon gas of 99.999% purity and the oxygen level was monitored to keep it below 20 ppm.

The chemical composition, temperature, roughness/topography, oxide layers and contamination are the materials factors affecting laser absorption [197]. The surface

condition of the spatter had a brown tint coloration and Al_2O_3 oxide was measured on its surface. This oxide could be the reason for the lower reflectivity and higher absorptivity of the spatter powder as shown in Figure 3.6(a). Studies by Gruber et al. [22]and Coste et al. [198] revealed that the surface oxidation of the spatter powder increased the laser absorptivity. Brandau et al. [199] reported that a flat surface of the same material has lower absorbance than the powder surface; and that the surface oxides also increase the laser energy absorption. Additionally, Zhou et al. [200] observed an increase in the laser absorptivity of the oxidized AISI 316L SS powder and a decrease in thermal conductivity. Furthermore, there was no significant difference among the XRD patterns for the powders and fabricated samples. It can be said that there is no change in crystallographic phases, although different solidification conditions lead to different microstructures.

A considerable microstructural difference was observed between the virgin and spatter powders, although there was no difference in terms of crystallographic phases. The average grain size of the spatter powder increased by around 209%, along with a 46.3% reduction in KAM and a 47.5% reduction in GND values due to the high-temperature laser exposure causing local reheating, melting, solidification and a shorter interaction with the inert gas compared to the gas-atomized virgin powder. Additionally, lower grain size of the virgin powder can be explained by higher cooling rates during the gas atomization process [26].

A slight microstructural difference between the fabricated samples (V and SV) is the average grain size on the XZ planes. The addition of only 10 wt.% spatter powder resulted in a 30.2 % average grain size increment in the SV sample (Table 3.5). The reason for the difference between the average grain size values on the XZ planes of the V and SV samples might be due to the spatter powder whose average particle size is larger than the virgin powder melted on the XZ plane during the production. Since the average particle size of the spatter powder is larger than the virgin powder, there might be differences in melting and solidification behaviour during the production. Larger particle size combined with higher laser absorptivity could increase the heat input and hence the temperature gradient during the production. This would result in more columnar grains, especially on the XZ plane.

The spatter powder has a lower nanohardness value compared to the virgin powder (Figure 3.10(e)). The reduction in the nanohardness of the spatter powder can be explained with the Hall-Petch equation. According to the Hall-Petch equation, as the grain size

increases, the yield strength as well as hardness decreases [201]. The spatter powder has a higher grain size compared to the virgin powder (Figure 3.9(a) and Table 3.5). For this reason, the reduction in the nanohardness value of the spatter powder is consistent with the Hall-Petch equation. Figure 3.15 shows the Hall-Petch relation if the fabricated samples and powders are grouped, separately. Both groups show almost the same Hall-Petch factor, 4.8-4.9 (by taking grain size in microns and hardness in GPa). The nanohardness tests probe the material at a single grain level, therefore the difference between (or grouping of) powders and fabricated samples can be attributed to crystallographic texture differences. Moreover, the dislocation density in virgin powder is higher, which increases the resistance to further plastic deformation and hence contributes to the higher hardness of that powder. On the other hand, although there is a slight difference in terms of average grain size values of the fabricated samples, there is no considerable difference in terms of hardness values. Moreover, the higher porosity of the SV sample would be expected to reduce its hardness. Nevertheless, the hardness difference between the powder and spatter is more significant than the difference between the fabricated samples.

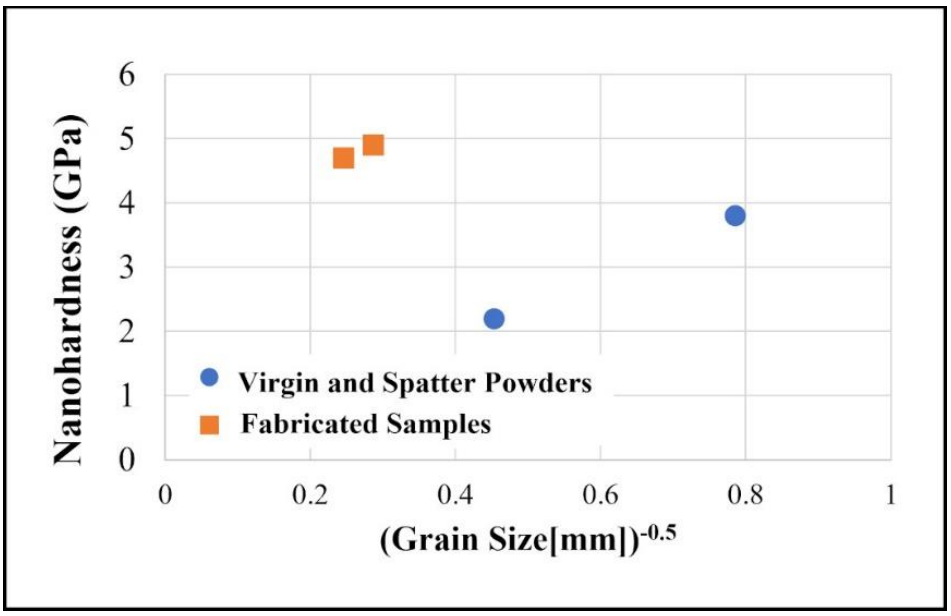

Figure 3.15 Hall-Petch like relation between nanohardness and grain size in the powders and fabricated samples.

Both the V and SV samples exhibit <001>//BD texture, which is the most common solidification texture. The intensity of this texture is higher in the SV sample. The spatter powder contains already melted and solidified particles, which re-melt and re-solidify during the PBF-LB process again. For this reason, spatter powder twice intensifies the solidification texture, seen in SV samples. Nevertheless, both V and SV samples exhibit

the same solidification texture with slightly different intensities. Therefore, it can be concluded that spatter powder does not change the overall texture components.

3.6 Conclusions

In this work, a comprehensive study on the virgin and spatter IN939 powders was conducted. The effect of the addition of 10 wt.% of spatter powder to the virgin powder on the part quality was examined. The surface roughness, density, and microstructure of IN939 fabricated by the PBF-LB were examined. An investigation of a systematic study on the spatter powder and spatter's effect on IN939 fabricated by the PBF-LB was lacking and this study aimed to fill these gaps in the literature. Based on the observed results, the main findings can be summarized as follows:

1) A significant difference was observed between virgin and spatter powders in terms of morphology, particle size distribution, color and the presence of oxides. Spatter caused a brown tint coloration, Al_2O_3 and pore formation, a 124.4% increase in the average particle size, a 10.2% decrease in the powder circularity, and a 7.5% decrease in the powder aspect ratio. Moreover, the addition of only 10 wt.% of spatter powder to the virgin powder caused a reduction in the powder flowability.
2) The average grain size of the spatter powder increased by around 209%, along with a 46.3% reduction in KAM and a 47.5% reduction in GND values due to the high-temperature laser exposure. Additionally, the spatter powder has a lower nanohardness value compared to the virgin powder obeying the Hall-Petch equation.
3) The addition of only 10 wt.% of spatter powder to the virgin powder caused a 0.3% relative density reduction and an 80.8% surface roughness increment in the fabricated samples (V and SV). Therefore, this must be considered when the density and surface roughness are critical for the parts fabricated by the PBF-LB.
4) There was no considerable microstructural difference between the fabricated samples, although the addition of only 10 wt.% spatter powder resulted in a 30.2 % average grain size increment in the SV sample. Also, there was no significant difference between the fabricated samples in terms of hardness values (SV has a slightly lower hardness value compared to V).
5) Spatter powder does not change the overall texture as both V and SV samples exhibit (001)//BD component, which is the most common solidification

component. The intensity of this component is slightly higher in the SV sample, which was attributed to the presence of re-melted and re-solidified particles.

3.7 Contribution to Thesis Objectives

Powder is one of the most significant PBF-LB process parameters as everything starts with powder in the PBF-LB process. Understanding powder properties is crucial to improve the PBF-LB process. After a thorough review of the existing literature, it was found that there was no systematic study regarding the characteristics of IN939 powder, both virgin and spatter, as well as the phenomena of spatter and its impact on the properties of fabricated parts. This chapter significantly addressed this gap by understanding the effects of virgin and spatter IN939 powders on the PBF-LB process. It provided a detailed comparison of virgin and spatter IN939 powders, revealing key differences in morphology, particle size distribution, and oxide formation. By mixing 10 wt.% spatter powder with virgin powder, the research evaluated the effects on powder flowability, noting a reduction that impacts processing efficiency and fabricated part quality. The study also examined the impact of 10 wt.% spatter powder on the fabricated part density and surface roughness, underscoring the importance of powder quality for optimal part properties. Despite the addition of 10 wt.% spatter powder, no significant microstructural differences were observed between the samples fabricated using virgin and mixed powder, though an increase in grain size was noted, and minimal impact on hardness was found. Furthermore, the research confirmed that the overall texture of the fabricated parts remained consistent with the addition of spatter powder. Overall, this study systematically investigated virgin and spatter characteristics, and spatter powder effects, offering theoretical insights and practical recommendations for the PBF-LB process with IN939 alloy.

Chapter 4: Powder Bed Fusion-Laser Beam of IN939: Effect of Process Parameters on the Relative Density, Defect Formation, Surface Roughness, and Microstructure

Publication Status: Published

M.N. Doğu, M.A. Obeidi, H. Gu, C. Teng, D. Brabazon, **Powder Bed Fusion–Laser Beam of IN939: The Effect of Process Parameters on the Relative Density, Defect Formation, Surface Roughness and Microstructure**, Materials 17 (2024). https://doi.org/10.3390/ma17133324.

4.1 Abstract

This study investigates the effects of process parameters in the powder bed fusion-laser beam (PBF-LB) process on IN939 samples. The parameters examined include laser power (160, 180, and 200 W), laser scanning speed (400, 800, and 1200 mm/s) and hatch distance (50, 80, and 110 μm). The study focuses on how these parameters affect surface roughness, relative density, defect formation and the microstructure of the samples. Surface roughness analyses revealed that the average surface roughness (Sa) values of the sample ranged from 4.6 μm to 9.5 μm, while the average height difference (Sz) varied from 78.7 μm to 176.7 μm. Furthermore, increasing the hatch distance from 50 μm to 110 μm while maintaining constant laser power and scanning speed led to a decrease in surface roughness. Relative density analysis indicated that the highest relative density was 99.35%, and the lowest was 93.56%. Additionally, the average porosity values were calculated, with the lowest being 0.06% and the highest reaching 9.18%. Although some samples had identical average porosity values, they differed in porosity/mm^2 and average Feret size. Variations in relative density and average porosity were noted in samples with the same volumetric energy density (VED) due to different process parameters. High VED led to large, irregular pores in several samples. Microcracks, less than 50 μm in length, were present, indicating solidification cracks. The microstructural analysis of the XZ planes revealed arc-shaped melt pools, columnar elongated grains aligned with the build direction, and cellular structures with columnar dendrites. This study provides insights for optimizing PBF-LB process parameters to enhance the quality of IN939 components.

4.2 Introduction

PBF-LB is a metal additive manufacturing (AM) technique offering notable advantages over traditional manufacturing methods. These include the capacity to produce intricate metal parts with geometric complexity in a single step, enabling design freedom through near-net-shape production, and reducing material waste and tooling costs. The PBF-LB process begins by spreading a layer of metal powder onto a build plate, then selectively melting the desired areas within the powder layer using a laser beam according to a 3D computer-aided design (CAD) file. This layer-by-layer production continues until the part is fully fabricated [15,172].

In the PBF-LB process, there are over 100 processing parameters to consider [133,202]. These parameters can be broadly categorized into laser-related factors (i.e., laser power and spot size), scan-related variables (including laser scanning speed, hatch

distance, scanning pattern, and rotation angle), powder-related characteristics (like powder particle morphology, size, and distribution, and layer thickness), as well as macroscopic parameters such as powder bed temperature and gas flow [169,202]. The laser power, layer thickness, laser scanning speed, and hatch distance are among the most extensively studied process parameters in the PBF-LB process. Laser power controls the energy transferred from the system to the powder, while layer thickness determines the height of each molten powder layer. Laser scanning speed dictates the rate at which the laser moves across the powder surface, and hatch distance affects the degree of overlap between adjacent laser paths. These parameters play critical roles in determining the quality and characteristics of the fabricated parts [17,203].

Despite its advantages, the PBF-LB process can still show certain unavoidable defects when improper scanning parameters and insufficient powder melting occur. These issues can compromise mechanical properties and impede large-scale industrial commercialization. They include partially melted powder, undesired microstructures, poor surface finish, porosity defects, balling defects, high residual stress, surface and internal cracks, and inadequate bonding between layers. Additionally, pore defects in the PBF-LB process can be categorized based on their formation mechanisms. These defects include gas pores, which can be categorized into keyhole pores and powder feedstock pores, as well as lack of fusion (LOF) defects, such as inter-track LOF, inter-layer LOF, and LOF caused by spattering. The unstable melt pools can be shown as the primary reason for these defects [169,171,172,203]. Moreover, the rapid solidification, high cooling rates (10^5-10^7 K/s), and repeated thermal cycles lead to non-equilibrium solidification, causing residual stress [103,204].

IN939 is a precipitation-hardenable Ni-base superalloy, primarily strengthened by the formation of the L12-ordered γ' phase (Ni_3(Al, Ti)). Originally, it was developed in the late 1960s as a cast alloy to meet the demand for a robust, highly corrosion-resistant material capable of prolonged operation at temperatures reaching 850 °C. It has found extensive application in higher-temperature applications within aerospace engines, particularly in hot sections such as turbine blades and nozzle guide vanes, owing to its exceptional properties. The microstructure of as-cast IN939 consists of a gamma (γ) phase solid-solution matrix, with the gamma prime (γ') phase serving as the primary strengthening component.

While IN939 was initially developed as a cast alloy [62,78,79], recent attention has been given to its production using the PBF-LB process [11,14,15,18,33,74,85,89,90,178,205]. However, there are limited studies in the literature focusing on optimizing process parameters for achieving the desired relative density in IN939 produced via the PBF-LB process. Table 4.1 summarizes the details of existing studies on process parameter optimization for IN939 fabricated by PBF-LB, revealing variations in powder suppliers, PBF-LB machines, and process parameters used. It is important to note that powder characteristics, such as particle size distribution, flowability, chemistry, and morphology, significantly influence the build quality and porosity distribution in the PBF-LB process. Additionally, the PBF-LB machines themselves can introduce defects due to issues with the laser beam scanning system, build chamber environment, powder spreading system, and baseplate [169,179,206]. For instance, Obeidi et al. [152] reported significant variations in the mechanical performance and properties of 316L samples produced on different PBF-LB machines despite using the same process parameters.

Although IN939 is a well-established Ni-base superalloy, its application in the PBF-LB process is relatively new, necessitating further research to understand the effects of this process on IN939. This study aims to address this gap by systematically investigating the influence of key process parameters, such as laser power, laser scanning speed, and hatch distance, on the relative density, defect formation, surface roughness, and microstructure of IN939 fabricated by the PBF-LB process. By optimizing these parameters, this research seeks to enhance the performance and reliability of IN939 components produced using PBF-LB technology, contributing to the advancement of additive manufacturing techniques for high-performance superalloys.

Table 4.1 Studies for process parameters optimization of IN939 fabricated by PBF-LB.

Reference	**Marchese et al.** [11]	**Dursun et al.** [90]	**Rodríguez-Barber et al.** [18]
Powder	Gas-atomized IN939 powder (LPW Carpenter Additive)	-	Gas-atomized IN939 powder (Eckart TLS GmbH)
PBF-LB machine	CONCEPT Mlab Cusing R system	EOS M290	Renishaw AM400
Laser power (W)	95 (fixed)	200- 350	250- 300
Laser speed (mm/s)	100-2000	800-1400	1000-1750
Hatch distance (mm)	0.02-0,15	0.1 (fixed)	0.05- 0,09
Layer thickness (µm)	20 (fixed)	40 (fixed)	60 (fixed)
Scanning strategy	Stripes of 5 mm with a rotation of 67º	-	Bidirectional scanning strategy, with a 67◦ rotation
Laser mode	Continuous (CW)	Continuous (CW)	Pulsed (PW)
VED (J/mm^3)	30-320	35-109	26-100
Preheating (ºC)	-	80	-
Characterization	Cubic samples	Single-tracks and cubic samples	Cubic samples

4.3 Materials and Methodology

4.3.1 IN939 Fabrication by the PBF-LB Process

The research employed gas-atomized IN939 powder whose particle size distribution is between 17.4 µm and 52 µm (Truform 939-N65, Praxair Surface Technologies) to produce IN939 samples. The chemical composition of the powder is given in Table 4.2, and a detailed powder characterization was presented in a prior study conducted by the authors [15].

Table 4.2 The **c**hemical composition (wt.%) of the gas atomized IN939 powder.

Elements	**Al**	**Co**	**Cr**	**Nb**	**Ta**	**Ti**	**W**
wt.%	1.9	18.9	22.8	1.0	1.4	3.8	2.0
	Zr	**Ni**	**B**	**C**	**O**	**N**	
	0.028	Bal.	0.004	0.16	0.014	0.009	

An Aconity MINI (GmbH) metal 3D printer equipped with an Ytterbium fiber laser from IPG, model YLR-200-WC-Y11, 2011 series with a wavelength of 1068 nm was used to fabricate IN939 samples. All fabrications were carried out under a protective argon

atmosphere maintained using 99.999% pure argon gas, ensuring oxygen levels remained below 20 ppm. Additionally, CK45 steel was used as a build plate for all prints.

IN939 cubic samples (10 mm × 10 mm × 10 mm with 2 mm support) were fabricated with the Aconity MINI. Figure 4.1 presents images of the build plate post-fabrication, along with a schematic representation of the as-built samples. A full factorial Design of Experiment (DoE) model with 3 factors at 3 levels (3^3) was created to analyze the impact of input processing parameters on output characteristics. The input parameters included laser power, laser scanning speed, and hatch distance, and the PBF-LB process parameters used in this study are given in Table 4.3. The full factorial DoE combination of the PBF-LB process parameters and VED values are listed in Table 4.4 with the corresponding sample number. The input VED [207] was calculated according to the following Equation (4.1):

$$VED = \frac{P}{V \text{ x } h \text{ x } t} \ (J/mm^3) \tag{4.1}$$

where, P represents laser power (W), V stands for laser scanning speed (mm/s), h presents hatch distance (μm), and t denotes layer thickness (μm).

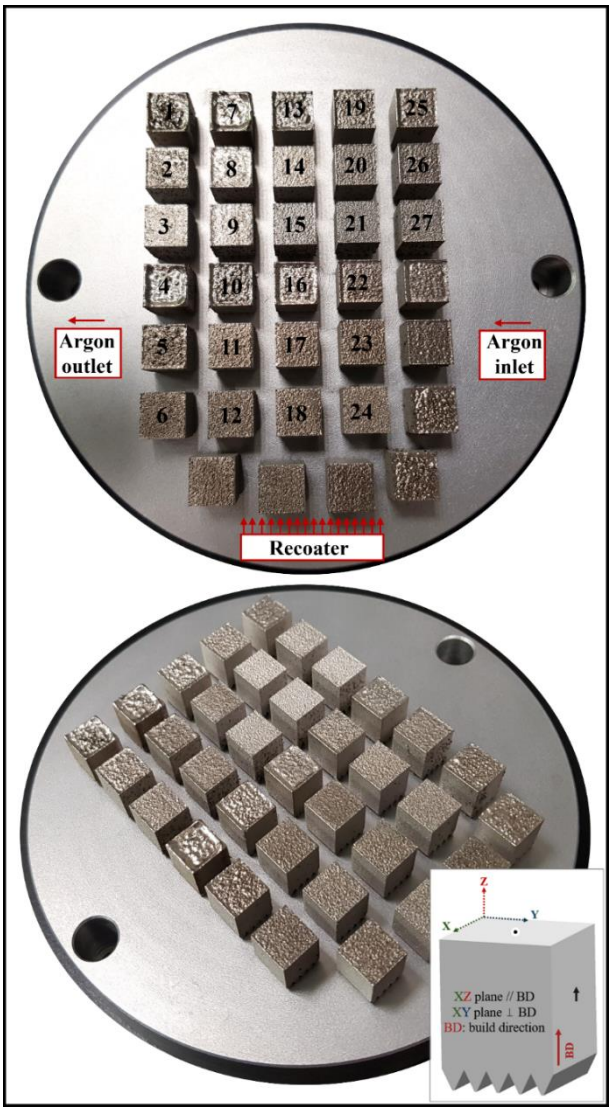

Figure 4.1 Images of the build plate after fabrication and schematic of the as-built IN939 samples.

Table 4.3 PBF-LB process parameters used in the present study and their levels.

Process Parameters	Level-1	Level-2	Level-3
Laser power (W)	160	180	200
Laser scanning speed (mm/s)	400	800	1200
Hatch distance (μm)	50	80	110
Layer thickness (μm)	40 (fixed)		
Spot size (μm)	80 (fixed)		
Contour (μm)	50		
Scanning strategy	Alternating bi-directional scan with 67^{o} rotation		

Table 4.4 PBF-LB process parameters for the entire DoE, along with the sample numbers.

Sample	Laser power (W)	Hatch distance (µm)	Laser scanning speed (mm/s)	VED (J/mm^3)
1	160	50	400	200.0
2	160	50	800	100.0
3	160	50	1200	66.7
4	180	50	400	225.0
5	180	50	800	112.5
6	180	50	1200	75.0
7	200	50	400	250.0
8	200	50	800	125.0
9	200	50	1200	83.3
10	160	80	400	125.0
11	160	80	800	62.5
12	160	80	1200	41.7
13	180	80	400	140.6
14	180	80	800	70.3
15	180	80	1200	46.9
16	200	80	400	156.3
17	200	80	800	78.1
18	200	80	1200	52.1
19	160	110	400	90.9
20	160	110	800	45.5
21	160	110	1200	30.3
22	180	110	400	102.3
23	180	110	800	51.1
24	180	110	1200	34.1
25	200	110	400	113.6
26	200	110	800	56.8
27	200	110	1200	37.9

4.3.2 Surface Roughness Measurement

Surface roughness measurements of the as-built samples were conducted using the Bruker ContourGT, focusing on the XZ planes over a 2 mm × 2 mm area. The Sa value, indicating the arithmetical mean height, was utilized to quantify surface roughness. Additionally, the Sz value represents the summation of the maximum peak height and maximum pit depth. A rainbow scale bar, ranging from +100 μm to -87 μm, was employed to enhance the visualization of surface roughness disparities among the samples.

4.3.3 Relative Density and Porosity Measurements

The relative density of the as-built samples was measured by Archimedes' method using a Sartorius Entris II Essential BCE124I-1S analytical balance having an accuracy and repeatability of ± 0.1 mg according to ASTM B311-17 [208]. The measurements were repeated three times for each sample to obtain the average relative density value of each sample. Before the measurements, the as-built samples were ground lightly to flat on all faces with 80 SiC abrasive paper and cleaned thoroughly. Ethanol (Lenox, 99.99 %) was used as the fluid. Additionally, the theoretical density of a fully dense IN939 was taken as 8.15 g/cm^3 to calculate the relative density values of the samples [68].

Conventional optical microscopy was employed to analyze the distribution of porosity. Optical images of the as-polished cross-sections, captured from both XZ and XY planes, were taken utilizing the stitching capability of the Keyence 3D optical microscope. For the porosity calculation, the stitched optical images including at least 20 images for XZ planes and 10 images for XY planes were analyzed using ImageJ software.

The response surface method (RSM) is a collection of mathematical and statistical techniques used for modelling and predicting the output response. To analyze the relationship between input laser process parameters and relative density (%) and surface roughness (μm), the RSM of experimental design was employed by using Design-Expert 13 software.

4.3.4 Microstructural Characterization

The as-built samples were precision-cut to investigate both XZ and XY planes (XZ plane which is parallel to the building direction and XY plane which is perpendicular to the building direction) and were hot-mounted with Bakelite. Then, mounted samples were automatically ground using conventional SiC grinding papers (up to 1200 grit sizes) and

polished with progressively finer diamond suspensions (9, 3, and 1 μm) using the Struers Tegramin-20 machine. After that, as-polished samples were etched with the Glyceregia reagent (15 ml HCl, 10 ml glycerol and 5 ml HNO_3) for further microstructural examination. For microstructural examinations, Keyence VHX2000E optical 3D digital microscope (OM), and Zeiss EVO LS-15 Scanning Electron Microscope (SEM) were utilized. Zeiss EVO LS 15 equipped with Oxford EDS detector was used for energy dispersive X-ray spectroscopy (EDS) analysis (an acceleration voltage of 15 kV, 1.0 nA probe current, WD: 8.5 mm).

4.4 Results

4.4.1 Surface Roughness

Table 4.5 displays the average surface roughness (Sa), ranging from 4.6 μm to 9.5 μm, and the maximum height (Sz), ranging from 78.7 μm to 176.7 μm, for the XZ planes of the as-built samples. Among the samples, the lowest Sa value (4.6 μm) belongs to sample 26, whereas samples 1 and 2 have the highest Sa value (9.5 μm). Moreover, Figure 4.2 shows the surface roughness profiles of the selected as-built IN939 samples (samples 1, 8, 17, and 21). Additionally, optical images of the XZ planes of the as-built IN939 samples are presented in Figure 4A1 in Appendix A. It can be seen from the optical images that PBF-LB process parameters have a direct influence on the dimensional accuracy and surface roughness. High VED resulted in the formation of devil horns due to over-melting. This defect was particularly pronounced in samples 1, 4, and 7, which had the highest VED values. Moreover, a strong correlation was found between the input processing parameters and the surface roughness (μm), as shown in Figure 4.3. Each graph displays the full range of two process parameters versus the surface roughness (μm), with the other parameters held constant. The model developed for the effect of the laser input power, laser scanning speed, and hatch distance on the resulting surface roughness was statistically significant (p-value < 0.0008).

Table 4.5 Average surface roughness (Sa) and the maximum height (Sz) values for the XZ planes of the as-built IN939 samples.

Sample	Sa (µm)	Sz(µm)	Sample	Sa (µm)	Sz(µm)
1	9.5	157.6	**15**	5.3	118.2
2	9.5	164.7	**16**	8.9	141.1
3	7.6	137.8	**17**	5.4	99.1
4	9.2	153.5	**18**	6.8	129.8
5	8.8	154.2	**19**	6.0	168.3
6	7.1	138.4	**20**	5.1	124.1
7	6.0	78.7	**21**	6.3	117.3
8	8.2	160.3	**22**	6.2	85.0
9	7.7	173.0	**23**	5.7	133.4
10	7.9	130.2	**24**	6.7	134.1
11	6.0	138.6	**25**	6.6	107.0
12	7.6	154.5	**26**	4.6	95.0
13	9.3	176.7	**27**	5.5	150.4
14	5.0	87.0			

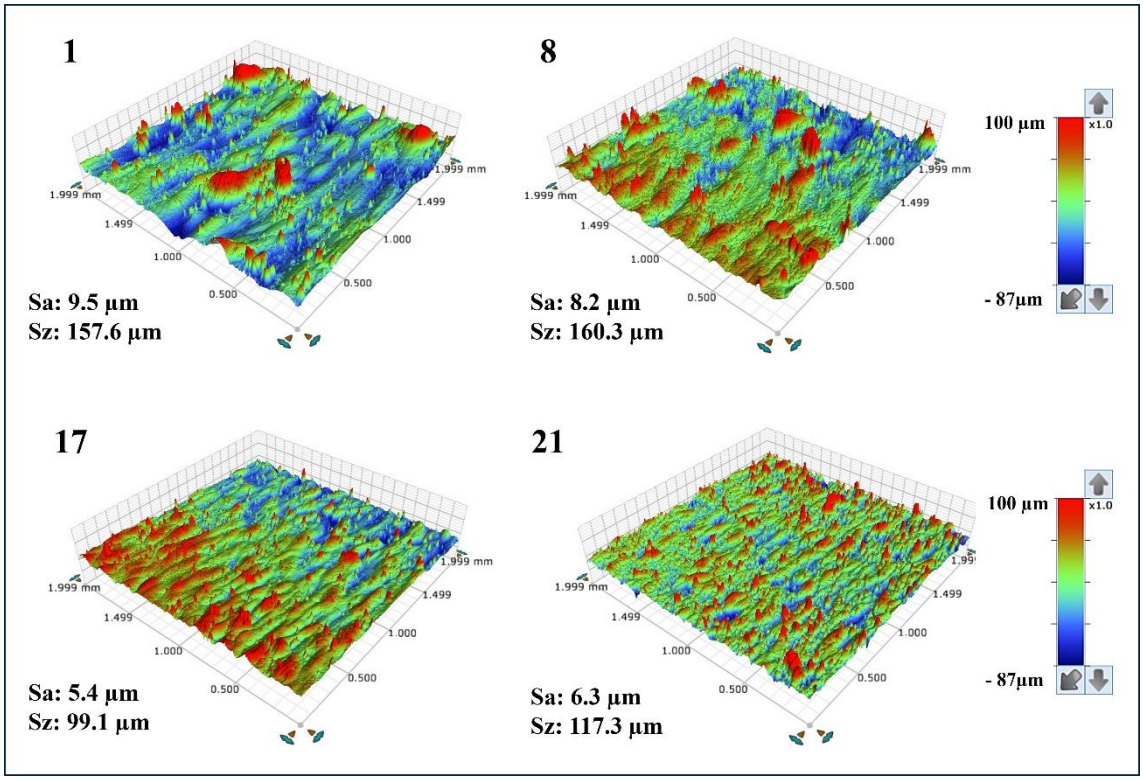

Figure 4.2 Surface roughness profiles of the selected as-built IN939 samples (samples 1, 8, 17, and 21).

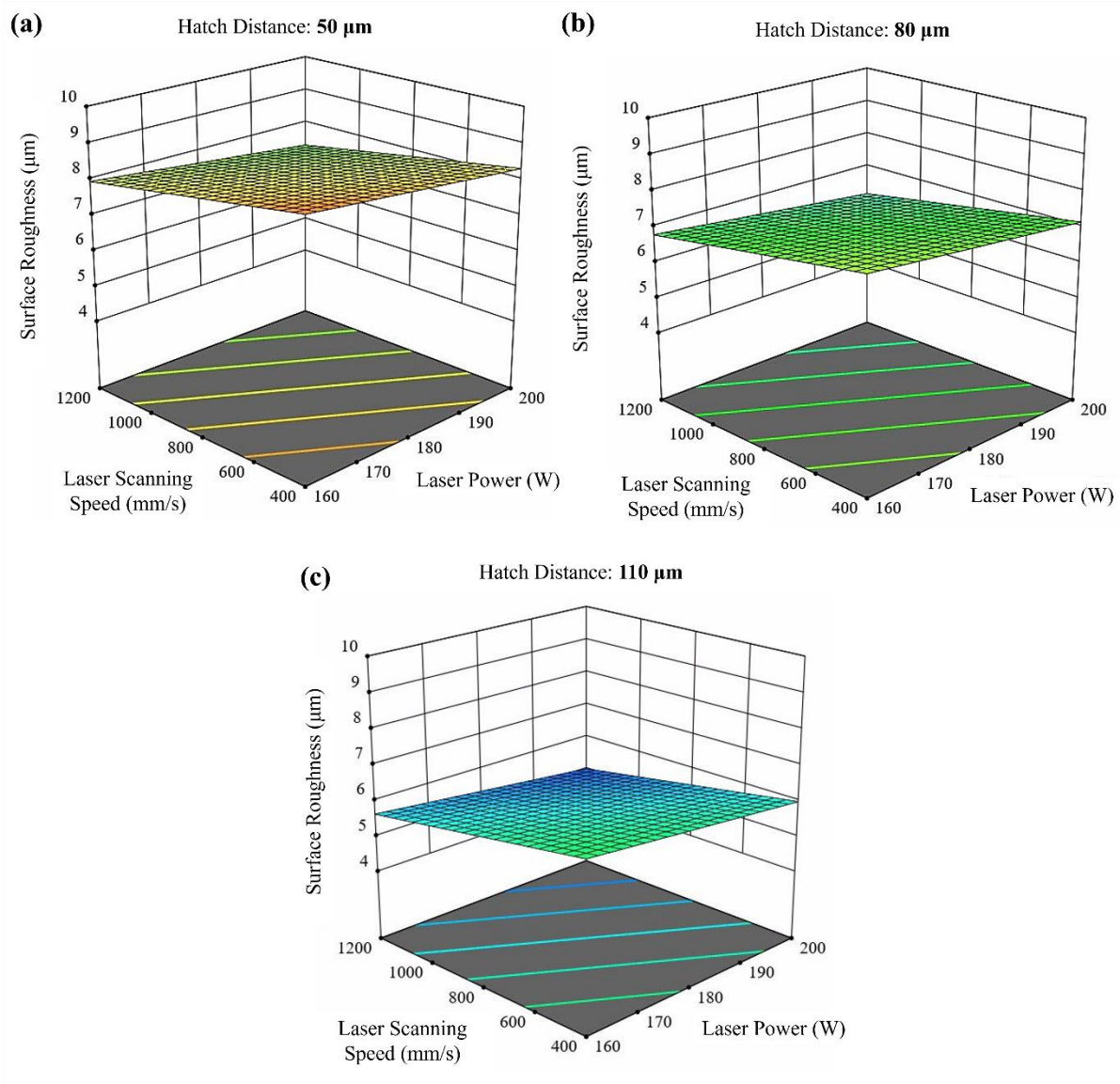

Figure 4.3 RSM graphs of the surface roughness (µm) versus the different input processing parameters.

4.4.2 Relative Density

Relative density values are depicted in Table 4.6. Additionally, Figure 4A2(a) in Appendix A shows the relative density (%) versus VED (J/mm^3) graph. The results indicate that sample 8 exhibits the highest relative density at 99.35%, whereas sample 21 shows the lowest relative density at 93.56%. Furthermore, samples 14, 6, 9, and 17 exhibit also high relative densities at 99.25%, 99.23%, 99.20%, and 99.20%, respectively. On the other hand, sample 1 has a very low relative density (94.19%) after sample 21. Moreover, the same VED (125 J/mm^3) values, obtained using different process parameters, resulted in different relative densities for samples 8 and 10. Furthermore, a strong correlation was found between the input processing parameters and the relative density (%), as shown in

Figure 4.4. Each graph displays the full range of two process parameters versus the relative density (%), with the other parameters held constant. The model developed for the effect of the laser input power, laser scanning speed, and hatch distance on the resulting relative density was statistically significant (p-value < 0.0001).

Table 4.6 Relative density (%) values of the as-built IN939 samples (errors show 95% CI).

Sample	P (W)	h (µm)	V (mm/s)	VED (J/mm^3)	Relative density (%)
1	160	50	400	200.0	94.19 ± 0.009
2	160	50	800	100.0	98.83 ± 0.008
3	160	50	1200	66.7	99.05 ± 0.010
4	180	50	400	225.0	96.50 ± 0.006
5	180	50	800	112.5	98.97 ± 0.003
6	180	50	1200	75.0	99.23 ± 0.003
7	200	50	400	250.0	96.02 ± 0.007
8	200	50	800	125.0	99.35 ± 0.011
9	200	50	1200	83.3	99.20 ± 0.006
10	160	80	400	125.0	95.93 ± 0.002
11	160	80	800	62.5	99.08 ± 0.004
12	160	80	1200	41.7	97.18 ± 0.001
13	180	80	400	140.6	96.16 ± 0.007
14	180	80	800	70.3	99.25 ± 0.010
15	180	80	1200	46.9	98.76 ± 0.001
16	200	80	400	156.3	97.12 ± 0.004
17	200	80	800	78.1	99.20 ± 0.002
18	200	80	1200	52.1	98.87 ± 0.007
19	160	110	400	90.9	97.92 ± 0.003
20	160	110	800	45.5	98.71 ± 0.005
21	160	110	1200	30.3	93.56 ± 0.009
22	180	110	400	102.3	98.02 ± 0.003
23	180	110	800	51.1	98.81 ± 0.002
24	180	110	1200	34.1	94.40 ± 0.011
25	200	110	400	113.6	97.92 ± 0.013
26	200	110	800	56.8	99.10 ± 0.016
27	200	110	1200	37.9	97.40 ± 0.008

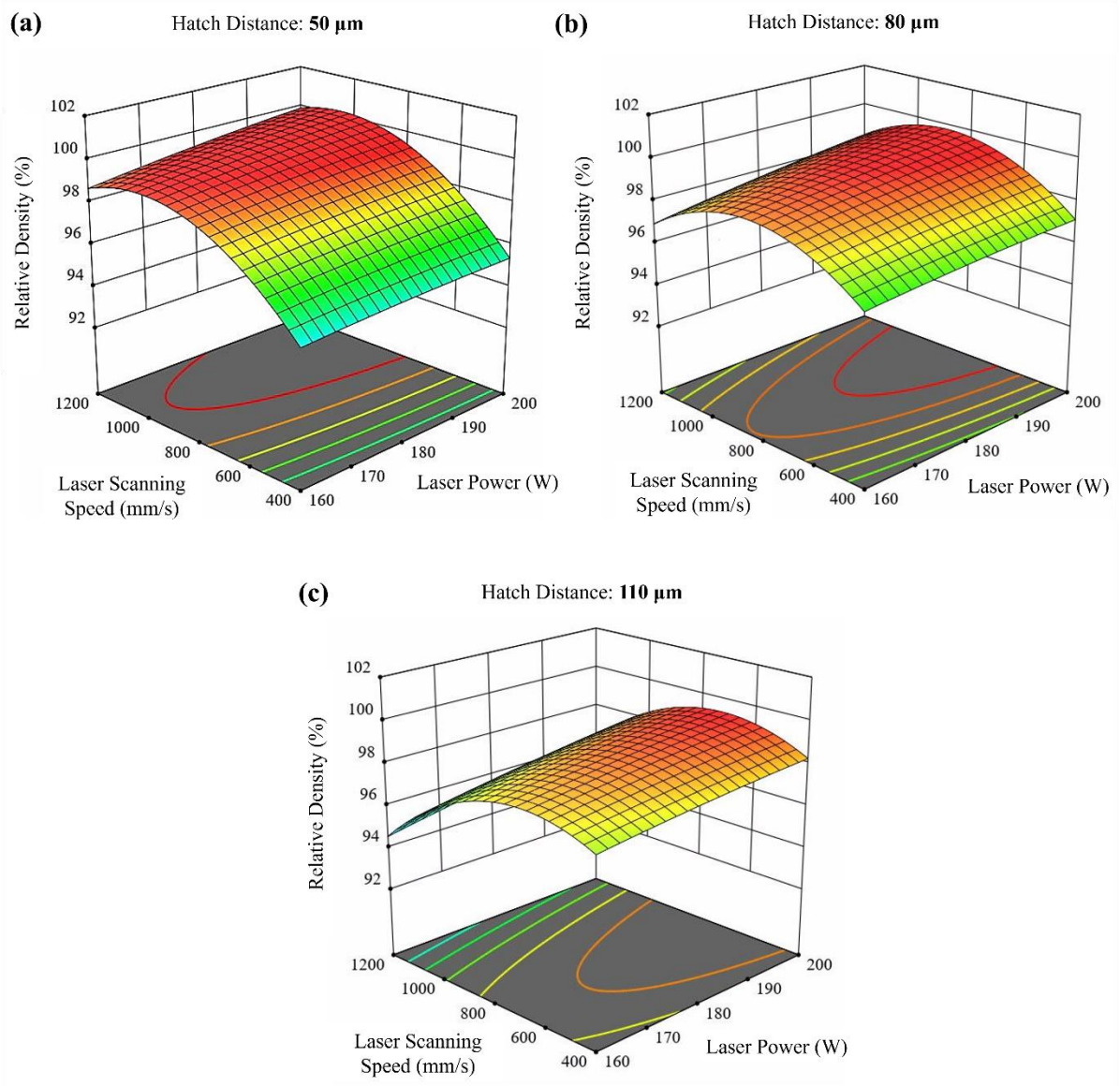

Figure 4.4 RSM graphs of the relative density (%) versus the different input processing parameters.

4.4.3 Defect Formation

The porosity percentages of the samples were calculated by including all voids, such as gas porosity and lack of fusion (LOF) defects by using ImageJ. Table 4.7 presents the results of the ImageJ porosity analysis for the samples, along with the average results, including average porosity (%), pores/mm^2, and average Feret size (µm). Additionally, Figure 4A2(b) in Appendix A shows the average porosity (%) versus VED (J/mm^3) graph. Furthermore, Figure 4.5**,** Figure 4.6 and Figure 4.7 show the as-polished optical micrographs of the XZ planes of the samples. In addition to this, the results of the ImageJ porosity analysis for the XZ and XY planes of the samples are given in Table 4A1 in

Appendix A, and the as-polished optical micrographs of the XY planes of the samples are displayed in Figure 4A3 in Appendix A.

A higher pores/mm^2 value indicates a higher concentration of pores, which can decrease mechanical properties such as strength and fatigue resistance. Conversely, a lower pores/mm^2 value suggests fewer pores, indicating better material quality and integrity. Additionally, the average Feret size provides insight into pore dimensions, with a larger average Feret size indicating the presence of larger pores, and a smaller average Feret size indicating predominantly smaller pores. According to the results, sample 1 exhibits the highest average porosity (%) at 9.18%, while samples 14 and 17 show the lowest average porosity at 0.06%. Additionally, the average porosity (%) for sample 11 is 0.07%, closely resembling that of samples 14 and 17. Although samples 14 and 17 have the same average porosity (%) values, their porosity/mm^2 and average Feret size values are different (Table 4.7). On the other hand, samples 8 and 10 have completely different average porosity (%) values at 0.09% and 3.50% even though they have the same VED value. Very high VED resulted in large, irregular pores for samples 1, 4, and 7 (Figure 4.5) and samples 10, 13, and 16 (Figure 4.6). Additionally, these samples contain a high number of small pores, leading to high pores/mm² values. However, the combination of very large and very small pores reduced the average Feret size. On the other hand, the lowest VED, which is 30.3 J/mm^3, belongs to sample 21. This sample exhibits the lowest relative density and high porosity due to insufficient energy for melting (Figure 4.7). Additionally, samples 24 and 27 exhibit low relative density and high porosity due to their low VED values.

Table 4.7 ImageJ porosity analysis of the as-built samples.

Sample	Average Porosity (%)	Average Pores/mm^2	Average Feret Size (μm)
1	9.18	38.27	39.53
2	0.64	5.69	61.52
3	0.31	2.36	190.37
4	2.71	40.68	30.63
5	0.45	6.79	70.72
6	0.14	2.80	108.30
7	5.15	44.94	32.90
8	0.09	5.64	46.80
9	0.28	18.37	14.06
10	3.50	47.99	29.99
11	0.07	13.76	8.82
12	2.70	24.56	39.37
13	3.49	28.74	38.74
14	0.06	3.12	15.01
15	0.39	4.11	35.21
16	2.83	30.30	43.42
17	0.06	6.73	11.32
18	0.46	11.46	30.38
19	1.51	29.11	32.84
20	0.50	12.56	39.55
21	6.41	63.72	44.59
22	1.38	31.03	27.33
23	0.63	32.54	20.41
24	5.98	63.86	38.42
25	1.21	28.70	25.06
26	0.10	2.24	78.23
27	1.85	36.18	36.99

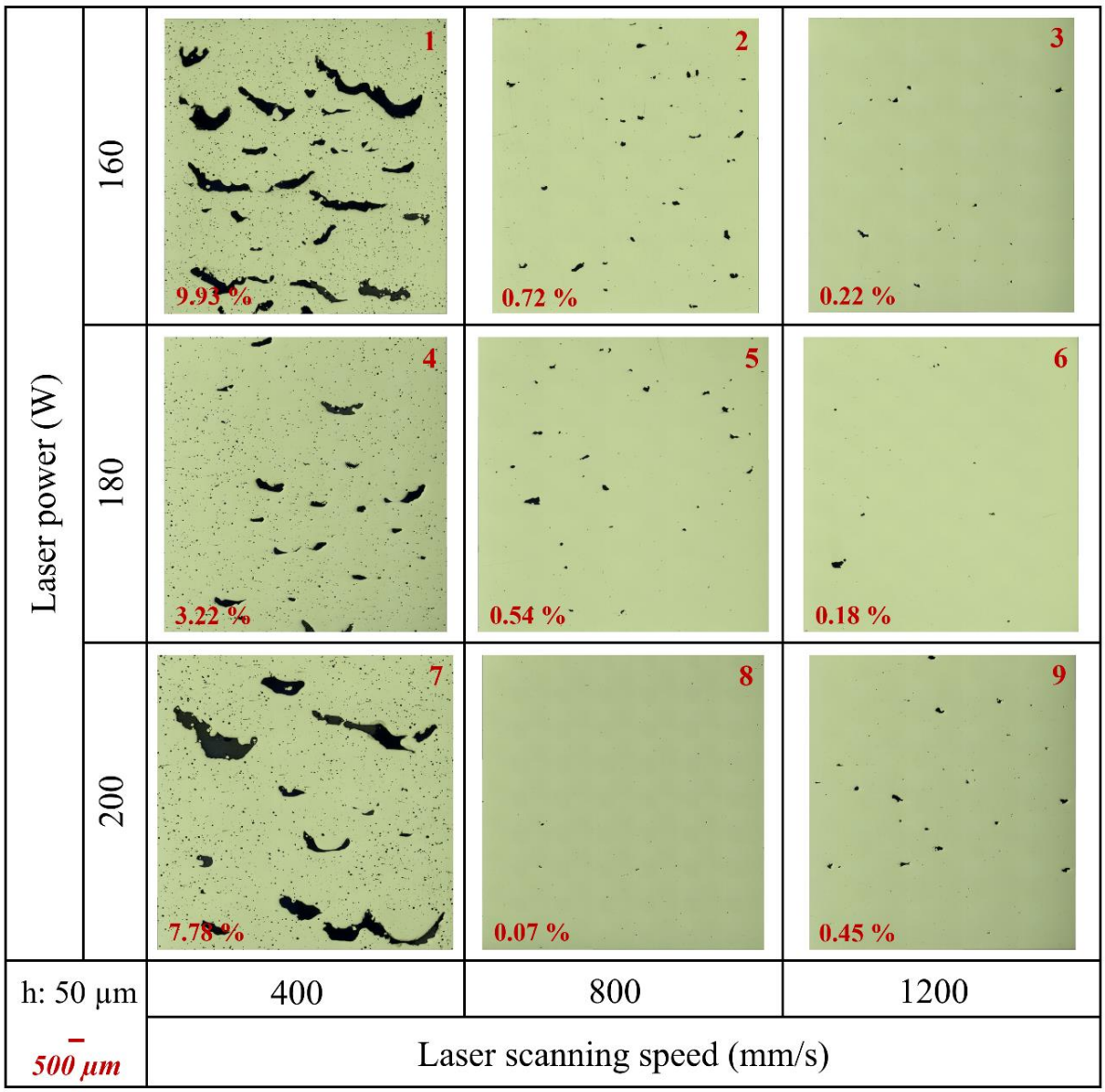

Figure 4.5 The as-polished optical micrographs of as-built samples (1-9) in the XZ plane (parallel to the build direction). Porosity (%) values are indicated on the micrographs (hatch distance: 50 µm).

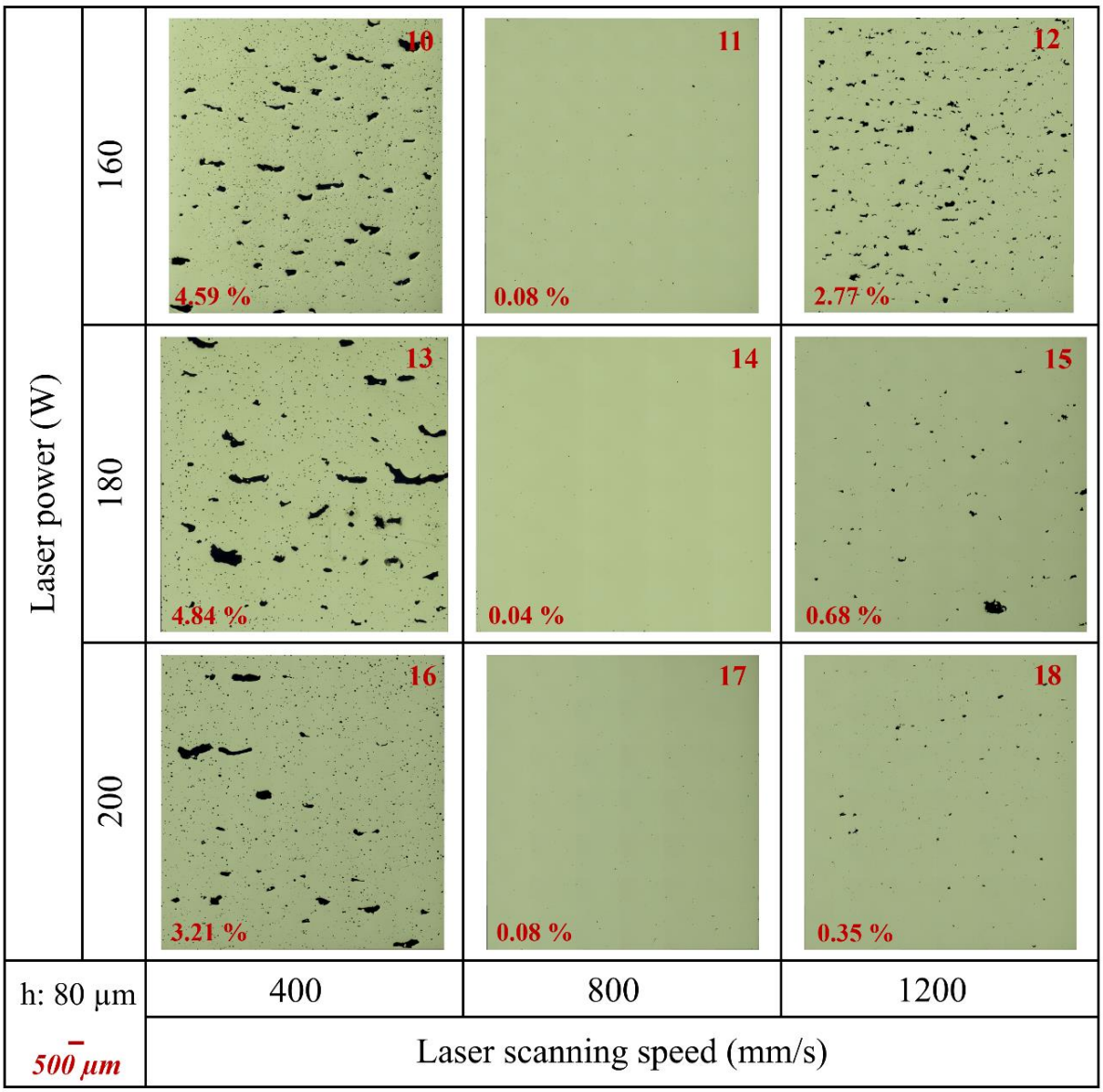

Figure 4.6 The as-polished optical micrographs of as-built samples (10-18) in the XZ plane (parallel to the build direction). Porosity (%) values are indicated on the micrographs (hatch distance: 80 µm).

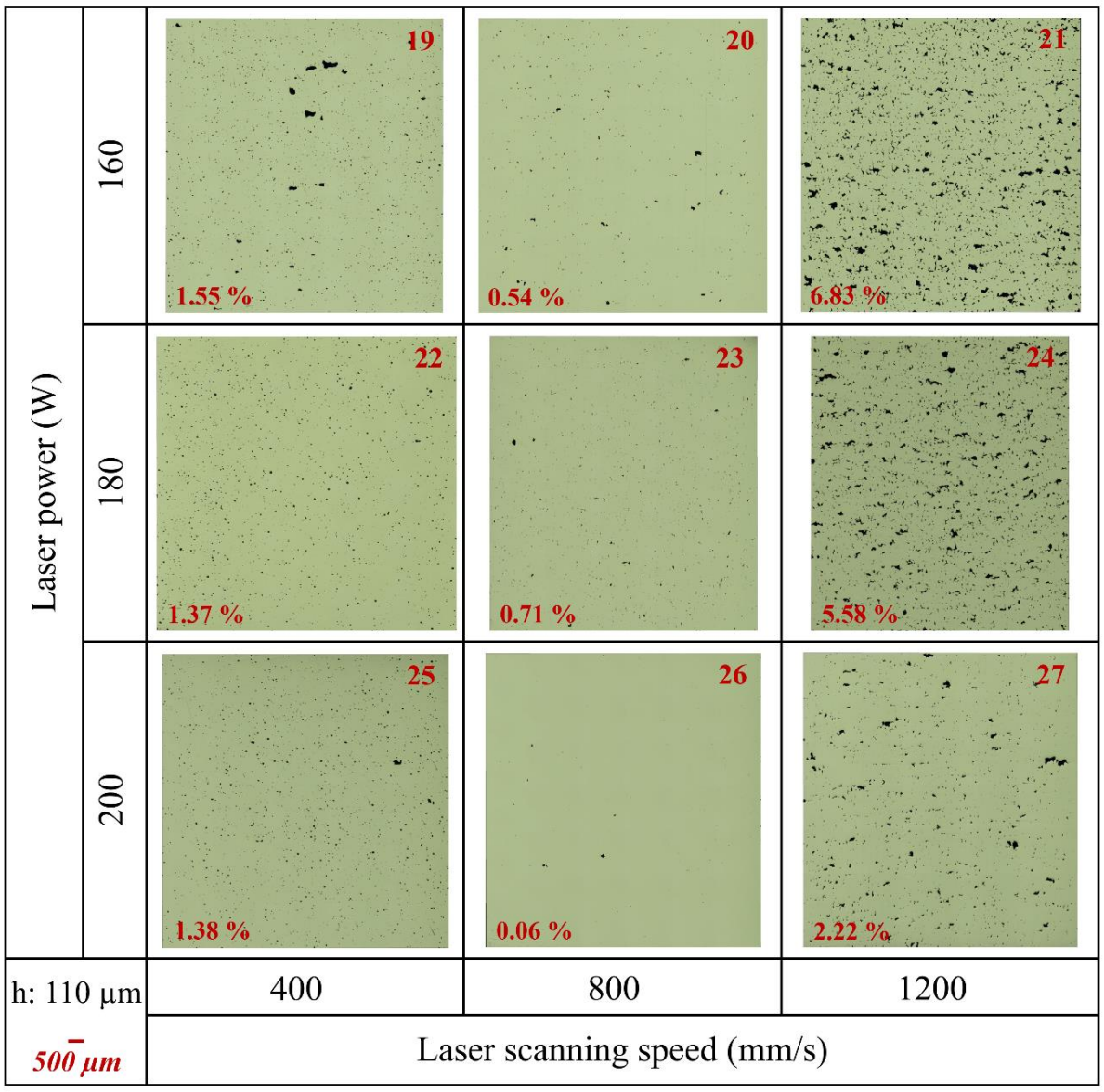

Figure 4.7 The as-polished optical micrographs of as-built samples (19-27) in the XZ plane (parallel to the build direction). Porosity (%) values are indicated on the micrographs (hatch distance: 110 µm).

4.4.4 Microstructure

The grain structures of the selected samples (1, 8, 11, 12, 14, 17, 21, 25, and 26) can be seen from the optical micrographs (Figure 4.8). The Gaussian energy distribution of the laser beam in the PBF-LB process results in arc-shaped melt pools in the XZ planes, which are parallel to the build direction. The arc-shaped melt pools, along with a microstructure composed of the columnar elongated grains along the build direction were observed in the XZ planes of the samples. Furthermore, samples fabricated with high VED (i.e., sample 1) have regions having dendritic microstructure. The cross-section micrographs of the top

layers of selected samples (1, 8, 14, 17, and 26) are displayed in Figure 4A4 in Appendix A. The micrographs reveal that melt pools with a higher depth/width aspect ratio (keyhole melting mode) were formed in samples 1 and 8 due to the higher applied VED, indicating a dynamic melt pool motion occurred during melting.

SEM images of the selected samples, which are samples 1, 8, 14, 17 and 26, show cellular structures and columnar dendrites within the microstructure (Figure 4.9). Furthermore, according to EDS analyses taken from the dendritic region of sample 1, fine irregular-shaped MC-type (rich in Ti, Ta, and Nb) carbides were observed. During SEM analysis, a few microcracks (less than 50 μm in length) were observed in the samples, although these microcracks were not visible in as-polished micrographs. The authors recommend that SEM examination of samples should be conducted after etching to ensure a thorough assessment for cracks. It was noted that some microcracks, invisible after polishing, became apparent after etching. This additional step ensures a more comprehensive assessment of crack formation.

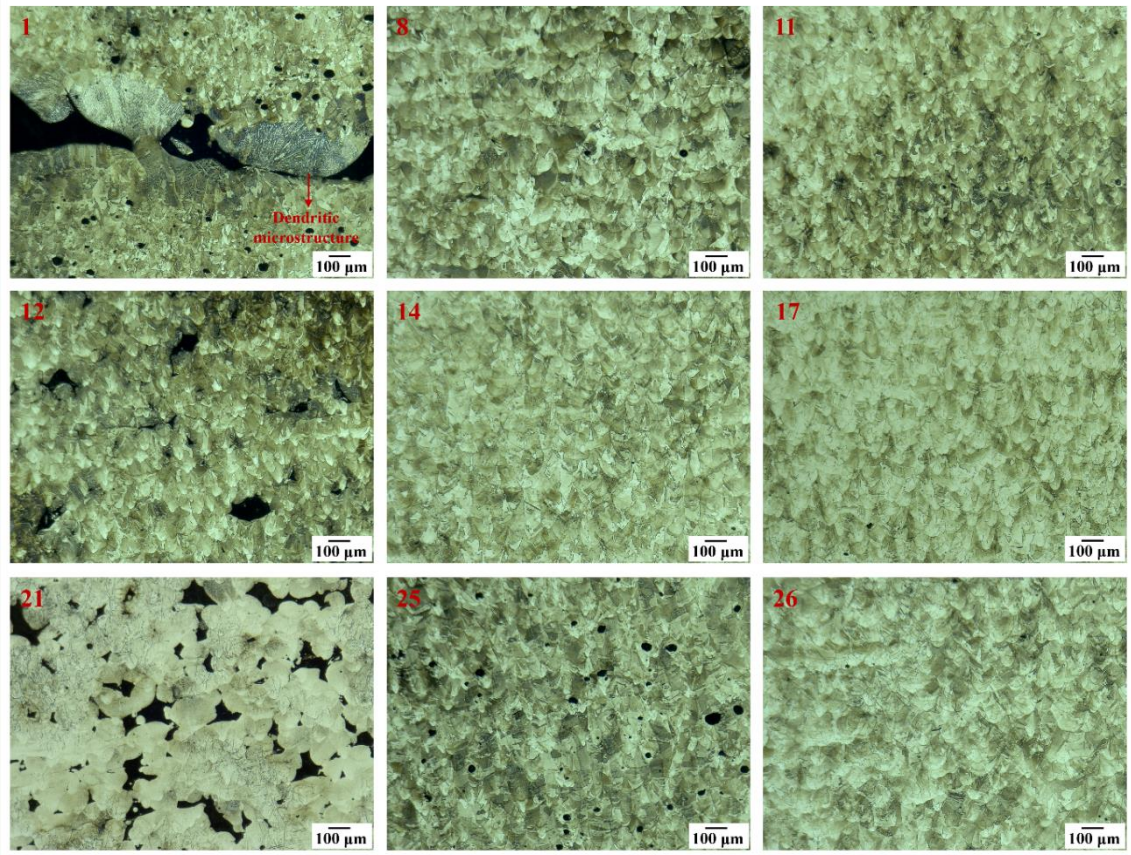

Figure 4.8 Optical micrographs of the XZ planes of the selected as-built samples (1, 8, 11, 12, 14, 17, 21, 25, and 26).

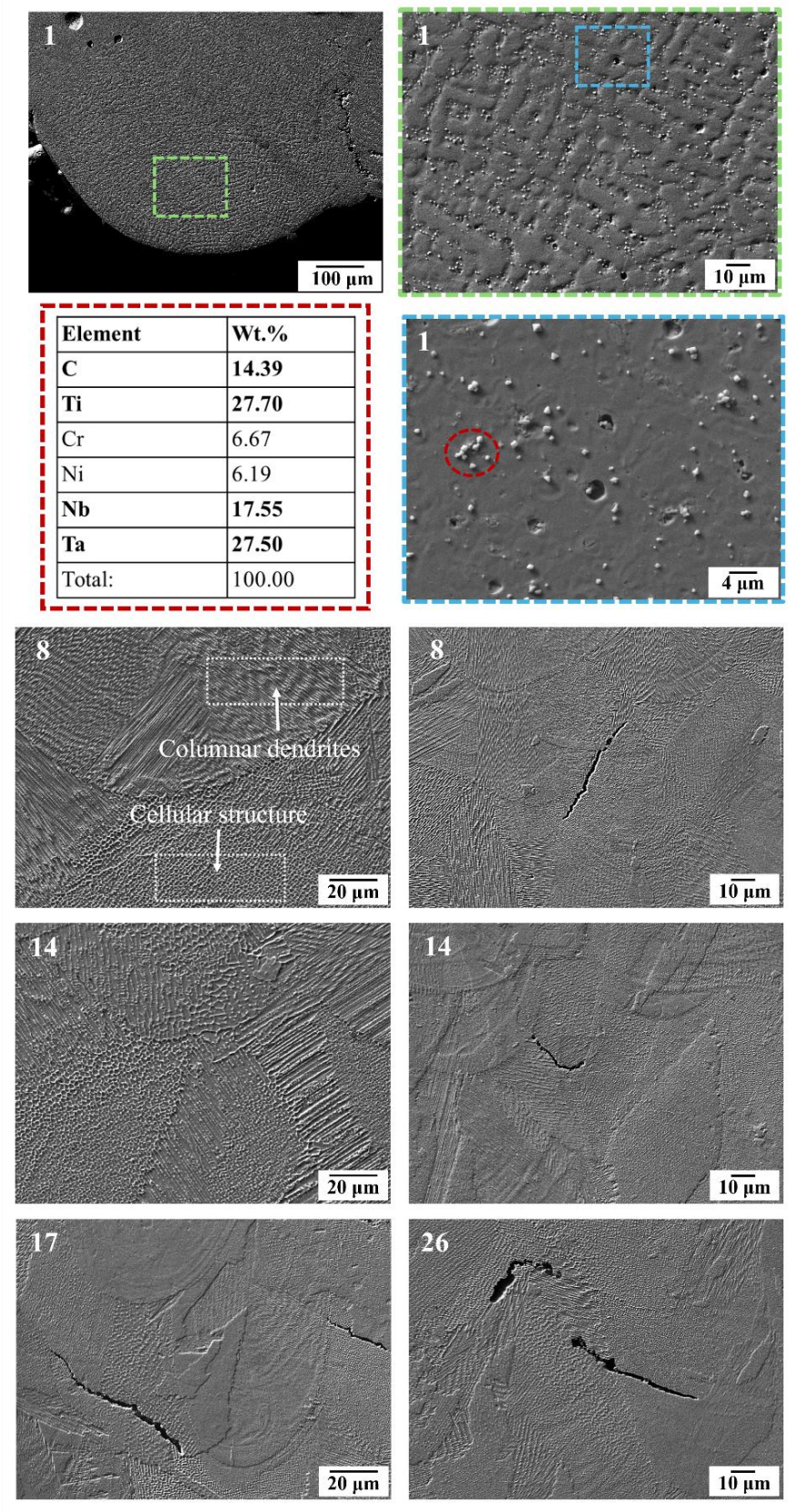

Element	Wt.%
C	**14.39**
Ti	**27.70**
Cr	6.67
Ni	6.19
Nb	**17.55**
Ta	**27.50**
Total:	100.00

Figure 4.9 SEM images of the XZ planes of the selected as-built samples (1, 8, 14, 17, and 26), along with EDS results of the MC-carbides.

4.5 Discussion

Among the PBF-LB process parameters, laser power, laser scanning speed, hatch distance, layer thickness, and scanning strategy are the main factors [130]. The combination of these processing parameters significantly influences melt pool geometry, local microstructure, defect size and morphology [172]. The current study demonstrates that the relative density, defect formation, surface roughness, and microstructure of as-built IN939 samples can be directly controlled by adjusting the PBF-LB process parameters. In literature, an effective process window, defined by LOF, keyhole, and bead-up porosity boundaries, is created to optimize process parameters for the PBF-LB process, enabling the production of parts with nominally full density. It should be noted that even if a sample is fully dense (volumetric density > 99.9%), it may still have large defects [169,172]. In our study, sample 6 is a good example for this. Although it has a high relative density (99.23%) and low average porosity (0.14%), the average Feret size is calculated as 108.3 µm. This can be also seen from the as-polished micrographs (Figure 4.5 and Figure 4A3 in Appendix A).

The combination of high laser power, low laser scanning speed, and small layer thickness results in excessive energy, leading to a highly fluctuated molten pool. This melt pool exhibits a keyhole melting mode, often resulting in keyhole porosity [203]. Keyhole formation occurs in four stages: liquid vaporization in the melt pool, depression of the liquid surface, instability, and keyhole formation. The formation of a keyhole indicates that the melt pool enters a volatile state, where surface tension, drag force, recoil pressure, and other forces are coupled in the molten pool. This dynamic environment causes continuous keyhole fluctuations, which play a vital role in the formation of keyhole pores. Additionally, keyhole melt pools have often a "J" shape [171]. Aboulkhair et al. [157] reported that keyhole pores are irregularly shaped and larger than 100 µm. Specifically, samples 1, 4, 7, 10, 13, and 16 exhibit very large, irregular keyhole pores attributed to high VED, along with small spherical pores. On the other hand, low laser power combined with large layer thickness and high laser scanning speed can generate insufficient energy. This often results in high surface tension, unmelted powder, and poor wetting of the molten pool, leading to balling and dimensional errors. Intertrack LOF, interlayer LOF, and spattering-induced LOF are the three main types of LOF defects. Intertrack LOF stems from inadequate melt pool overlap due to factors like melt pool shape, size, and hatch spacing. Interlayer LOF arises from incomplete bonding between layers, primarily due to low laser energy density, limiting melt pool depth and flow. Spattering-induced LOF

occurs when spatters deposited on the part's surface hinder uniform powder spreading, leading to numerous LOF defects [171,203]. Especially, samples 12, 21, 24, and 27 are good examples of LOF defects due to insufficient energy. Furthermore, hatch distance significantly influences the overlapping rate of scan tracks, impacting densification and surface roughness. A high hatch space can cause insufficient overlap between adjacent tracks, leaving unmelted powder on the layer. Conversely, a low hatch space can result in excessive melting of the previous track, leading to a rough surface and a heat-affected zone [203]. RSM graphs for surface roughness (Figure 4.3) and relative density (Figure 4.4) clearly show the importance of the hatch distance.

It should be noted that relative densities for PBF-LB materials produced using different processing parameters can vary by up to 5%, despite having the same energy density. For instance, if hatch spacing is increased and layer thickness is decreased by the same proportion, the energy density remains constant, yet porosity outcomes differ [172]. Samples 8 and 10 illustrate this phenomenon. Despite having the same VED of 125 J/mm^3, their relative densities and average porosity values differ significantly: sample 8 exhibited a relative density of 99.35% and an average porosity of 0.09%, while sample 10 had a relative density of 95.93% and an average porosity of 3.50%. This demonstrates that VED alone does not reliably predict porosity or density outcomes in PBF-LB materials.

Spatter formation is inherently due to the nature of the PBF-LB process. Alleviating defects caused by spatter powder is challenging because the landing position of the spatter during the PBF-LB process is unpredictable. For this reason, spattering affects the microstructure, part quality, and properties of the PBF-LB materials [15]. A dendritic microstructure was observed near keyhole pores shown in Figure 4.8 (sample 1), which can be attributed to the thermal conductivity difference between the air trapped in the keyhole pores and the solid material [157]. Additionally, these dendritic regions can be partially melted spatter powder. Rapid solidification during the PBF-LB process causes the segregation of certain elements, leading to the formation of MC-type (i.e., Ti-, Ta-, Nb-rich) and $M_{23}C_6$-type carbides (i.e., Cr-, W-rich $M_{23}C_6$ carbides). The effects of MC-type carbides on the mechanical properties of Ni-base superalloys can be either beneficial or detrimental, primarily depending on their distribution and morphology. They can negatively affect the mechanical properties of Ni-base superalloys when they act as nucleation sites for crack formation. However, when located within grains, they can act as barriers to dislocation movement, like precipitates, thereby potentially enhancing the mechanical properties [4,14,46].

Furthermore, in the PBF-LB process, rapid cooling and non-equilibrium solidification significantly affect the solidification microstructure. This microstructure is influenced by parameters such as solidification rate (R), undercooling (ΔT), and temperature gradient (G), alongside PBF-LB process parameters. The size and morphology of the solidification microstructure, whether planar, cellular, equiaxed dendritic, or columnar dendritic, are determined by GxR and G/R. Lower cooling rates result in coarser structures (GxR), while higher cooling rates lead to finer structures [44,124]. A high G/R ratio results in a planar solidification morphology, while a moderate G/R ratio leads to cellular structures, and a low G/R ratio produces columnar or equiaxed dendritic structures. PBF-LB process has high cooling rates, which can change according to process parameters used in the process, so typically yielding high G/R values that favour the formation of cellular structures [209]. Moreover, columnar dendritic structures can also be seen in the PBF-LB process [14]. The cellular structures exhibit a honeycomb-like morphology, varying with the observation direction: they appear as parallel boundaries along the building direction and as circular features on the transverse section. Consequently, the cellular structures can manifest as circles, ellipses, or parallel lines in different cross-sections, a characteristic widely observed in additively manufactured metals and alloys [209].

Superalloys like IN939, rich in Al and Ti, form the L12-ordered γ' phase (Ni_3(Al, Ti)) but are prone to cracking in the PBF-LB process [99]. Two primary crack types are observed in IN939 during the PBF-LB process: solidification cracks and solid-state cracks. Solidification cracks, or "hot tears," occur in the semisolid state within the mushy zone due to interdendritic stress concentration. Solid-state cracks include strain-age cracks, ductility-dip cracks (DDC), and cold cracks. Additionally, oxides can contribute to crack formation by causing stress concentrations, increased boundary brittleness, and constitutional liquation at the oxide-matrix interface [16,102,103,210]. In this study, a few cracks, which became visible after the etching process, were observed, and appeared to be solidification cracks.

4.6 Conclusions

Optimizing process parameters is crucial for achieving desired properties such as defect-free samples in the PBF-LB process. This study aims to fill the existing research gap by investigating the effects of process parameters such as laser power, laser scanning speed, and hatch distance on the relative density, defect formation, surface roughness, and

microstructure of IN939 fabricated by the PBF-LB. The main findings from the observed results are summarized as follows:

1) The average surface roughness (Sa) of the XZ planes of the as-built samples ranged from 4.6 μm to 9.5 μm, while the average height difference (Sz) ranged from 78.7 μm to 176.7 μm. Sample 26 had the lowest Sa (4.6 μm), while samples 1 and 2 had the highest (9.5 μm).
2) Sample 8 had the highest relative density at 99.35%, and sample 21 had the lowest at 93.56%. Samples 14, 6, 9, and 17 also showed high relative densities of 99.25%, 99.23%, 99.20%, and 99.20%, respectively. Sample 1 had a notably low relative density of 94.19%, just above sample 21. Samples 8 and 10, despite having the same VED (125 J/mm^3), exhibited different relative densities (%) and porosity (%) due to varying process parameters.
3) Sample 1 had the highest average porosity at 9.18%, while samples 14 and 17 had the lowest at 0.06%. Sample 11 showed a similar low porosity at 0.07%. Despite the same average porosity, samples 14 and 17 differ in porosity/mm^2 and average Feret size. High VED resulted in large, irregular pores for samples 1, 4, 7, 10, 13, and 16. Sample 21, with the lowest VED (30.3 J/mm^3), showed high porosity due to insufficient melting energy.
4) The samples contained few microcracks, each less than 50 microns in length, indicative of solidification cracks.
5) Observations in the XZ planes of the samples revealed arc-shaped melt pools and a microstructure characterized by columnar elongated grains aligned along the build direction. Additionally, cellular structures and columnar dendrites were observed within the microstructure of the samples.

4.7 Contribution to Thesis Objectives

PBF-LB process has over 100 process parameters according to the literature. The understanding of these process parameters and their effects on the properties of the fabricated parts is crucial for both academia and industry. After a thorough review of the existing literature, it was found that there were limited studies on the understanding of how PBF-LB process parameters impact the material properties such as densification, surface roughness, and microstructure of IN939 samples. Moreover, there was no study reported on the fabrication of IN939 using an Aconity MINI PBF-LB machine. It should be noted that the PBF-LB machine itself is also a process parameter. This chapter significantly

advances the understanding of how PBF-LB process parameters (laser power, laser scanning speed, and hatch distance) impact the relative density, defect formation, surface roughness, and microstructure of IN939 samples. Key contributions included the identification of optimal parameters for achieving the highest relative density (99.35%) and the lowest surface roughness (4.6 μm). The study revealed the complex relationship between process parameters and defect formation, including porosity and microcracks, demonstrating that different volumetric energy densities (VED) lead to significant variations in porosity and pore characteristics. Furthermore, the microstructural analysis provided insights into the formation of arc-shaped melt pools, columnar grains, and dendritic structures, essential for understanding the material's behaviour during solidification. By systematically analyzing and presenting the effects of PBF-LB process parameters, this research offers valuable guidelines for optimizing manufacturing processes to enhance the quality and performance of IN939 components.

4.8 Appendix A

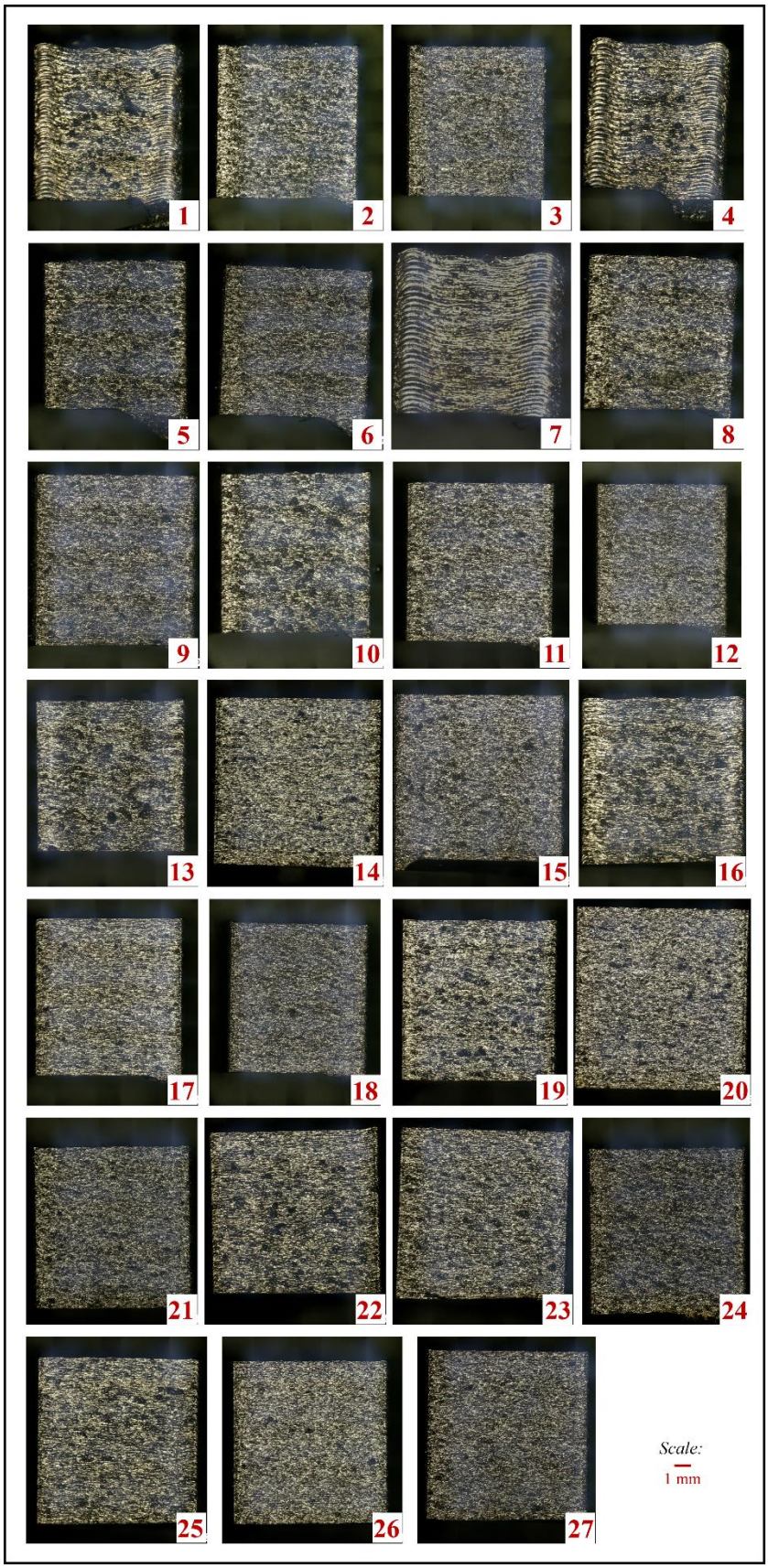

Figure 4A1 Optical images of the XZ planes of the as-built IN939 samples.

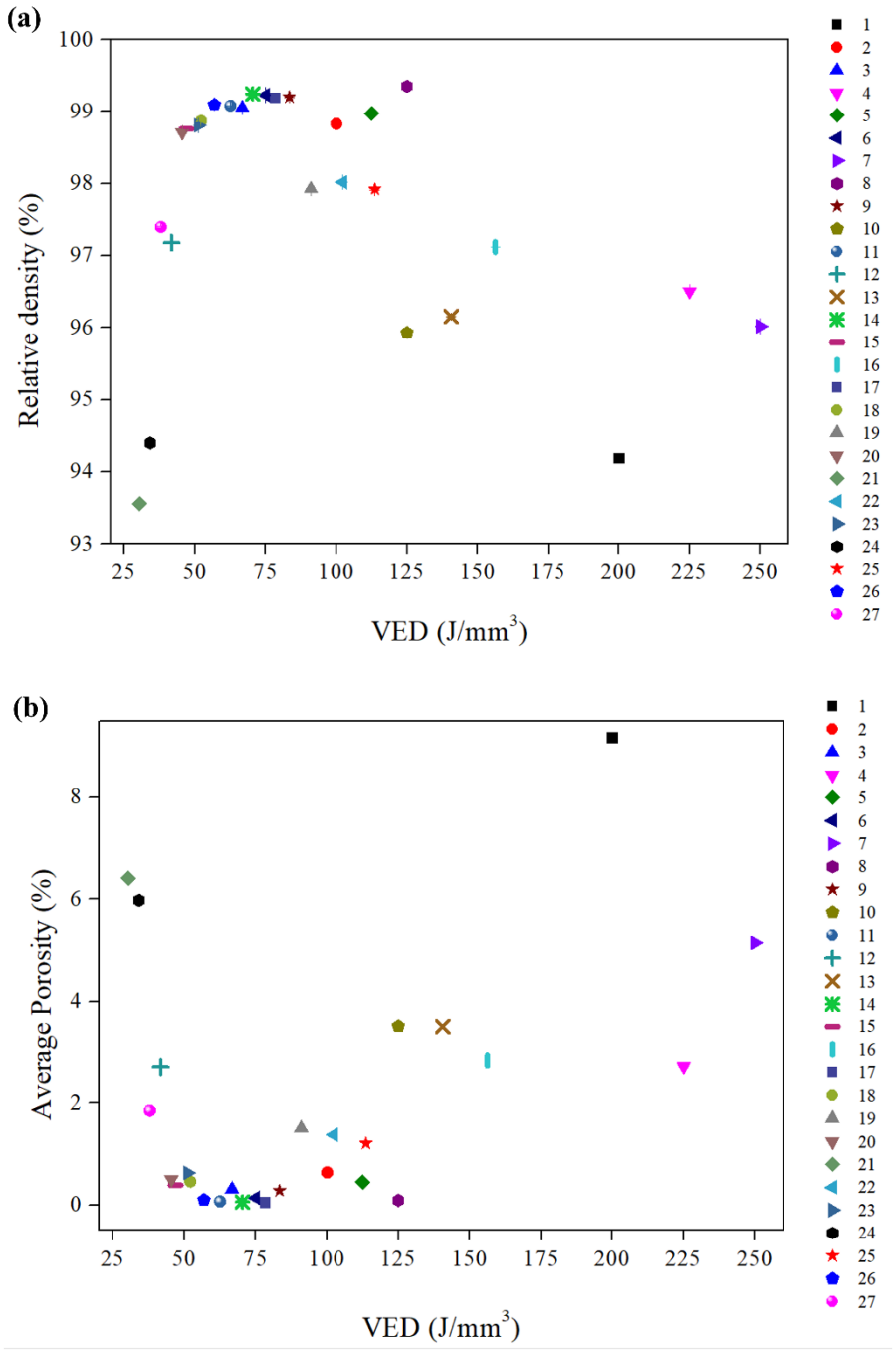

Figure 4A2 (a) Relative density (%) and (b) average porosity (%) versus VED (J/mm^3) graphs of the as-built samples.

Table 4A1 ImageJ porosity analysis for the XZ and XY planes of the as-built samples.

Sample	Porosity (%)	Pores/mm^2	Average Feret Size (µm)
1-XZ	9.93	39.26	37.23
1-XY	8.43	37.28	41.83
1-Average	**9.18**	**38.27**	**39.53**
2-XZ	0.72	4.78	34.25
2-XY	0.57	6.60	88.79
2-Average	**0.64**	**5.69**	**61.52**
3-XZ	0.22	2.64	63.54
3-XY	0.40	2.07	317.20
3-Average	**0.31**	**2.36**	**190.37**
4-XZ	3.22	33.17	31.99
4-XY	2.21	48.20	29.26
4-Average	**2.71**	**40.68**	**30.63**
5-XZ	0.54	2.91	92.30
5-XY	0.35	10.66	49.14
5-Average	**0.45**	**6.79**	**70.72**
6-XZ	0.18	2.29	83.92
6-XY	0.10	3.31	132.67
6-Average	**0.14**	**2.80**	**108.30**
7-XZ	7.78	42.51	35.32
7-XY	2.51	47.37	30.48
7-Average	**5.15**	**44.94**	**32.90**
8-XZ	0.07	6.48	11.87
8-XY	0.11	4.80	81.73
8-Average	**0.09**	**5.64**	**46.80**
9-XZ	0.45	7.75	20.15
9-XY	0.12	28.99	7.98
9-Average	**0.28**	**18.37**	**14.06**
10-XZ	4.59	52.47	25.93
10-XY	2.41	43.52	34.05
10-Average	**3.50**	**47.99**	**29.99**
11-XZ	0.08	9.53	10.24
11-XY	0.06	18.00	7.39
11-Average	**0.07**	**13.76**	**8.82**
12-XZ	2.77	15.18	48.80
12-XY	2.64	33.94	29.95
12-Average	**2.70**	**24.56**	**39.37**
13-XZ	4.84	23.63	36.87
13-XY	2.13	33.85	40.61
13-Average	**3.49**	**28.74**	**38.74**
14-XZ	0.04	2.76	13.86
14-XY	0.09	3.49	16.17
14-Average	**0.06**	**3.12**	**15.01**
15-XZ	0.68	5.43	30.25
15-XY	0.10	2.79	40.17
15-Average	**0.39**	**4.11**	**35.21**
16-XZ	3.21	28.36	39.94
16-XY	2.46	32.24	46.91
16-Average	**2.83**	**30.30**	**43.42**
17-XZ	0.08	7.79	12.96
17-XY	0.05	5.66	9.69
17-Average	**0.06**	**6.73**	**11.32**
18-XZ	0.35	9.51	21.61
18-XY	0.56	13.42	39.15
18-Average	**0.46**	**11.46**	**30.38**
19-XZ	1.55	35.86	23.25

19-XY	1.48	22.36	42.43
19-Average	**1.51**	**29.11**	**32.84**
20-XZ	0.54	8.36	56.31
20-XY	0.46	16.75	22.78
20-Average	**0.50**	**12.56**	**39.55**
21-XZ	6.83	54.49	45.66
21-XY	5.99	72.95	43.52
21-Average	**6.41**	**63.72**	**44.59**
22-XZ	1.37	34.71	28.54
22-XY	1.40	27.35	26.13
22-Average	**1.38**	**31.03**	**27.33**
23-XZ	0.71	32.37	21.38
23-XY	0.54	32.72	19.45
23-Average	**0.63**	**32.54**	**20.41**
24-XZ	5.58	62.21	38.60
24-XY	6.38	65.51	38.23
24-Average	**5.98**	**63.86**	**38.42**
25-XZ	1.38	36.03	23.94
25-XY	1.04	21.37	26.18
25-Average	**1.21**	**28.70**	**25.06**
26-XZ	0.06	2.84	15.05
26-XY	0.14	1.64	141.41
26-Average	**0.10**	**2.24**	**78.23**
27-XZ	2.22	23.71	49.40
27-XY	1.48	48.66	24.59
27-Average	**1.85**	**36.18**	**36.99**

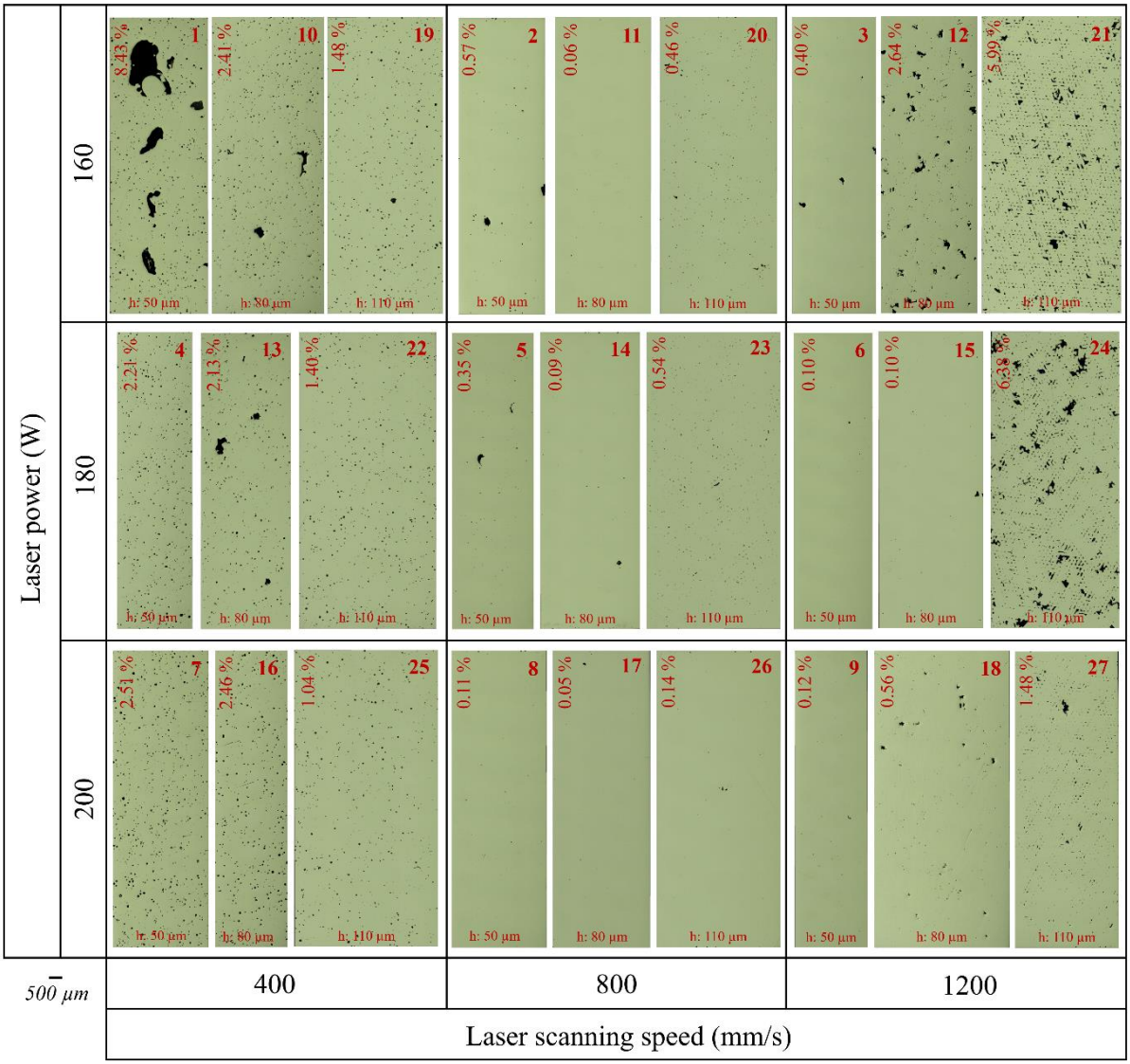

Figure 4A3 The as-polished optical micrographs of as-built samples (1-27) in the XY plane (perpendicular to the build direction). Porosity (%) values are indicated on the micrographs.

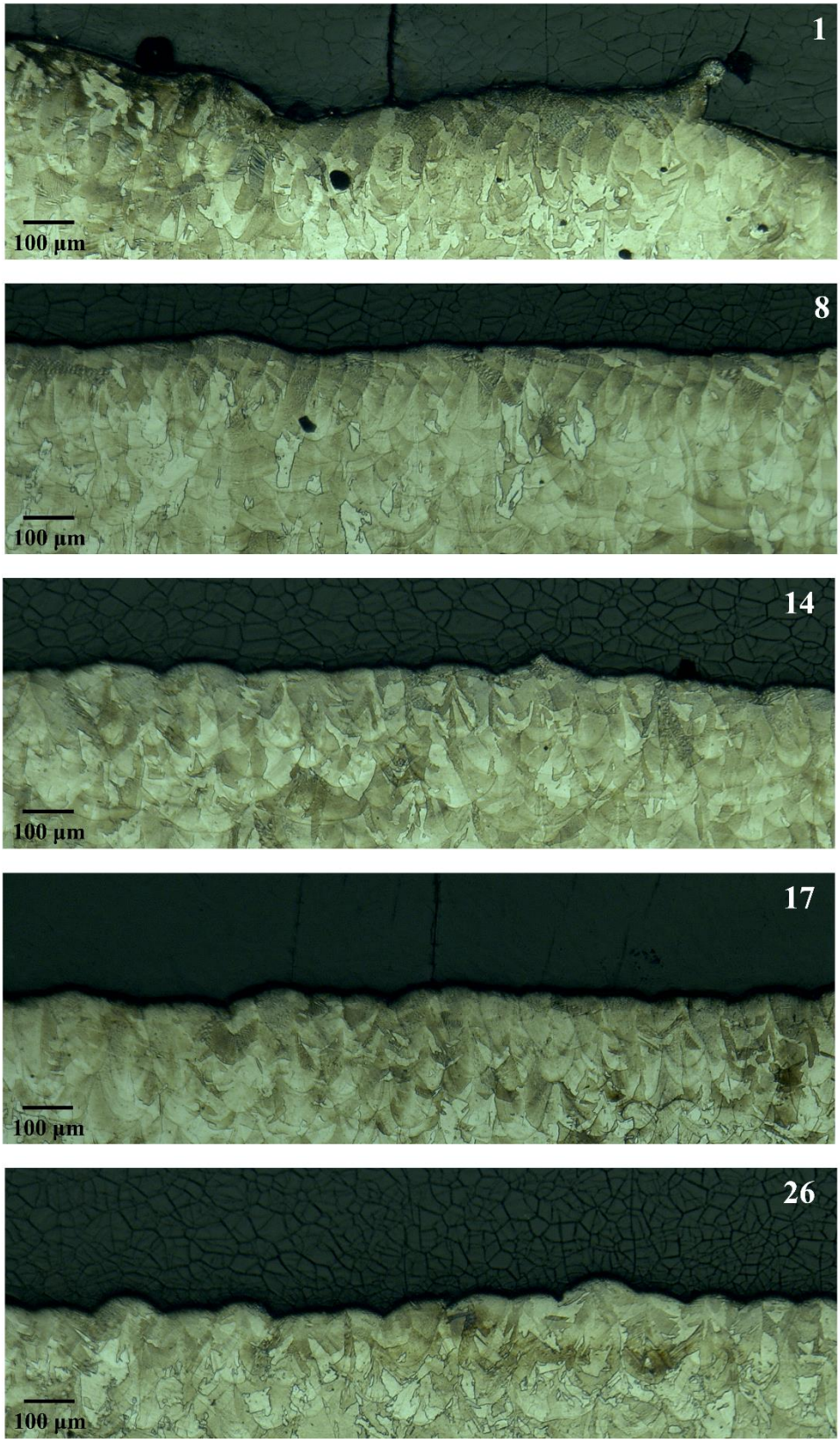

Figure 4A4 Optical micrographs of the XZ planes of the selected as-built samples (1, 8, 14, 17, and 26).

Chapter 5: A Comprehensive Characterization of the Effect of Scanning Strategy on IN939 Fabricated by Powder Bed Fusion-Laser Beam

Publication Status: Journal review completed; Revised manuscript submitted.

M.N. Doğu, S. Ozer, M.A. Yalçın, K. Davut, M.A. Obeidi, C. Simsir, H. Gu, C. Teng, D. Brabazon, **A comprehensive characterization of the effect of scanning strategy on IN939 fabricated by powder bed fusion-laser beam**, Journal of Materials Research and Technology.

5.1 Abstract

This study provides a comprehensive investigation into the effects of different scanning strategies on the material properties of IN939 fabricated using the powder bed fusion-laser beam (PBF-LB) process. The scanning strategies examined included alternating bi-directional scanning with rotation angles of 0°, 45°, 67°, and 90° between adjacent layers (named as shown), as well as alternating chessboard scanning with rotation angles of 67° and 90° (named as Q67° and Q90°). The results revealed that the 45° and 67° samples had the highest relative density, while the 0° and Q67° samples showed the highest average porosity. Moreover, various types of cracks, including solidification, solid-state, and oxide-induced cracks, were observed. Among the bi-directional scan samples, the 0° sample displayed the most extensive cracking and the highest σ_{max} residual stress values in both XZ and XY planes. Conversely, the 45° and 67° samples exhibited fewer cracks. Notably, the lowest σ_{max} residual stress in the XZ planes among the bi-directional scan samples was observed in the 67° sample. Additionally, microstructural analyses indicated differences in grain size and morphology, among the samples. Texture analysis indicated that the 0° and 90° samples exhibited strong cube textures, whereas the texture intensity weakened for the 45° and 67° samples. Moreover, the alternating chessboard scanning strategy led to rougher surfaces (higher Sa and Sz values) compared to the alternating bi-directional scanning strategy, regardless of the rotation angles. Furthermore, the microhardness values among the samples showed minimal variance, ranging between 321 ± 14 HV and 356 ± 7 HV.

5.2 Introduction

Metal additive manufacturing (AM) provides significant advantages over traditional manufacturing techniques. These include the production of metal parts with intricate geometric complexity in a single step, the ability to achieve design freedom through near-net-shape production, as well as reductions in material waste and tooling costs [15,211]. Among the metal AM processes, the PBF-LB process stands out as one of the most widely utilized processes. It has gained significant attention from both industry and academia due to the aforementioned advantages [44,172]. Typically, the PBF-LB process begins by spreading a layer of metal powder onto a build plate. Then, a laser beam selectively melts the desired area within the powder layer based on the 3D computer-aided design (CAD) file. This layer-by-layer process continues until the part is fully fabricated [45,130].

Nevertheless, despite its advantages, the PBF-LB process may still exhibit some inevitable defects when the combined effect of improper scanning parameters and inadequate powder melting occurs. This can lead to various issues that compromise the mechanical properties and hinder large-scale industrial commercialization. These issues include partially melted powder, undesired microstructures, poor surface finish, porosity, balling, surface and internal cracks, and poor bonding between layers, all of which are primarily associated with an unstable melt pool status [171,203]. Moreover, the inherent characteristics of the PBF-LB process, such as rapid solidification, high cooling rates (10^5-10^7 K/s), and repeated thermal cycles, result in non-equilibrium solidification, leading to significant residual stress [103,204].

In the PBF-LB process, there are over 100 processing parameters to consider [133]. The laser power, layer thickness, laser scanning speed, hatch distance (the distance between successive laser passes) are the most studied parameters. By adjusting these parameters, the printing process can be optimized to achieve the desired material properties [133]. Moreover, the scanning strategy, involving various factors such as scanning directions, scanning sequence, scanning vector length, scanning vector rotation angle, scanning time, and hatch distance, plays a crucial role in determining the thermal history and the arrangement of melt tracks within the fabricated parts. Thus, it enables precise control over the microstructure and overall performance of the fabricated parts [28,31,130]. The most utilized scanning strategies in the PBF-LB process include uni-directional, bi-directional (zigzag), and chessboard/checkboard/island scanning strategies. In the uni-directional scanning strategy, the energy beam moves in the same direction throughout the process, resulting in long scanning vectors. In the bi-directional scanning strategy, adjacent parallel scanning vectors move in opposite directions, still with long scanning vectors. On the other hand, the chessboard/checkboard/island scanning strategy divides the area into small square cells, reducing the scan vector length. This strategy is achieved by alternately scanning adjacent cells, resembling the pattern of a chessboard or checkered board [28,161].

Jia et al. [28] conducted a comprehensive review of the effects of the scanning strategy in the PBF-LB process on the microstructure, surface roughness, density, mechanical properties, and residual stress. In large parts, a shorter scan vector length is generally advantageous for reducing residual stress and enhancing the mechanical properties of the fabricated parts. Strategies such as island or bi-directional scanning can effectively mitigate residual stresses and minimize distortion by controlling local temperature

gradients and thermal cycles during the build process. Additionally, implementing a re-melting strategy can be beneficial for achieving enhanced densification, minimizing surface roughness and defects, improving mechanical properties, and reducing residual stresses [28,212–215]. Overall, the choice of scanning strategy in the PBF-LB process significantly impacts the material properties. Understanding these effects is significant for optimizing the process parameters and achieving desired material properties for specific applications.

The effect of scanning strategies on the material properties of Ni-base superalloys fabricated by the PBF-LB process such as IN625 [214,216,217], IN718 [30,31,162,163,212,213,215,218], Hastelloy X [29,218,219], CM247LC [220], and IN738 [32] has recently gained more attention. Wan et al. [30] investigated the grain structure and crystallographic texture of IN718 fabricated by the PBF-LB process. They found that applying a bi-directional strategy with 90° rotation scanning led to a pronounced competitive grain growth mechanism and a strong cube texture in the fabricated parts. Furthermore, Xu et al. [32] investigated the grain refinement and crack inhibition of IN738 by altering the scanning strategy (rotation of 0^o, 67^o, and 90^o between layers, respectively) during the PBF-LB process. They reported that by rotating the scanning direction 67^o during the PBF-LB fabrication of IN738, resulted in nearly crack-free microstructures with local equiaxed grains and columnar grains, resulting in an excellent balance of strength and ductility. This demonstrates the potential for grain refinement and enhanced crack suppression in a hard-to-weld superalloy through alterations in the scanning strategy, without modifying the alloy composition.

IN939 is a precipitation-hardenable Ni-base superalloy, strengthened mainly by the formation of the L12-ordered γ' phase (Ni_3(Al, Ti)). It was developed in the late 1960s as a cast alloy to fulfill the need for a robust, highly corrosion-resistant alloy capable of prolonged operation at temperatures up to 850 °C. Its superior properties include microstructural stability at elevated temperatures, high-temperature corrosion, oxidation and creep resistance. It has been widely used for land-based (blades and vanes) and marine gas turbines, fuel nozzles, diffusers, turbine airfoils and aircraft engines [14,15]. The weldability of superalloys is often assessed based on the total concentration of Al and Ti elements, as they influence the volume fraction of the γ' phase. When the combined concentration of Al and Ti exceeds 6 wt.%, the risk of crack formation increases [221]. IN939 is considered fairly weldable yet crack-susceptible. Liquation cracking, attributed to factors such as MC carbides, γ′ phase particles, the eutectic γ–γ′ phase, and low melting

phases, has been reported in the heat affected zone (HAZ) of cast IN939 during tungsten inert gas (TIG) welding processes [92,117]. Additionally, solidification cracking and solid-state cracking have been observed in IN939 fabricated by the PBF-LB [16,85].

Research on IN939 fabricated by the PBF-LB is notably limited compared to studies on other Ni-base superalloys [4,11,17,18,85,86,89,90,178,222]. Despite recent interest in IN939 fabricated by the PBF-LB, there is a significant lack of understanding regarding the impact of scanning strategies on its material properties. This study aims to address the existing gap in research by examining the effects of various scanning strategies on the material properties of IN939 fabricated by the PBF-LB. Specifically, the effects of different scanning strategies, including alternating bi-directional scanning with rotations of 0^o, 45^o, 67^o, and 90^o between adjacent layers, as well as alternating chessboard scanning with rotations of 67^o and 90^o between adjacent layers were investigated on the relative density, pore and crack formation, surface roughness, microstructure, crystallographic texture, microhardness, and residual stress of IN939 fabricated by the PBF-LB.

5.3 Materials and Methods

5.3.1 Fabrication of IN939 Samples by the PBF-LB Process

In this study, gas atomized IN939 powder (Truform 939-N65, Praxair Surface Technologies) whose chemical composition is given in Table 5.1 was used to fabricate IN939 samples. Additionally, a comprehensive characterization of powder was reported in our previous study [15].

Table 5.1 The chemical composition (wt.%) of the gas atomized IN939 powder.

Elements	Al	Co	Cr	Nb	Ta	Ti	W	Zr	Ni	B	C	O	N
wt.%	1.9	18.9	22.8	1.0	1.4	3.8	2.0	0.028	Bal.	0.004	0.16	0.014	0.009

IN939 cubic samples (10 mm × 10 mm × 10 mm with 2 mm support), as shown in Figure 5.1, were fabricated under a protective argon atmosphere (which kept the oxygen level below 100 ppm) using Aconity MINI (GmbH) metal 3D printer equipped with an ytterbium fibre laser from IPG, model YLR-200-WC-Y11, 2011 series with a wavelength of 1068 nm.

Process parameters used for the fabrication of the samples, along with details of the samples are given in Table 5.2. During the processing, a supply factor of 3 was used to

provide enough powder to build area for each layer. In addition, the volumetric energy density, VED (J/mm^3) was calculated as 62.5 J/mm^3 by taking the laser power, P (W), laser speed, υ (mm/s), layer thickness, t (mm) and hatch spacing, h (mm). The same formula was used in our previous study to calculate VED [14].

Table 5.2 PBF-LB process parameters utilized in the present study.

Laser power (W)	**Laser scan speed (mm/s)**	**Layer thickness (mm)**	**Hatch spacing (mm)**	**Off-set (contour) (mm)**	**Spot size (mm)**	**VED (J/mm^3)**
200	1000	0.04	0.08	0.05	0.08	62.5
Sample	**Scanning strategy**					
0°	Alternating bi-directional scan with no rotation between the adjacent layers					
45°	Alternating bi-directional scan with 45° rotation between the adjacent layers					
67°	Alternating bi-directional scan with 67° rotation between the adjacent layers					
90°	Alternating bi-directional scan with 90° rotation between the adjacent layers					
Q67°	Alternating chessboard scan with 67° rotation between the adjacent layers					
Q90°	Alternating chessboard scan with 90° rotation between the adjacent layers					

Figure 5.1 shows six different scanning strategies used to fabricate IN939 samples in this study, along with the build plate pictures after fabrication. Additionally, Table 5.2 also gives the details about the scanning strategies used to fabricate IN939 samples. Netfabb software (a product of Autodesk) was used to prepare files for fabrication. Scanning strategy in the software includes the combination of the scanning pattern (or hatching type), hatch starting angle and position, hatch rotating angle per build layer, off-set (contour), and up and down skin [130]. As Table 5.2 displays, the first four scanning strategies were called alternating bi-directional scan (also called simple scan in Netfabb) and the only difference between them is the rotation angle (0°, 45°, 67°, 90°) between the adjacent layers shown in Figure 5.1(a-d). The last two scanning strategies were called alternating chessboard scan (also called quad scan in Netfabb software) with two different rotation angles (67° and 90°) exhibited in Figure 5.1(e, f). In the chessboard scanning strategy, each layer was divided into small islands (island size 2.5 mm x 2.5 mm) forming a chessboard pattern and the overlapping gap was 0 mm.

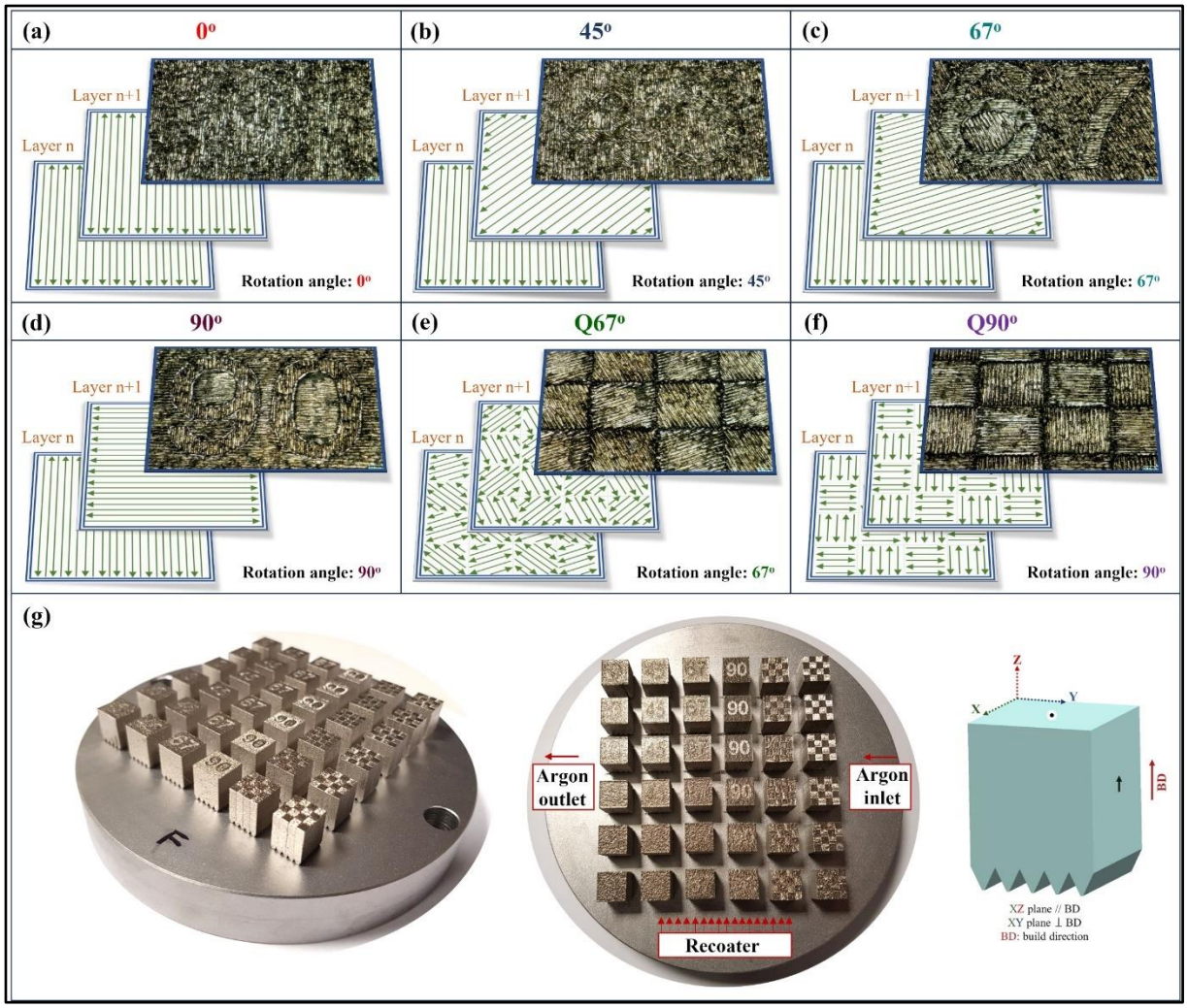

Figure 5.1 Schematics of the scanning strategies: alternating bi-directional scan with (a) no rotation (b) 45° rotation, (c) 67° rotation, (d) 90° rotation between the adjacent layers, and alternating chessboard scan with (e) 67° rotation and (f) 90° rotation between the adjacent layers. (e) Pictures of build plate after fabrication and schematic of the as-built samples.

5.3.2 Surface Roughness Measurements

The surface roughness measurements of the as-built samples were characterized with Bruker ContourGT from three samples for each scanning strategy to obtain the average values of the samples (over an area of 2 mm × 2 mm on the XZ planes of the samples). Sa value, which expresses the height of each point compared to the arithmetical mean plane, was used to describe the surface roughness directly. Also, the Sz value, which represents the sum of the maximum peak height and the maximum pit depth, was calculated. Additionally, the rainbow scale bar is fixed between +85 µm and -85 µm to show the difference in surface roughness between the samples.

5.3.3 Microstructural Characterization

For the metallographic examination, IN939 cubic samples were sectioned by a precision abrasive cutter (Buehler IsoMet 5000) to investigate both observation directions shown in Figure 5.1(g) (XZ plane which is parallel to the building direction and XY plane which is perpendicular to the building direction). Before the analyses, the as-built samples were hot mounted with conductive Bakelite and were automatically ground using conventional SiC grinding papers (320, 500, and 800 grit sizes) and polished with progressively finer diamond suspensions (9, 3, 1 μm). An additional final polishing step using 0.25 μm fumed silica (OP-S) was applied for electron backscatter diffraction (EBSD) analysis. Then, as-polished samples were etched with the Glyceregia reagent (15 ml HCl, 10 ml glycerol and 5 ml HNO_3) for further microstructural examination.

Keyence VHX2000E optical 3D digital microscope (OM) and Carl Zeiss Merlin Field Emission Gun Scanning Electron Microscope (FEG-SEM) were used for microstructural examinations. Zeiss EVO LS 15 equipped with Oxford EDS detector was used for energy dispersive X-ray spectroscopy (EDS) analysis (an acceleration voltage of 15 kV, 3.0 nA probe current, WD: 8.5 mm).

EBSD analysis was carried out with the ZEISS Merlin SEM using 15 kV acceleration voltage, 6.0 nA probe current. EBSD maps of 325 μm × 325 μm were measured on a hexagonal grid with a step size of 0.75 μm. EBSD raw data was post-processed using TSL OIM Analysis v7.3.1 software and points having CI (confidence index) below 0.1 were removed from datasets. Additionally, texture analyses were performed using the generalized spherical harmonic series expansion method of Bunge [188]. The harmonic series were expanded to a rank (L) of 34, and a Gaussian smoothing with a half-width of 5° was used.

The phase contents of the samples were determined by X-ray diffraction (XRD) analysis with Bruker D8 Advance Eco device using Cu-Kα radiation at 40 kV via continuous scanning between 30° and 100° 2θ angles with a scan speed of 0.5 °/min. All samples were ground using SiC papers before the XRD analysis.

5.3.4 Relative Density and Porosity Measurements

The relative density of the as-built samples was measured by Archimedes' method from six samples for each scanning strategy to obtain the average relative density values of each scanning strategy with the help of Sartorius Entris II Essential BCE124I-1S

analytical balance having an accuracy and repeatability of ± 0.1 mg according to ASTM B311-17 [208]. Acetone (Honeywell, purity ≥ 99.80% and density (20 °C): 0.79 g/cm^3) was used as the fluid. The measurements were repeated three times for each sample. Additionally, the theoretical density of a full dense IN939 was taken as 8.15 g/cm^3 to calculate the relative density values of the samples [68].

In addition to Archimedes' method, the conventional optical microscopy method was also used to analyze porosity distribution. The as-polished cross-section optical images (from both XZ and XY planes) were taken using the stitching property of the Keyence 3D optical microscope. For the porosity calculation, the stitched optical images including at least 20 images at 100X were analyzed using ImageJ software.

5.3.5 Microhardness and Residual Stress Measurements

The Vickers microhardness values of the as-built samples were calculated from the average of 15 measurements for each XZ and XY plane of the samples using Zwick/Roell ZHV10 microhardness tester with a load of 1 kg and by the ASTM E384 standard [189].

The electropolishing process was conducted on the both XZ and XY planes of the as-built samples using Struers Movipol-5 equipment with specific parameters: 45 volts, 20 seconds duration, and 20 flow rates. An A2 electrolyte solution, consisting of 90 ml distilled water, 730 ml ethanol, 100 ml butoxyethanol, and 78 ml perchloric acid, was utilized for layer removal and depth profile measurements [223]. Around 100 μm of material was removed from the surface of the samples with electropolishing, and the depth was measured using a Mitutoyo micrometer gauge.

XRD residual stress measurements were conducted using the Xstress_3000_G2R measurement device manufactured by Stresstech, with XTronic software version V1.14.0. This equipment and measurement strategy comply with the European X-ray residual stress testing standard EN 15305. Before the experiments, the system is aligned according to the ASTM E915 standard [224] and focal length is determined by using an interlaboratory certified IN625 powder and interlaboratory calibrated shot peened IN718. For measurements, manganese (Mn-Kα) radiation having a wavelength of 2.10314 Å was used as the X-ray source. A collimator with a 2 mm diameter was utilized, positioned at 10 mm from lower-left corner of all samples. The detector distance from the samples was 50 mm, with an arc radius of 50 mm. Exposure time was maintained at 10 seconds, and the number of tilts ranged from -8 to +8 (with a tilt angle of -45° to +45° and without oscillation). The

Poisson's Ratio (ν) and Modulus of Elasticity (E) values used were 0.28 and 167 GPa, respectively. Stress values were then calculated at angles of 0°, 45°, and 90°, from those values principal stress (σ_{max} and σ_{min}) and the orientation of the maximum principal stress with respect to global axes ($\Phi(\sigma_{max})$) were determined under plane-stress assumption.

5.4 Results

5.4.1 Relative Density and Porosity

The relative density values are depicted in Figure 5.2(a). The results indicate that the 45^o sample exhibits the highest relative density at 99.29%, whereas the Q90^o sample shows the lowest relative density at 99.05%. Furthermore, the 67^o sample demonstrates a relative density value of 99.28%, which is nearly identical to that of the 45^o sample. In addition to the relative density values, Figure 5.2(b) presents the results of the ImageJ porosity analysis for the XZ and XY planes of the samples, along with the average results, including porosity (%), pores/mm^2, and average Feret size (μm). According to the results, the 0^o and Q67^o samples exhibit the highest average porosity (%) at 0.27%, while the 90^o samples show the lowest average porosity at 0.06%. Additionally, the average porosity (%) for the 67^o sample is 0.07%, which closely resembles that of the 90^o sample. The as-polished optical micrographs of the as-built samples in both XZ and XY planes are shown in Figure 5.3. Among the alternating bi-directional scanning strategy, the highest defect formation such as pores and cracks were observed in the XZ plane of 0^o sample (Figure 5.3(a)) and this is supported by the pores/mm^2 value of 17.74, which is the highest among them. It should be noted that the pores/mm^2 value obtained from the ImageJ analysis of the PBF-LB fabricated samples provides insight into the porosity density within the material. A higher pores/mm^2 value indicates a higher concentration of pores, which can lead to decreased mechanical properties such as strength and fatigue resistance. Moreover, a lower pores/mm^2 value suggests a lower density of pores, which may indicate better material quality and integrity. Additionally, the typical size of pores in the sample can be interpreted from the average Feret size (a larger average Feret size suggests the presence of larger pores, whereas a smaller average Feret size indicates predominantly smaller pores). Therefore, controlling and minimizing the porosity, pores/mm^2, and average Feret size values are crucial for optimizing the quality and performance of the PBF-LB fabricated components. Furthermore, a chessboard-like distribution of porosity was observed in the XY planes of the Q67^o and Q90^o samples. This pattern is likely attributed to a non-optimized overlapping ratio, as the overlapping gap was set to 0 mm in this study.

Pores were also present in the overlapping regions of the XZ planes of the Q67° and Q90° samples. Moreover, pores/mm^2 is higher in the XY planes of these samples, whereas this is the opposite in the 67^o and 90^o samples. Among the six samples, the average Feret size is the lowest in the 67° sample, indicating that the smallest pores were formed when using the alternating bi-directional scan with a 67^o rotation between adjacent layers.

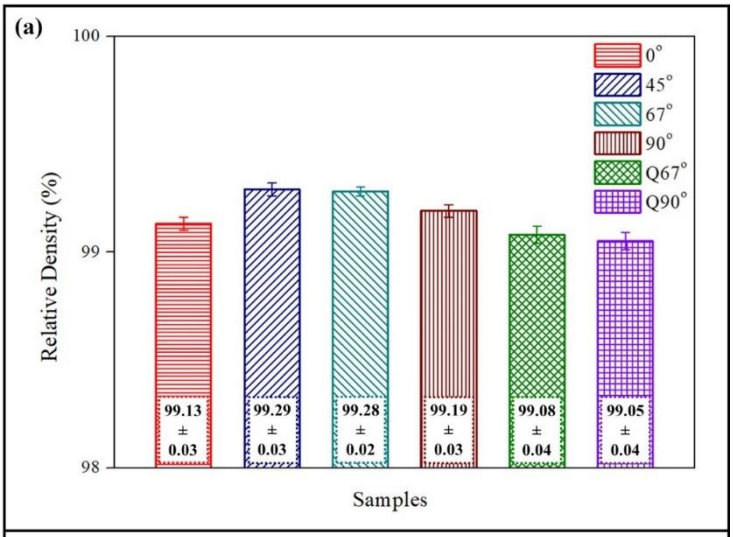

(b)

Sample	Porosity (%)	Pores/mm^2	Average Feret Size (μm)
0°-XZ	0.39	17.74	20.47
0°-XY	0.14	10.14	22.04
0°-Average	0.27	13.94	21.26
45°-XZ	0.09	7.69	15.38
45°-XY	0.12	2.69	34.64
45°-Average	0.11	5.19	25.01
67°-XZ	0.08	5.77	13.47
67°-XY	0.05	3.92	16.57
67°-Average	0.07	4.85	15.02
90°-XZ	0.05	5.93	17.43
90°-XY	0.08	3.43	21.66
90°-Average	0.06	4.68	19.54
Q67°-XZ	0.07	1.67	23.31
Q67°-XY	0.47	13.02	19.52
Q67°-Average	0.27	7.35	21.41
Q90°-XZ	0.14	4.43	19.85
Q90°-XY	0.27	9.28	19.01
Q90°-Average	0.20	6.86	19.43

Figure 5.2 (a) The relative density (error bars show 95% CI) and (b) ImageJ porosity analysis of the as-built samples obtained by different scanning strategies.

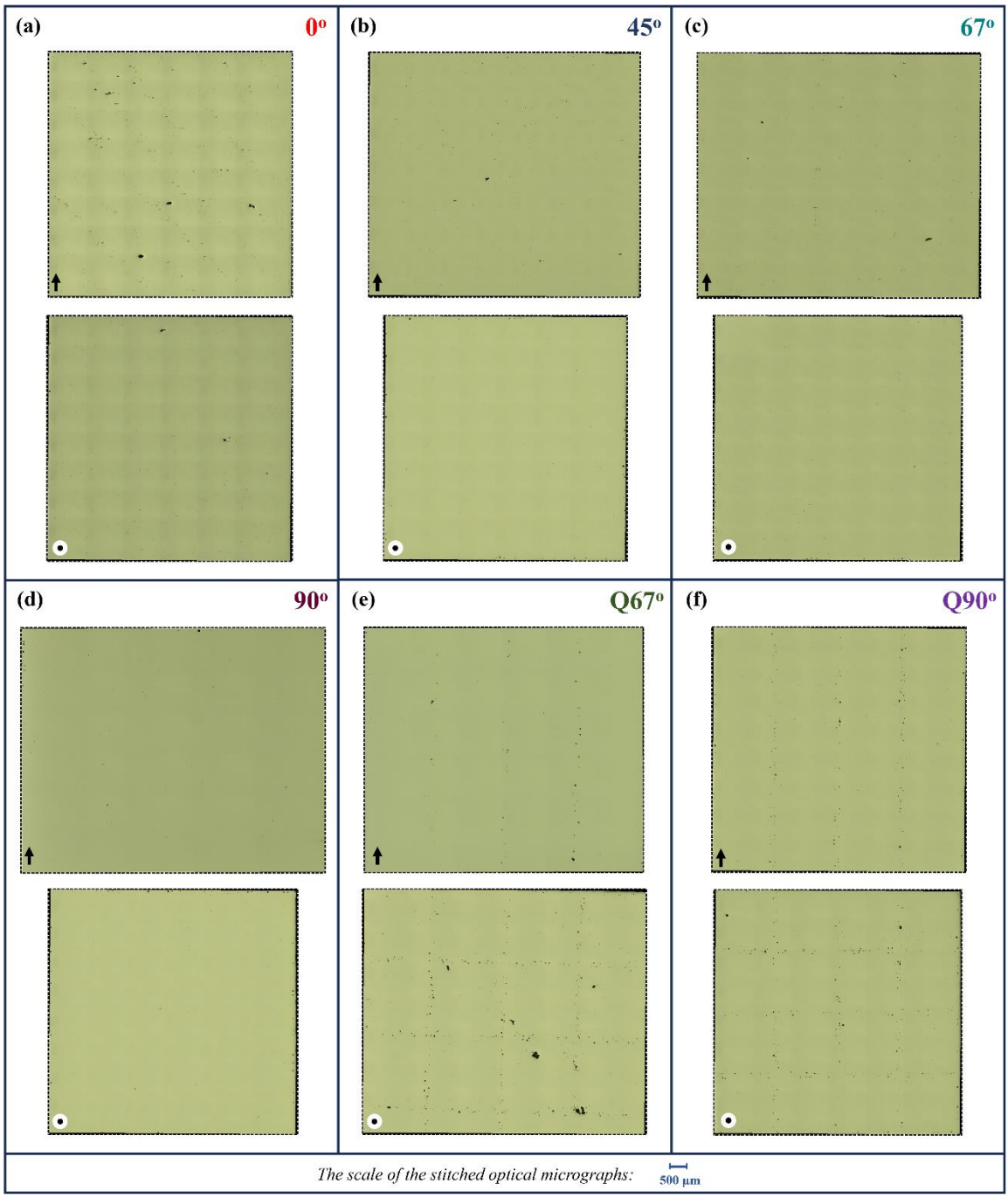

Figure 5.3 The as-polished optical micrographs of as-built samples; (a) 0º, (b) 45º, (c) 67º, (d) 90º, (e) Q67º, and (f) Q90º in both XZ plane (parallel to the build direction) and XY plane (perpendicular to the build direction) are indicated with arrows and dots, respectively.

5.4.2 Characterization of Cracks

In the literature, the observed cracks for IN939 fabricated by the PBF-LB were categorized as solidification cracks and solid-state cracks, including ductility dip cracking (DDC) and/or strain-age cracking (SAC) [16]. Figure 5.4 displays SEM images depicting the distribution of cracks observed in the XZ and XY planes of the as-built samples, with additional optical micrographs of these cracks provided in Figure 5B1 of Appendix B. Among the samples, the 0^o sample exhibits the highest degree of cracking. While most cracks propagate along the build direction (BD) in the XZ plane (especially near the edge of the sample shown in Figure 5.4(a2)), some cracks extend perpendicular to the BD (examples in Figure 5.4(a1, a3)). The cracks observed in the XZ plane of the 0^o sample are notably long elongated through BD, changing between about 5-450 μm in length. Consequently, these cracks traverse numerous deposition layers (40 mm layer thickness) along the BD.

The presence of a dendritic structure is characteristic of the solidification crack regions, with cracks typically initiating between grains and propagating across the resolidified layers. This dendritic structure is evident in Figure 5.4(a1, a5, b2, b3, c1, c3, d3, e3 and f2), indicating the presence of solidification cracks [16,102]. Furthermore, some researchers suggest that initiation and propagation of cracks perpendicular to the scanning direction are more probable due to the stress distribution along the laser path (an example in Figure 5.4(a5)) [103,210]. On the other hand, the presence of Al and O in the same region, confirming the existence of aluminum oxide (Al_2O_3), was observed near some cracks as shown in Figure 5.4(a3, a6). In addition to the 0^o sample (Figure 5.4(a2)), long cracks approximately 15-200 μm in length were observed near the edge of the 90^o sample in the XZ plane, as shown in Figure 5.4(d1). Tang et al. [16] reported similar kinds of cracks in IN939 fabricated by the PBF-LB, categorizing them as solid-state cracks. In contrast, the 45^o and 67^o samples exhibit fewer cracks in both the XZ and XY planes compared to the 0^o and 90^o samples. The cracks observed in the 45^o and 67^o samples are notably shorter in length, ranging approximately from 7 to 50 μm (Figure 5.4(b, c)). Furthermore, cracks, along with pores and lack of fusion (LOF) defects, were particularly observed in and near the overlapping regions of the Q67^o and Q90^o samples.

Furthermore, the authors recommend that examination of samples under SEM should be conducted after etching to check if the samples are crack-free. It was noted that

while some micro-cracks were not visible after polishing, they became apparent after etching. This additional step ensures a more comprehensive assessment of crack formation.

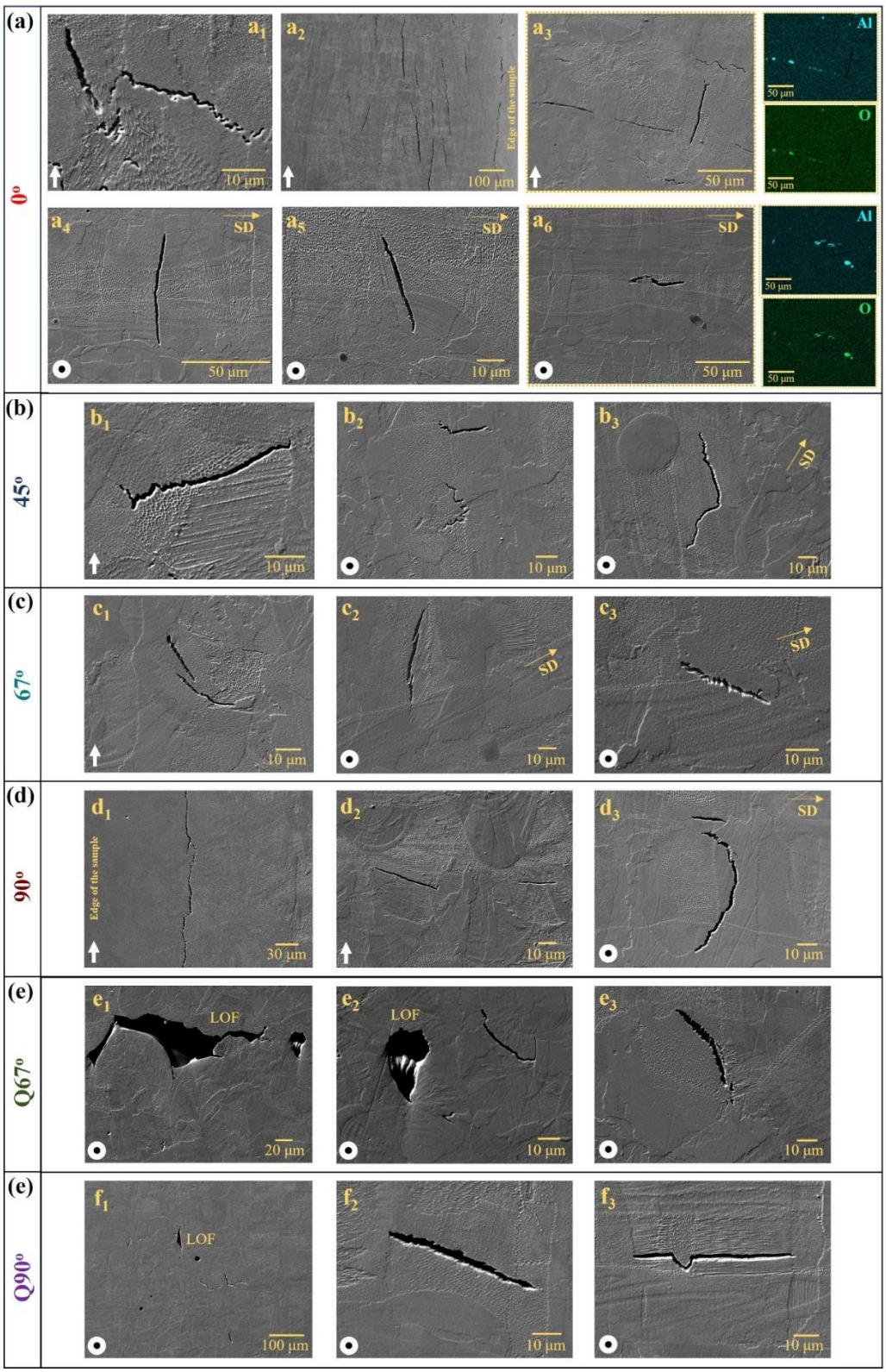

Figure 5.4 SEM images of the crack distribution in the XZ and XY planes of the as-built samples: (a) 0°, (b) 45°, (c) 67°, (d) 90°, (e) Q67°, and (f) Q90°. (LOF: lack of fusion and SD: scanning direction).

5.4.3 Surface Roughness

Figure 5.5 displays the surface roughness profiles with average surface roughness (Sa) and the maximum height (Sz) values for the XZ planes of the as-built samples. Among the samples, the lowest Sa value (4.61 μm) belongs to the 90^{o} sample, whereas the Q67^{o} sample has the highest at 9.95 μm. Furthermore, the alternating bi-directional scan with a 67° rotation between adjacent layers results in the Sa value of 5.01 μm, whereas the alternating chessboard scan with a 67° rotation between adjacent layers yields the highest Sa value. Analysis of the surface roughness profile of the Q67° sample (Figure 5.5(e)) reveals that the highest surface roughness is concentrated, particularly in the overlapping region. Additionally, the interior regions of the island in the Q67° sample exhibit random high surface roughness peaks. This is likely attributed to the increased spattering effect observed in this sample. Although the Sa value of the 0^{o} sample (4.69 μm) is very similar to the 45^{o} sample, there is a difference between Sz values (95.19 μm and 70.78 μm for the 0^{o} and 45^{o} samples, respectively).

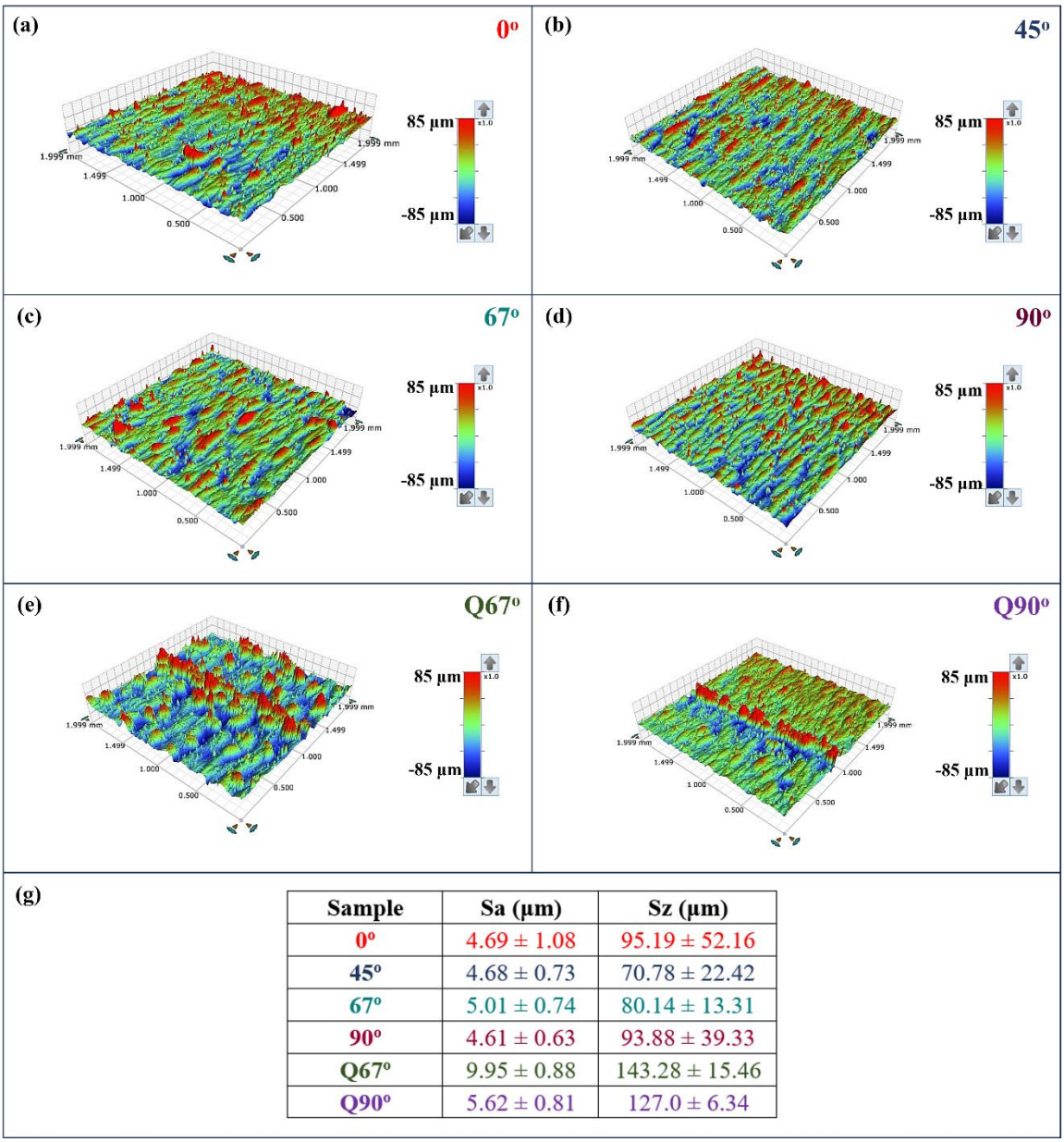

(g)

Sample	Sa (µm)	Sz (µm)
0º	4.69 ± 1.08	95.19 ± 52.16
45º	4.68 ± 0.73	70.78 ± 22.42
67º	5.01 ± 0.74	80.14 ± 13.31
90º	4.61 ± 0.63	93.88 ± 39.33
Q67º	9.95 ± 0.88	143.28 ± 15.46
Q90º	5.62 ± 0.81	127.0 ± 6.34

Figure 5.5 The surface roughness profiles of the XZ planes of the (a) 0º, (b) 45º, (c) 67º, (d) 90º, (e) Q67º, and (f) Q90º samples, along with (g) Sa and Sz values.

5.4.4 Microstructure and Crystallographic Texture

The grain structure of the samples can be seen from the optical micrographs (Figure 5B2 of Appendix B), the inverse pole figure (IPF) maps with respect to the BD, and image quality & grain boundaries (IQ & GBs) maps (Figure 5.6, Figure 5.7, and Figure 5.8). The Gaussian energy distribution of the laser beam in the PBF-LB process results in arc-shaped melt pools in the XZ planes, which are parallel to the build direction [15]. The arc-shaped melt pools, along with a microstructure composed of the columnar elongated grains along the build direction were observed in the XZ planes of the 45º, 67º, 90º, Q67º, and Q90º samples (Figure 5B2 of Appendix B and Figure 5.6). However, the XZ plane of the 0º

samples did not show arc-shaped melt pools, whereas near directionally elongated columnar grains, and a few fine irregular grains were observed. On the other hand, the XY planes of the 67°, 90°, and Q90° samples (shown in Figure 5.7) exhibited a distinct cross-like structure (chessboard pattern) attributed to the scanning rotation per layer [225]. Among them, the clearest chessboard pattern was observed in the XY plane of the 90° sample. Additionally, the Q67° sample displayed a slight chessboard pattern in the XY plane, whereas equiaxed grains were visible in the XY plane of the 45° sample. Moreover, the laser scan path was visible in the XY plane of the 0° sample, which did not show any chessboard pattern due to the absence of scanning rotation per layer. Furthermore, it can be said that all XY planes of the samples exhibited the equiaxed grains. In addition to this, Figure 5.8 and Figure 5B2 of Appendix B show the overlapping regions of the islands in the XY planes of the Q67° and Q90° samples. It can be especially seen from the IPF and IQ & GBs maps that the overlapping regions showed a mixture of equiaxed and columnar grains which are small and fine compared to the inside of the islands. Moreover, there was no significant difference between XRD patterns attributed to γ (gamma) phase of the as-built samples (Figure 5B3 of Appendix B).

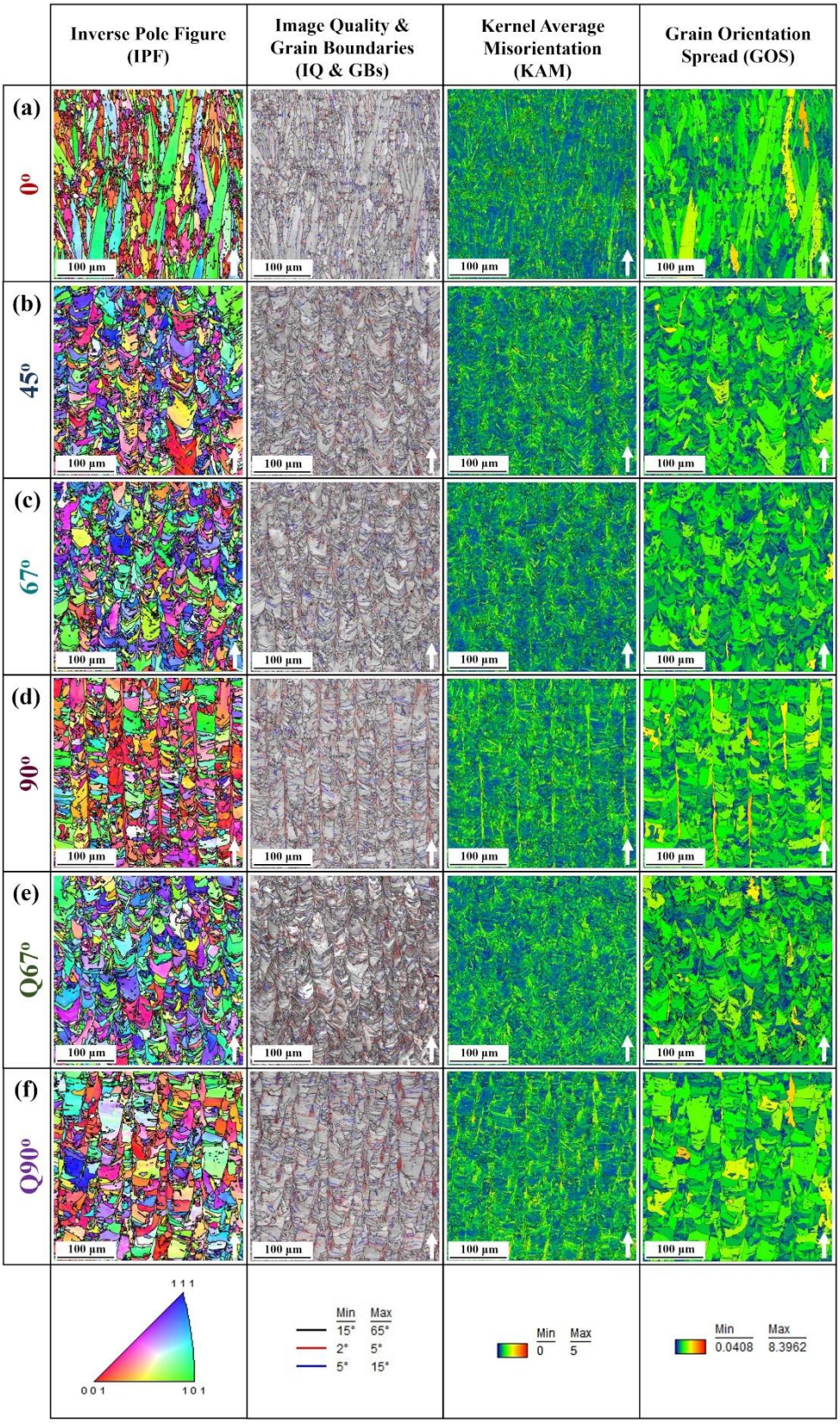

Figure 5.6 EBSD maps of the XZ planes of the as-built samples: (a) 0°, (b) 45°, (c) 67°, (d) 90°, (e) Q67° and (f) Q90°.

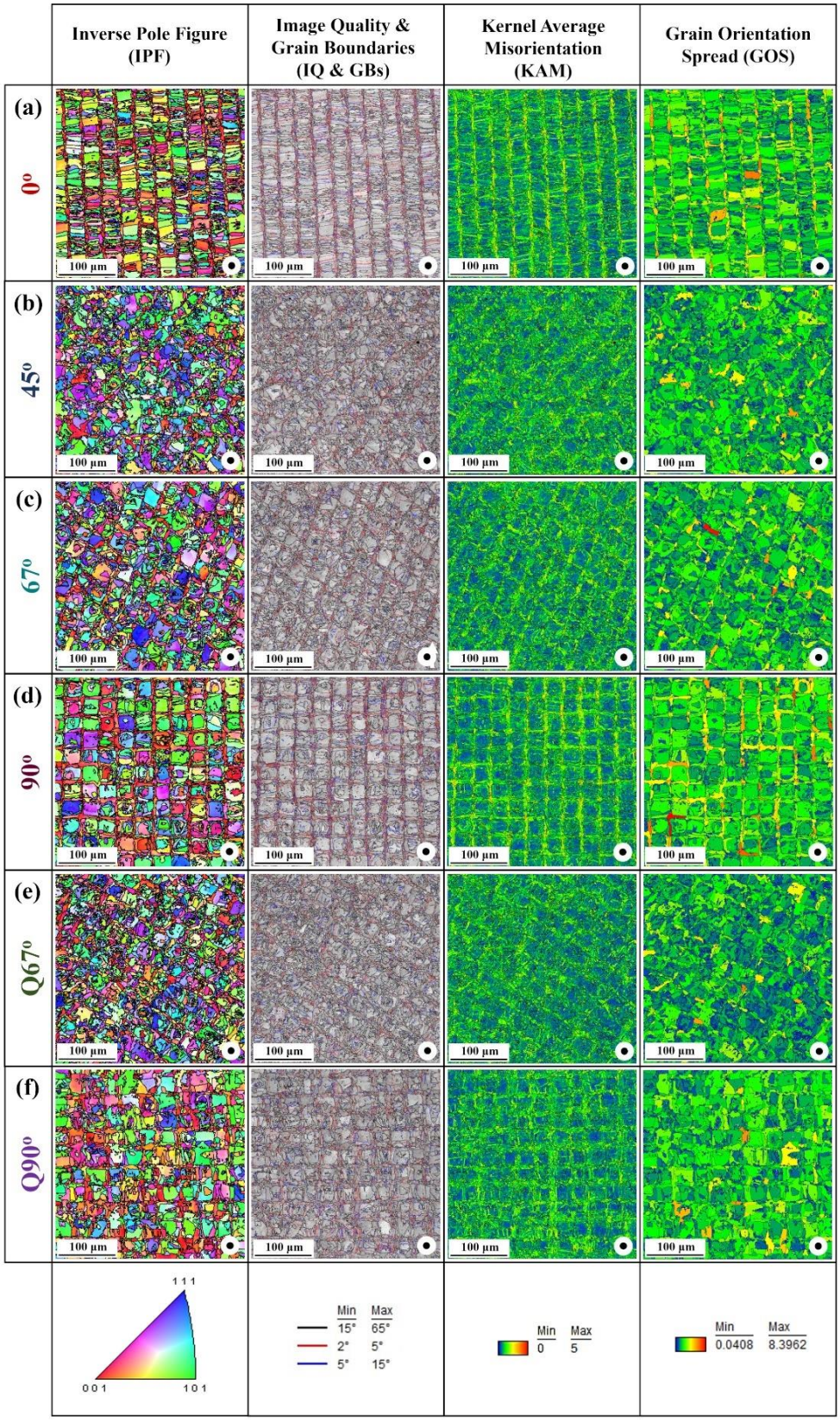

Figure 5.7 EBSD maps of the XY planes of the as-built samples: (a) 0º, (b) 45º, (c) 67º, (d) 90º, (e) Q67º and (f) Q90º.

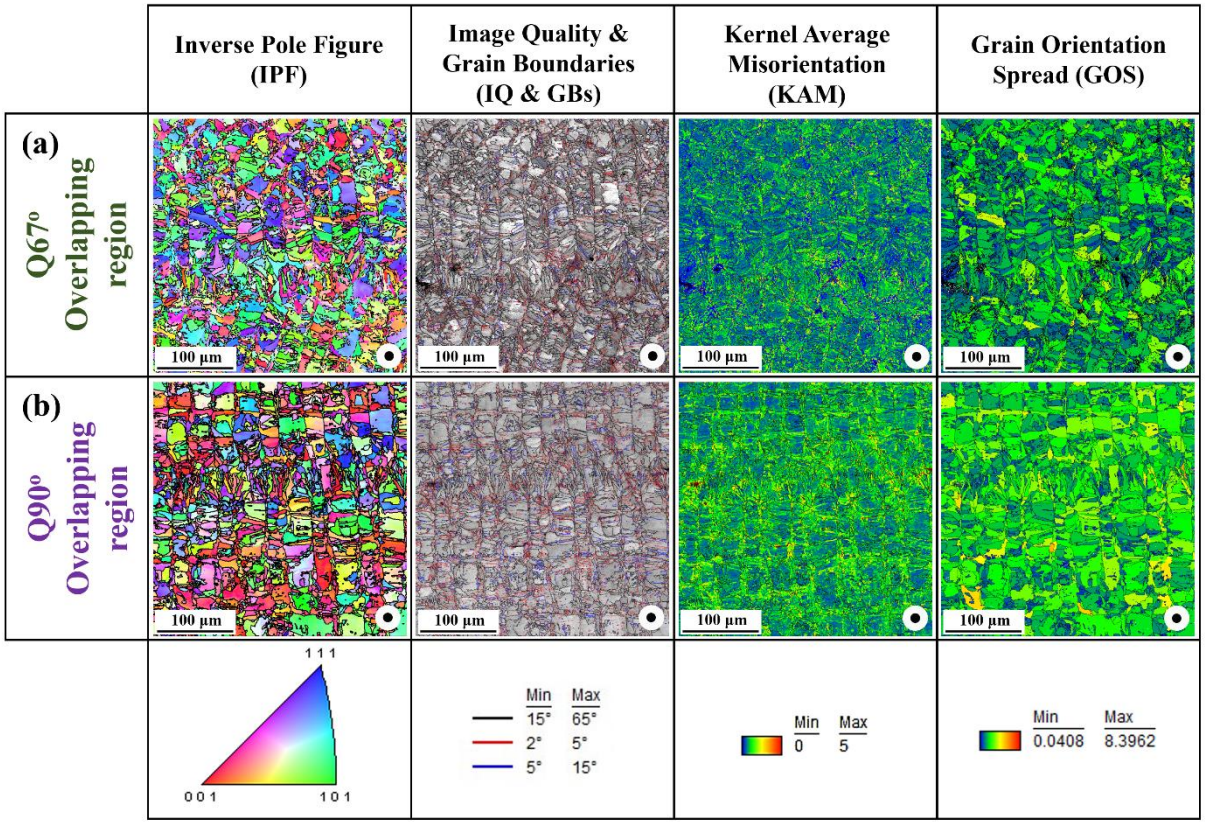

Figure 5.8 EBSD maps of the overlapping regions of the as-built samples: (a) Q67^{o} and (b) Q90^{o}.

Grain major axis length, grain minor axis length, grain shape aspect ratio and grain shape orientation distribution graphs, and their values are exhibited in Figure 5.9 and Table 5.3, respectively. In the 0^{o} sample, the columnar grains were approximately twice as large as those in the other samples. Furthermore, the XZ planes of all the as-built samples possessed larger grains than the XY planes (Table 5.3). Additionally, the 45^{o} and 67^{o} samples exhibited smaller grains compared to the 90^{o} sample, and the grains of the Q67^{o} and Q90^{o} samples were very similar to the 67^{o} and 90^{o} samples in terms of grain major and minor axis lengths. The grain major axis length distribution graphs (Figure 5.9(a)) indicate a tri-modal distribution for the XZ plane of the 0^{o} sample (peaks at around 100, 30, and 8 µm) and a bi-modal distribution for the rest of the samples (peaks at around 20 and 8 µm). On the other hand, bi-modal distribution was observed in the XY planes of all the samples, along with a higher peak at 20 µm and a minor peak at 10 µm for the 0^{o}, 90^{o}, Q67^{o}, and Q90^{o} samples. The grain minor axis lengths of the XZ planes are slightly larger than those of the XY planes, however, the differences among the samples are very low compared to the grain major axis length. The 90^{o} sample exhibited the largest grain minor axis length among all as-built samples, with minor axis lengths in the XZ and XY planes being nearly

identical. Nevertheless, the largest differences between XZ and XY planes were observed in the 45°, Q67°, and Q90° samples. It can be seen from Figure 5.9(b) that the grain minor axis length distribution graphs also exhibit bimodality (peaks around 2 and 10 μm). In the 90° and Q90° samples, the peak at 10 μm was notably higher, whereas in the other samples, the peak at 2 μm was more pronounced.

The grain shape aspect ratio was notably smaller in the XZ plane of the 0° sample compared to the other samples, indicating an exceptionally elongated grain structure (see Figure 5.6(a) and Figure 5B2 of Appendix B). Additionally, the grain aspect ratios for all samples were smaller in the XZ planes compared to the XY planes, primarily due to the presence of columnar grains. Also, note that the grain shape aspect ratio distribution graphs (Figure 5.9(c)) show a minor peak around 0.8 aspect ratio (indicating an equiaxed grain structure); however, since those grains are smaller in size, their area fraction is less compared to more elongated grains. Moreover, the 90° and Q90° samples exhibited a narrower distribution of around 0.4 aspect ratio in the XZ plane, while the other samples displayed wider distributions for aspect ratio.

The grain shape orientation distributions exhibited variations among samples and planes (Figure 5.9(d)). The XZ plane of the 0° sample showed grains whose major axis is oriented vertically, which is parallel to the heat flow direction. Conversely, the remaining samples of the XZ planes displayed wider distributions, nevertheless having minor peaks around 45°, 67°,115°, and 135°. These peaks were also evident at similar angles in the XY plane. Here, grains in the samples were oriented such that their grain major axis is approximately 45° to the scan direction in the XY plane. For instance, in the XY plane, the 90° sample displayed a peak around 45°, whereas the 0° sample exhibits a peak at 135°.

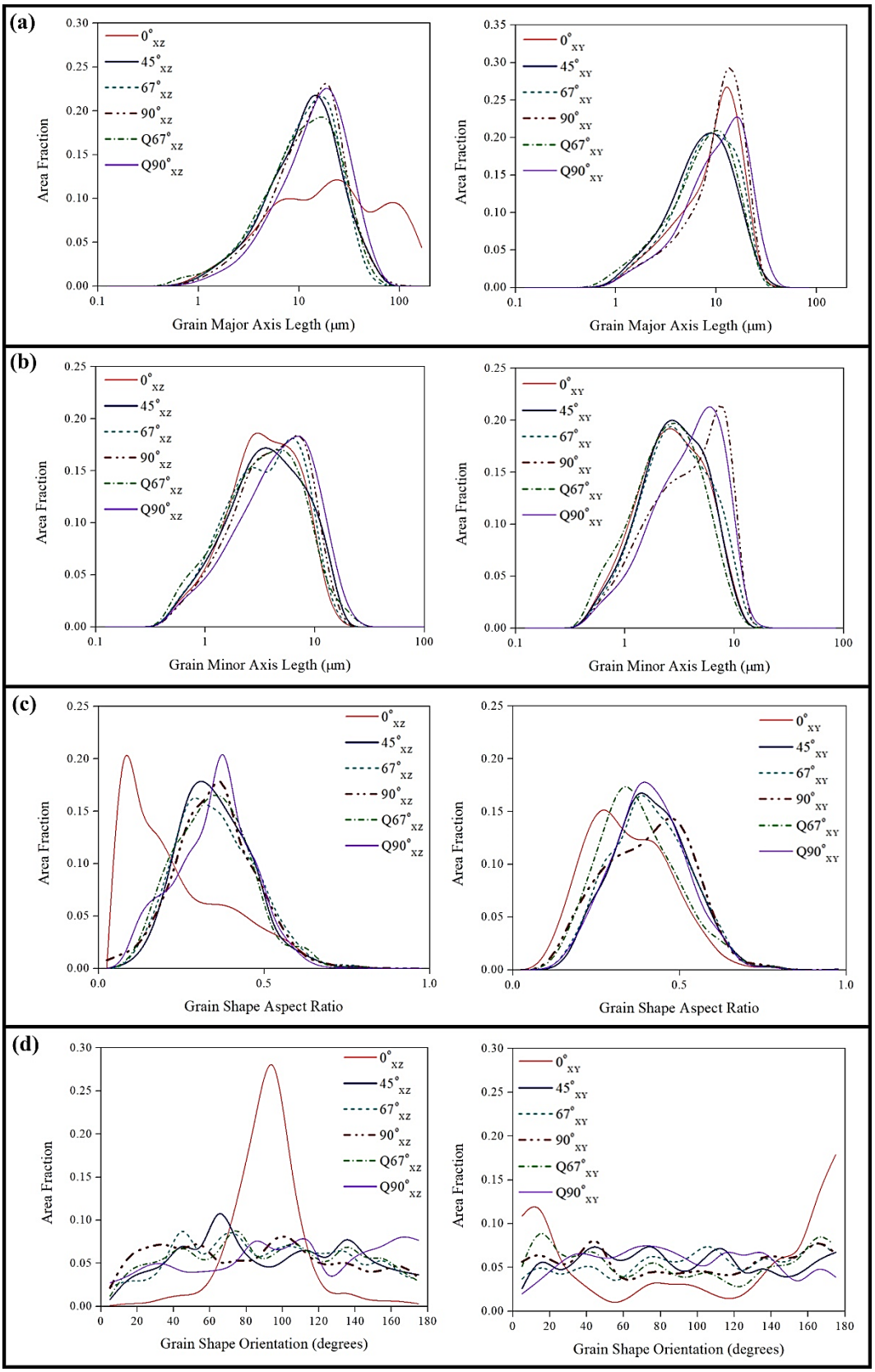

Figure 5.9 (a) Grain major axis length, (b) grain minor axis length, (c) grain shape aspect ratio, and (d) grain shape orientation distribution graphs of the as-built samples.

Table 5.3 Grain major axis length, grain minor axis length, grain shape aspect ratio, and grain shape orientation values of the as-built samples.

Sample	Grain Major Axis Length (µm)	Grain Minor Axis Length (µm)	Grain Shape Aspect Ratio	Grain Shape Orientation (degrees)
0^{o}_{XZ}	36.37	4.23	0.23	91.52
0^{o}_{XY}	9.90	3.22	0.34	99.21
45^{o}_{XZ}	14.15	4.67	0.35	92.41
45^{o}_{XY}	8.42	3.27	0.41	89.85
67^{o}_{XZ}	13.09	4.36	0.35	91.15
67^{o}_{XY}	8.92	3.56	0.40	97.48
90^{o}_{XZ}	15.08	4.70	0.35	85.67
90^{o}_{XY}	10.97	4.42	0.40	91.66
$Q67^{o}_{XZ}$	13.15	4.27	0.34	91.47
$Q67^{o}_{XY}$	8.44	2.92	0.37	88.17
$Q90^{o}_{XZ}$	16.95	5.62	0.35	100.90
$Q90^{o}_{XY}$	11.30	4.41	0.40	89.90

The area-weighted average grain size, grain orientation spread (GOS), geometrically necessary dislocation (GND) density, and misorientation angle distribution graphs are given in Figure 5.10. Also, Table 5.4 shows the area-weighted average grain size, GOS, kernel average misorientation (KAM), and GND density values. For all samples, the area-weighted average grain size values were larger in the XZ planes, showing a similar trend with the grain major axis length. In the XZ planes, the 0^{o} sample exhibited the largest area-weighted average grain size of 23.7 µm, attributed to elongated columnar grains, while the 67^{o} sample had the smallest size at 14.6 µm. Conversely, in the XY planes, the $Q90^{o}$ sample had the largest area-weighted average grain size of 13.9 µm, and the $Q67^{o}$ sample had the smallest at 9.7 µm. Moreover, the 0^{o} sample showed the largest anisotropy between the XZ and XY planes, with the XZ plane having the largest area-weighted average grain size (23.7 µm) and the XY plane having a smaller size (10.9 µm). In contrast, the 90^{o} sample exhibited relatively consistent area-weighted average grain sizes in both the XZ and XY planes compared to other samples.

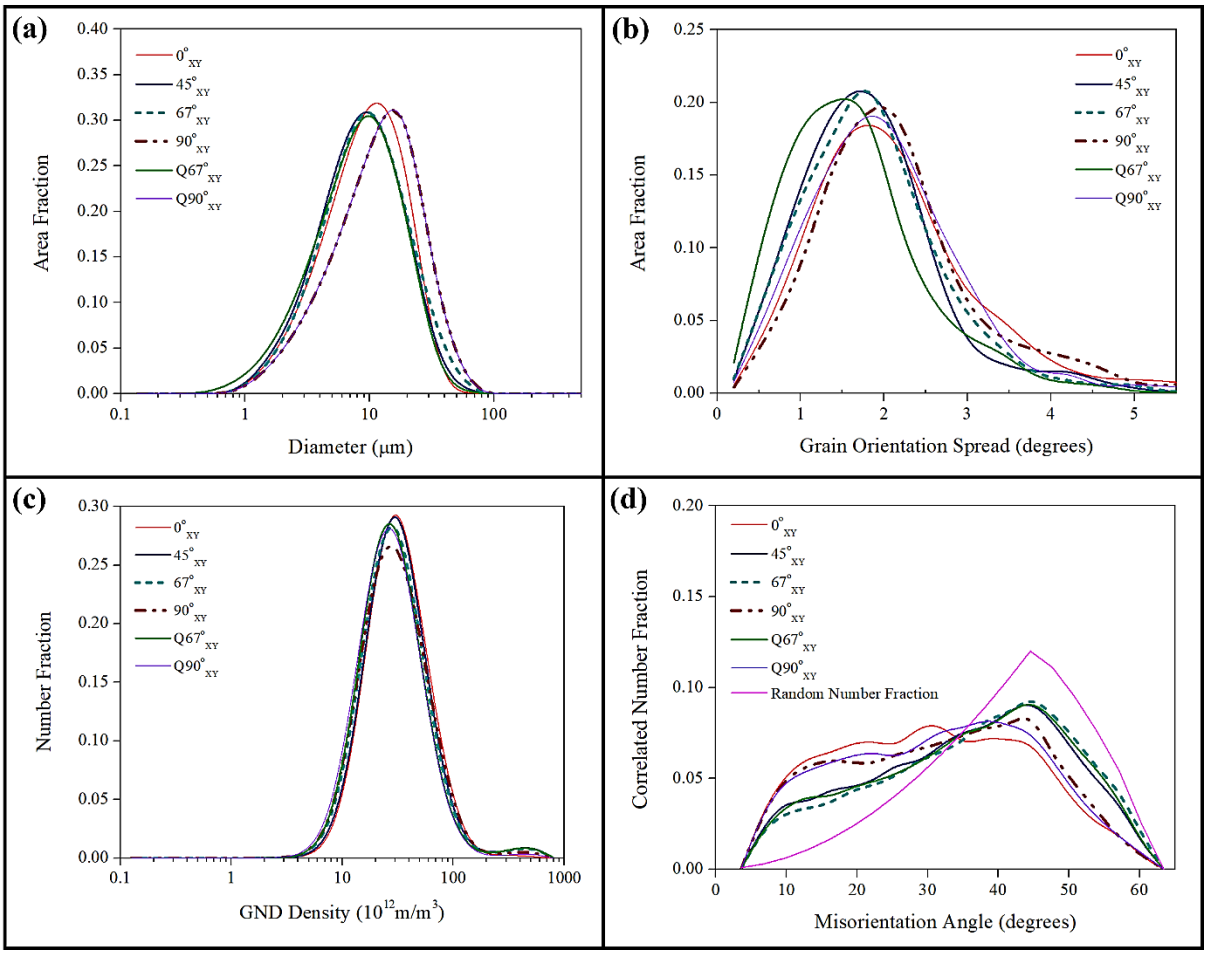

Figure 5.10 (a) Area-weighted average grain size, (b) GOS, (c) GND density and (d) misorientation angle distribution graphs of the as-built samples.

Table 5.4 Area-weighted average grain size, GOS, KAM, and GND density values of the as-built samples.

Sample	Average grain size (µm)	GOS (degrees)	KAM (degrees)	GND (10^{12} m/m^3)
0^{o}_{XZ}	23.7 ± 21.3	2.03 ± 0.90	0.86 ± 0.47	34.36
0^{o}_{XY}	10.9 ± 6.3	2.14 ± 1.03	1.07 ± 0.60	37.78
45^{o}_{XZ}	15.7 ± 12.2	1.86 ± 0.77	0.87 ± 0.47	39.14
45^{o}_{XY}	10.2 ± 6.3	1.82 ± 0.83	0.99 ± 0.52	42.59
67^{o}_{XZ}	14.6 ± 9.7	1.74 ± 0.71	0.84 ± 0.45	38.50
67^{o}_{XY}	11.0 ± 7.0	1.88 ± 0.91	0.97 ± 0.52	40.42
90^{o}_{XZ}	16.2 ± 10.1	2.08 ± 0.90	0.93 ± 0.50	39.27
90^{o}_{XY}	13.6 ± 7.8	2.23 ± 1.12	1.04 ± 0.59	38.90
$Q67^{o}_{XZ}$	15.5 ± 10.5	1.87 ± 0.79	0.87 ± 0.46	40.57
$Q67^{o}_{XY}$	9.7 ± 6.1	1.63 ± 0.85	0.93 ± 0.49	39.62
$Q90^{o}_{XZ}$	19.1 ± 13.2	2.15 ± 0.91	0.96 ± 0.54	37.81
$Q90^{o}_{XY}$	13.9 ± 8.0	2.01 ± 0.90	0.96 ± 0.52	34.14

KAM is a measure of local misorientations and is closely associated with defect density. High KAM values are often attributed to high plastic strain and dislocation density within the material. It is calculated for each point in the EBSD map by determining the misorientations between a specific point and its surrounding points, followed by averaging these misorientations. Notably, misorientations exceeding 5^{o} are excluded from the calculation of average misorientation, as they typically represent grain boundaries. The KAM maps (shown in Figure 5.6, Figure 5.7 and Figure 5.8) are color-coded using a rainbow scale, where blue and red represent the minimum misorientation and maximum misorientation (0^{o}-5°). The chessboard pattern was prominently observed in the KAM maps of the XY planes for the 67^{o}, 90^{o}, and $Q90^{o}$ samples (Figure 5.7). This pattern revealed regions with high lattice rotation and increased dislocation densities, corresponding to the centers of the melt pools. These areas indicated the presence of fine grains, as evidenced by the IPF, and IQ and GB maps [14,15]. Aota et al. [225] reported that the melt pool centerline has fine grains (at the borders of the chessboard pattern) and the overlapping regions of the melt pools (center of the chessboard pattern) have coarse grains. The XY planes of the samples had slightly higher KAM values than the XZ planes

and there were minimal differences among the samples in terms of the KAM values (Table 5.4). The highest and lowest KAM values are 1.07^{o} (in the XY plane of the 0^{o} sample) and 0.86^{o} (in the XZ plane of the 0^{o} sample), respectively. Furthermore, in metallic materials, dislocation density includes both geometrically necessary dislocations (GNDs) and statistically stored dislocations (SSDs), and it is noted that GNDs constitute a significant portion of the total dislocations in face-centered cubic (FCC) metals. The rapid cooling rate during solidification induces local strain variations, leading to a higher dislocation density. GNDs arise from internal plastic strain gradients. Therefore, a high GND density is indicative of high plastic strain gradients [14,45]. The GND density values showed minimal variation like KAM values among the samples. The highest GND density was observed in the XY plane of the 45^{o} sample (42.59×10^{12} m/m^{3}), while the lowest GND density was in the XY plane of the Q90^{o} sample (34.14×10^{12} m/m^{3}). Additionally, there was variation between the XZ and XY planes in terms of KAM and GND values, similar to the area-weighted average grain size values, indicating anisotropy between the two planes

GOS is a measure of local misorientation, focusing on grain-based local misorientation within the material. It is calculated by first determining the average orientation of a grain, followed by calculating the misorientation between this average orientation and the orientation of each individual measurement point within the grain. Subsequently, the average of these misorientations is calculated and assigned to each point within the grain. The rainbow scale is used for labelling the GOS maps like the KAM maps, where blue represents the minimum and red represents the maximum values (Figure 5.6, Figure 5.7 and Figure 5.8). High defect density and deformation lead to an increase in GOS values, while recrystallization tends to decrease them [14,15]. The XY plane of the 90^{o} sample exhibited the highest GOS value at 2.23°, while the XY plane of the Q67^{o} sample had the lowest GOS value at 1.63° among all the samples. GOS is also utilized to distinguish recrystallized grains from others. It is important to note that the choice of threshold GOS value for determining recrystallization fraction in EBSD analysis can vary depending on the material and analysis criteria. While there is no universally agreed-upon threshold value, a common threshold value used in some studies changes from 1^{o} to 2.5^{o} [14,32,225–228]. This threshold is chosen based on the assumption that grains with GOS values below this threshold have undergone recrystallization and are considered recrystallized grains, while grains with GOS values above this threshold are considered deformed grains. In this study, a threshold GOS value of <1.5^{o} was selected to calculate

the recrystallization fraction, with GOS values below this threshold indicating recrystallized grains. The calculated recrystallization fractions of the samples are exhibited in Figure 5.11 for both the XZ and XY planes. The highest recrystallization fraction was observed in the XY plane of the Q67^{o} sample at 53.6%, while the lowest was in the XY plane of the 90^{o} sample at 28.8%. Interestingly, in the XZ planes, the highest recrystallization fraction occurred in the 67^{o} sample at 43.8%, and the lowest was in the Q90^{o} sample at 31%. Furthermore, the detailed distribution of grain boundary characters of the samples extracted from IQ & GBs maps is presented in Figure 5B4 of Appendix B.

The misorientation angle distribution graph is displayed in Figure 5.10(d) and the pink line represents the Mackenzie distribution for completely random-oriented cubic polycrystals. In the distributions of the as-built samples, a prevalence of low-angle grain boundaries (<15^{o}) was observed, indicating the presence of more substructure regions and higher dislocation density. On the other hand, above 15^{o}, which indicates high angle grain boundaries, misorientations approach to the Mackenzie. The 0^{o} and 67^{o} samples had the highest and lowest misorientations, respectively below 15^{o}.

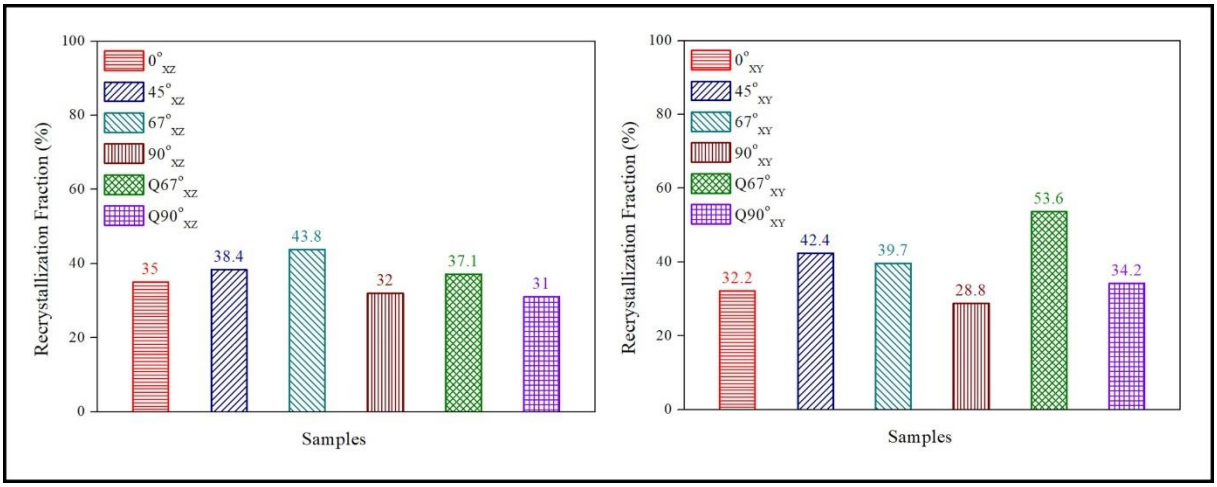

Figure 5.11 Recrystallization fractions for both the XZ and XY planes of the as-built samples.

The corresponding {001}, {011}, and {111} pole figures (PFs) and inverse pole figures (IPFs) with respect to the build direction taken from the XY planes of the as-built samples are displayed in Figure 5.12. Here, the intensity values are given in units of multiple random distribution (MRD), where an intensity value of 1 indicates a completely random distribution of crystallographic texture. The 0^{o} and 90^{o} samples exhibited a dominant cube texture having <100> parallel to scan and built directions. The intensity values of the PFs were 9.301 for the 0^{o} sample and 6.930 for the 90^{o} sample, while the

intensity values of the IPFs were 3.999 for the 0° sample and 4.514 for the 90° sample. In addition to them, the Q67° sample also showed cubic texture (<100> // BD) with relatively lower intensity values of 2.250 for PFs and 1.675 for IPFs. Moreover, the 45°, 67° and Q90° samples displayed both <001> // BD and <101> // BD textures. Among them, the Q90° sample had higher intensity values (6.243 for PFs and 2.238 for IPFs) than the 45° and 67° samples. Among all samples, the 0° sample had the most intense texture, whereas the 45°, 67°, and Q67° samples had low intensity values which are close to the random distribution of crystallographic texture.

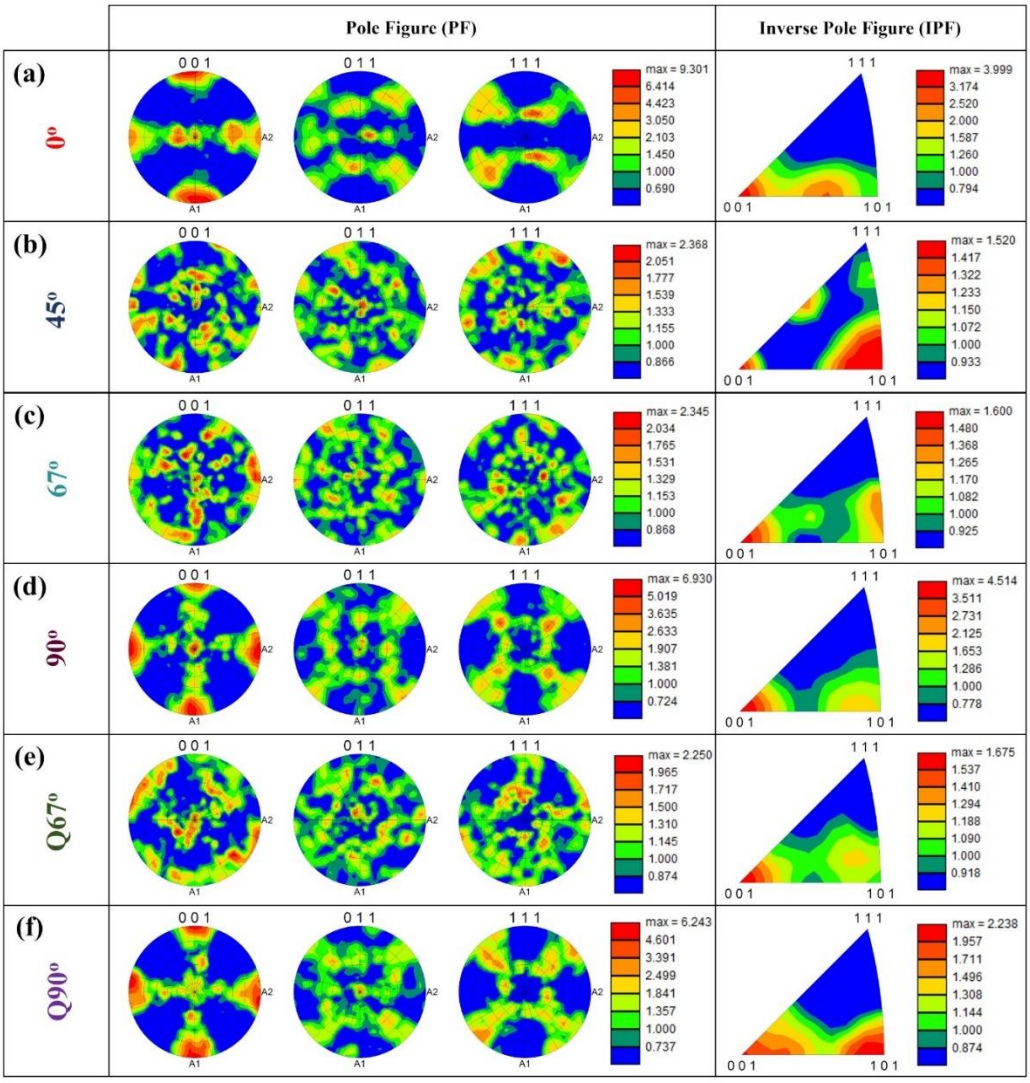

Figure 5.12 Pole figures (PFs) and inverse pole figures (IPFs) with respect to the normal direction taken from the XY planes of the (a) 0°, (b) 45°, (c) 67°, (d) 90°, (e) Q67°, and (f) Q90° samples.

5.4.5 Microhardness and Residual Stress

Figure 5.13 shows the microhardness graphs of the as-built samples. There was a minimal variance in microhardness values among the samples. Within the XZ planes, the 0^o sample displayed the highest microhardness value (356±7 HV), whereas the Q90^o sample exhibited the lowest (321±14 HV). Conversely, the microhardness values in the XY planes were largely uniform across the samples. Notably, the microhardness graphs also highlighted anisotropy between the XZ and XY planes.

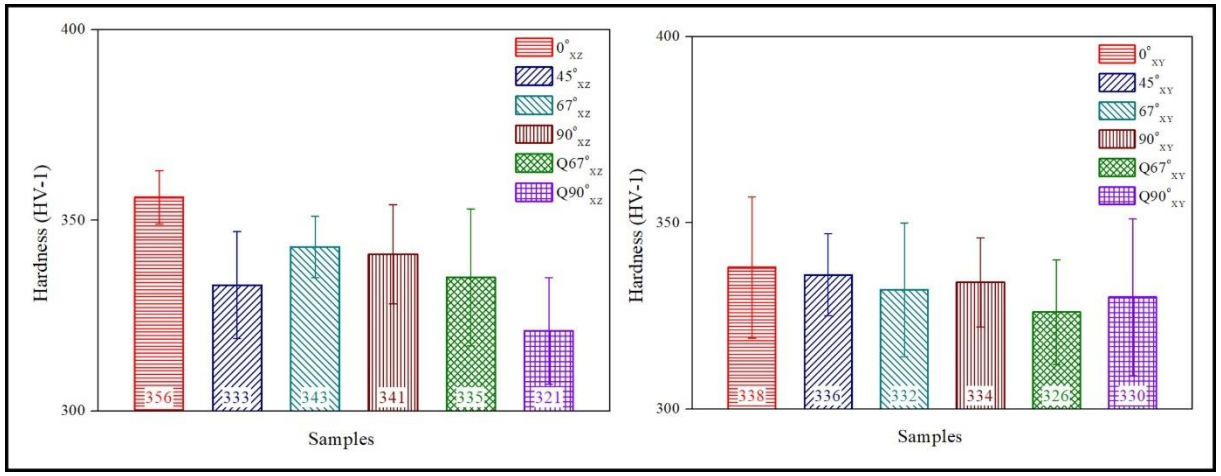

Figure 5.13 Microhardness graphs for both the XZ and XY planes of the as-built samples.

XRD residual stress measurements were conducted to determine the principal residual stresses (σ_{max} and σ_{min}) and the angle Φ (σ_{max}) (°) values, which are given in Figure 5.14, according to the scanning strategy. The angle made by the X-axis and the maximum principal stress (σ_{max}) is denoted by Φ (phi) and Φ (σ_{max}) is the orientation of the maximum principal stress with respect to global axes. Among the XZ planes of the samples, the Q90^o sample exhibited the highest σ_{max} residual stress (961.1 MPa), while the 67^o sample showed the lowest (542.6 MPa). Additionally, the XZ plane of the Q67^o sample displayed the lowest σ_{min} residual stress (129.3 MPa), whereas the Q90^o sample demonstrated the highest (270 MPa). On the other hand, σ_{max} residual stress values of the XY planes of the as-built samples were close to each other. Among them, the Q67^o sample had the lowest (408.4 MPa), whereas the 0^o sample had the highest (581.6 MPa). Furthermore, the XY plane of the 67^o sample possessed the lowest σ_{min} residual stress value (155.5 MPa), while the Q90^o sample had the highest (493.9 MPa).

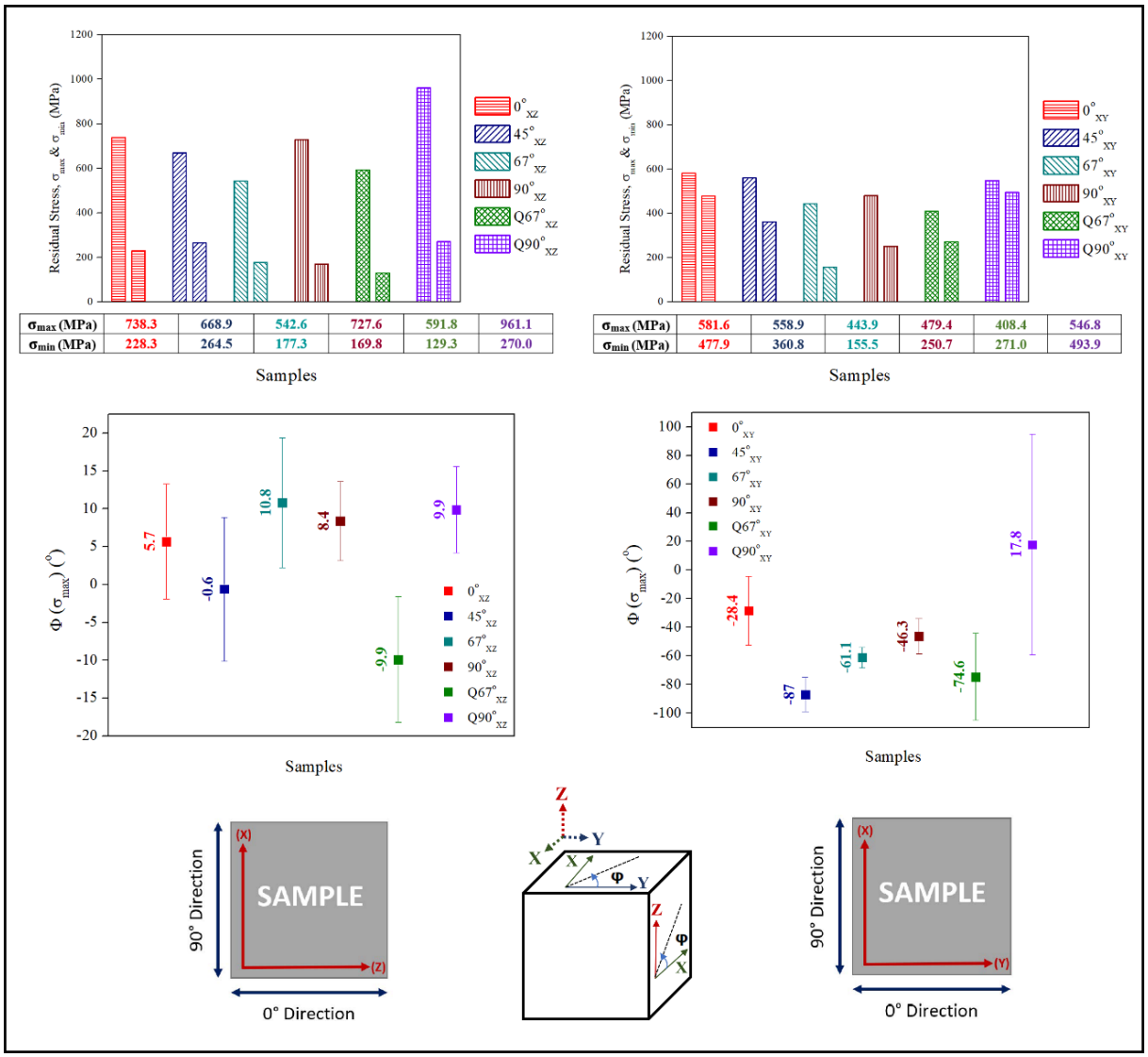

Figure 5.14 The principal residual stresses (σ_{max} and σ_{min}) and Φ (σ_{max}) (°) graphs for both the XZ and XY planes of the as-built samples, along with a schematic representation of the Φ (°) corresponding to the observed planes.

5.5 Discussion

5.5.1 Density and Defect Analysis

Optimizing PBF-LB process parameters is significant for achieving desired outcomes, such as minimizing defects and reducing surface roughness. The scanning strategy plays an important role in tailoring material properties among these parameters, as evidenced by the current study [28,133]. The rotation between the adjacent layers increased the relative density of the samples, while reducing the pores/mm^2. This can be explained that layer-by-layer rotation promotes material fusion and fills voids between tracks, thus enhancing part density [31]. The lowest relative density observed in the

chessboard scanning strategy, coupled with the presence of porosity and crack formation in the overlapping regions of small islands, can be attributed to the rapid opening, and closing of the laser. This rapid action introduces instability in laser energy input, potentially causing defects like pores and unmelted spatter powder at the boundaries of small islands [31]. Additionally, optimizing the overlapping gap, which was 0 mm in this study, between the islands for the chessboard scanning strategy can mitigate defects in the overlapping regions. Moreover, Lu et al. [158] reported that the island size significantly influences the formation of pores in IN718 fabricated by the PBF-LB. Smaller islands tend to result in the presence of unmelted and spatter powders in overlapping regions, leading to reduced density and increased porosity. According to their findings, as island size increased from 2x2 mm^2 to 7x7 mm^2, pore quantity, and size decreased notably with larger island sizes, indicating that denser parts can be achieved through the utilization of larger island scanning strategies [28,229]. In our study, using an island size of 2.5x2.5 mm^2 may have contributed to the observed low relative density, high porosity, and increased surface roughness. This is likely due to the greater presence of spattered powders associated with the smaller island size.

Superalloys rich in Al and Ti, such as IN939, are utilized to generate the L12-ordered γ' phase (Ni_3(Al, Ti)). However, these alloys are susceptible to cracking, presenting a significant challenge in the PBF-LB process for high γ' phase Ni-base superalloys [99]. The microcracking observed in IN939 produced by the PBF-LB process was reported in two primary types: solidification and solid-state cracks [16]. Solidification cracks, also known as "hot tears", occur within the solidifying melt pool or mushy zone, where the material is in a semisolid state. The development of dendrite structures during solidification restricts the flow of residual liquid in the interdendritic regions, concentrating solidifying stress and potentially causing the tearing of liquid films and the formation of cracks. Furthermore, solid-state cracks can include various types, such as strain-age cracks, ductility-dip cracks (DDC), and cold cracks. These cracks can traverse both grains and grain boundaries, typically following a straight or slightly curved path within the grain structure, while also delineating and separating grains along their boundaries [99,102]. On the other hand, it has been reported that the presence of oxide can also contribute to crack formation through various mechanisms, such as stress concentration near the oxide, increased brittleness of boundaries, and constitutional liquation at the oxide-matrix interface [103,210]. In the current study, dendritic structures indicative of solidification cracks were observed within the cracks. Long and straight

cracks, typically associated with solid-state cracks, were also noted. Additionally, Al_2O_3 was detected in some of the cracks, suggesting the presence of oxide-induced cracks.

Mukherjee et al. [177] highlighted the significance of grain structure in determining susceptibility to cracking. Specifically, the presence of long columnar grains can lead to their separation under high tensile stress during solidification, thereby contributing to the occurrence of solidification cracking. In our study, the XZ plane of the 0^o sample, characterized by large columnar grains, exhibited the highest degree of cracking, aligning with this explanation. Moreover, fewer cracks were observed in the 45^o and 67^o samples compared to the 0^o sample aligns with the study of Xu et al. [32] which highlights the critical role of scanning rotation angle in crack formation during the PBF-LB process. A 0^o rotation accumulates strain in the same direction across layers, leading to high residual stresses and uneven temperature distribution, which promotes crack formation. In contrast, a 67^o rotation angle distributes thermal stresses more evenly and reduces strain accumulation, resulting in fewer cracks. Similarly, a 45^o rotation also improves stress distribution compared to 0^o, but not as effectively as 67^o as can be seen from the residual stress results in this study. While a 90^o rotation can enhance long-term temperature uniformity, it may induce localized stresses due to abrupt changes in scanning direction, potentially increasing crack formation. The long and straight cracks observed near the edge of the 90^o sample could be likely the result of these localized stresses. Overall, the 45^o and 67^o rotations offer better control over thermal gradients and stress distribution, minimizing the possibility of cracks.

5.5.2 Microstructural and Crystallographic Texture Evolution

In the PBF-LB process, rapid cooling and non-equilibrium solidification influence the solidification microstructure, which is governed by parameters such as solidification rate (R), undercooling (ΔT), and temperature gradient (G). The size and morphology of the solidification microstructure (planar, cellular, equiaxed dendritic, or columnar dendritic) are determined by GxR and G/R, respectively [14,45,177,230]. Lower cooling rates result in coarser microstructures due to the lower product of the temperature gradient and solidification rate ($G \times R$), whereas higher cooling rates lead to finer microstructures. An extremely high G/R ratio results in planar solidification, while a moderate G/R ratio forms cellular structures, and a low G/R ratio generates columnar or equiaxed dendritic structures. In the PBF-LB process, typically high cooling rates lead to high G/R values, which favour cellular structures. Additionally, columnar dendritic structures can also

occur. In this study, both columnar dendritic and cellular microstructures were observed (Figure 5.4). Cellular structures, with a honeycomb-like morphology, appear as parallel boundaries along the building direction and as circular features on the transverse section, resulting in varied appearances in different cross-sections. This characteristic is widely observed in additively manufactured metals and alloys [222].

The findings of the current study revealed that altering the scanning strategy in the PBF-LB process has a substantial impact on the grain structure and texture of IN939. In the 0^o sample, where the melt pools from successive layers are nearly aligned, a consistent temperature gradient is maintained between layers. This alignment results in a significant overlap of melt pools, effectively remelting portions of the previous layer and eliminating nucleation barriers. Consequently, the predominant heat flow direction aligns with the build direction, promoting epitaxial growth of columnar grains that extend along the build direction [31]. In the PBF-LB process, a laser forms a melt pool in the powder bed, melting new powder and partially remelting the previously solidified layer. This overlap creates a re-melting zone, influencing both the new and existing materials. Nucleation barriers, such as those from thermal gradients or existing grain structures, can impede the formation of new grains. However, high temperatures during remelting can dissolve these barriers, facilitating a more uniform material composition. This process enhances grain formation, leading to a more consistent microstructure with diverse grain orientations and sizes compared to areas where barriers persist. High nucleation barriers typically result in fewer, larger grains growing in a single orientation, creating an anisotropic microstructure. In contrast, low nucleation barriers allow for easier grain formation, promoting finer, more homogeneous, and isotropic microstructures. Moreover, the 45^o and 67^o samples have angled thermal gradients and varied melt pool orientations. This results in less uniform melt pool overlap and reduced removal of nucleation barriers, leading to more complex thermal conditions. These conditions can disrupt columnar grain growth, resulting in finer grains and reduced anisotropy. Research conducted by Liu et al. [31] and Song et al. [231] indicates that rotating the scanning direction by 15^o and 47^o between layers can disturb columnar growth, hindering the epitaxial development of elongated grains and leading to more refined microstructures. Furthermore, the heat flow direction becomes perpendicular to the build direction in the 90^o sample. This strategy enhances the uniformity of melt pool overlap and supports a competitive grain growth mechanism, thus promoting predominant epitaxial growth and potentially improving overall microstructural uniformity [31]. On the other hand, the chessboard scanning strategy promotes a uniform microstructure by

preventing excessive heat buildup and ensuring consistent cooling rates, which refine grains in overlapping regions. This strategy disrupts the preferential growth of columnar grains, leading to finer grains. Steep temperature gradients in overlapping regions, caused by intersecting laser paths and varying thermal histories, significantly influence nucleation and growth dynamics, resulting in diverse grain orientations and sizes. The fine grains in the Q67^{o} and Q90^{o} samples' overlapping regions are due to complex heat flow and faster cooling rates from intersecting laser points. The intermittent laser movement at island edges further accelerates cooling in these areas compared to island interiors.

In the PBF-LB process, recrystallization occurs due to thermal cycling during fabrication. High temperatures during melting and solidification cycles facilitate the creation of strain-free grains, replacing deformed ones [45,225–227,232]. Dynamic recrystallization (DRX), a subset of recrystallization, occurs in hot deformation processes like hot rolling or forging. It typically occurs above the recrystallization temperature of the materials, inducing the formation of new grains [233]. Recent research has shown that DRX can occur not only in traditional hot deformation processes but also in the PBF-LB process [32,234,235]. The expansion and contraction during the uniform rapid heating and cooling leads to a severe local plastic deformation that combined with the high cyclic temperatures and thermal stress in the PBF-LB process can be considered as a thermo-mechanical process. This process promotes the creation of new grains with lower dislocation densities, often resulting in a finer grain structure. Among the samples analyzed, the XZ plane of the 67^{o} sample and the XY plane of the Q67^{o} sample had the highest recrystallization fractions and the smallest area-weighted average grain sizes. These high recrystallization fractions indicate that the thermal cycles during these specific scanning strategies effectively dissolve existing nucleation barriers and facilitate the formation of new grains. This enhanced recrystallization leads to improved material homogeneity, potentially resulting in more consistent mechanical properties across the material.

The texture is determined by the combined effects of maximum heat flow directions and the alignment of easy grain growth directions at melt pool boundaries. In cubic crystal structures, the preferred grain growth direction is <100>. This preference is due to the faster atomic movement along less densely-packed planes, which are more prevalent in this direction. These planes facilitate quicker and easier grain growth, making the <100> direction energetically favourable for grain development. By locally altering the heat flow direction and the balance between G and R through adjustments in the PBF-LB process

parameters like scanning strategy and energy density, the texture and microstructure can be modified [45,124,177]. Among the samples, the 0^o and 90^o samples exhibited a strong cube texture. In the 0° sample, the <001> crystallographic direction aligns with laser trajectories in each layer. This uniform thermal flux across layers promotes epitaxial growth, favouring the <001> crystal orientation due to reduced thermal gradients that encourage grain alignment along the easy growth direction. Moreover, in the 90° sample, achieving epitaxial growth of the <100> texture requires grains to orient themselves at 15^o to the maximum local heat flow direction. Perfect alignment with the heat flow direction results in a fiber texture, while misalignment leads to a cube texture. Additionally, an alternating bi-directional scanning strategy with 90° rotation between layers was found to strengthen the <001> textures [30,230]. On the other hand, an alternating bi-directional scanning strategy with 45^o and 67^o rotations was found weaken the texture by producing finer microstructural features, as reported in previous studies [163,177,236,237]. This weakening is attributed to the reduction in the coincidence of laser scanning vectors between adjacent layers and minimized heat accumulation. The frequent changes in scanning direction and angle reduce thermal gradients, leading to more uniform temperature distribution across the build. Consequently, more nuclei participate in competitive growth, resulting in grain refinement and a more random grain orientation, which diminishes the strength of any preferred texture. Therefore, it can be said that the scanning strategy has a direct effect on the microstructure, recrystallization fraction, and grain size tailoring.

5.5.3 Residual Stress Evolution

Residual stress remains within the bulk of a material even in the absence of external loads. It typically arises from the accumulation of material hardening due to various factors such as phase transformations and temperature gradients during solidification and crystalline state changes. It is a common outcome of thermomechanical manufacturing processes, including AM, where layer-by-layer fabrication induces thermal expansion and contraction, leading to substantial residual stress levels in the final components [103,168,238]. In the PBF-LB process, when a new layer is added and heated above the temperature of the underlying part, it initially expands uniformly but is restricted by the cooler underlying material. This results in compressive stresses in the new layer and tensile stresses in the underlying part. During cooling, the new layer contracts faster than the underlying part, resulting in tensile stresses in the new layer and compressive stresses in the underlying part. This heterogeneous solidification process creates residual stresses with

the sign of the residual stress typically opposite to the sign of the plastic strain during solidification due to the material strain accommodation between the regions. These stresses are primarily tensile in the new layer and compressive in the underlying material [238]. When stress levels surpass the yield strength of a Ni-base superalloy material, the material tends to release this stress through plastic deformation, leading to distortion of the component's shape or severe cracking, potentially resulting in component failure. Residual stress is identified as the primary factor driving crack initiation. Predictions regarding the likelihood of cracking or distortion during the PBF-LB process must consider the size and shape of the components, as these characteristics are closely linked to residual stress levels [103]. Among the PBF-LB process parameters, the scanning strategy is one of the most important process parameters to control residual stress [28,103,163,168,212,223,229,238].

In our study, Figure 5.14 presents the principal residual stress graphs of the samples, showing a notable difference between the XZ and XY planes, highlighting anisotropy between these planes. This aligns with findings by Bartlett and Li [238], who reported that anisotropy in in-plane stresses is significant in additive manufacturing due to the non-uniform melting of layers by discrete beam tracks. Longitudinal stresses along the beam motion direction are generally much higher than transverse stresses because of the non-uniform temperature distribution and contraction during solidification and cooling. Experimental data indicate that longitudinal stresses can be 1.5–2.5 times greater than transverse stresses. This anisotropy is present within each beam track and combines to produce an anisotropic total stress field in each layer. Furthermore, the observed differences in residual stress values among the samples are attributed to the distinct thermal histories and cooling rates associated with each scanning strategy in the PBF-LB process.

The alternating bi-directional scanning strategies, including the 0^o and 90^o rotation between layers, create linear and consistent heat input paths that generate higher thermal gradients and uneven cooling, resulting in elevated residual stresses. Specifically, the 0^o sample exhibited the highest residual stress in both the XZ and XY planes, consistent with previous findings by Zhang et al. [239] and Robinson et al. [240] and was associated with crack formation. Also, the cracks observed in the XZ plane of the 90^o sample (Fig. 4(d)) can be attributed to the high σ_{max} residual stress present in those areas. In contrast, the 45^o and 67^o samples, which introduce angled thermal gradients, lead to more even heat distribution and smoother temperature gradients, thereby reducing the magnitude of residual stresses compared to the linear scanning methods. The 67^o sample exhibited the lowest σ_{max} residual stress in the XZ planes of the samples due to uniform thermal

conditions during laser scanning, consistent with Xu et al. [32]. This uniformity helps to distribute the heat more evenly across the build area, reducing the magnitude of thermal gradients and resulting in lower residual stresses. Additionally, the high recrystallization fraction in the XZ plane of the 67^{o} sample may further contribute to the reduction of residual stress.

The island/chessboard scanning strategy, with small island sizes and short scan vectors, helps to reduce temperature gradients and residual stress in additively manufactured parts. Combined with rotated scan strategies, this method effectively mitigates residual stress formation by facilitating better heat dissipation and more uniform cooling. [28,168]. Among these, the Q67^{o} sample displayed the lowest maximum residual stress in the XZ plane, due to more uniform thermal conditions and a higher recrystallization fraction. However, the Q90^{o} sample showed unexpectedly high residual stress in the XZ plane. The reason for this can be explained as follows. The measured area for residual stress analysis is crucial for accuracy. The results may be affected if the focus is on overlapping regions rather than inside the islands. This is particularly relevant for intricate scanning patterns like the chessboard strategy. Also, it is important to consider that the collimator diameter directly influences XRD residual stress measurements, particularly for the chessboard scanning strategy. About eight small islands of the chessboard scanning strategy should be within the measured area to accurately observe the residual stress. However, in this study, a 2 mm collimator diameter was used, which does not allow for fitting eight different islands in the measured area. As a result, the measured residual stress in the chessboard scanning strategy can be affected by this limitation.

5.6 Conclusions

This study comprehensively examined the effects of various scanning strategies, including alternating bi-directional scanning with rotation angles of 0^{o}, 45^{o}, 67^{o}, and 90^{o} between adjacent layers, and alternating chessboard scanning with rotation angles of 67^{o} and 90^{o} between adjacent layers. The investigation focused on the relative density, formation of pores and cracks, surface roughness, microstructure, crystallographic texture, microhardness, and residual stress of IN939 fabricated by the PBF-LB process. Aiming to address the research gap, this study explores how different scanning strategies impact the material properties of IN939 fabricated by the PBF-LB. The main findings from the observed results are summarized as follows:

1) The 45^{o} and 67^{o} samples had the highest relative density at 99.3%, while Q90^{o} had the lowest at 99.05%. The 0^{o} and Q67^{o} samples showed the highest porosity at 0.27% and the largest pore sizes. Defect formation was highest in the XZ plane of the 0^{o} sample with bi-directional scanning and the Q67^{o} sample with chessboard scanning. The alternating bi-directional scanning strategy with 67^{o} rotation is optimal for achieving high relative density and small pore size.
2) Solidification, solid-state, and oxide-induced (Al_2O_3) cracks were observed in the as-built samples. The 0° sample had the most severe cracking, with cracks predominantly propagating along the BD in the XZ plane, especially near the edge, and some extending perpendicular to the BD. The 90° sample also showed long cracks in the XZ plane, particularly at the edge. In contrast, the 45° and 67° samples had fewer cracks.
3) The chessboard scanning strategy resulted in higher Sa and Sz values compared to the alternating bi-directional strategy, attributed to overlapping regions and increased spattering from small islands, regardless of rotation angles. Microhardness values across samples were similar, ranging from 321 ± 14 HV to 356 ± 7 HV.
4) The XZ planes of the 45^{o}, 67^{o}, 90^{o}, Q67^{o}, and Q90^{o} samples featured arc-shaped melt pools and columnar grains, while the 0° samples had directionally elongated grains and fine irregular grains. Distinct chessboard patterns appeared in the XY planes of the 67^{o}, 90^{o}, and Q90^{o} samples, with the 90^{o} sample being the most pronounced, whereas equiaxed grains were visible in the XY plane of the 45^{o} sample. The 0^{o} sample had the largest area-weighted average grain size in the XZ plane but smaller grains in the XY plane compared to the other samples, showing notable anisotropy between the planes.
5) The 0^{o} and 90^{o} samples exhibited a strong cube texture, with PF intensity values of 9.301 and 6.930, and IPF intensity values of 3.999 and 4.514, respectively. Additionally, the 45^{o}, 67^{o}, and Q90^{o} samples showed both <001> // BD and <101> // BD textures, with the Q90^{o} sample having the highest intensity values (6.243 for PFs and 2.238 for IPFs). Overall, the 0^{o} sample showed the most intense texture due to the alignment of the scan, heat flow, and growth directions, while the texture intensity weakened for the 45^{o} and 67^{o} samples.
6) Alternating bi-directional scanning strategies with 0^{o} and 90^{o} rotation angles created significant thermal gradients and uneven cooling, leading to high residual

stresses. The 0^o sample exhibited the highest σ_{max} residual stress in both the XZ (738.3 MPa) and XY (581.6 MPa) planes. In contrast, 45^o and 67^o rotation angles provided more uniform heat distribution and lower residual stresses. Among the alternating bi-directional scanning strategies, the 67^o sample achieved the lowest σ_{max} residual stress in both the XZ (542.6 MPa) and XY (443.9 MPa) planes due to better thermal uniformity and enhanced recrystallization. Although the island/chessboard strategy reduced temperature gradients, struggled with accuracy because of limitations with collimator diameter and overlapping regions. Overall, the XY plane of the $Q67^o$ sample achieved the lowest σ_{max} residual stress (408.4 MPa).

5.7 Contribution to Thesis Objectives

Scanning strategy is one of the significant PBF-LB process parameters for controlling defects such as pores and microcracks, as well as influencing microstructure and residual stress. After a thorough review of the existing literature, it was found that there was no systematic study regarding the scanning strategy effects on IN939. This chapter significantly addressed this gap by understanding the effects of scanning strategy on IN939 fabricated by the PBF-LB. Through a systematic examination of various scanning strategies, including bi-directional and chessboard patterns with different rotation angles, the study investigated their impact on relative density, defect formation, surface roughness, microstructure, crystallographic texture, microhardness, and residual stress of IN939. Key findings revealed that samples scanned at 45° and 67° exhibited the highest relative density, while those scanned at 0° and Q67° displayed the highest average porosity. Moreover, the 0° sample showed the most extensive cracking, while the 45° and 67° samples had fewer cracks, indicating the influence of scanning strategy on defect formation. Surface roughness was found to be influenced by scanning patterns, with chessboard scanning resulting in rougher surfaces, while microhardness values varied minimally among samples. Microstructural analysis revealed differences in grain size, morphology, and texture intensity among samples, providing insights into solidification behaviour and texture development. Additionally, significant variations in residual stress were noted among samples, with the 0° sample exhibiting the highest stress due to thermal gradients along the build direction. Overall, this research addressed critical gaps by comprehensively exploring the effects of laser scanning strategy on IN939 material properties, offering valuable guidance for optimizing scanning parameters in PBF-LB processes to improve component quality and performance.

5.8 Appendix B.

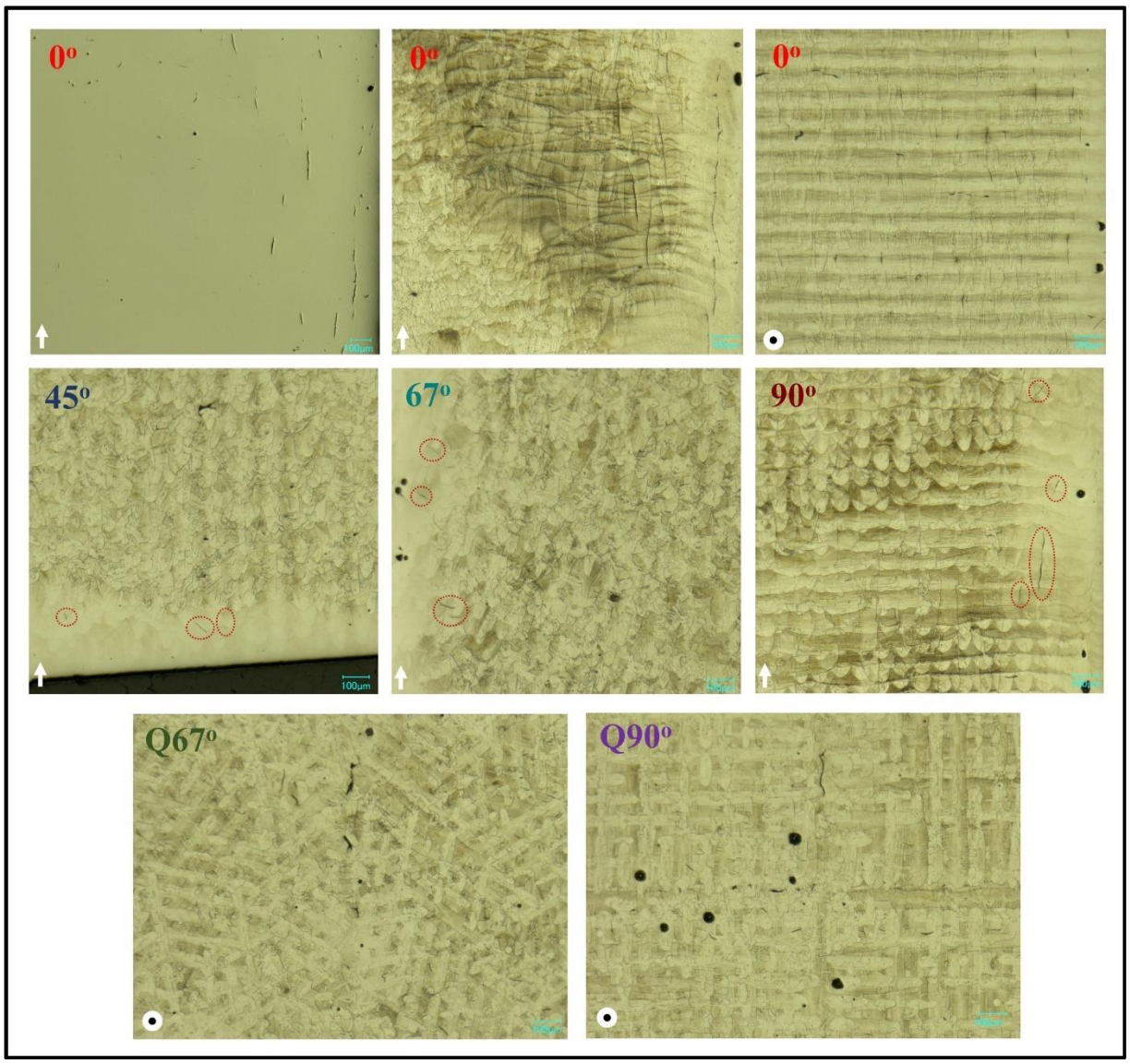

Figure 5B1 Optical micrographs of the crack distribution in the XY and XZ planes of the as-built samples: (a) 0º, (b) 45º, (c) 67º, (d) 90º, (e) Q67º, and (f) Q90º.

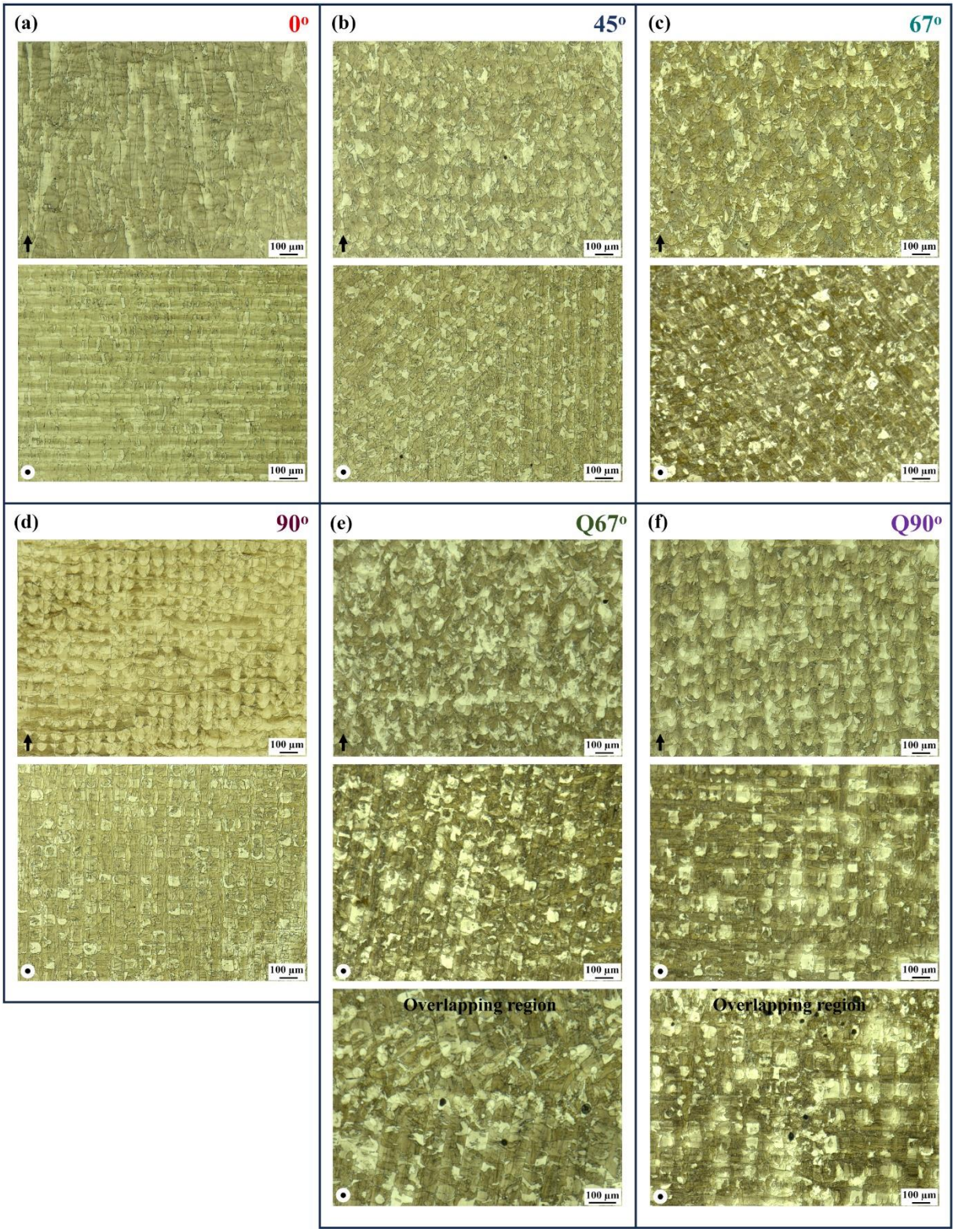

Figure 5B2 Optical micrographs of the as-built samples: (a) 0º, (b) 45º, (c) 67º, (d) 90º, (e) Q67º, and (f) Q90º.

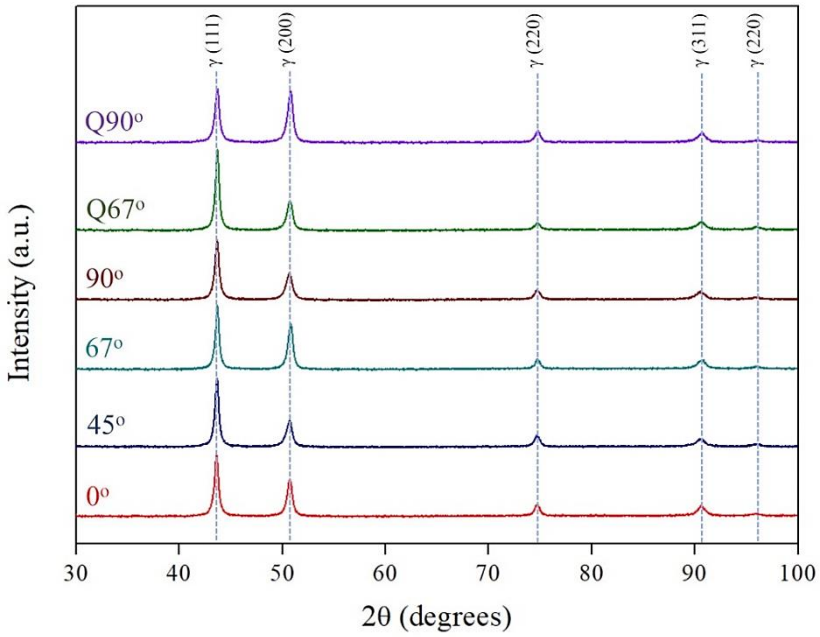

Figure 5B3 XRD pattern of the as-built samples.

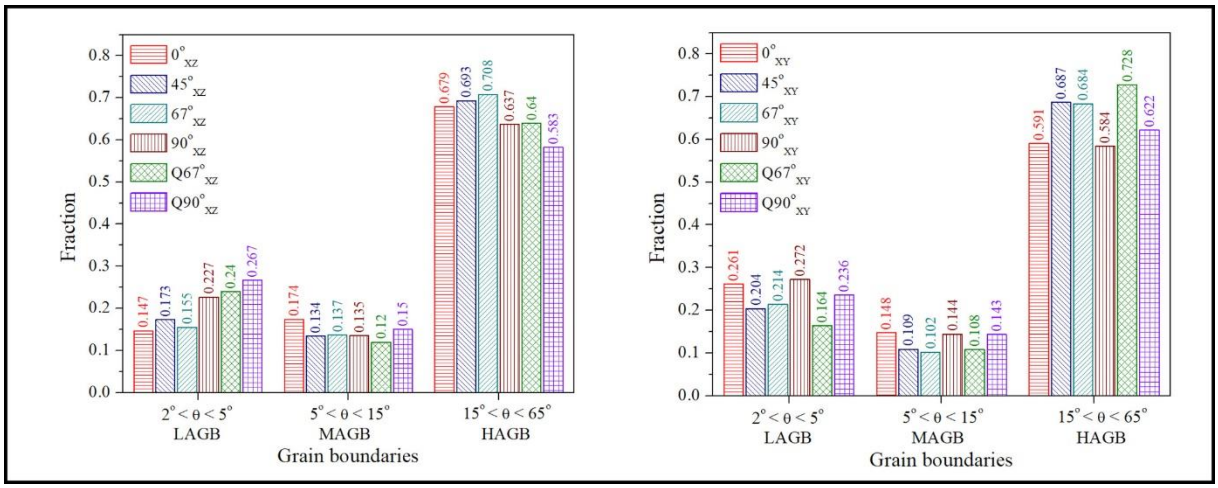

Figure 5B4 Grain boundary character distributions for both the XZ and XY planes of the as-built samples.

Here, low-angle grain boundaries (LAGBs) refer to the misorientation angle between 2° and 5°, medium angle grain boundaries (MAGBs) refer to the misorientation angle between 5° and 15°, and high-angle grain boundaries (HAGBs) correspond to grain boundaries with a misorientation angle higher than 15°. According to the literature, HAGBs, which act as repulsive boundaries, are more susceptible to cracking due to their high misorientation and associated energy. They are more readily wetted by liquid films at lower temperatures compared to LAGBs. This results in a wider temperature range for liquid film presence when the misorientation angle is higher [32,99,102].

Chapter 6: Effect of Solution Heat treatment on the Microstructure and Crystallographic Texture of IN939 Fabricated by Powder Bed Fusion-Laser Beam

Publication Status: Published

M.N. Doğu, S. Ozer, M.A. Yalçın, K. Davut, G.M. Bilgin, M.A. Obeidi, H. Brodin, H. Gu, D. Brabazon, **Effect of solution heat treatment on the microstructure and crystallographic texture of IN939 fabricated by powder bed fusion-laser beam**, Journal of Materials Research and Technology, 24 (2023).

https://doi.org/10.1016/j.jmrt.2023.05.152

6.1 Abstract

The effect of various solution heat treatment temperatures (i.e., 1120, 1160, 1200 and 1240 °C) on the microstructure, grain morphology and crystallographic texture of IN939 fabricated by powder bed fusion-laser beam (PBF-LB) was investigated. Microstructural analyses showed that the high-temperature gradient and rapid solidification of the PBF-LB processing caused different resulting microstructures compared to conventionally produced counterparts. The melt pool morphologies and laser scanning paths were examined in the as-fabricated samples in the XZ- and XY-planes, respectively. After the application of solution heat treatment at 1120 °C, the as-fabricated PBF-LB initial microstructure was still apparent. For solution heat treatments of 1200 °C and above, the melt pool and scanning path morphologies disappeared and converted into a mixture of columnar grains in the XZ-plane and equiaxed grains in the XY-plane. On the other hand, large equiaxed grains were observed when the samples were solutionized at 1240 °C for both observation directions, showing with this heat treatment a transition from microstructure anisotropy to isotropy. Additionally, spherical-like nano-sized γ' phase precipitated within the matrix after all solution heat treatment conditions, which led to increase in the microhardness values. According to electron backscatter diffraction (EBSD) analyses, both as-fabricated and solution heat-treated samples had intense texture with {001} plane normal parallel to the building direction. The first recrystallized grains began to appear when the samples were subjected to the solution heat treatment at 1160 °C and the fraction of the recrystallized grains increased with increasing temperature, as supported by kernel average misorientation (KAM) and grain spread orientation (GOS) analyses. Moreover, it was found that the fraction of low angle grain boundaries (LAGBs), the geometrically necessary dislocation (GND) density and the average grain size decreased with increasing solution heat treatment temperature.

6.2 Introduction

The production of aerospace components, which are mainly made from nickel-based superalloys, is often challenged by conventional manufacturing methods due to their intricate geometries, e.g., cooling channels in the turbine blade. Some undesired microstructural features including macro-segregation of alloying elements and uncontrolled grain growth may develop in the cast material due to the slow cooling rate [11,63]. In recent years, an alternative method called powder bed fusion-laser beam (PBF-LB), which is one of the well-known metal additive manufacturing (AM) techniques, has

received significant attention in various industries to produce components. The PBF-LB method utilizes a focused laser beam to melt the powders layer-by-layer based on a 3D computer-aided-design (CAD) model data [241]. This method provides an improvement in product quality by enabling the production of functional metallic components with complex geometries in a single step that eliminates assembly operations [242]. In contrast to the conventional manufacturing methods, it offers a wide range of advantages in terms of design freedom, net-near-shaping capability, increasing component life-time as well as reduction of material waste and tooling cost [211,243]. However, the high-temperature gradient and rapid solidification rate of the PBF-LB method may cause some process-induced defects in the microstructure of produced components. These defects can be described as the formation of topologically close-packed (TCP) phases, directional grain growth, segregation of elements, high residual stresses, formation of porosities and lack of fusion (LOF) and micro-cracks [244,245]. These micro-cracks can be divided into liquation/solidification cracks due to the formation of low melting phases on the grain boundaries and strain-age cracks due to residual stress from the gamma-prime phase development [4]. The effect of process parameters and post-processing heat treatments on the mechanical performance of nickel-based superalloys such as IN718 fabricated by the PBF-LB has recently been investigated [246]. However, its applications are limited to operating temperatures up to ~ 650 °C because of the coarsening of the grains [11] and the transformation of the strengthening γ" (Ni_3Nb) phase into the stable and brittle δ phase at higher temperatures, as reported in detail in our previous study [46]. On the other hand, Inconel 939 (IN939) is a promising candidate used for producing gas turbine engine components that require prolonged working periods at operating temperatures up to ~ 850 °C [11]. Nevertheless, there are only a few studies in the literature on the microstructure and mechanical properties of IN939 fabricated by additive manufacturing methods. IN939 is a precipitation-hardenable nickel-based superalloy, which is strengthened mainly by the formation of L12-ordered γ′ ($Ni_3(Al,Ti)$) precipitates in the γ matrix [11,247]. Nowadays, gas turbine blades/vanes, fuel nozzles, casing and other structural components are produced using the cast form of this alloy due to its remarkable properties such as good creep resistance and high-temperature strength combined with excellent oxidation and corrosion resistance [63,81,178]. Kanagarajah et al. [178] investigated the effect of the standard heat treatment (solutionizing at 1160 °C for 4 h followed by aging at 850 °C for 16 h) on the microstructure and mechanical behaviour of the IN939 produced by the PBF-LB. They reported that the as-produced samples showed higher tensile properties than the

cast material owing to its finer microstructure. However, the results obtained from high-temperature mechanical tests revealed that the samples exhibited lower tensile properties than the cast ones, suggesting that solution heat treatment should be adapted for materials produced by PBF-LB. Another study conducted by Philpott et al. [74] mainly focused on the effect of various heat treatments on the microstructure of the IN939 produced by PBF-LB, particularly the precipitation of the strengthening γ' phase and carbides.

It should be noted that the microstructure and the resulting properties of the materials produced by the PBF-LB method are quite different from their conventional counterparts. Therefore, the standard heat treatment applied to conventionally produced IN939 may not sufficiently improve the properties of materials produced with the PBF-LB. The typical heat treatment procedure for IN939 includes solution heat treatment followed by aging. Solution heat treatment is usually carried out above the γ' solvus temperature to obtain a homogeneous distribution of alloying elements throughout the solid solution. In addition, the dissolution of TCP phases is another issue that is significant for the aging step, which is effective in improving the mechanical properties [247]. The above-mentioned findings from the literature reveal that a detailed study of the microstructure, grain morphology and crystallographic texture on the as-fabricated and solution heat-treated parts is still missing. Furthermore, there are limited studies on the recrystallization phenomena and grain growth kinetics of the IN939 produced by the PBF-LB method. This study aims at closing this gap by studying the influence of solution heat treatment carried out at four different temperatures (1120, 1160, 1200 and 1240 °C) on the microstructure, recrystallization and texture of IN939 samples fabricated by the PBF-LB.

6.3 Materials and Methods

6.3.1 Starting Material

Gas-atomized IN939 powder (Truform 939-N65, Praxair Surface Technologies) was used as a starting material for the fabrication of the samples by the PBF-LB method. The chemical composition of the powder (as given in Table 6.1) delivered by the material supplier was also verified by the energy dispersive spectroscopy (EDS) analysis, using scanning electron microscope (SEM) (ZEISS Merlin® FE-SEM, Germany).

Table 6.1 Elemental composition of the starting gas-atomized IN939 powder.

Elements (wt.%)					
Al	**Co**	**Cr**	**Nb**	**Ta**	**Ti**
1.9	18.9	22.8	1.0	1.4	3.8
W	**B**	**C**	**O**	**N**	**Ni**
2.0	0.004	0.16	0.014	0.009	Bal.

As shown in Figure 6.1(a, b), the powder is mostly spherical, containing a few satellite particles which may form due to the rapid solidification associated with the gas atomization process or the recycling of the PBF-LB precursor powder [248]. A Malvern Mastersizer 3000 with an Aero S dispersion unit was used to measure the particle size distribution which was in the range of 17.6 (D_{10}) to 52.4 (D_{90}) µm with an average particle size of 30.2 µm (D_{50}). The cross-section of the powder particle (Figure 6.1(c)) revealed that the powder exhibited a dendritic microstructure including some small pores around 1-2 µm, especially near the surface of the particles. Additionally, the average grain size of the random-texturized particles was measured as 1.6 ± 0.4 µm, as can be seen in the inverse pole figure (IPF) map (Figure 6.1(d)). It should be noted that the morphology and average particle size of the powder are important parameters to enable good powder fluidity and packing within the PBF-LB process, in order to obtain fully dense components and related good mechanical properties.

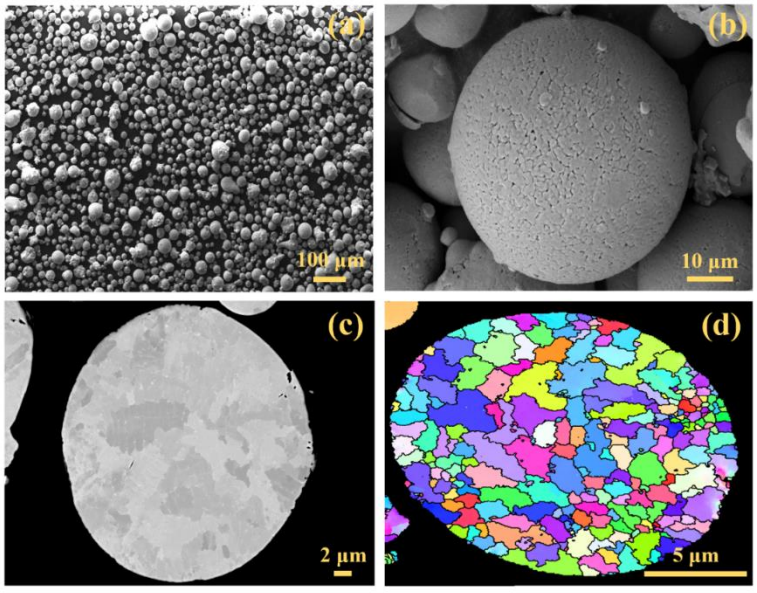

Figure 6.1 Gas-atomized IN939 powder utilized for the PBF-LB processing: (a, b) SEM images, (c) SEM-BSE image of a cross-section of a particle showing a dendritic microstructure and (d) the IPF map of the cross-section of a particle.

6.3.2 Fabrication of IN939 with the PBF-LB Method

IN939 cubic samples (10×10×10 mm^3), as shown in Figure 6.2, were fabricated under a protective argon atmosphere using Aconity MINI (GmbH) metal 3D printer equipped with a 200 W fiber laser manufactured by IPG Photonics with a wavelength of 1068 nm. Process parameters used for the fabrication of the samples are given in Table 6.2. During the processing, a supply factor of 3 was used to provide enough powder to build area for each layer. In addition, the volumetric energy density, VED (J/mm^3) was calculated as 104.2 J/mm^3 by taking the laser power, P (W), laser speed, υ (mm/s), layer thickness, t (mm) and hatch spacing, h (mm) into account using the following equation.

$$VED = \frac{P}{\upsilon.t.h} \tag{6.1}$$

Table 6.2 PBF-LB process parameters utilized in the present study.

Laser power	Laser scan speed	Layer thickness	Hatch spacing	Hatch rotation
200 W	800 mm/s	0.04 mm	0.06 mm	67˚

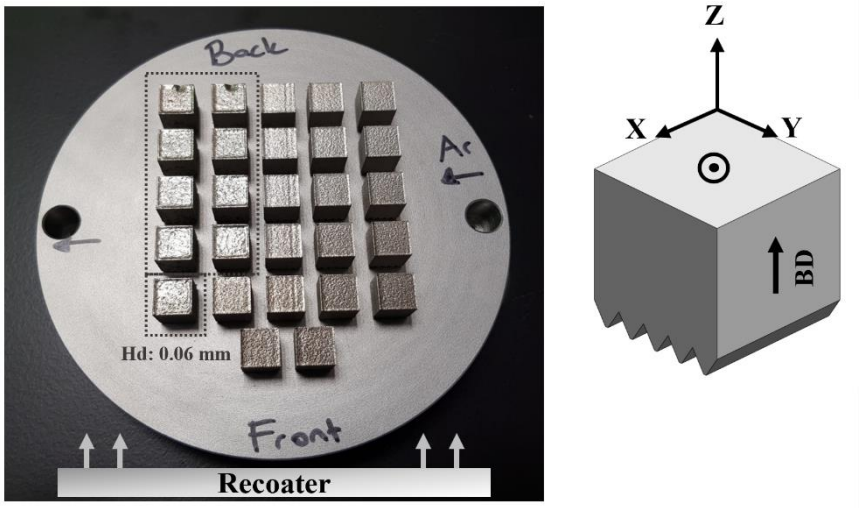

Figure 6.2 Picture of the PBF-LB built samples and schematics of the observation directions used for microstructural examinations (BD: build direction).

6.3.3 Solution Heat Treatment Procedure

To investigate the effect of the underlying microstructure on the crystallographic texture, some of the as-fabricated samples were subjected to solution heat treatment at 1120, 1160, 1200 and 1240 °C for 4h, followed by air-cooling to room temperature. Those samples are named as "SHT" followed by the solutionizing temperature, e.g., SHT1120.

6.3.4 Microstructural Characterization

Microstructural observations of the samples were carried out using both an optical microscope (Nikon Eclipse LV150) and SEM operated at 20 kV accelerating voltage. For the metallographic examination, IN939 cubic samples were sectioned by a precision abrasive cutter (Buehler IsoMet 5000) to investigate both observation directions, i.e., parallel to the building direction and perpendicular to the building direction, attributed to XZ-plane and XY-plane, respectively. Before the analyses, the surfaces of the samples were prepared using standard metallographic methods (i.e., ground with SiC emery papers up to 2500 grit size and polished with progressively finer diamond suspensions (first 6 μm and then 1 μm)), then cleaned with deionized water and ethanol, and subsequently etched using Glyceregia reagent (15 ml HCl, 10 ml glycerol and 5 ml HNO_3) for 50 to 60 seconds. In addition, at least five EDS analyses were performed to obtain the average atomic and/or weight percentages of the elements for accurately compositional analyses.

Electron back-scatter diffraction (EBSD) technique was carried out to examine the microstructural details including grain structure, misorientation and crystallographic texture of both as-fabricated and solution heat-treated samples. Unlike the previous preparation methods, samples were polished with a colloidal silica suspension using the oxide polishing suspension (OP-S) (Struers Inc., Denmark) after grinding and polishing steps. For analyses, a Zeiss Merlin field emission gun (FEG) scanning electron microscope (SEM) equipped with EDAX/TSL EBSD system and a Hikari EBSD camera were utilized with an accelerating voltage of 15 kV, beam current of 6.0 nA and a working distance of 14 mm; the mapping areas of 500 x 500 μm were indexed on a hexagonal grid with a step size of 1 μm. Raw EBSD data was processed using TSL-OIM Analysis v7.3.1 software. Additionally, texture analyses were performed using the generalized spherical harmonic series expansion method of Bunge [188]. The harmonic series were expanded to a rank (L) of 34, and a Gaussian smoothing with a half-width of 5° was used.

6.3.5 Microhardness Tests

Vickers microhardness tests were performed on the polished surfaces of the as-fabricated and solution heat-treated samples using a Zwick/Roell Zhu microhardness tester 2.5 with a load of 1 kg (denoted as HV1) and loading time of 20 s. The microhardness measurements were taken from at least 10 different points on each observation plane (i.e., XZ- and XY-planes) to obtain the average values of each sample.

6.4 Results

6.4.1 Microstructural Analyses of the As-Fabricated and Solution Heat-Treated IN939 Samples

The relative density of the as-fabricated sample was measured to be ca. 99.4% by Archimedes' method using an analytical balance (Sartorius Entris II Essential BCE124I-1S) having accuracy and repeatability of ± 0.1 mg according to ASTM B962-13 [187]. Figure 6.3 exhibits gas pores and some LOF regions (seen as black colored defects) in the PBF-LB as-fabricated and solution heat-treated samples. These defects generally form in nickel-based superalloys during the PBF-LB processing due to some reasons that will be further explained in the discussion section. Additionally, the relative density after solution heat-treatment as measured to the same level as in the as-fabricated material condition.

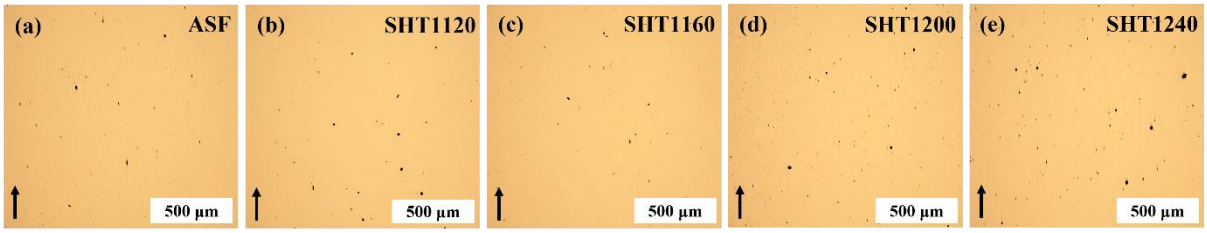

Figure 6.3 As-polished micrographs of the as-fabricated and solution heat-treated IN939 samples in the XZ-plane: (a) as-fabricated (ASF), (b) SHT1120, (c) SHT1160, (d) SHT1200 and (e) SHT1240 (the arrow represents the building direction).

Figure 6.4 shows optical microscope and SEM images of the as-fabricated IN939 sample for both observation directions. An arc-shaped melt pool morphology was observed in the XZ-plane (Figure 6.4(a, c)) which was formed due to the Gaussian energy distribution of the laser beam which is applied during the PBF-LB process [245]. Whereas the laser beam scanning paths were observed in the XY-plane (Figure 6.4(b, d))**.** Similar morphologies have been reported as typical characteristic microstructures found in additively manufactured parts in many studies [11,249]. It should be noted that the physical and mechanical properties of as-fabricated parts are highly dependent on the geometry of the melt pool morphology (i.e., shape, width and depth) influenced by the thermal history of the PBF-LB method. High magnification SEM image (Figure 6.4(e)) showed that some cellular structures with sizes of ~ 0.5 µm and columnar dendrites with an average dendrite arm spacing of ~ 0.7 µm occurred within the structure.

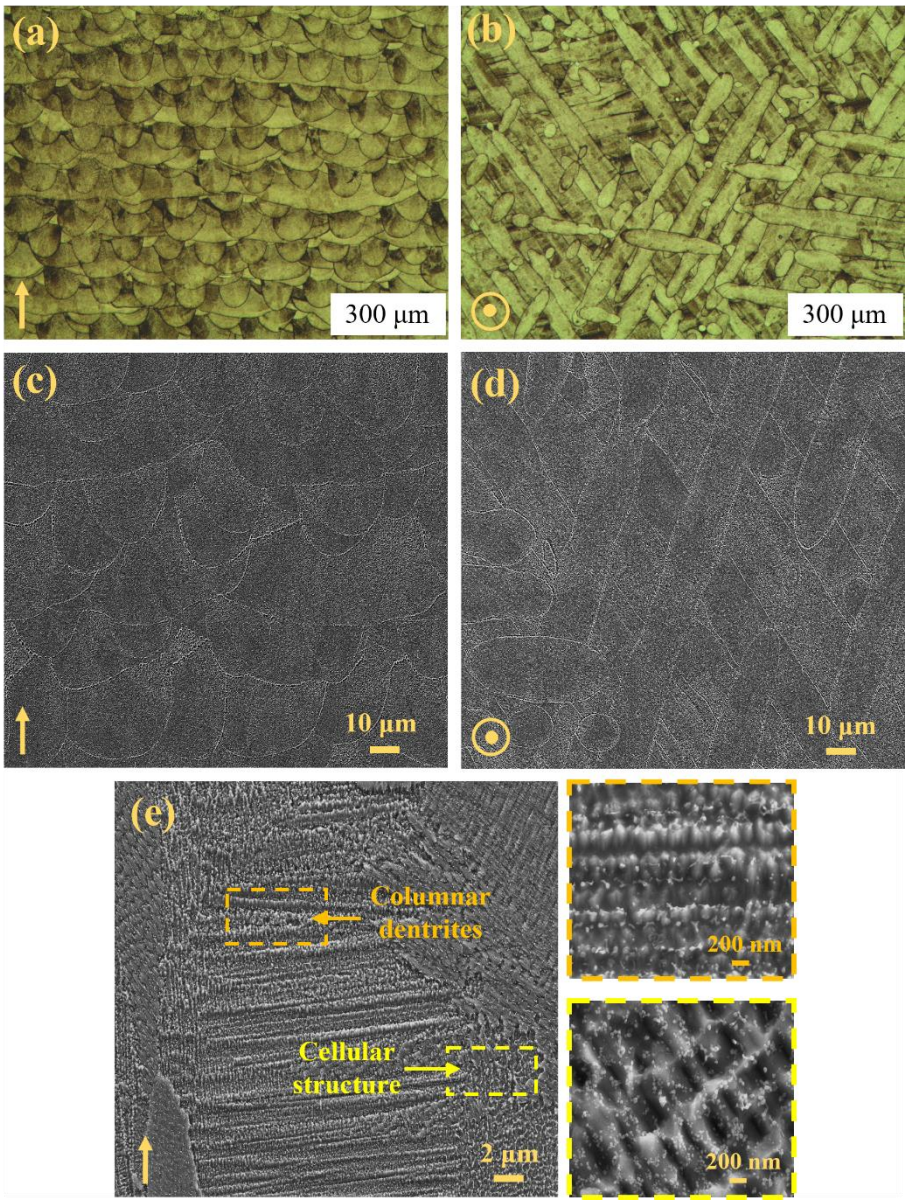

Figure 6.4 Optical microscope and SEM images of the as-fabricated IN939 sample: (a, c) the melt pool morphology in the XZ-plane, (b, d) the laser beam scanning paths in the XY-plane (XZ- and XY- planes are shown with an arrow and a dot, respectively) and (e) the high magnification image showing the cellular and columnar structures developed within the matrix.

Figure 6.5 shows the optical images of the solution heat-treated samples in both observation directions. It can be seen in Figure 6.5(a, b), the melt pool and scanning paths observed in the as-fabricated sample were still presented for the SHT1120 sample which means the solution temperature was insufficient to dissolve the initial microstructure. With increasing solution heat treatment temperature up to 1200 °C, the melt pool and scanning path morphologies disappeared and converted into a mixture of columnar grains in the XZ-plane and equiaxed grains in the XY-plane. On the other hand, large equiaxed grains were

observed in the SHT1240 sample for both observation directions which indicates most of the grains started to grow after recrystallization. A more detailed examination of the microstructure results is given in the texture analysis section.

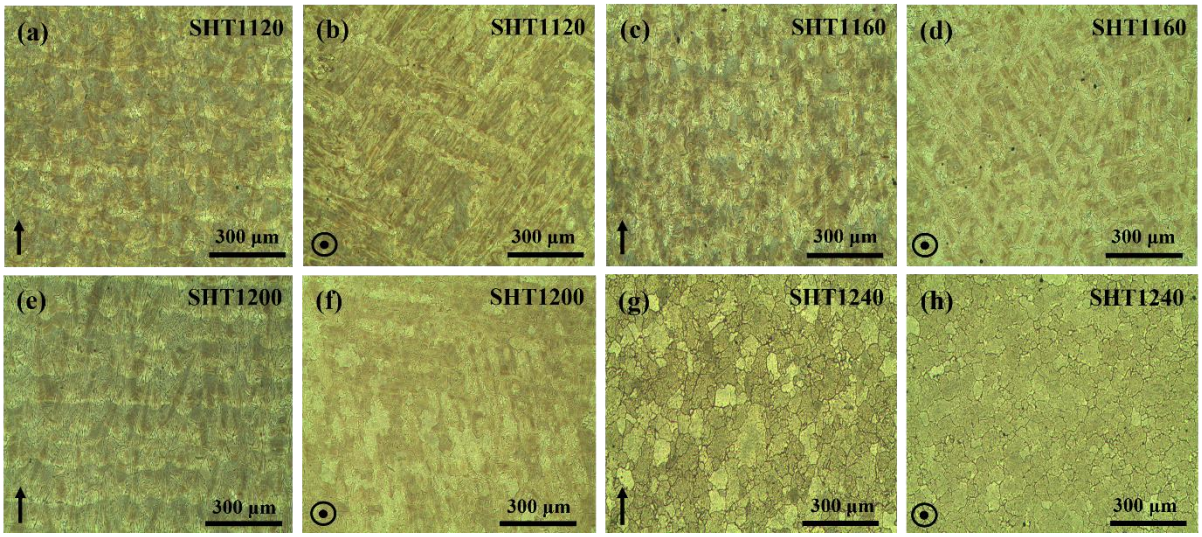

Figure 6.5 Optical microscope images of the solution heat-treated samples: (a, b) SHT1120, (c, d) SHT1160, (e, f) SHT1200 and (g, h) SHT1240 in the XZ- and XY-planes, respectively.

Further investigations revealed that many undissolved white particles with an average size of ~ 0.5 µm were observed in the grains, particularly along the grain boundaries, as given in Figure 6.6(a-h). The low diffusion rate of the large elements makes the dissolution of this type of particles difficult as also stated by Komarasamy et al. [243]. Moreover, a large number of spherical-like nano-sized precipitates corresponding to γ′ phase homogeneously distributed in the matrix was observed, as can be seen in higher magnification SEM micrographs in Figure 6.6(a1, c1, e1, g1). This observation is also in agreement with the study conducted by Shaikh AS [4]. According to the results obtained from Image J analyses, the size of γ′ phase was measured as 35 ± 12 nm, 56 ± 11 nm, 49 ± 9 nm and 40 ± 7 nm for the SHT1120, SHT1160, SHT1200 and SHT1240 samples, respectively. Additionally, plate-like phases were not observed during the SEM analyses. For this reason, it can be said that no significant η-phase was presented in the microstructures. According to EDS analyses given in Figure 6.7 and Table 6.3, some irregular-shaped MC type (rich in Ti, Nb and Ta) carbides were observed at the grain boundaries and also grain interior (Spot 1 and 2). Note that the accuracy of W detection in EDS analyses is limited due to the overlapping of W and Ta peaks and the minor alloying of this element in IN939.

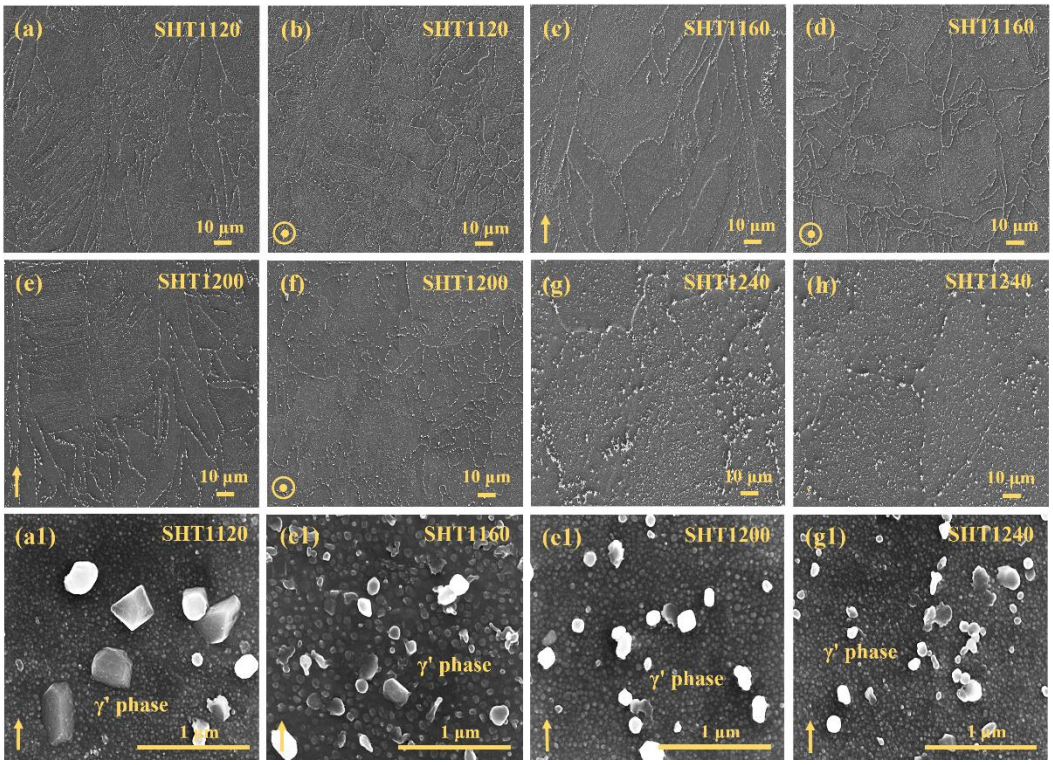

Figure 6.6 SEM images of the solution heat-treated samples: (a, b) SHT1120, (c, d) SHT1160, (e, f) SHT1200 and (g, h) SHT1240 in the XZ- and XY-planes, respectively, and (a1, c1, e1, g1) magnified images of the solution heat-treated samples, showing γ' phases along with MC-type carbides.

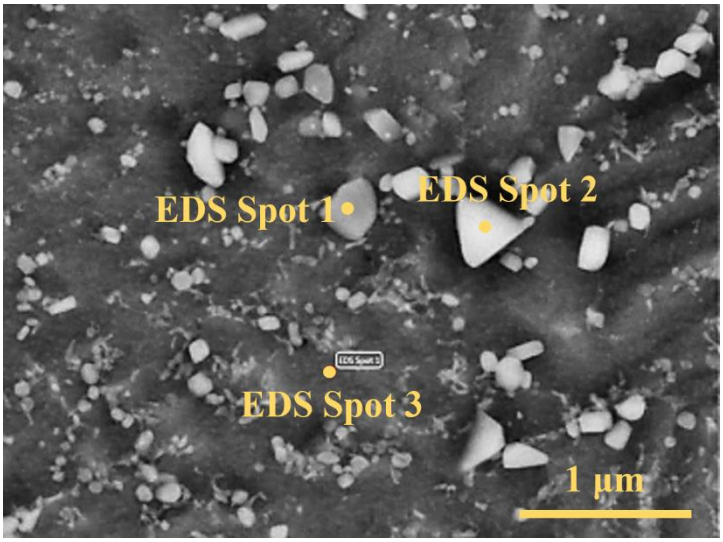

Figure 6.7 SEM image of the SHT1160-treated sample showing the MC type carbides.

Table 6.3 EDS analyses of the MC-type carbides formed in the IN939 matrix.

	Elements (wt.%)								
EDS spot	**Ni**	**Co**	**Cr**	**Ti**	**Nb**	**W**	**Ta**	**Al**	**C**
1	32.86	12.96	17.61	11.46	4.01	1.27	8.49	1.24	10.01
2	15.06	5.78	8.78	20.54	10.06	1.58	18.96	1.11	17.57
3	48.25	18.6	22.63	3.88	0.34	1.18	0.48	1.47	3.18

6.4.2 Texture Analysis of the As-Fabricated and Solution Heat-Treated IN939 Samples

From PBF-LB processing, the grain structure and crystallographic texture vary along building and scanning directions, resulting in microstructure anisotropy. Detailed EBSD analyses were performed on the IN939 samples to investigate microstructure and texture. The grain structure of the samples can be clearly seen in the inverse pole figure (IPF) and image quality & grain boundaries (IQ & GBs) maps for both XZ- and XY-planes, as given in Figure 6.8 and Figure 6.9. The as-fabricated sample showed a microstructure composed of columnar elongated grains along the build direction (in the XZ-plane). In contrast, equiaxed grains were present in the XY-plane. Additionally, the area-weighted average grain size of the as-fabricated sample was measured as 10.8 μm in the XZ-plane and 21.3 μm in the XY-plane. It has been reported that the rapid solidification of the melt pools during the PBF-LB processing causes the formation of finer microstructures compared to conventional manufacturing methods along with the improvement of mechanical performance of the alloys [250]. For the SHT1120, SHT1160 and SHT1200 samples, the elongated columnar grains in the XZ-plane and equiaxed grains in the XY-plane were still observed, similar to the as-fabricated one. Unlike the other samples, large equiaxed grains were observed in the SHT1240 sample for both observation directions. Thus, it can be revealed that the columnar grain structure was almost completely replaced by equiaxed grains when the sample was solutionized at 1240 °C. Furthermore, the average grain size of the samples increased with increasing solution heat treatment temperature, as can be seen in Figure 6.11 and Table 6.4.

Pole figures (PFs) of the samples were obtained from the corresponding EBSD data to estimate the crystallographic orientations, as given in Figure 6.10. Note that only the corresponding {001} PF and IPF with respect to building direction were represented for

the texture analyses. As can be seen, the {001}// BD texture component was dominant, for both as-fabricated and solution heat-treated samples. The maximum intensity values of the as-fabricated sample were determined as 2.875 for IPFs and 2.989 for PFs. When we compare the solution heat-treated samples among themselves, the maximum intensity values of IPFs and PFs increased with increasing solution heat treatment temperature.

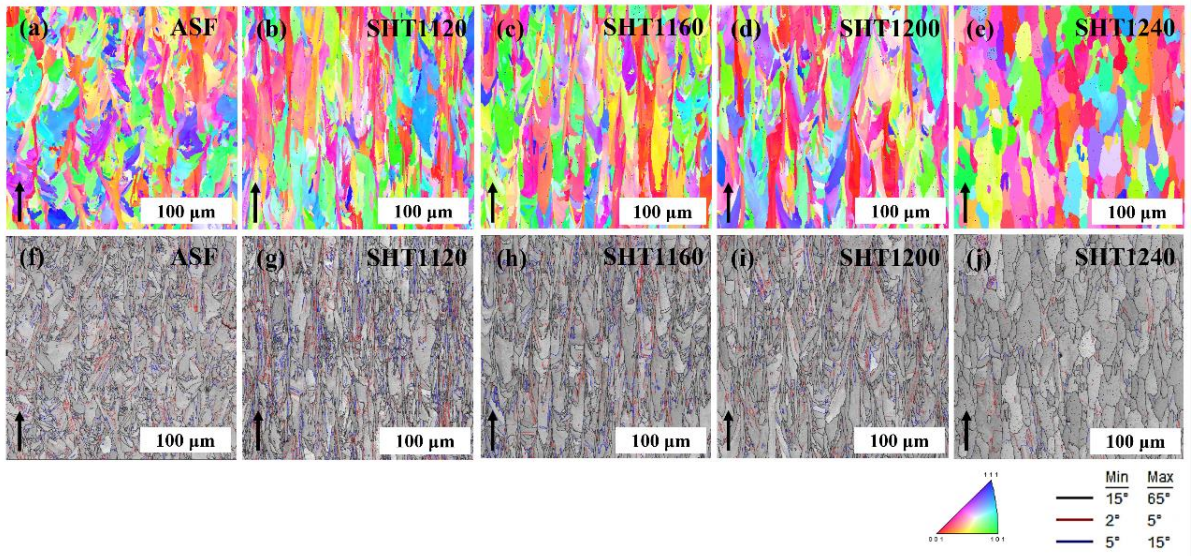

Figure 6.8 (a-e) IPF and (f-j) IQ-GBs maps of the as-fabricated and solution heat-treated IN939 samples in the XZ-plane.

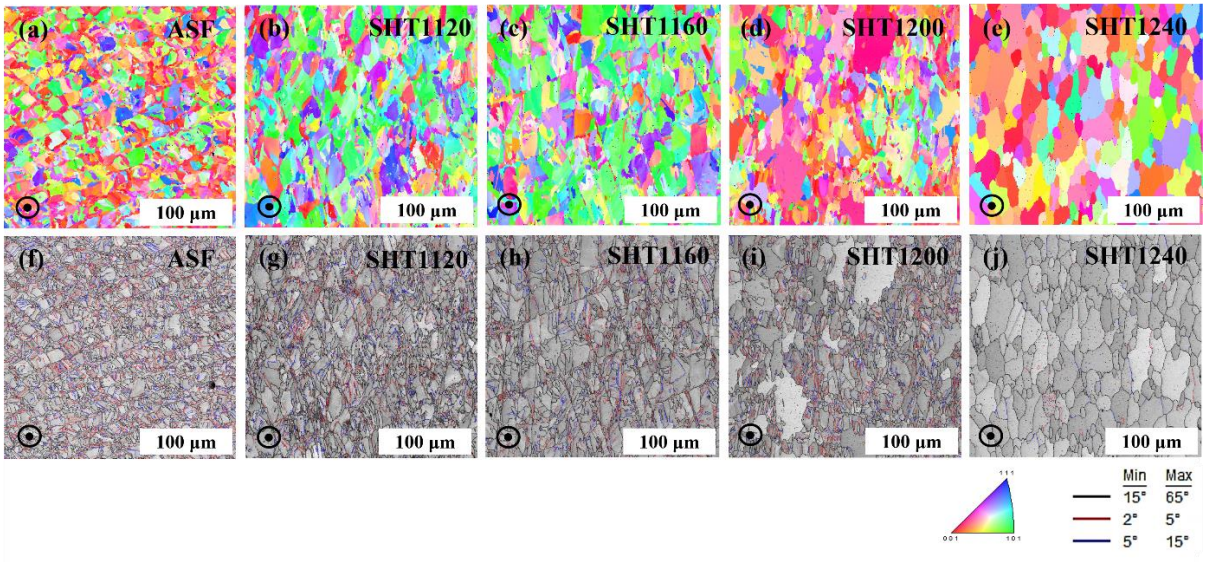

Figure 6.9 (a-e) IPF and (f-j) IQ-GBs maps of the as-fabricated and solution heat-treated IN939 samples in the XY-plane.

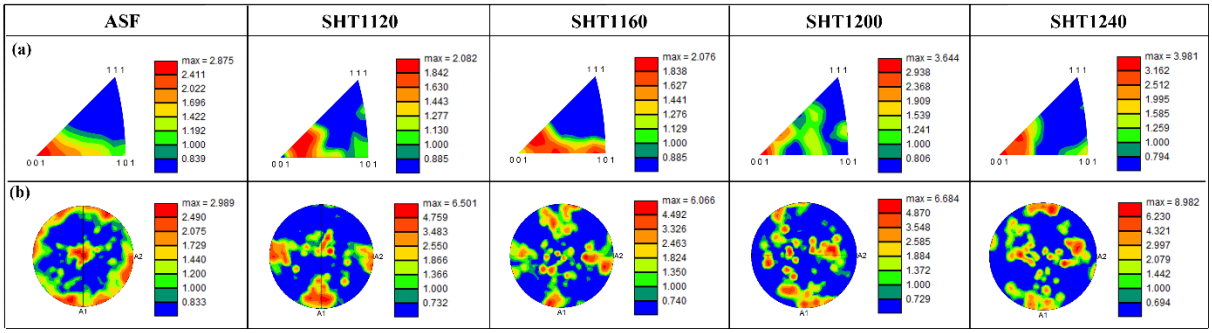

Figure 6.10 IPF and PF maps of the as-fabricated and solution heat-treated IN939 samples in the XZ-plane.

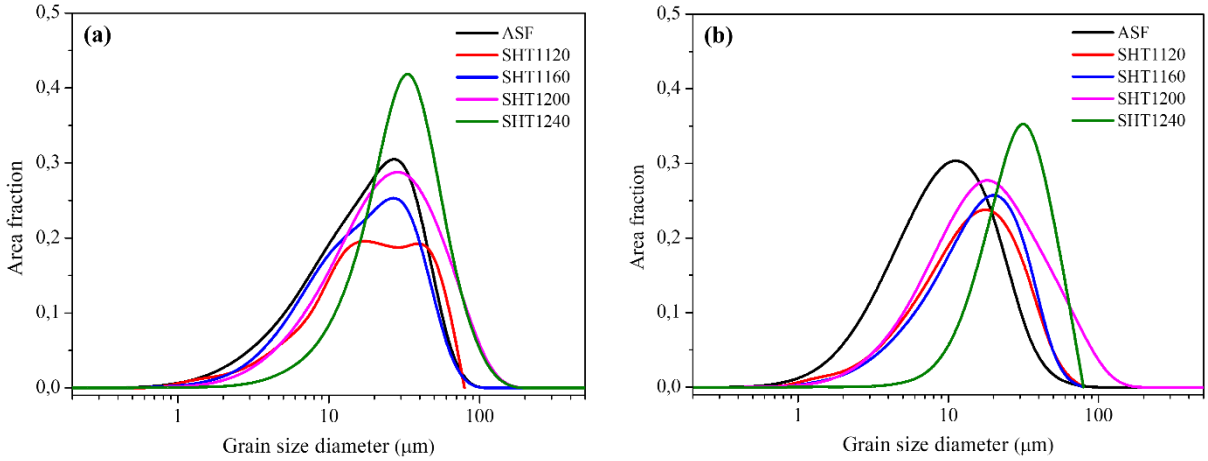

Figure 6.11 Grain size distributions of the as-fabricated and solution heat-treated IN939 samples for both observation directions: (a) in the XZ-plane, and (b) in the XY-plane.

Table 6.4 Average grain size diameter of the as-fabricated and solution heat-treated IN939 samples.

Observation direction	The area-weighted average grain size diameter (μm)				
	ASF	SHT1120	SHT1160	SHT1200	SHT1240
XZ-plane	10.8 ± 1.1	16.6 ± 1.2	17.7 ± 2.3	23.5 ± 3.8	31.1 ± 5.3
XY-plane	21.3 ± 4.6	24.4 ± 3.3	25.9 ± 3.1	28.7 ± 3.5	33.8 ± 4.8

The kernel average misorientation (KAM) and grain orientation spread (GOS) maps of the as-fabricated and solution heat-treated samples were displayed in Figure 6.12(a-e) and Figure 6.12(f-j), respectively. KAM is examined to estimate the local misorientations, which is also related to dislocation density. In other words, a large KAM value represents a higher defect (e.g., dislocation) density. As can be seen in Figure 6.12(a), the rapid solidification rate of the PBF-LB processing causes local strain inhomogeneity,

accordingly formation of high dislocation density in the as-fabricated sample. In the SHT1120 sample (Figure 6.12(b)), there was no significant difference when compared to the as-fabricated one, possibly due to the similar microstructure present in the samples. However, the dislocation density was decreased with increasing solution heat treatment temperature, as expected (Figure 6.12(c-e)). Grain orientation spread (GOS) maps shown in Figure 6.12(f-j) represent grain based local misorientations. For GOS calculations first the average orientation of a grain is calculated. Then the misorientation between this average and the orientation of each individual measurement point within the grain is calculated. Lastly, the average of these misorientations is calculated and assigned to each point within the grain. Fully recrystallized grains have very low GOS values, whereas high defect density and deformation increases GOS. As shown in Figure 6.12(h), the first recrystallized grains were observed when the samples were solution heat treated at 1160 °C. Also, increasing the solution heat treatment temperature caused an increase in the recrystallization fraction.

For better quantification, the distributions of KAM and GOS maps in the as-fabricated and solution heat-treated samples are also given in Figure 6.13. The KAM distributions of both as-fabricated and solution heat-treated samples exhibited a single peak (Figure 6.13(a)). The as-fabricated and SHT1120 samples had a close peak value of around 0.64 and 0.68 degrees, respectively. Whereas the other solution heat-treated samples had lower peak values of around 0.52 for the SHT1160 and SHT1200 samples and 0.41 for the SHT1240 sample. The decrease in dislocation density after solution heat treatments caused a decrease in KAM values. It is known that the GOS distributions are highly affected by the changes in the grain structure and the characteristics of the phases formed in the structure. In our cases, the smaller grains' orientation spread is lower than those of larger grains, especially for the SHT1240 sample (as given in Figure 6.13(b)). Similar to the KAM values, the GOS values of the as-fabricated and SHT1120 samples were also close to each other and were determined as 1.98 and 1.92, respectively. However, with increasing solution heat treatment temperature, the value decreased to 1.74 for SHT1160, 1.56 for SHT1200 and 0.44 for SHT1240 due to the recrystallization of the grains.

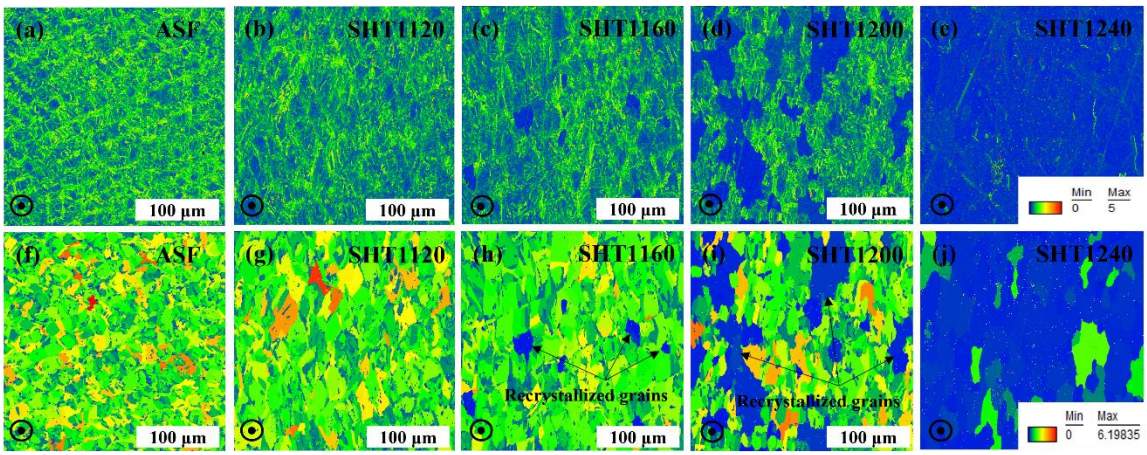

Figure 6.12 (a-e) KAM and (f-j) GOS maps of the as-fabricated and solution heat-treated IN939 samples in the XY-plane.

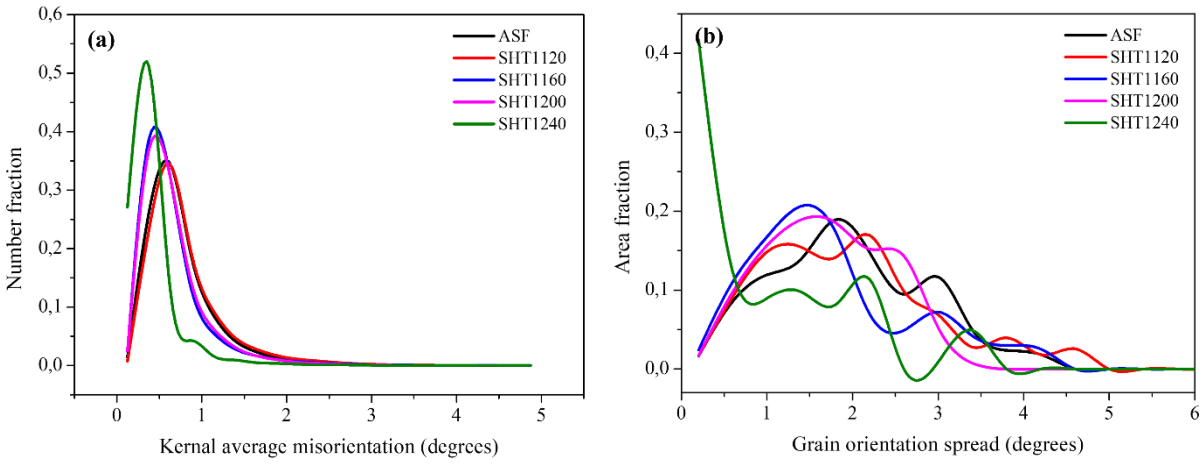

Figure 6.13 (a) KAM and (b) GOS distributions of the as-fabricated and solution heat-treated IN939 samples in the XY-plane.

The dislocation density in metallic materials includes geometrically necessary dislocations (GND) and statistically stored dislocations. It is reported that GNDs account for most dislocations in FCC cubic metals [193], thus GND density (Figure 6.14(a)) obtained from the EBSD analyses can be used to estimate the effect of the production with PBF-LB as well as the effect of solution heat treatment on the dislocation density. The average GND density of the as-fabricated sample was determined as $36.4 \cdot 10^{12}$ m/m^3 which was close to the SHT1120 samples with an average of $35.3 \cdot 10^{12}$ m/m^3. With increasing solution heat treatment temperature, the value decreased to $28.7 \cdot 10^{12}$ m/m^3 for SHT1160, $25.9 \cdot 10^{12}$ m/m^3 for SHT1200, and $10.9 \cdot 10^{12}$ m/m^3 for SHT1240 samples, probably due to the recrystallization of the grains. Furthermore, the misorientation angle distributions are given in Figure 6.14(b). The light green line represents the Mackenzie distribution for

completely random oriented cubic crystals. As expected, the misorientation distribution of the as-fabricated sample exhibited the predominance of low-angle grain boundaries (<10°), implying that the grains were composed of substructure and dislocations, as also observed in the high-magnification SEM images (Figure 6.4(e)). When the samples subjected to the solution heat treatment, the misorientation distribution within the grains exceeded 15° and even approached the Mackenzie distribution for the SHT1240 sample. This indicates randomization of the crystallographic texture during the heat treatment.

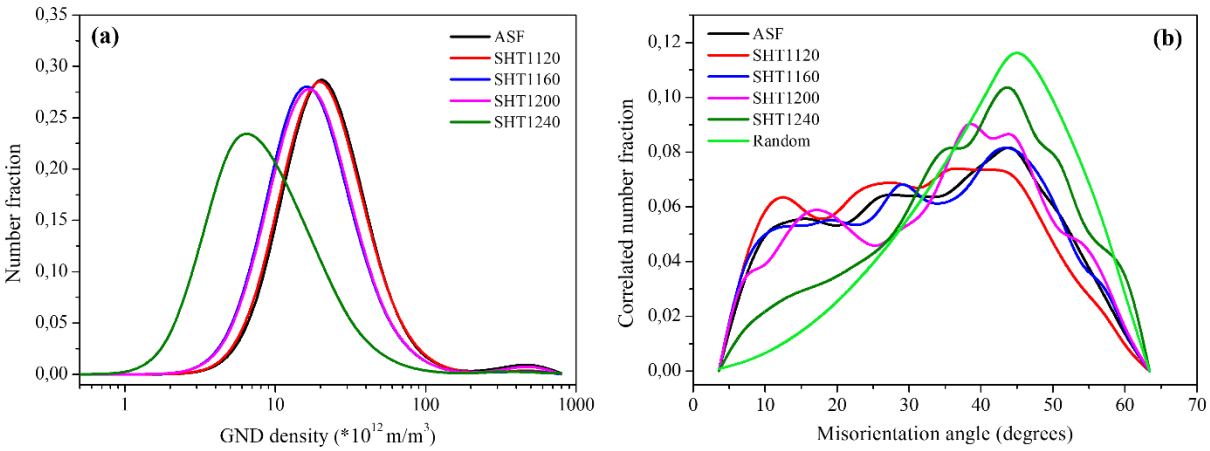

Figure 6.14 GND and (b) misorientation angle distributions of the as-fabricated and solution heat-treated IN939 samples in the XY-plane.

6.4.3 Microhardness Measurements of the As-Fabricated and Solution Heat-Treated IN939 Samples

The average Vickers microhardness values of the samples in as-fabricated and solution heat-treated conditions are tabulated in Table 6.5. The hardness measurements were conducted on both observation planes. As can be seen in Table 6.5, the hardness value of the as-fabricated sample increased with the application of solution heat treatment. As mentioned previously (Figure 6.6), spherical-like γ' phase was observed for all of the solution heat treatment temperatures. The peak hardness values were observed as 531 ± 17 HV and 503 ± 14 HV for XZ- and XY-planes, respectively, when the samples were subjected to solution heat treatment at 1120 °C. On the other hand, the hardness values decreased with increasing solution heat treatment temperatures, which can be attributed to the increase in the average grain size (Figure 6.11and Table 6.4) and decrease in the GND density values (Figure 6.14(a)). The reduction of GND density can be attributed to recrystallization phenomena, as clearly shown in the GOS maps (Figure 6.12(f-j)), and this is also another reason for the reduction in the hardness values.

Table 6.5 Average Vickers microhardness values of the as-fabricated and solution heat-treated IN939 samples.

Observation direction	Hardness (HV1)				
	ASF	**SHT1120**	**SHT1160**	**SHT1200**	**SHT1240**
XZ-plane	358 ± 12	531 ± 17	446 ± 19	463 ± 43	448 ± 45
XY-plane	380 ± 10	503 ± 14	435 ± 24	466 ± 27	445 ± 21

6.5 Discussion

6.5.1 Microstructural Evolution of the As-Fabricated and Solution Heat-Treated IN939 Samples

The analyses did not reveal any significant differences in the relative densities of the IN939 samples. For both as-fabricated and solution heat-treated samples, only some lack of fusion regions and gas pores were detected; other than that, no cracks were found in the structure, as given in Figure 6.3. Such defects can occur because some of the powders that are greater than the layer thickness may lead to insufficient melting during the PBF-LB processing and result in lack-of-fusion regions in the structure. In this work, the layer thickness was set at 0.04 mm and the range of powder particle size was 17.6 to 52.6 μm. On the other hand, gas pores may form due to the trapping of gases dissolved in the molten metal or released from the starting powder in the molten pools [219]. It is known that the process parameters (i.e., scanning strategy, laser power and speed, hatch distance and layer thickness and etc.) of the PBF-LB method strongly influence the physical properties of the produced components [251]. Since other precipitation-hardenable nickel-based superalloys such as IN718 have been studied for a long time, there are many studies in the literature on process parameter optimization, heat treatment and even alloying addition for these materials. Despite the few studies on IN939, there are many shortcomings that need to be worked on. The process parameters used in our study can contribute to the studies on production optimization since micro or macro cracks were not observed in the materials. Note that the hot isostatic pressing (HIP) process is one of the effective methods used to eliminate process-induced defects in the nickel-based superalloys. Rezaei et al. [252] studied the effect of the HIP process on the as-produced and standard heat-treated IN718 alloy in terms of relative density, microstructure, and room- and high-temperature mechanical behaviours. They reported that the relative density of the as-produced sample

was increased from 99.50 % to 99.96 % due to the elimination of the intrinsic porosities and large contour defects observed near the surfaces. They also found that the anisotropy in mechanical properties and microstructure were highly enhanced after HIP process.

The grain morphology (i.e., planar, cellular structure and columnar dendrites) of the samples fabricated with additive manufacturing methods is mainly dependent on the ratio of the thermal gradient (G) to the solidification rate (R) which is described as the G/R ratio [44,253]. Columnar and cellular structures formed in the melt pool morphology and laser scanning paths detected in the XZ and XY-planes, respectively, can be developed in produced parts, as shown in Figure 6.4. Further investigation revealed that the size of the columnar grains was larger than the melt pools (Figure 6.8(a and f)), and some overlapping regions were observed, particularly in the XZ-plane (Figure 6.4(a)). The occurrence of this type of morphology can be attributed to the remelting of previously solidified layers due to the thermal gradient, which provides a strong bonding between successively deposited layers and results in better mechanical properties [205]. After the solution heat treatments, the microstructure composed of columnar elongated grains in the XZ-plane and equiaxed grains in the XY-plane were observed for the SHT1120, SHT1160 and SHT1200 samples (Figure 6.8 and Figure 6.9). The main difference between solution heat-treated samples is that the average grain size of the samples increased with increasing solution heat treatment temperature. On the other hand, equiaxed grains with an average size of 32 μm were observed in the SHT1240 sample for both observation directions. This grain morphology contributes to microstructural anisotropy, which is then reduced significantly when the solution heat treatment was applied at 1240 °C (Figure 6.11 and Table 6.4).

As mentioned earlier, segregation of certain elements is one of the limitations of the PBF-LB processing which results in the formation of various brittle TCP phases such as the η (eta) phase as well as some MC and $M_{23}C_6$ type (i.e., Ti-, Ta-, Nb- and/or Cr-, W-rich, respectively) carbides. It is mostly reported that these phases negatively influence the mechanical properties of the alloys because they act as nucleation sites for crack formation [254]. However, it also should be noted that the effect of carbides on tensile properties is strongly dependent on the characteristics, including morphology, size, amount and distribution of them [255]. As given in Figure 6.7 and Table 6.3, some irregular-shaped MC type carbides enriched with Ti, Nb and Ta elements were found at the grain boundaries and inside the grains for all conditions. The average size of the carbides was measured to be ~ 0.7 μm, which is smaller than that found in conventionally manufactured counterparts.

The slow cooling rate of conventional manufacturing methods results in the formation of larger block-shaped carbides in the structure [253]. Moreover, the EDS results obtained from EDS spot 1 (see Figure 6.7 and Table 6.3) indicated the concentrations of C, Ta, Ti and Nb elements in that MC carbide were considerably lower than for the MC carbide at EDS spot 2. Conversely, Ni, Cr and Co concentrations increased. In the literature, it is mentioned that there are two different transformations related to this, as given below. The first is attributed to the precipitation of the brittle η phase (Ni_3(Ti, Ta, Nb, Al)) and the second to the precipitation of the strengthening γ' phase, along with formation of the $M_{23}C_6$ type carbide which are formed by the following reactions, respectively [256];

$$MC + \gamma \rightarrow M_{23}C_6 + \eta \tag{6.2}$$

$$MC + \gamma \rightarrow M_{23}C_6 + \gamma' \tag{6.3}$$

Jahangiri et al. [257] reported that the η phase with platelet morphology is enriched with Cr, Co, Ta, Ti, Nb and Al elements. The concentration distribution of the elements is different from our studies and, no platelet-like phases were observed during the microstructural observations.

The hardness of the as-fabricated sample increased after solution heat treatments. It is known that most of the contribution to the mechanical properties of the IN939 alloy arises from the formation of γ' phase. As shown in the high magnification SEM images in Figure 6.6(a1, c1, e1, g1), solution heat treatment led to the precipitation of spherical-like nano-sized γ' phase within the matrix, which is consistent with the obtained hardness results.

6.5.2 Texture evolution of the as-fabricated and solution heat-treated IN939 samples

The EBSD analyses were performed to address a comprehensive investigation of the effect of various solution heat treatments on the crystallographic texture, grain morphology, and recrystallization phenomena. As given in the corresponding IPFs and PFs (Figure 6.10), the <001>//BD texture was dominant for all samples. The solution heat treatments did not cause a significant change in the texture of the samples produced, but still affected their maximum intensity values. These values were highest for SHT1240 samples (i.e., 3.981 for IPF and 8.982 for PF) most likely due to recrystallization and subsequent grain growth mechanism. IQ & GBs maps of the samples showed that the as-fabricated and SHT1120 samples contained high amounts of low-angle grain boundaries

(LAGBs), indicated by the red and blue lines. As seen in the figures of SHT1160 and SHT1200 samples, LAGB density decreased with increasing solution heat treatment temperature. The misorientation distribution of the samples also indicated that most of the grain boundaries are LAGBs, as given in Figure 6.14(b). On the other hand, these boundaries changed into high-angle grain boundaries (HAGBs) and approached the Mackenzie distribution for the SHT1240 sample, which is attributed to the randomization of texture due to recrystallization phenomenon.

It is well known that the high-temperature gradient and rapid solidification rate of the PBF-LB processing cause high defect density along with the high residual stress in the fabricated parts. According to the results obtained from KAM (Figure 6.12(a-e)) and GND (Figure 6.14(a)) analyses, it was observed that the as-fabricated sample had high dislocation densities, especially along grain boundaries rather than grain interiors. The dislocation density of the SHT1120 sample was close to its as-fabricated counterpart. The GND value decreased by 18.7 %, 26.8 % and 69.1 % for the SHT1160, SHT1200 and SHT1240 samples, respectively. Moreover, the reduction in the KAM values (Figure 6.13(a)) was calculated as approximately 23.4 % for the SHT1160 and SHT1200 samples and 49.2 % for the SHT1240 sample. It can be revealed that a significant decrease in both dislocation density and residual stress were observed with increasing solution heat treatment temperature.

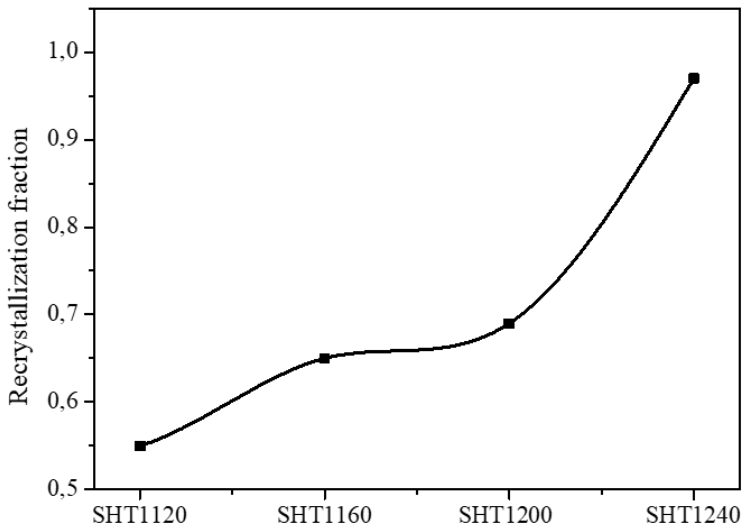

Figure 6.15 Recrystallization fractions of the as-fabricated and solution heat-treated samples.

GOS is also used to distinguish recrystallized grains from others. Grains with a GOS value less than 1.5 represent recrystallized ones [32]. As seen in the GOS maps and

distributions (and Figure 6.12(f-j) and Figure 6.13(b)), the GOS values of the as-fabricated and SHT1120 sample were higher and GOS values decreased with increasing temperature of the solution heat treatment. Figure 6.15 shows the recrystallization fractions of the as-fabricated and solution heat-treated samples. Here, a threshold GOS value of 1.8 degrees was selected to distinguish recrystallized grains. The first recrystallized grains, as indicated in Figure 6.12(h), began to appear when the samples were subjected to the solution heat treatment at 1160 °C and the GOS value decreased by 10.3%. The fraction of the recrystallized grains increased from 0.55 (this value was calculated for the as-fabricated sample) to 0.56 for SHT1120, 0.66 for SHT1160 and 0.68 for SHT1200 samples as the solution heat treatment temperature increased with decreasing the GOS value. Moreover, most of the grains were recrystallized for the SHT1240 sample, as its recrystallization fraction was calculated to be 0.97. The recrystallization starts from high defect density regions, such as overlapping melt pools and cross-over points of laser-beam scanning paths (hatch pattern). Those regions exhibit higher local misorientations and higher GND density than the rest of the sample. The local misorientations and GND density decrease with increasing solution heat treatment temperature. Those findings are in agreement with our previous study on recrystallization kinetics and grain growth in PBF-LB produced IN718 [45]. IN718 involved twinning-assisted recrystallization mechanism and exhibited significant grain growth over 1150 °C. For IN939 the distribution of defects (i.e., dislocations) coming from the as-fabricated structure, and the size and distribution of MC type carbides determine the recrystallization kinetics of IN939. It was also found that the carbides and precipitates limited the grain growth of IN939, compared to IN718.

6.6 Conclusions

The effect of solution heat treatment on the microstructure, grain morphology and crystallographic texture of the IN939 fabricated by the PBF-LB method were systematically investigated. Based on the results of this study, the main findings can be summarized as follows:

1- For solution heat treatment of 1200 °C, the arc-shaped morphologies seen in the as-fabricated samples disappeared and turned into a mixture of columnar and equiaxed grains in the XZ and XY-planes, respectively. When the samples were solution heat-treated at 1240 °C, microstructural anisotropy was eliminated by forming equiaxed grains with an average size of 32 μm.

2- Texture analyses showed that both as-fabricated and solution heat-treated samples had a preferential <001>// BD texture. The intensity values increased with increasing solution heat treatment temperature.
3- The high amount of LAGBs and GNDs density formed in the as-fabricated sample due to the high-temperature gradient and rapid solidification rate of the PBF-LB processing decreased after solution heat treatment. Moreover, their fractions decreased as the solution heat treatment temperature increased.
4- As shown in the KAM and GOS maps and distributions, the first recrystallized grains began to appear when the samples were subjected to the solution heat treatment at 1160 °C and the fraction of the recrystallized grains increased with increasing solution heat treatment temperature. Here the size and distribution of MC type carbides determine the recrystallization kinetics, and they also limit the grain growth.
5- High magnification SEM images showed that a large amount of spherical-like nano-sized the γ' phase formed within the matrix after all solution heat treatment conditions, which caused to increase in the hardness values.

6.7 Contribution to Thesis Objectives

IN939 is a precipitation hardenable Ni-base superalloy. Precipitation hardening heat treatment has two steps: SHT and aging. After a thorough review of the existing literature, it was found that there was a limited study on the understanding of how various SHT temperatures on the material properties of IN939 fabricated by the PBF-LB. This chapter significantly advanced the understanding of the influence of various solution heat treatment temperatures on the microstructure, crystallographic texture, and microhardness of IN939 fabricated by the PBF-LB. Notably, it identified that the recrystallization started at 1160 °C, and microstructural anisotropy was eliminated at 1240 °C. Furthermore, the study highlighted the formation of spherical-like nano-sized γ' phase precipitates within the matrix after SHT, increasing microhardness. These findings collectively offered valuable insights into optimizing SHT processes in PBF-LB fabrication, contributing to advancements in the manufacturing of high-performance IN939 components. It should be noted that aging treatment should be optimized as a future study.

Chapter 7: Recrystallization and Grain Growth Kinetics of IN718 Manufactured by Powder Bed Fusion-Laser Beam

Publication Status: Published

M.N. Doğu, K. Davut, M. A. Obeidi, M. A. Yalçın, H. Gu, T. Song En Low, J. Ginn, D. Brabazon, **Recrystallization and grain growth kinetics of IN718 manufactured by laser powder bed fusion**, Journal of Materials Research and Technology, 19 (2022).

https://doi.org/10.1016/j.jmrt.2023.05.152

7.1 Abstract

The recrystallization and grain growth behaviour of IN718 alloy additively manufactured by powder bed fusion-laser beam (PBF-LB) is presented herein. The effects of three different temperatures (1050, 1150 and 1250 °C) and holding times (15, 45 and 90 min) were investigated. The texture evolution of the samples was recorded via electron backscatter diffraction (EBSD). The as-built sample is composed of bowl-shaped melt pools, a chessboard-like grain pattern and has a cube texture {100}<001>. Recrystallized grains were observed in the samples treated at 1150 °C for 15 minutes, as well as the samples treated for longer periods and at higher temperatures. Recrystallization was observed to start from high dislocation density regions, including the overlapping melt pools and the borders of the chessboard-like pattern. The initial cube texture transforms into a first-generation cube-twin texture {122}<212> via a twinning-assisted recrystallization mechanism. Then, those recrystallization nuclei sweep through the high defect density matrix; during which almost no new twins are formed. The samples treated at 1250 °C are almost completely recrystallized, which forms a weaker cube texture and a stronger P-orientation {011}<112>. However, the growth of recrystallized grains is very limited due to the presence of non-coherent precipitates.

7.2 Introduction

Ni-base superalloys, the most extensively-developed superalloy family, have been widely used for aerospace and industrial applications over the past four decades for their outstanding high-temperature mechanical properties [258,259]. IN718, developed by the Nickel Corporation in the 1950s, possesses superior properties such as excellent oxidation and corrosion resistance, good weldability and high-temperature mechanical property stability up to 650 °C [46,52,260]. For this reason, IN718 is used in the aerospace industry (i.e. aircraft gas turbine disks, vanes, combustion chamber, rocket engine parts), chemical and petrochemical industries (i.e. bolts, valves, fans, tubing), nuclear power systems, marine architecture and pollution control equipment [7].

IN718 can have multiple phases shown in Table 7.1 depending on the elemental composition, heat-treatment conditions, and solidification. IN718 is a precipitation-strengthened Ni-base superalloy based on the austenite (γ) matrix. The primary strengthening phase is γ" (Ni_3Nb, $D0_{22}$) and the auxiliary strengthening phase is γ' (Ni_3(Al, Ti), $L1_2$). These phases have a coherent or semi-coherent particle-matrix interface. The γ" (a coherent disc-like morphology with {100} habit plane) has higher coherency strain and

antiphase boundary (APB) energy, so the strengthening effect of γ" is greater than γ' [261]. The metastable γ" can transform into the stable orthorhombic δ phase (Ni_3Nb, $D0_a$) over a long period of exposure to high temperatures (above 700 °C). δ phase, Laves (brittle intermetallic compound) and MC carbide have incoherent particle-matrix interfaces. However, these phases can be detrimental to the mechanical properties when they are extremely coarse and acicular. On the other hand, the δ phase can also lead to grain refinement. The mechanical properties can also be controlled by adjusting the size and distribution of the IN718 phases [52,53].

Conventional manufacturing techniques such as casting, wrought and powder metallurgy are used to produce IN718, and these methods provide reasonable mechanical properties. However, the machining of IN718 is difficult due to its low material removal rate and high shear strength. Additionally, many industries, particularly the aerospace industry, require highly complex geometries which are difficult to produce in a single production step with conventional manufacturing techniques [120,258] For this reason, a more convenient manufacturing technique is necessary to produce IN718 geometries.

Additive manufacturing (AM) techniques provide significant advantages over conventional manufacturing techniques such as greater design freedom, near-net-shape fabrication, high material-use efficiency and alleviating the machining difficulty resulting from conventional manufacturing techniques [146,180]. The PBF-LB process, also known as selective laser melting (SLM), is a metal AM technique that uses a focused laser beam to melt metal powder [44,179]. The production mechanism of the PBF-LB process is based on layer-by-layer production according to the created CAD model and was explained in a detail in previous studies [126,152,262,263]. Furthermore, the PBF-LB process possesses a low buy-to-fly ratio, enabling the manufacturing of complex geometries in a single production step and often provides cost and time-saving advantages over conventional manufacturing [53]. However, the high cooling rate of the PBF-LB process causes rapid solidification leading to the formation of non-equilibrium phases such as Laves and carbides, inhibition of the precipitation strengthening phases, and microsegregation of the refractory elements such as Nb and Mo and residual stresses. These can decrease mechanical performance [244,264]**.** For this reason, post-heat treatments are often used as a common practice to dissolve detrimental phases (i.e. Laves), reduce possible residual stresses, and to optimize the microstructure and mechanical properties of the IN718 produced by the PBF-LB [264].

Different post-heat treatments provide different microstructure and mechanical properties. These post-heat treatments can be categorized as solution heat treatment (SHT) improving mechanical properties by dissolving detrimental phases, stress-relieve heat treatment reducing residual stress and texture, aging (single or double) providing precipitation of strengthening phases, homogenization reorienting columnar grains and hot isostatic pressing (HIP) increasing density by decreasing defects [7]. Thus, optimization of the post-heat treatments is a significant step to obtain desired properties. Recently, the effects of heat treatments on IN718 produced with the PBF-LB process have been investigated in several studies [232,241,244,260,261,264–267].

In the literature, solution heat treatment was generally performed with fast cooling (water quench or air cooling) for the IN718 produced by the PBF-LB. Although a few studies [232,241,267,268] investigated solution heat treatment followed by furnace cooling (FC), a detailed investigation of the effects of FC during solution heat treatment on the IN718 produced by the PBF-LB is necessary to fill a gap in the literature. Moreover, there are limited studies on the recrystallization and grain growth kinetics of PBF-LB manufactured IN718. In this work, the influence of three different solution heat treatment temperatures (1050, 1150 and 1250 °C) and holding times (15, 45 and 90 min) followed by FC under argon atmosphere on the recrystallization and grain growth behaviour of IN718 produced by the PBF-LB was investigated. Microstructure and grain examination of the samples was performed using an optical microscope (OM), scanning electron microscope (SEM) and EBSD. Texture evolution of the samples was investigated using EBSD and microhardness values of the samples were measured by the Vickers microhardness test.

Table 7.1 Phases in IN718 (adapted from [34,261]).

Phase	Crystal structure	Chemical formula	Solvus temperature (°C)
gamma (γ)	FCC	Ni	1227-1320 (solidus) 1260-1364 (liquidus)
gamma prime (γ')	FCC (ordered $L1_2$)	$Ni_3(Al,Ti)$	850-970
gamma double-prime (γ'')	BCT (ordered $D0_{22}$)	Ni_3Nb	910-940
delta (δ)	Orthorhombic (ordered $D0_a$)	Ni_3Nb	990-1020
Laves	Hexagonal (C_{14})	$(Ni, Cr, Fe)_{2(}Nb, Ti)$	1010-1160
metal carbide (MC)	Cubic (B_1)	(Nb, Ti)C	1260-1305

7.3 Materials and Methods

7.3.1 Raw Materials and PBF-LB Process Parameters

Gas atomized IN718 powder with the particle size ranging from 10 to 45 µm was used for the PBF-LB process. The chemical composition of the IN718 powder and the standard specification for Additive Manufacturing of Ni alloy (ASTM F3055-14a [269]) are given in Table 7.2. In this study, ten IN718 cubes (10 x 10 x 10 mm^3) were fabricated using SLM Solutions 280HL machine with the identical process parameters shown in Table 7.3. All of the IN718 cubes were produced in the Z direction which is parallel to the build direction. Then, all IN718 cubes were removed from the build plate using wire-EDM prior to heat treatment.

Table 7.2 Chemical composition of the gas atomized IN718 powder, and ASTM F3055-14a standard [269].

Elements (wt.%)	Ni	Cr	Fe	Mo	Co	Al	Ta+Nb	Ti	C	Cu	Mn	Si	P	S	B
IN718 Powder	53.15	19.58	Balance	3.12	0.14	0.14	5.01	1.0	0.03	0.04	0.03	0.04	0.004	0.001	<0.01
ASTM F3055-14a	50-55	17.0-21.0	Balance	2.80-3.30	0-1	0.2-0.8	4.75-5.50	0.65-1.15	0-0.8	0-0.3	0-0.35	0-0.35	0-0.015	0-0.015	0-0.006

7.3.2 Heat Treatments

Before heat treatments, IN718 cubes were cleaned using acetone and ethanol, respectively. Then, the cleaned and dried IN718 cubes were placed into an atmosphere-controlled horizontal tube furnace (Lenton Tube Furnace 1500 ºC LTF 16) at room temperature. After purging with high purity argon gas for 5 min, solution heat treatment was carried out under high purity argon gas flow at various temperature and holding time combinations. Subsequently, samples were cooled down to room temperature in the furnace under high purity argon gas (cooling rate of 5 °C/min). Table 7.4 shows the summary of the solution heat treatments applied for the IN718 cubes.

Table 7.3 PBF-LB process parameters for the IN718 cubes.

Process Parameters	Unit	Value
Layer thickness	µm	30
Preheating temperature	^{o}C	200
Beam diameter	µm	85
Laser power	W	200
Laser speed	mm/s	945
Hatch distance	mm	0.12
Stripe length	mm	10
Starting angle	^{o}	45
Rotation angle	^{o}	90
Energy density	(J/mm^3)	59

Cubes were all fabricated using a (45, 90) scan pattern, which refers to a 45° laser starting scan angle with respect to the cube x-axis direction, and a 90° rotation angle per layer.

Table 7.4 Summary of the solution heat treatments applied for IN718 cubes.

Description	Temperature (^{o}C)	Holding time (min)	
AB (as-built)	None	None	
1050-15	1050	15	Furnace cooling (5 ^{o}C/min) under argon atmosphere
1050-45	1050	45	
1050-90	1050	90	
1150-15	1150	15	
1150-45	1150	45	
1150-90	1150	90	
1250-15	1250	15	
1250-45	1250	45	
1250-90	1250	90	

7.3.3 Materials Characterization

For the metallographic examination, IN718 cubes were cut as shown in Figure 7.1 to examine both Z (parallel to the build direction) and XY (perpendicular to the build direction) planes. After that, the samples were mechanically ground using conventional

SiC grinding papers up to 1200 grit size, then polished with progressively finer diamond suspensions (9, 3, 1 µm). The etching step was a challenge for this study. Different etchants such as Waterless Kalling's were tried on the samples. However, the Glyceregia reagent (15 ml HCl, 10 ml glycerol and 5 ml HNO_3) provided the best result [270]. Although generally swabbing is recommended for the Glyceregia reagent, it caused scratches for the solution heat-treated samples. Also, the immersion method provided heterogeneous etched surfaces. Therefore, the etchant was dropped on the samples using a pipette to obtain homogeneously etched surfaces. Microstructures of the AB and solution heat-treated samples were examined by OM (Nikon Eclipse LV150) and SEM (ZEISS Merlin Scanning Electron Microscope). Additionally, EBSD analysis was carried out in the ZEISS Merlin SEM using an acceleration voltage of 15 kV and 6.0 nA probe current. In addition to the above polishing steps, an additional final polishing step was applied using 0.25 µm fumed silica (OP-S) was applied before the EBSD analysis. The mapping areas of 500 µm x 500 µm were indexed with a step size of 1 µm. EBSD raw data was post-processed using TSL OIM Analysis™ software. Points with CI (confidence index) below 0.1 were removed and twin boundaries were excluded for grain size calculations. The Vickers microhardness tests were carried out for both Z and XY planes from 15 points for each plane using Zwick/Roell Zhu microhardness tester 2.5 with a load of 1 kg according to ASTM 384-17 [189].

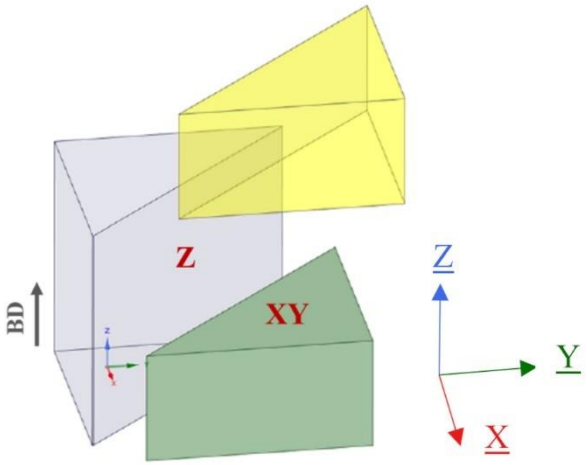

Figure 7.1 Schematic of Z and XY examination planes cut from the IN718 cubes (BD: build direction).

7.4 Results

7.4.1 Microstructure and Hardness in the AB Condition

Figure 7.2 shows the microstructure of the AB sample. Optical micrographs of the Z and XY planes are shown in Figure 7.2(a, b), respectively. Similar to other studies [241,262,271,272] bowl-shaped melt pools (Z plane) resulting from the Gaussian energy distribution of the laser beam and laser scanning paths line by line (XY plane) were observed in the AB sample. The columnar dendritic microstructure, the columnar grains with cellular structure and very fine dendrites are the typical microstructure of IN718 produced by the PBF-LB and the melt pool boundary indicated with a white dashed line are displayed in Figure 7.2(c). The magnified SEM images exhibit columnar and cellular substructures with an average spacing of 477±171 nm and 581±125 nm, respectively. Additionally, the brittle Laves phase which should be dissolved with solution heat treatment and γ matrix can be observed in the magnified SEM images indicated by red arrows. Although the overall heat flow direction is almost parallel to the building direction, the columnar dendrites have different grain growth directions resulting from complicated temperature fields in the melt pool [262].

The grain morphologies of the Z and XY planes can be clearly seen in the inverse pole figure (IPF) maps displayed in Figure 7.2(d, e) and image quality and grain boundaries (IQ & GBs) maps shown in Figure 7.2(f, g). The Z plane contains mainly elongated grains which are parallel to the build direction. On the other hand, the XY plane contains a chessboard-like grain pattern due to the scanning strategy (45^{o} starting angle with 90^{o} rotation angle between layers). Additionally, the area-weighted average grain size values were obtained from EBSD, and the grain size values are 24.2±5.8 μm and 13.3±3.9 μm which are similar to those reported in the literature [162,193] for the Z and XY planes, respectively (Table 7.5 and Figure 7.3(a)).

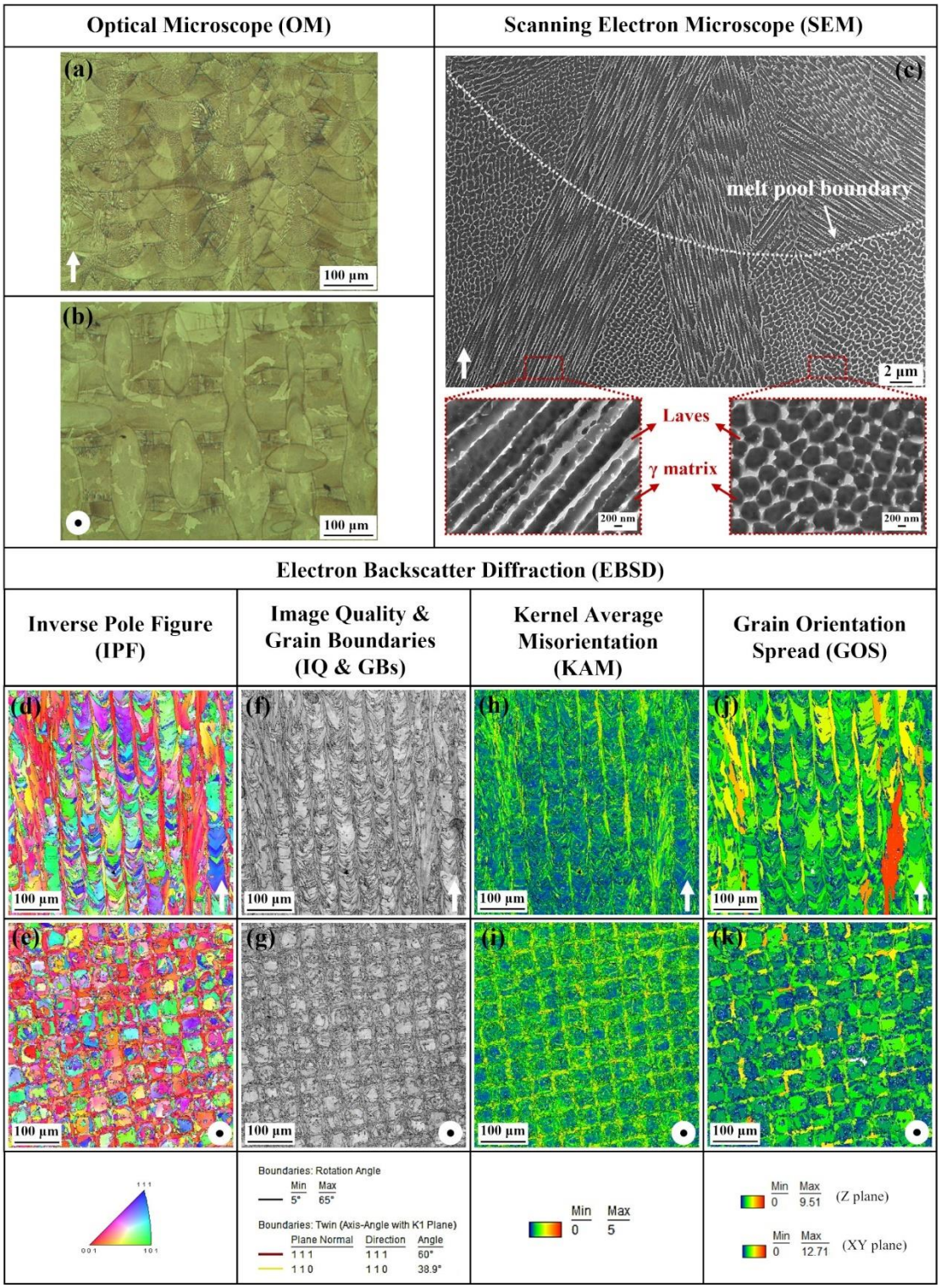

Figure 7.2 (a-b) Optical micrographs, (c) SEM image, (d-e) IPF maps, (f-g) IQ and GBs maps, (h-i) KAM maps and (j-k) GOS maps of the AB sample. Z plane (parallel to build direction) and XY planes (perpendicular to build direction) are indicated with an arrow and a dot, respectively.

The kernel average misorientation (KAM) maps of the Z and XY planes are displayed in Figure 7.2(h) and (i), respectively. KAM can be defined as the measure of the local grain misorientation, and the KAM map displays the average misorientation of each pixel with respect to its neighbours. In general, high KAM values represent high plastic strain and dislocation density [273,274]. The KAM maps are labelled with a rainbow scale; where blue and red represent the minimum and maximum misorientation (0-5^{o}), respectively. The overlapping regions have a lower KAM value compared to inside of the melt pools shown in Figure 7.2(h) and the KAM value of the Z plane is 0.99^{o} (Table 7.6). Furthermore, the KAM value of the XY plane is 1.19^{o} shown in Table 7.6 and the borders have a higher KAM value compared to the center of the chessboard-like pattern as shown in Figure 7.2(i). This finding is consistent with the study of Aota et al. [225] who reported that the coarse grains are located at the center of the chessboard-like pattern having a lower KAM value and the borders of the chessboard-like pattern contain the fine grains having a higher KAM value. Additionally, the number fraction versus the KAM graph is shown in Figure 7.3(b).

The high cooling rate during solidification causes local strain inhomogeneity and accordingly a high dislocation density. The internal plastic strain gradients cause the geometrically necessary dislocations (GND). Thus, a high GND density indicates high plastic strain gradients [225]. Figure 7.3(c) shows the number fraction versus the GND density graph. The average GND densities of the Z and XY planes are 28.61 and 36.33 shown in Table 7.6, respectively. The grain orientation spread (GOS) can be defined as the average of the misorientation angles to the grain mean orientation [273]. The GOS maps labelled with a rainbow scale and blue and red colours show minimum and maximum GOS angles. A similar trend with the KAM was observed for the GOS of Z and XY planes. The columnar grain regions have a higher GOS value compared to inside of the melt pools shown in Figure 7.2(j) and the borders have a higher GOS value compared to the center of the chessboard-like pattern as shown in Figure 7.2(k). The correlated number fraction versus misorientation angle graph is displayed in Figure 7.3(d). The yellow line shows the Mackenzie distribution for randomly oriented cubic polycrystals. The misorientation distribution of the AB sample shows the predominance of low angle grain boundaries (<10^{o}) having more substructure and dislocation density [275].

The hardness values of the Z and XY planes were measured as 327.1 $\pm$ 4.6 HV and 323.5 $\pm$ 7.4 HV respectively (see Table 7.5). Similar hardness values were reported in the review article of Sanchez et al. [7].

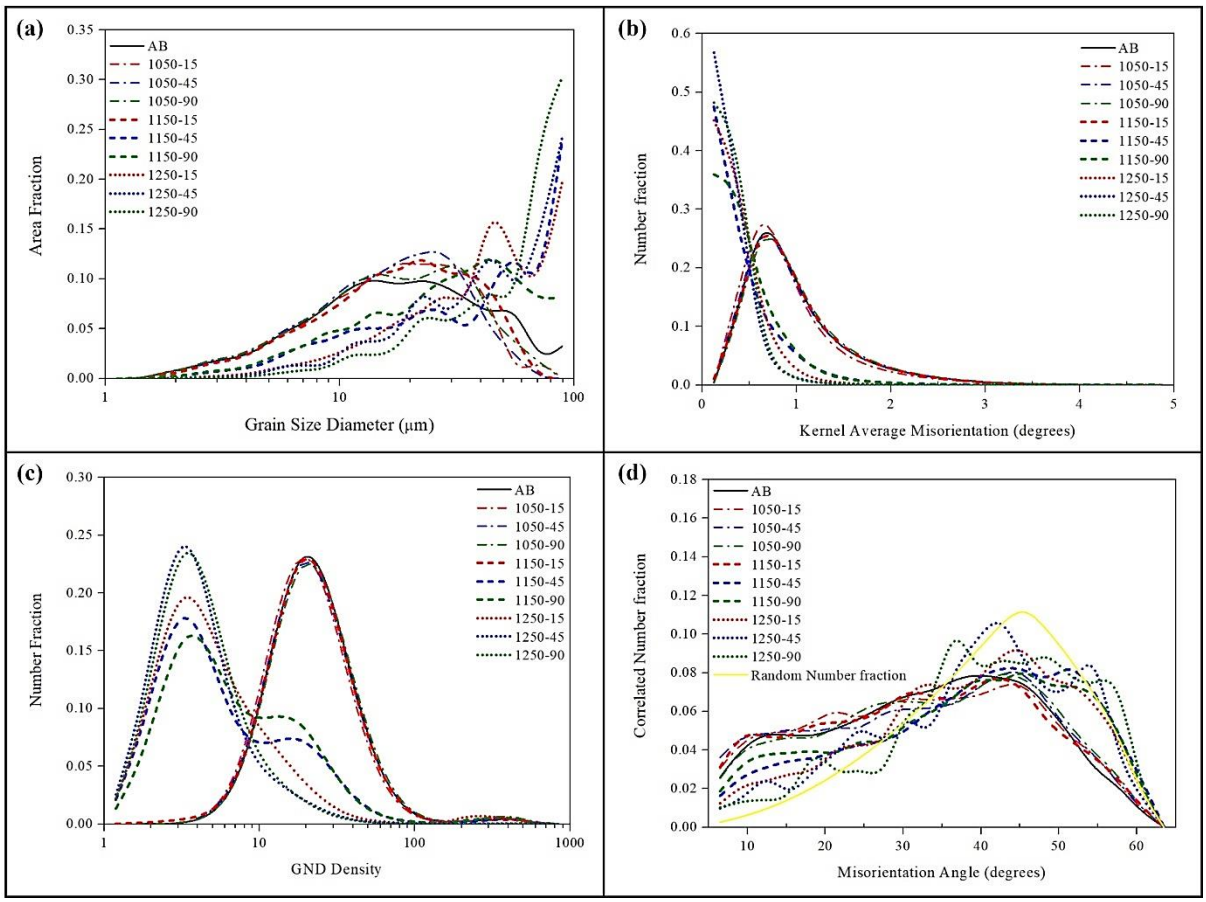

Figure 7.3 (a) Grain size, (b) KAM, (c) GND density and (d) misorientation angle distributions of the AB and solution heat-treated samples.

7.4.2 Microstructure and Hardness in the Solution Heat-Treated Condition

The applied solution heat treatments in this study are displayed in Table 7.4. Optical micrographs of the solution heat-treated samples in different conditions show the microstructural evolution according to the solution heat treatment temperature and holding time (Figure 7.4). There is no significant difference among the microstructures of the 1050-15, 1050-45, 1050-90 and 1150-15 samples and the bowl-shaped melt pools and scanning paths are still visible (Figure 7.4(a-d)). The first recrystallized grains indicated by the red dashed lines were observed in the 1150-15 sample (Figure 7.4(d)). Therefore, 1150 ^{o}C for 15 min can be accepted as starting of the recrystallization in this study. On the other hand, there is a significant difference in the microstructure of the 1150-45 sample compared to the previous samples and twin boundaries with the recrystallized grains can be clearly seen in Figure 7.4(e). For this reason, the recrystallization start temperature can be accepted as 1150 ^{o}C for IN718 produced by the PBF-LB in this study. Additionally, the area-weighted average grain size values are similar up to 1150-15 sample; however, two times increment in grain size was observed for the 1150-45 sample having 46.2±10 μm and 41.3±9.4 μm

area-weighted average grain size values for the Z and XY planes, respectively (see Table 7.5 and Figure 7.3(a)). Furthermore, the grain growth followed the trend of increased recrystallization with the solution heat treatment temperature increment (see Figure 7.4(f-i) and Table 7.5).

Table 7.5 The average hardness and grain size values of the AB and solution heat-treated samples.

Sample	Hardness (HV1)		Average grain size (μm)	
	Z plane	XY plane	Z plane	XY plane
AB	327.1 ± 4.6	323.5 ± 7.4	24.2 ± 5.8	13.3 ± 3.9
1050-15	394.9 ± 4.9	400.3 ± 7.2	20.5 ± 5.7	13.1 ± 3.8
1050-45	399.8 ± 6.2	399.8 ± 7.8	19.5 ± 5.7	14.5 ± 4.1
1050-90	397.2 ± 6.3	395 ± 4.3	21.1 ± 5.8	13.4 ± 3.9
1150-15	401.6 ± 3.3	398.4 ± 5.3	21.6 ± 6.2	14.1 ± 4.1
1150-45	414.1 ± 6.5	414.9 ± 6.2	46.2 ± 10.0	41.3 ± 9.4
1150-90	411.7 ± 8.4	417.1 ± 7.5	35.8 ± 9.0	39.8 ± 9.5
1250-15	415.7 ± 4.4	426.3 ± 6.2	45.9 ± 13.3	60.1 ± 19.8
1250-45	414.7 ± 5.4	420.3 ± 8.2	50.8 ± 14.6	63.4 ± 21.4
1250-90	409.4 ± 6.2	418.4 ± 6.0	58.7 ± 18.1	63.2 ± 19.7

Figure 7.5 shows the SEM images of the 1050-45, 1150-15, 1150-45 and 1250-45 samples. All of the samples have precipitates which can be MC carbide, δ phase (needle-like precipitates at the grain boundaries) and Laves at the grain boundaries (Figure 7.5(a-d)). Additionally, the high magnified SEM images indicated by red dashed lines display the strengthening precipitate phases (γ" and γ') which precipitate during the slow cooling. However, transmission electron microscopy (TEM) is required to better understand how the precipitated phases formed according to the solution temperature and time.

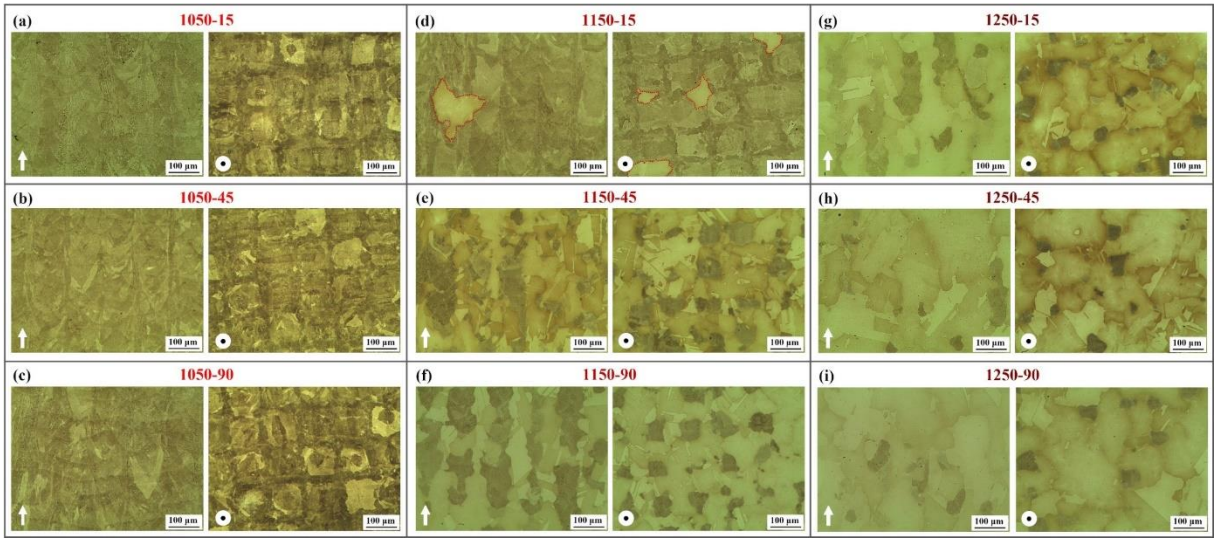

Figure 7.4 Optical micrographs of the solution heat-treatment conditions, (a) 1050 ^{o}C for 15 min, (b) 1050 ^{o}C for 45 min, (c) 1050 ^{o}C for 90 min, (d) 1150 ^{o}C for 15 min, (e) 1150 ^{o}C for 45 min, (f) 1150 ^{o}C for 90 min, (g) 1250 ^{o}C for 15 min, (h) 1250 ^{o}C for 45 min and (i) 1250 ^{o}C for 90 min. Z plane and XY plane are shown with an arrow and a dot, respectively.

EBSD maps of the Z and XY planes of 1050-45, 1150-15, 1150-45 and 1250-45 samples are shown in Figure 7.6 and Figure 7.7, respectively. As it was observed in the optical micrographs (Figure 7.4), the grain morphologies of the 1050-45 and 1150-15 samples are similar for both Z and XY planes and it can be seen in both IPF maps (Figure 7.6(a, b)) as well as IQ & GBs maps (Figure 7.7(a, b)). On the other hand, the microstructural change in the 1150-45 sample, along with the mostly recrystallized grains also mentioned above section can be clearly seen in Figure 7.6(c) and Figure 7.7(c) for both Z and XY planes. Twin boundaries indicated by the red lines in IQ & GBs maps were firstly observed in the 1150-45 sample (Figure 7.6(c) and Figure 7.7(c)). Twin boundaries can be called as coherent twin boundaries (Σ3) and twin-related grain boundaries (Σ9 and Σ27), are special boundaries and they can contribute to the material strength and resistance to intergranular degradation [276,277]. The twin boundary fractions are 0.366 (at 60^{o} on (111)) and 0.026 (at 38.9^{o} on (110)) for the Z plane and 0.377 (at 60^{o} on (111)) and 0.023 (at 38.9^{o} on (110)) for the XY plane. Moreover, twin boundaries are also visible in the optical micrographs (Figure 7.4(e)). Additionally, the twin boundaries were observed in the 1250-45 sample (Figure 7.4(h), Figure 7.6(d) and Figure 7.7(d)). The twin boundary fractions are 0.509 (at 60^{o} on (111)) and 0.026 (at 38.9^{o} on (110)) for the Z plane and 0.503 (at 60^{o} on (111)) and 0.026 (at 38.9^{o} on (110)) for the XY plane. It can be said that the twin boundary fraction increased with the increment of solution heat treatment temperature.

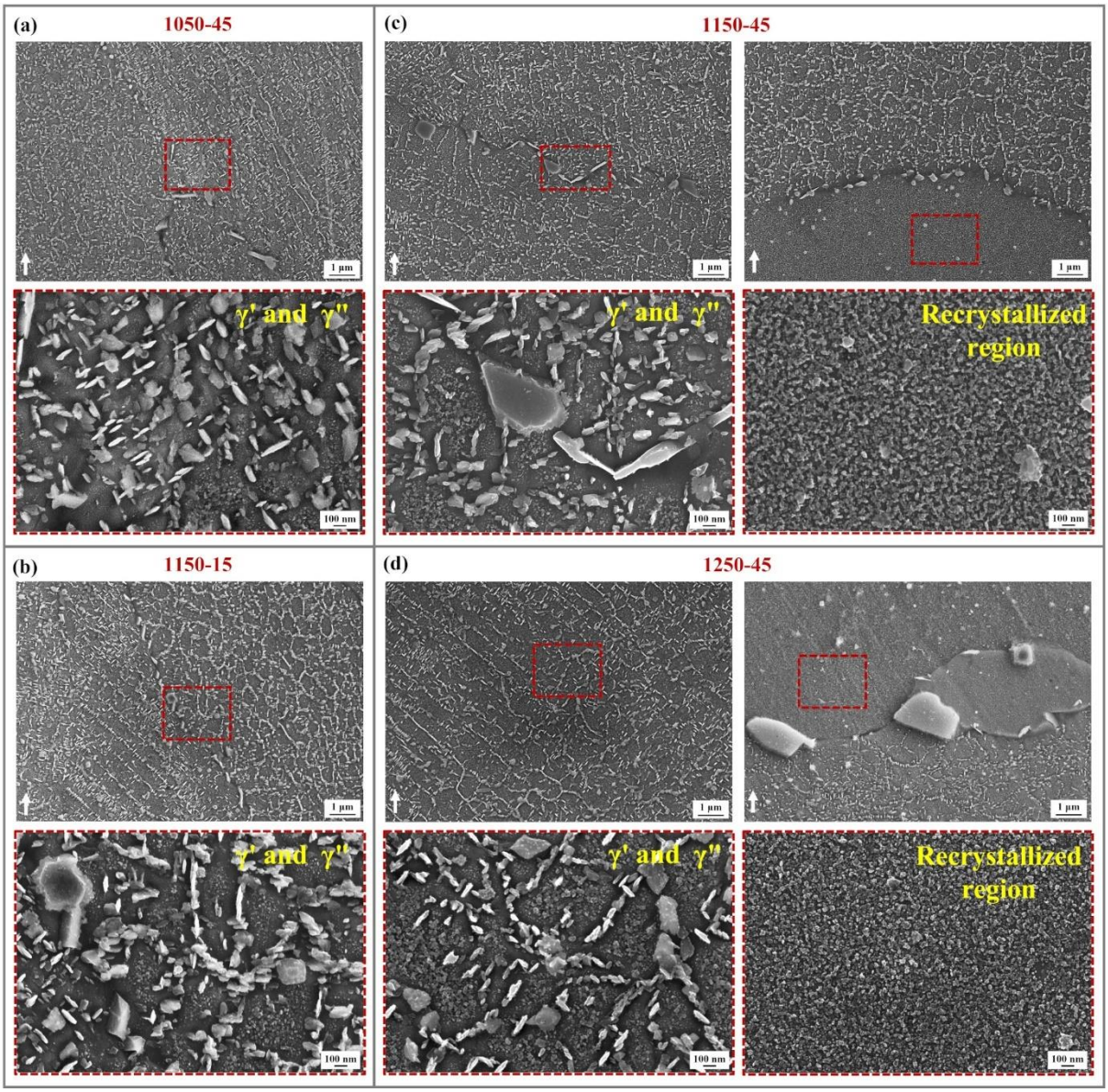

Figure 7.5 SEM images of the solution heat-treated samples at (a) 1050 ºC for 45 min, (b) 1150 ºC for 15 min, (c) 1150 ºC for 45 min and (d) 1250 ºC for 45 min; the red dashed lines represent first recrystallized grains.

As it was explained in section 3.1., the overlapping regions and the borders of the chessboard-like pattern have a higher KAM value due to the higher dislocation density [225]. There is no significant difference in the AB, 1050-45 and 1150-15 samples in terms of the KAM values shown in Table 7.6 and Figure 7.3(b). However, there is about 57% decrease in the KAM value of the 1150-45 sample due to the recrystallization. The blue regions which are on the KAM maps of the 1150-45 sample (Figure 7.6(c) and Figure 7.7(c)) can be called as recrystallized grains. Additionally, as it was expected, the KAM value decreased with the increment of solution heat treatment temperature (Table 7.6 and Figure 7.3(b)). Furthermore, the 1250-45 sample has more recrystallized grains compared

to the 1150-45 sample (Figure 7.6(d) and Figure 7.7(d). On the other hand, the average GND density values (Table 7.6) reduced with the recrystallization. The 1150-45 sample has about 54% less GND density and the 1250-45 sample has about 81% less GND density compared to the AB, 1050-45 and 1150-15 samples. Moreover, the recrystallization and grain growth can be seen in the GOS maps shown in Figure 7.6(a-d) and Figure 7.7(a-d) for the 1150-45 and 1250-45 samples. Additionally, the misorientation angle graphs of the 1150-45 and 1250-45 samples (Figure 7.3(d)) approach to the Mackenzie distribution and also there is a second peak at 60^{o} for the 1150-45 and 1250-45 samples.

The hardness values of the Z and XY planes of the samples are given in Table 7.5. In contrast to the AB sample, higher hardness values were obtained in the solution heat-treated samples due to precipitated phases during the slow cooling. Moreover, there was no significant difference in the hardness values of the Z and XY planes of the samples. The 1150-45 and 1250-45 samples have higher hardness values (around 414 HV for the Z plane) than the 1050-45 and 1150-15 samples.

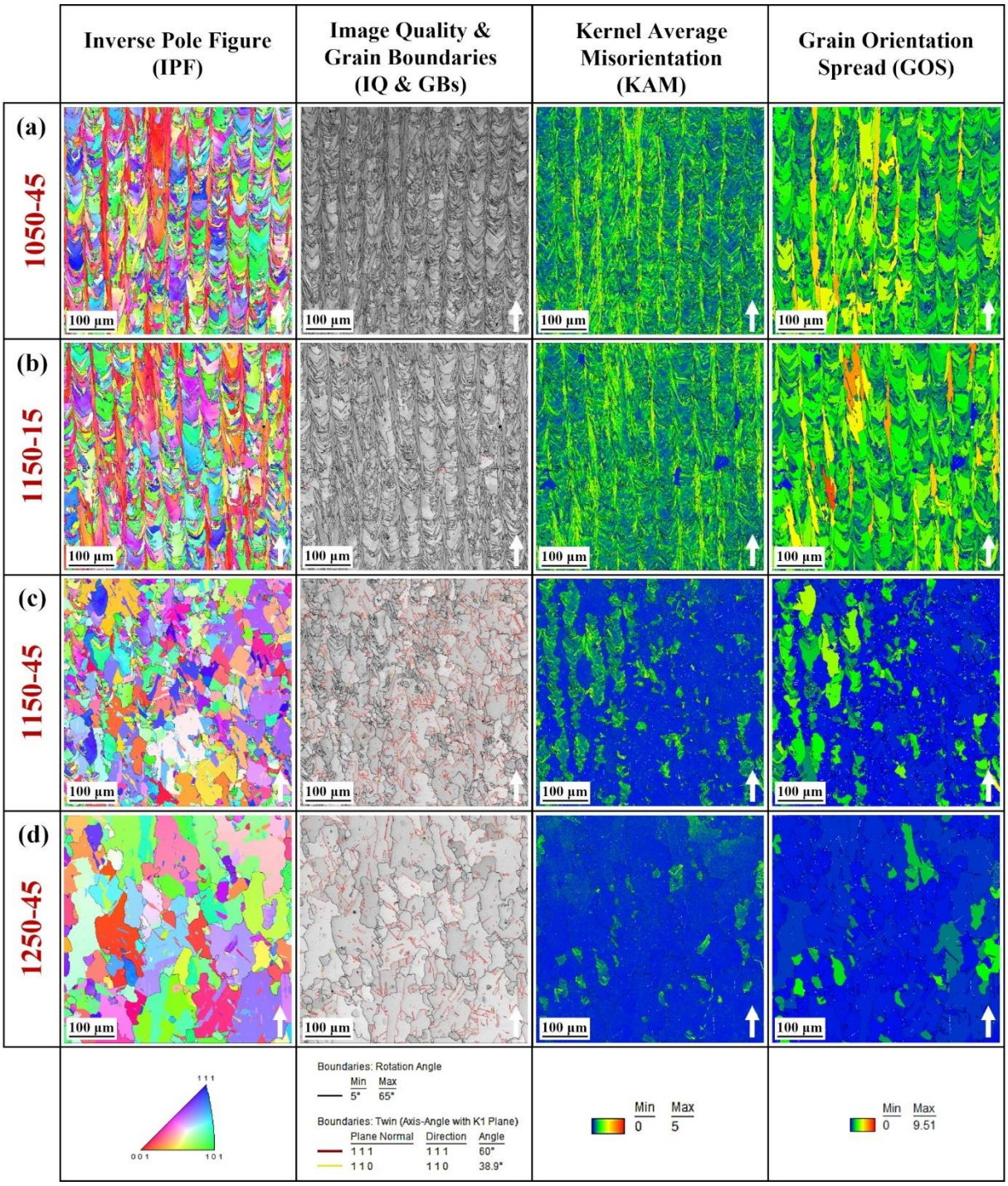

Figure 7.6 EBSD maps of the solution heat-treated samples; (a) 1050-45, (b) 1150-15, (c) 1150-45 and (d) 1250-45. Z plane (parallel to build direction) is indicated with an arrow.

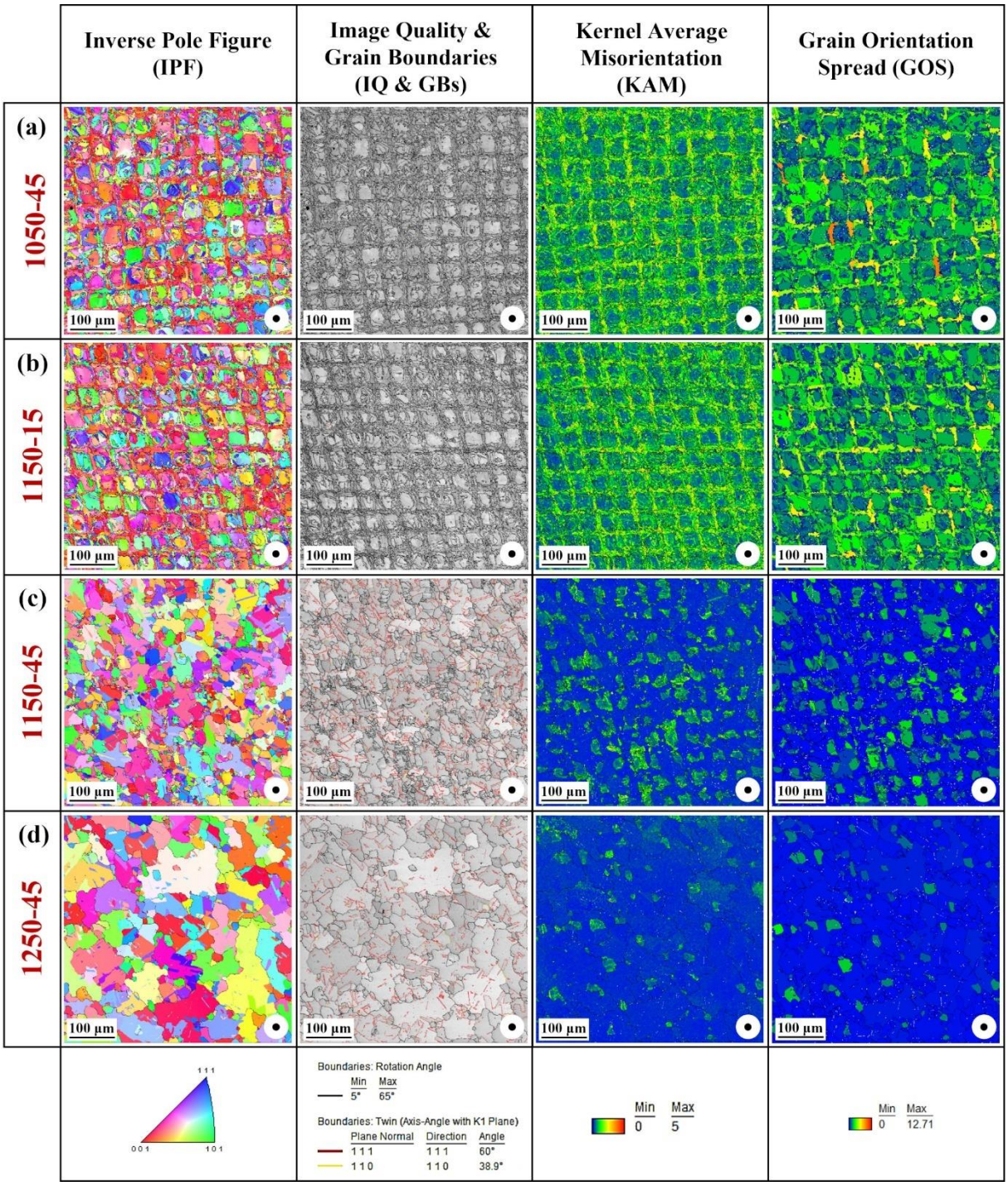

Figure 7.7 EBSD maps of the solution heat-treated samples; (a) 1050-45, (b) 1150-15, (c) 1150-45 and (d) 1250-45. XY plane (perpendicular to build direction) is indicated with a dot.

Table 7.6 The kernel average misorientation (KAM), geometrically necessary dislocation density (GND), recrystallization fraction values of the AB and solution heat-treated samples.

Sample	KAM (º)		GND density		Recrystallization Fraction
	Z plane	XY plane	Z plane	XY plane	
AB	0.99 ± 0.58	1.19 ± 0.66	28.61	36.34	0.24
1050-15	0.93 ± 0.58	1.16 ± 0.66	27.74	34.66	0.31
1050-45	0.99 ± 0.58	1.12 ± 0.64	29.15	34.07	0.34
1050-90	1.02 ± 0.58	1.15 ± 0.63	31.22	35.21	0.42
1150-15	0.98 ± 0.56	1.08 ± 0.62	28.15	31.53	0.31
1150-45	0.42 ± 0.38	0.40 ± 0.37	13.10	11.05	0.76
1150-90	0.45 ± 0.36	0.41 ± 0.37	14.60	11.15	0.82
1250-15	0.35 ± 0.28	0.26 ± 0.21	11.81	6.53	0.90
1250-45	0.28 ± 0.20	0.29 ± 0.20	5.33	6.67	0.92
1250-90	0.30 ± 0.19	0.27 ± 0.16	6.05	5.97	0.96

7.4.3 Texture in the AB and Solution Heat-Treated Conditions

The texture of the samples was examined by using the EBSD technique. Figure 7.8 shows the PF and IPF maps, only the corresponding {001} PF and [001] IPF were represented, of the AB, 1050-45, 1150-15, 1150-45 and 1250-45 samples. The maps belong to the Z plane which is parallel to the BD (build direction) of the samples. During the solidification from the liquid phase to the solid phase, the atoms prefer to move to the less close-packed planes and the grain growth direction occurs along <100> for FCC metals. For this reason, the typical solidification texture is well known as <100>//BD for the cubic materials because the grain growth occurs faster for the grains which have the <100> directions // the temperature gradient during the solidification. Moreover, the typical cube texture is represented as {001}//<100> [273].

The texture was observed in the middle and four edges of the {001} PF map of the AB sample with the maximum intensity value of 6.159 (Figure 7.8(a)) and this texture is a typical example for the cube texture. Moreover, the IPF map of the AB sample shows the <001>//BD texture component with the maximum intensity value of 4.372. It can be said that the AB sample has the {001}//<001> cube texture.

The PF and IPF maps of the 1050-45 and 1150-15 samples are shown in Figure 7.8(b, c). When we compare the PF and IPF maps of these samples with the AB sample, there is no significant difference except similar intensity value differences and these samples also have the {001}//<001> Cube texture. Indeed, it was expected for these samples because there was no significant difference in the microstructure, grain size, KAM, GND density and misorientation angle compared to the AB sample. On the other hand, the texture of the 1150-45 sample changed compared to the previous samples (Figure 7.8(d)). This sample exhibits first generation cube twin texture {122}<212>. The 1250-45 sample shows a weaker cube texture and a more intense P-orientation {011}<122>.

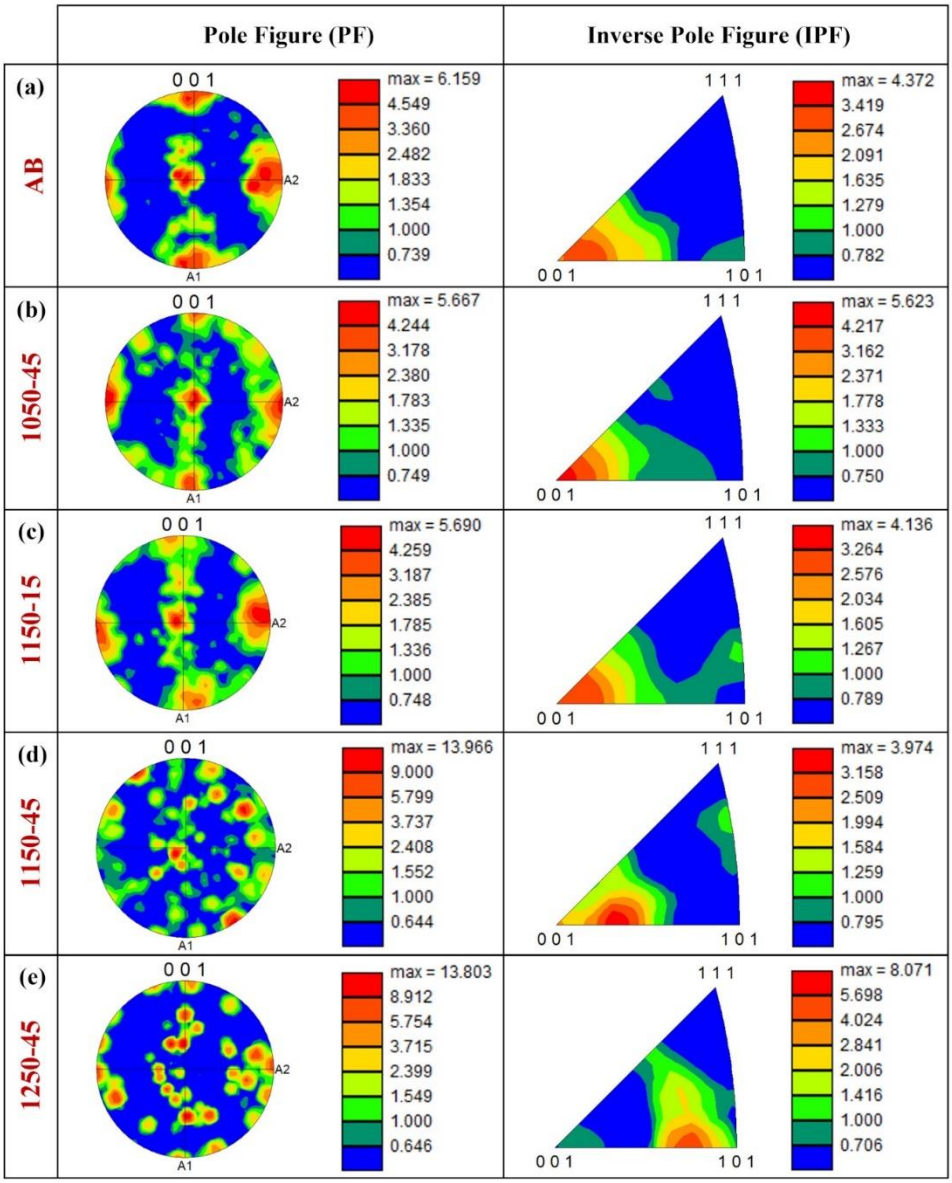

Figure 7.8 Pole figure (PF) and inverse pole figure (IPF) with respect to build direction of (a) AB, (b) 1050-45, (c) 1150-15, (d) 1150-45 and (e) 1250-45 samples.

7.5 . Discussion

7.5.1 Microstructural and Texture Evolution of the AB Sample

The growth process of the sub-structures during the PBF-LB process was well explained in the study of Li et al. [244]. The nature of the PBF-LB process provides rapid cooling and non-equilibrium solidification. The solidification microstructure is affected by the solidification rate (R), undercooling (ΔT), and temperature gradient (G), along with the process parameters of PBF-LB. The structure size and morphology of solidification microstructure (planar, cellular, equiaxed dendritic, or columnar dendritic) are determined by GxR and G/R, respectively. For example, the low cooling rates provide coarser structures (GR), whereas the finer structures can be obtained by increasing the cooling rate (GxR). On the other hand, reducing the G/R ratio can give the planar, cellular, equiaxed dendritic, or columnar dendritic solidification microstructure [44,124,268]. The columnar dendritic and cellular microstructure was observed in this study (Figure 7.2(c)). The solidification sequence of IN718 is well established as follows: Liquid → γ → γ + MC → γ + MC + Laves [278]. The segregation of Nb in the inter-dendritic regions is inevitable due to its partitioning behaviour during the solidification of IN718. Deng et al. [271] reported that the cooling rate affects the segregation of Nb and the size of Laves phase, which can be significantly minimized by increasing the cooling rate. Indeed, the low amount and size of Nb precipitates can be obtained with the PBF-LB process compared to casting due to rapid cooling [52]. According to the study of Tucho et al. [260] Laves phase, NbC and TiC can be observed in the sub-grain boundaries of the as-printed IN718. Although the main reason for these precipitates is the microsegregation Nb, Mo and Ti also segregate during the solidification. Additionally, Laves phase requires at least 10 wt.% Nb to form and it is well known that most of the segregated Nb are consumed by Laves phase [264]. In our study, Laves phase can be seen in the AB sample (Figure 7.2(c)). Moreover, Laves is a brittle intermetallic phase and degrades the high-temperature tensile properties [53].

The combined effects of both the maximum heat flow directions and the alignment of easy grain growth directions at the melt pool boundaries determine the texture [272]. The preferred grain growth direction is <100> along the heat-flow direction for the FCC crystal structure because atoms can move faster to the less close-packed planes [273]. The heat flow direction and the balance between G and R can be locally changed by altering the process parameters of the PBF-LB (i.e., scanning strategy and energy density). Thus,

the texture and microstructure can be modified [162]. Moreover, the cube texture {001}//<100> also observed in our study (Figure 7.8(a)) was reported in the studies on IN718 produced by the PBF-LB [7,162,272,279]. Additionally, when the heat flow direction is not parallel to the BD, weak <100>//BD and <110>//BD textures also can be observed in the FCC crystal structure [272]. Gokcekaya et al. [162] reported the unique crystallographic texture formation for IN718 produced by the PBF-LB with a bidirectional scanning strategy. According to their study, a crystallographic lamellar microstructure (composed of <110>//BD-oriented main grains and <100>//BD-oriented sub-grains), a <110>//BD-oriented single crystal-like microstructure, and polycrystalline microstructure were obtained by changing the scan speed and laser power.

7.5.2 Microstructural and Texture Evolution of the Solution Heat-Treated Samples

The effects of the solution heat treatment temperature and holding time on IN718 produced by the PBF-LB were given in section 3. There is no significant difference in the optical micrographs of 1050-15, 1050-45, 1050-90 and 1150-15 samples compared to the AB sample (Figure 7.4(a-c)) in terms of microstructure. Also, the area-weighted average grain size, KAM and GND density values of these samples are close to the AB sample. Although the microstructure of the 1150-15 sample is similar to the AB sample, the first recrystallized grains were observed in the 1150-15 sample (Figure 7.4(d)). Tucho et al. [260] reported 1100 ^{o}C as recrystallization start temperature which is reasonably consistent with the recrystallization start temperature found in this work (1150 ^{o}C). Moreover, recrystallization fraction and grain size diameter versus time graphs and also twin density versus grain size diameter graphs are shown in Figure 7.9(a, b).

On the other hand, significant microstructural differences were observed in the 1150-45 sample compared to the previous samples. Recrystallization was observed in the 1150-45 sample, although it was not completed. Additionally, twins which are a sign of recrystallization, along with 87.3% grain size increment were observed in the 1150-45 sample. As it was discussed before, the overlapping regions and the borders of the chessboard-like pattern have a higher KAM value due to the higher dislocation density. Therefore, the first recrystallized grains should be the grains that are in the overlapping regions and the boards of the chessboard-like pattern. This was clearly observed in the KAM map of the XY plane of the 1150-45 sample (Figure 7.7(c)) and the blue regions are strain-free recrystallized grains. Furthermore, the GND density reduced 54% in the 1150-45 sample due to recrystallization. When we looked at the 1250-45 sample, near-complete

recrystallization (92%) with the grain coarsening was observed. The grain size increment is around 118% compared to the AB sample. Most of the grains are strain-free recrystallized grains (Figure 7.6(d) and Figure 7.7(d)) and the average GND density reduced 81% in the 1250-45 sample compared to the AB sample. The coarsened grains in the 1150-45 and 1250-45 samples can be seen in the GOS maps (Figure 7.6(c, d) and Figure 7.7(c, d)). Moreover, there is a 39% increment of the twin boundary fraction compared to the 1150-45 sample. Jin et al. [280] reported that the density of annealing twins is inversely proportional to the grain size. Figure 7.9(c) shows the twin boundary length per 500 x 500-micron square area versus grain size graph. The misorientation angle of 60^{o} (observed in the 1150-45 and 1250-45 samples) corresponds to one of coincident site lattice (CSL) type of boundaries, namely the Σ3, which can also be identified as coherent twin boundary. The results shown at Figure 7.9(c) agrees well with this study [278]. Both studies indicate that, almost no new twins are formed during grain growth. Moreover, as seen in Figure 7.6(c) (IQ & GBs maps), the twins are mostly located at the grain edges next to non-recrystallized regions, rather than grain interiors. The same behaviour is observed in recrystallization of additively manufactured AISI 316 stainless steel samples reported by Aota et al. [225]. This behaviour was attributed to growth accident model, at which stacking faults are formed along a moving boundary, resulting in two different twin boundaries. One of them is an immobile, coherent twin boundary which is left behind, and the other is less coherent and highly mobile boundary that consumes the high defect density matrix [281–283].

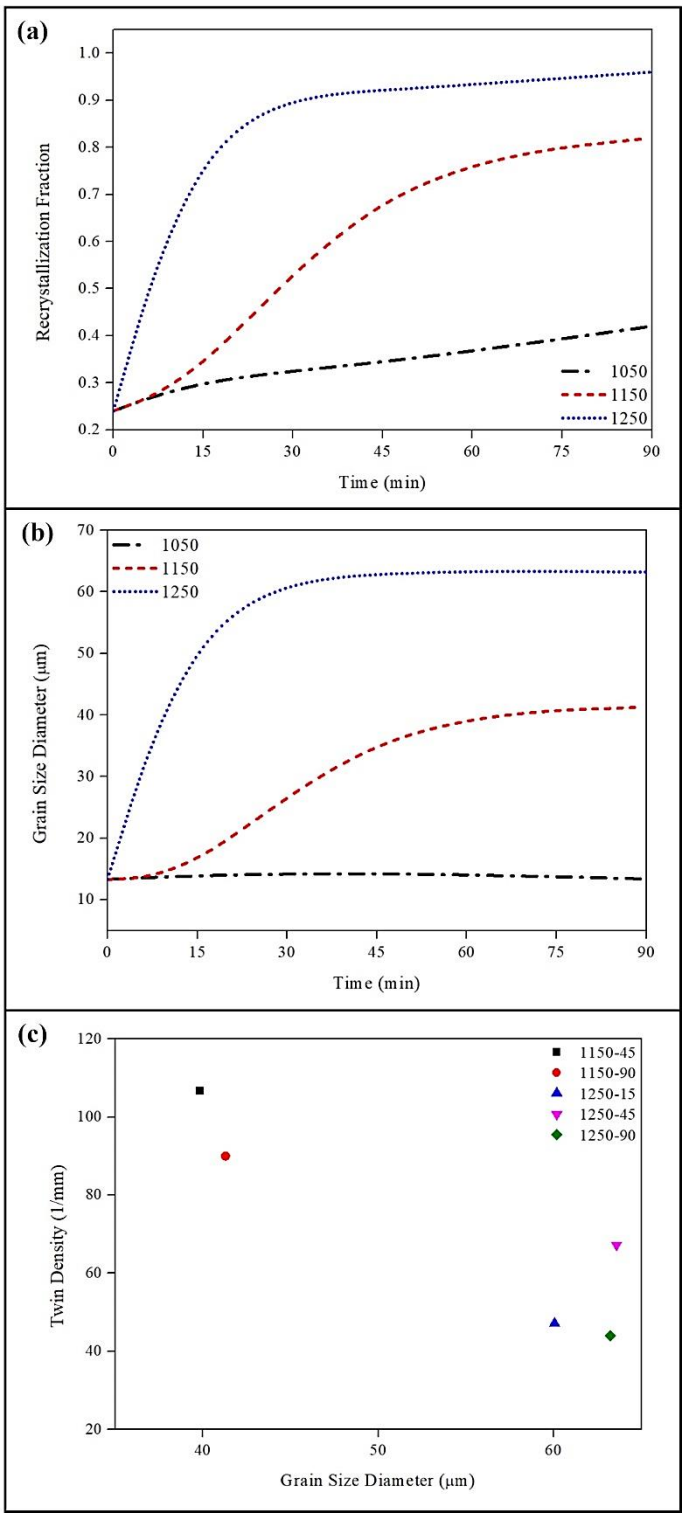

Figure 7.9 (a) Recrystallization fraction versus time, (b) grain size diameter versus time and (c) twin density versus grain size diameter graphs.

There is a significant difference between the AB sample and solution heat-treated samples in terms of phases shown in SEM images (Figure 7.2(c) and Figure 7.5) and the FC (5 ^{o}C/min) can be shown as a reason for this difference. The precipitated phases were observed at both matrix and grain boundaries of the solution heat-treated samples (Figure

7.5). The precipitation of γ" and γ' strengthening phases is possible in the range of 600-900 °C during double aging treatment [244]. During FC, the cooling from 900 °C to 600 °C took 60 min which is enough time for the precipitation of γ" and γ' strengthening phases [241]. In this study, the disk-like precipitates which are in the matrix of the solution heat-treated samples can be γ" shown in high magnified SEM images, which is consistent with the study of Huang et al. [241]. The slow cooling may cause the precipitation of δ phase, brittle Laves and the strengthening phases (γ" and γ') according to the TTT [284] and CCT [268] curves. Moreover, at least 6-8 wt.% Nb is required for the δ phase and the metastable γ" can transform into a stable δ phase at temperatures between 700 and 1010 °C [260,268,285]. Generally, the δ phase which precipitates at the grain boundaries during heat treatment is considered an undesirable phase due to the adverse effects on the fracture toughness and ductility. On the other hand, it can be beneficial due to the increment stress rupture resistance and grain stabilization effects. The needle-like δ phase which inhibits micro-cracks and granular-shaped δ phase which acts as a pin between grain boundaries can be seen in the literature [286] In this study, the needle-like δ phase was observed at the grain boundaries of the solution heat-treated samples. The local stress concentration, dislocation pile-up and premature failure can be due to too much δ phase along the grain boundaries whereas high-temperature strength are reduced due to the lack of the δ phase [286,287]. High-temperature strength can be achieved when the amount of δ phase is about 4% [53]. As it was discussed, the grain growth can be controlled by the δ phase at high temperatures. In addition to the δ phase, the grain boundary migration can be inhibited by MC carbides. However, they can cause intergranular cracking when they precipitate at the grain boundaries [285]. MC carbides were observed at the grain boundaries shown in Figure 7.5 and MC carbide coarsening can be seen due to diffusion of Nb from dissolved Laves. Additionally, the brittle Laves should be dissolved to release Nb and Ti elements with the solution heat treatment. Thus, more strengthening phases can be obtained during the subsequent aging treatment [260].

The average hardness values of the solution heat-treated samples increased compared to the AB sample while the area-weighted average grain size values were similar. The precipitated δ phase and strengthening phases (γ" and γ') can be shown as a reason for this. Huang et al. [241] investigated the effect of solution temperature, time and cooling rate on the IN718 produced by the PBF-LB. They did solution heat treatment at 1080 °C for 45 min followed by FC. Their findings are consistent with the current study. They concluded that the strengthening phases precipitating during FC is relatively small

compared to aging. Although these phases increase tensile strength, they will enlarge during the subsequent aging process. Therefore, the strengthening effect will be weakened. Moreover, Tucho et al. [260] reported that 1100 ^{o}C for 1 h is not enough to dissolve undesired phases to achieve a complete recrystallization during solution heat treatment. Also, tiny Laves precipitates were found at 1250 ^{o}C in their study. It can be assumed that the solution heat-treated samples may have the residual Laves phase in this study. Recently, Gruber et al. [267] reported stress-relief heat treatments at 1065 ^{o}C for 1.5 h and 1150 ^{o}C for 6 h with FC (6 ^{o}C/min). They indicated that most of the grains were non-recrystallized, along with intercellular microsegregation at 1065 ^{o}C for 1.5h. However, they reported complete dissolution of all secondary phases except coarsened primary carbides, along with reduced the macro- and micro-residual stresses at 1150 ^{o}C for 6h. This result differs from our finding because we observed the δ phase at the grain boundaries of the 1150-45 sample. Additionally, Kouraytem et al. [232] carried out recrystallization heat treatment at 1250 ^{o}C for 1 h with FC (10.4 ^{o}C/min). They observed the δ phase and MC carbide at the grain boundaries and strengthening phases (γ" and γ') in the matrix, along with dissolving Laves phase into the matrix. The results of the 1250-45 sample are similar to this study.

In addition to the PBF-LB process parameters (discussed in section 4.1.), the texture or crystal orientation can also change with the recrystallization which involves recovery and growth of new grains by the migration of high-angle grain boundary. The as built sample has an intense Cube texture {001}//<100>, which is a typical solidification texture for as-built additively manufactured materials with cubic crystal structure. This inherited cube texture is still intense in 1050-15, 1050-45 and 1150-15 samples. The recrystallization fraction does not change significantly for those samples (Table 7.6); also, there is no significant difference in terms of microstructure, grain size, KAM distribution and GND density compared to the AB sample. The 1150-45 sample shows significant reduction in GND density, slight increase in grain size and this sample is 76% recrystallized. The crystallographic texture of 1150-45 sample also changes significantly, the most intense texture component is no longer the cube component, but the first generation cube twin texture {122}<212> becomes intense. This texture component forms due to formation annealing twins and has an <111>60^{o} orientation relationship with the cube texture component. Figure 7.9(c) also shows that the highest twin density is present in 1150-45 sample, and this is also evident in EBSD maps showing twin boundaries (Figure

7.6(c) and Figure 7.7(c)). The crystallographic texture also proves the twinning-assisted recrystallization mechanism, which is also seen in PBF-LB produced AISI 316L samples

7.6 Conclusions

In this study, the effects of solution heat treatment followed by FC (5°C/min) with different temperatures (1050, 1150, 1250 °C) and holding times (15, 45, 90 min) were investigated. This study aimed to fill the gap in the literature about the effects of slow cooling during solution heat treatment on the microstructure and texture and hardness of IN718 produced by the PBF-LB, along with the recrystallization and grain growth kinetics. The main findings can be summarized as follows:

1) The bowl-shaped melt pools and chessboard-like grain pattern, along with the area-weighted average grain size, KAM and GND density values remained unchanged up to the 1150-15 sample. Although the first recrystallized grains were observed in the 1150-15 sample, a significant microstructural change was observed in the 1150-45 sample. It can be estimated that 1150 °C and 45 min are threshold values for recrystallization temperature and holding time, respectively. The twin boundaries, along with 87.3% grain size increment compared to the AB sample, were observed in the 1150-45 sample. Additionally, the recrystallization was almost completed in the 1250-45 sample, along with 118% grain size increment compared to the AB sample. Moreover, a 39% increment of the twin boundary fraction in the 1250-45 sample compared to the 1150-45 sample.
2) Recrystallization started from the high dislocation density regions such as overlapping regions and the borders of the chessboard-like pattern, and the average GND density values reduced 54% for the 1150-45 sample and 81% for the 1250-45 sample. Most of the residual stresses occurred during the PBF-LB process can be reduced with the solution heat treatment temperature of 1250 °C. Moreover, the recrystallization fractions of the 1150-45 and 1250-45 samples were calculated as 0.76 and 0.92, respectively.
3) The δ phase, the strengthening phases (γ'' and γ') and MC carbides were observed in the solution heat-treated samples due to the FC (5°C/min). Also, these samples may have brittle residual Laves phase.
4) The microhardness of the solution heat-treated samples increased around 20.5 – 26.6% compared to the AB sample due to the precipitated phases during FC.

Therefore, this must be considered for postprocessing operations as higher hardness may induce machining challenges.

5) The as-built sample exhibits cube texture {001}<100>, which transforms into first generation cube-twin texture {122}<212> due to twinning-assisted recrystallization mechanism. Almost no new twins are formed during growth stage, therefore other recrystallization texture components, cube and P-component, both of which are typical for FCC materials with intermediate SFE are formed.

7.7 Contribution to Thesis Objectives

This chapter was conducted as a preliminary study for this thesis to understand the microstructure of Ni-base superalloys fabricated by the PBF-LB process and heat treatment effects on the microstructural evaluation. Furthermore, this chapter was done to provide experimental data for ANSYS Inc. for their simulations on grain growth of IN718. With the help of this chapter, Chapter 6 was conducted easily.

Chapter 8: Conclusions and Future Work Directions

8.1 Investigation Summary

This study systematically investigated the material properties of IN939 precipitation-hardened Ni-base superalloy after the PBF-LB process and post-processing heat treatments. To achieve the research aims of this study, the objectives were completed to gain a comprehensive understanding of how PBF-LB process parameters and post-solution heat treatment affect the material properties of IN939. The original contributions corresponding to each of the investigations performed are summarised below:

1. The characteristics of IN939 powder, both virgin and spatter, as well as the phenomena of spatter and its impact on the properties of fabricated parts were investigated in Chapter 3. The chapter addresses a significant gap in research concerning the characteristics of IN939 powder, particularly focusing on both virgin and spatter powder and their impact on fabricated parts. A detailed comparative analysis between virgin and spatter IN939 powders revealed significant differences in terms of morphology, particle size distribution, color, and the presence of oxides. A brown tint coloration due to the interaction between the laser and metal powder, Al_2O_3 oxide formation, pores, a 124.4% increase in the average particle size, a 10.2% decrease in the powder circularity, and a 7.5% decrease in the powder aspect ratio were observed in the spatter powder. Furthermore, the spatter powder exhibited a larger average grain size and lower nanohardness, which was attributed to the difference in cooling rates between the gas-atomized process and the PBF-LB process. The observed increase in particle size and changes in circularity and aspect ratio provided valuable insights into the physical transformations that spatter powder undergoes during the PBF-LB process. By mixing 10 wt.% spatter powder with virgin powder, this research quantitatively evaluated the resultant effects on powder flowability and processing behaviour. The reduction in powder flowability and its implications for the PBF-LB process efficiency and fabricated part quality were critically analyzed, offering practical guidelines for industrial applications where powder recycling is considered. The study examined how 10 wt.% spatter powder affected part density and surface roughness, finding a 0.3% reduction in relative density and an 80.8% increase in surface roughness. These findings highlight the importance of powder quality for achieving optimal part properties. Despite the addition of spatter powder, no significant microstructural differences were observed between the samples fabricated using virgin and mixed powder, though an

increase in grain size was noted, and minimal impact on hardness was found. Furthermore, the research confirms that the overall texture of the fabricated parts remained consistent with the addition of spatter powder, maintaining the (001)//BD component essential for specific crystallographic textures. Overall, this study systematically investigated spatter powder effects, offering both theoretical insights and practical recommendations for the PBF-LB process with IN939 alloy.

2. A comprehensive study of the influence of PBF-LB process parameters, specifically laser power, laser scanning speed, and hatch distance, on the material properties of IN939 fabricated by the PBF-LB was investigated in Chapter 4. A detailed investigation was conducted to analyze the effects of varying laser power (160, 180, and 200 W), laser scanning speed (400, 800, and 1200 mm/s), and hatch distance (50, 80, and 110 μm) on the relative density, defect formation, surface roughness, and microstructure of IN939 samples. The study revealed that alterations in hatch distance significantly affect average surface roughness. The lowest surface roughness was 4.6 μm and it was found that the surface roughness can be decreased by reducing hatch distances while maintaining constant laser power and laser scanning speed. This observation is critical for applications requiring high-quality surface finishes. Findings indicated a spectrum of relative density values ranging from 93.56% to 99.35%, with variations attributed to the interactions of process parameters. Moreover, samples with equivalent VED obtained with different process parameters exhibited divergent relative densities and porosities, underscoring the importance of parameter optimization in mitigating defects such as porosity and microcracks. Noteworthy insights emerged regarding the correlation between process parameters and defect formation. High VED was linked to the genesis of large, irregular keyhole pores, while low VED yielded high porosity and LOF because of insufficient melting. The study also identified microcracks, indicative of solidification cracks, and outlined parameter adjustments to mitigate such defects. It was noted that some microcracks, invisible after polishing, became apparent after etching. This additional step ensures a more comprehensive assessment of crack formation. Furthermore, microstructural analysis showed the presence of arc-shaped melt pools and columnar elongated grains, which have cellular structures and columnar dendrites, oriented with the build direction. Through a comprehensive analysis, the study made significant strides in elucidating the relationship between PBF-LB process parameters and the quality attributes of IN939 components, thereby enriching both theoretical understanding and practical implementation within additive manufacturing.

3. A comprehensive investigation into the effects of different scanning strategies on the material properties of IN939 fabricated by the PBF-LB was given in Chapter 5. The study addresses a significant gap in research concerning the effects of different scanning strategies on the material properties of IN939 fabricated by the PBF-LB. By systematically analyzing various scanning strategies, including alternating bi-directional scanning with rotation angles of 0°, 45°, 67°, and 90° between adjacent layers, as well as alternating chessboard scanning with rotation angles of 67° and 90°, this study offered valuable insights into how these parameters influence the relative density, defect formation, surface roughness, microstructure, crystallographic texture, microhardness, and residual stress of IN939. Key findings from this research revealed that the 45° and 67° samples exhibited the highest relative density, while the 0° and Q67° samples demonstrated the highest average porosity. This indicated the critical role of scanning strategy in optimizing material properties to achieve desired performance. The study observed various types of cracks, including solidification, solid-state, and oxide-induced cracks, in the as-built samples. The 0° sample displayed the most extensive cracking and the highest σ_{max} residual stress values, while the 45° and 67° samples exhibited fewer cracks, indicating the influence of scanning strategy on defect formation. Surface roughness analysis revealed that the chessboard scanning strategy resulted in rougher surfaces compared to the bi-directional scanning, regardless of the rotation angles. Microstructural examination identified differences in grain size and morphology among the samples, with texture analysis indicating cube textures for the 0° and 90° samples and weakened texture intensity for the 45° and 67° samples. These observations underscored the influence of scanning strategy on solidification behaviour and texture development. Residual stress analyses showed significant variations among the samples, with the 0° sample exhibiting the highest σ_{max} residual stress due to pronounced thermal gradients along the build direction. The Q90° sample displayed the highest residual stress in the XZ plane, while the 67° sample exhibited the lowest, suggesting that more uniform thermal conditions during laser scanning can effectively reduce residual stress. In conclusion, this study addressed a critical research gap by providing a detailed understanding of how different scanning strategies affect the material properties of IN939 fabricated by the PBF-LB. The findings offered practical guidance for optimizing scanning parameters, ultimately enhancing the quality and performance of IN939 components.

4. A comprehensive investigation into the effects of various SHT temperatures on the material properties of IN939 fabricated by the PBF-LB was given in Chapter 6. This study

presents the effects of various SHT (1120 ^{o}C, 1160 ^{o}C, 1200 ^{o}C, and 1240 ^{o}C) on the microstructure, grain morphology, and crystallographic texture of IN939 fabricated by the PBF-LB. The study provided critical insights into how these conditions influence the material properties of IN939. Key findings from this research indicated that the high-temperature gradient and rapid solidification inherent to the PBF-LB process resulted in microstructures that differ significantly from those produced by conventional methods. The melt pool morphologies and laser scanning paths were distinct in as-fabricated samples but transformed markedly under different heat treatment conditions. Specifically, SHT at temperatures of 1200 °C and above led to the disappearance of the as-fabricated arc-shaped melt pool and laser scanning path morphologies, transitioning to a mixture of columnar grains in the XZ plane and equiaxed grains in the XY plane. At 1240 °C, a notable transition to isotropic large equiaxed grains occurred in both observation directions, indicating a reduction in microstructural anisotropy. The study also highlighted the precipitation of spherical-like nano-sized γ' phases within the matrix after SHT, contributing to an increase in microhardness values across all conditions. This precipitate formation underscored the influence of heat treatment on enhancing mechanical properties. EBSD analyses revealed that both as-fabricated and solution heat-treated samples maintained a strong {001} texture parallel to the build direction, with intensity values increasing at higher heat treatment temperatures. Recrystallization was observed at 1160 °C, with an increasing fraction of recrystallized grains at higher temperatures. Additionally, the study identified a decrease in the fraction of LAGBs, GND density, and an increase in the average grain size with rising SHT temperatures. In conclusion, this study significantly advanced the understanding of how SHT temperatures impact the microstructure, crystallographic texture, and microhardness of IN939 fabricated by the PBF-LB. The findings provided valuable guidance for optimizing heat treatment parameters to enhance the quality and performance of IN939 components, offering practical insights for both academic research and industrial applications. Future research should explore the aging heat treatment to further refine the mechanical and microstructural properties of IN939 fabricated by the PBF-LB.

5. Chapter 7 was conducted as a preliminary study to better understand the microstructure of Ni-base superalloys fabricated by the PBF-LB and post-heat treatment effects on the microstructural evolution. This study presented a comprehensive investigation into the recrystallization and grain growth behaviour of IN718 alloy fabricated using PBF-LB and subjected to various SHT temperatures (1050 °C, 1150 °C, and 1250 °C) and holding times

(15, 45, and 90 minutes). The primary findings provided significant insights into the microstructural evolution, and texture development of IN718, contributing valuable knowledge for optimizing post-processing techniques in additive manufacturing. The study revealed that the as-built sample exhibited bowl-shaped melt pools and a chessboard-like grain pattern with a cube texture {001}<100>, and significant microstructural changes began at 1150°C for 45 min, suggesting these as threshold values for noticeable recrystallization. Recrystallization started in high dislocation density regions, and the 1150-45 sample showed an 87.3% increase in grain size, while the 1250-45 sample exhibited a 118% increase and a 39% increase in twin boundary fraction. At 1250°C, almost complete recrystallization was achieved, transitioning the texture from the initial cube texture to a first-generation cube-twin texture {122}<212> through a twinning-assisted recrystallization mechanism, evolving further to include cube and P-orientation {011}<112> typical for FCC materials. Solution heat-treated samples contained δ phase, strengthening phases (γ" and γ'), MC carbides, and potentially brittle residual Laves phase due to the slow cooling rate of 5°C/min, resulting in a 20.5% to 26.6% increase in microhardness compared to the as-built sample. This enhancement in hardness, however, may pose machining challenges during post-processing operations. Overall, this study significantly advanced the understanding of the effects of solution heat treatment temperatures and holding times on the microstructure, crystallographic texture, and microhardness of IN718 fabricated by PBF-LB. The detailed analysis offered practical guidelines for optimizing post-processing treatments, ultimately improving the quality and performance of IN718 components in various industrial applications.

8.2 Recommendations for Further Research

The present study successfully achieved the aims by evaluating the influence of the PBF-LB process parameters and post-solution heat treatment on the material properties of IN939, yielding a considerable number of original findings. However, there remain some challenges and critical areas that should be addressed in future research. The following recommendations are suggested for future studies:

- 10 wt.% spatter powder addition into the virgin powder resulted in 0.3% relative density reduction, bigger pore formation and 80% surface roughness increment in the fabricated parts. However, it would be interesting to investigate the effects addition of different amounts of spatter powder (such as 30 wt.% and 50 wt.%) into

the virgin powder on the material properties of the fabricated parts. If the results are promising, spatter powder can be used to produce non-critical parts.

- A detailed investigation was conducted to analyze the effects of varying laser power, laser scanning speed, and hatch distance on the relative density, defect formation, surface roughness, and microstructure of IN939 samples. Mechanical testing such as tensile strength, microhardness and fatigue should be conducted on the samples that possess the highest relative density. Moreover, HIP can be conducted to eliminate defects.
- The effects of alternating bi-directional scanning with rotation angles of 0°, 45°, 67°, and 90° between adjacent layers and alternating chessboard scanning with rotation angles of 67° and 90° were investigated on the relative density, defect formation, surface roughness, microstructure, crystallographic texture, microhardness and residual stress. The tensile test on these samples will be interesting to pursue in the future. Additionally, microcracks were not eliminated as a few microcracks were observed. The effects of stripe scanning strategy, remelting and preheating on the microcracks would be interesting.
- The SHT step was investigated in detail. However, the aging step should be investigated for IN939 fabricated by the PBF-LB. It could be great to conduct mechanical tests such as tensile, fatigue and creep after complete precipitation hardening heat treatment.

References

[1] M.J. Donachie, S.James. Donachie, Superalloys: A Technical Guide, ASM International, 2002.

[2] J.R. Davis, Davis & Associates, ASM Specialty Handbook: Heat Resistant Materials, ASM International, 1997.

[3] J.R. Davis, Davis & Associates, ASM Specialty Handbook: Nickel, Cobalt, and Their Alloys, ASM International, 2000.

[4] A.S. Shaikh, Development of a γ' Precipitation Hardening Ni-Base Superalloy for Additive Manufacturing, Thesis (2018) 102.

[5] M.N. Doğu, Production of Ti-6Al-4V Alloy by 3D Electron Beam Melting Technique and Development of its Post Treatments, Thesis, 2019.

[6] S.E. Atabay, Laser Powder Bed Fusion of Precipitation-Hardened Rene 41 and Rene 77 Nickel Base Superalloys, Ph.D. Thesis, 2021.

[7] S. Sanchez, P. Smith, Z. Xu, G. Gaspard, C.J. Hyde, W.W. Wits, I.A. Ashcroft, H. Chen, A.T. Clare, Powder Bed Fusion of nickel-based superalloys: A review, Int J Mach Tools Manuf 165 (2021). https://doi.org/10.1016/j.ijmachtools.2021.103729.

[8] B. Barroqueiro, A. Andrade-Campos, R.A.F. Valente, V. Neto, Metal additive manufacturing cycle in aerospace industry: A comprehensive review, Journal of Manufacturing and Materials Processing 3 (2019) 1–21. https://doi.org/10.3390/jmmp3030052.

[9] W.E. King, A.T. Anderson, R.M. Ferencz, N.E. Hodge, C. Kamath, S.A. Khairallah, A.M. Rubenchik, Laser powder bed fusion additive manufacturing of metals; physics, computational, and materials challenges, Appl Phys Rev 2 (2015) 041304. https://doi.org/10.1063/1.4937809.

[10] L.N. Carter, M.M. Attallah, R.C. Reed, Laser Powder Bed Fabrication of Nickel-Base Superalloys: Influence of Parameters; Characterisation, Quantification and Mitigation of Cracking, in: 12th International Symposium on Superalloys, Superalloys 2012, 2012.

[11] G. Marchese, S. Parizia, A. Saboori, D. Manfredi, M. Lombardi, P. Fino, D. Ugues, S. Biamino, The influence of the process parameters on the densification and microstructure development of laser powder bed fused inconel 939, Metals (Basel) 10 (2020) 1–19. https://doi.org/10.3390/met10070882.

[12] O.C. Ozaner, G. Dursun, G. Akbulut, Effects of wire-EDM parameters on the surface integrity and mechanical characteristics of additively manufactured Inconel 939, Mater Today Proc 38 (2021) 1861–1865. https://doi.org/10.1016/j.matpr.2020.08.486.

[13] J.B. Wahl, K. Harris, Advanced Ni-Base Superalloys for Small Gas Turbines, The Canadian Journal of Metallurgy and Materials Science 50 (2011) 207–214. https://doi.org/https://doi.org/10.1179/1879139511Y.0000000010.

[14] M.N. Doğu, S. Ozer, M.A. Yalçın, K. Davut, G.M. Bilgin, M.A. Obeidi, H. Brodin, H. Gu, D. Brabazon, Effect of solution heat treatment on the microstructure and crystallographic texture of IN939 fabricated by powder bed fusion-laser beam, Journal of Materials Research and Technology 24 (2023). https://doi.org/https://doi.org/10.1016/j.jmrt.2023.05.152.

[15] M.N. Doğu, A. Mussatto, M.A. Yalçın, S. Ozer, K. Davut, M.A. Obeidi, A. Kumar, S. Hudson, D. O'Neill, R. O'Connor, H. Gu, D. Brabazon, A comprehensive characterization of the effect of spatter powder on IN939 parts fabricated by laser powder bed fusion, Mater Des 235 (2023). https://doi.org/10.1016/j.matdes.2023.112406.

[16] Y.T. Tang, C. Panwisawas, J.N. Ghoussoub, Y. Gong, J.W.G. Clark, A.A.N. Németh, D.G. McCartney, R.C. Reed, Alloys-by-design: Application to new superalloys for additive manufacturing, Acta Mater 202 (2021) 417–436. https://doi.org/10.1016/j.actamat.2020.09.023.

[17] G.M. Volpato, U. Tetzlaff, M.C. Fredel, A comprehensive literature review on laser powder bed fusion of Inconel superalloys, Addit Manuf 55 (2022). https://doi.org/10.1016/j.addma.2022.102871.

[18] I. Rodríguez-Barber, A.M. Fernández-Blanco, I. Unanue-Arruti, I. Madariaga-Rodríguez, S. Milenkovic, M.T. Pérez-Prado, Laser powder bed fusion of the Ni superalloy Inconel 939 using pulsed wave emission, Materials Science and Engineering: A 870 (2023). https://doi.org/10.1016/j.msea.2023.144864.

[19] Z. Li, H. Li, J. Yin, Y. Li, Z. Nie, X. Li, D. You, K. Guan, W. Duan, L. Cao, D. Wang, L. Ke, Y. Liu, P. Zhao, L. Wang, K. Zhu, Z. Zhang, L. Gao, L. Hao, A Review of Spatter in Laser Powder Bed Fusion Additive Manufacturing: In Situ Detection, Generation, Effects, and Countermeasures, Micromachines (Basel) 13 (2022) 1366. https://doi.org/10.3390/mi13081366.

[20] A.N.D. Gasper, B. Szost, X. Wang, D. Johns, S. Sharma, A.T. Clare, I.A. Ashcroft, Spatter and oxide formation in laser powder bed fusion of Inconel 718, Addit Manuf 24 (2018) 446–456. https://doi.org/10.1016/j.addma.2018.09.032.

[21] Z. Chen, A. Raza, E. Hryha, Influence of part geometry on spatter formation in laser powder bed fusion of Inconel 718 alloy revealed by optical tomography, J Manuf Process 81 (2022) 680–695. https://doi.org/10.1016/j.jmapro.2022.07.031.

[22] K. Gruber, I. Smolina, M. Kasprowicz, T. Kurzynowski, Evaluation of inconel 718 metallic powder to optimize the reuse of powder and to improve the performance and sustainability of the laser powder bed fusion (Lpbf) process, Materials 14 (2021). https://doi.org/10.3390/ma14061538.

[23] J. Yin, D. Wang, H. Wei, L. Yang, L. Ke, M. Hu, W. Xiong, G. Wang, H. Zhu, X. Zeng, Dual-beam laser-matter interaction at overlap region during multi-laser powder bed fusion manufacturing, Addit Manuf 46 (2021) 102178. https://doi.org/10.1016/j.addma.2021.102178.

[24] A. Raza, C. Pauzon, E. Hryha, A. Markström, P. Forêt, Spatter oxidation during laser powder bed fusion of Alloy 718: Dependence on oxygen content in the process atmosphere, Addit Manuf 48 (2021). https://doi.org/10.1016/j.addma.2021.102369.

[25] A.N.D. Gasper, D. Hickman, I. Ashcroft, S. Sharma, X. Wang, B. Szost, D. Johns, A.T. Clare, Oxide and spatter powder formation during laser powder bed fusion of Hastelloy X, Powder Technol 354 (2019) 333–337. https://doi.org/10.1016/j.powtec.2019.06.004.

[26] R. Esmaeilizadeh, U. Ali, A. Keshavarzkermani, Y. Mahmoodkhani, E. Marzbanrad, E. Toyserkani, On the effect of spatter particles distribution on the quality of Hastelloy X parts made by laser powder-bed fusion additive manufacturing, J Manuf Process 37 (2019) 11–20. https://doi.org/10.1016/j.jmapro.2018.11.012.

[27] C. Schwerz, A. Raza, X. Lei, L. Nyborg, E. Hryha, H. Wirdelius, In-situ detection of redeposited spatter and its influence on the formation of internal flaws in laser powder bed fusion, Addit Manuf 47 (2021) 102370. https://doi.org/10.1016/j.addma.2021.102370.

[28] H. Jia, H. Sun, H. Wang, Y. Wu, H. Wang, Scanning strategy in selective laser melting (SLM): a review, International Journal of Advanced Manufacturing Technology 113 (2021) 2413–2435. https://doi.org/10.1007/s00170-021-06810-3.

[29] K. Dai, X. He, W. Zhang, D. Kong, R. Guo, M. Hu, K. He, C. Dong, Tailoring the microstructure and mechanical properties for Hastelloy X alloy by laser powder bed fusion via scanning strategy, Mater Des 235 (2023). https://doi.org/10.1016/j.matdes.2023.112386.

[30] H.Y. Wan, Z.J. Zhou, C.P. Li, G.F. Chen, G.P. Zhang, Effect of scanning strategy on grain structure and crystallographic texture of Inconel 718 processed by selective laser melting, J Mater Sci Technol 34 (2018) 1799–1804. https://doi.org/10.1016/j.jmst.2018.02.002.

[31] L. Liu, D. Wang, Y. Yang, Z. Wang, Z. Qian, S. Wu, J. Tang, C. Han, C. Tan, Effect of Scanning Strategies on the Microstructure and Mechanical Properties of Inconel 718 Alloy Fabricated by Laser Powder Bed Fusion, Adv Eng Mater 25 (2023). https://doi.org/10.1002/adem.202200492.

[32] J. Xu, Y. Ding, Y. Gao, H. Wang, Y. Hu, D. Zhang, Grain refinement and crack inhibition of hard-to-weld Inconel 738 alloy by altering the scanning strategy during selective laser melting, Mater Des 209 (2021) 109940. https://doi.org/10.1016/j.matdes.2021.109940.

[33] A.S. Shaikh, M. Rashidi, K. Minet-Lallemand, E. Hryha, On as-built microstructure and necessity of solution treatment in additively manufactured Inconel 939, Powder Metallurgy 66 (2023) 3–11. https://doi.org/10.1080/00325899.2022.2041787.

[34] D. Newell, Solution Anneal Heat Treatments to Enhance Mechanical Performance of Additively Manufactured IN718, Ph.D. Thesis, 2020.

[35] R.C. Reed, The superalloys: fundamentals and applications, Cambridge University Press, 2006.

[36] A.P. Mouritz, Introduction to Aerospace Materials, Woodhead Publishing Limited, 2012. https://doi.org/10.2514/4.869198.

[37] T. Saraçyakupoğlu, The Temperature and Material Distribution Inside a Gas Turbine Engine Mini Review, (2022) 4–6. https://doi.org/10.31031/EME.2022.04.000576.

[38] R.H. AL-Nafeay, A.O. AL-Roubaiy, H. Omidvar, Overview of Joining and Repairing Techniques of Ni-Based Superalloy for Industrial Gas Turbine Applications, IOP Conf Ser Mater Sci Eng 1094 (2021) 012141. https://doi.org/10.1088/1757-899x/1094/1/012141.

[39] K. Minet, A. Saharan, A. Loesser, N. Raitanen, Superalloys, powders, process monitoring in additive manufacturing, in: Additive Manufacturing for the Aerospace Industry, Elsevier Inc., 2019: pp. 163–185. https://doi.org/10.1016/B978-0-12-814062-8.00009-1.

[40] B. Geddes, H. Leon, X. Huang, Superalloys: Alloying and Performance, ASM International, 2010.

[41] S. Özer, Effect of Post-Processing Heat Treatment on the Mechanical Properties of Inconel 718 Fabricated by Selective Laser Melting, M.Sc. Thesis, 2020.

[42] T.M. Pollock, S. Tin, Nickel-based superalloys for advanced turbine engines: Chemistry, microstructure, and properties, J Propuls Power 22 (2006) 361–374. https://doi.org/10.2514/1.18239.

[43] C.T. Sims, A History of Superalloy Metallurgy for Superalloy Metallurgists, Superalloys (1984) 399–419. https://doi.org/10.7449/1984/Superalloys_1984_399_419.

[44] M.N. Dogu, E. McCarthy, R. McCann, V. Mahato, A. Caputo, M. Bambach, I.U. Ahad, D. Brabazon, Digitisation of metal AM for part microstructure and property control, International Journal of Material Forming 15 (2022). https://doi.org/10.1007/s12289-022-01686-4.

[45] M.N. Doğu, K. Davut, M.A. Obeidi, M.A. Yalçın, H. Gu, T.S.E. Low, J. Ginn, D. Brabazon, Recrystallization and grain growth kinetics of IN718 manufactured by laser powder bed fusion, Journal of Materials Research and Technology 19 (2022) 4242–4257. https://doi.org/10.1016/j.jmrt.2022.06.157.

[46] S. Ozer, G. Mert, K. Davut, Z. Esen, A.F. Dericioglu, Effect of post fabrication aging treatment on the microstructure, crystallographic texture and elevated temperature mechanical properties of IN718 alloy fabricated by selective laser melting, Journal of Materials Processing Tech. 306 (2022) 117622. https://doi.org/10.1016/j.jmatprotec.2022.117622.

[47] S. Singh Handa, Precipitation of Carbides in a Ni-based Superalloy, M.Sc. Thesis, 2014.

[48] J. Risse, Additive Manufacturing of Nickel-Base Superalloy IN738LC by Laser Powder Bed Fusion, Ph.D. Thesis, 2019.

[49] R.A. Ricks, A.J. Porter, R.C. Ecob, The Growth of γ′ Precipitates Superalloys in Nickel-Base, Acta Metall. 31 (1983) 43–53.

[50] A. Baldan, Review Progress in Ostwald ripening theories and their applications to the γ-precipitates in nickel-base superalloys Part II Nickel-base superalloys, J Mater Sci 37 (2002) 2379–2405.

[51] F. Masoumi, D. Shahriari, M. Jahazi, J. Cormier, A. Devaux, Kinetics and Mechanisms of γ′ Reprecipitation in a Ni-based Superalloy, Sci Rep 6 (2016). https://doi.org/10.1038/srep28650.

[52] D. Zhang, Z. Feng, C. Wang, W. Wang, Z. Liu, W. Niu, Comparison of microstructures and mechanical properties of Inconel 718 alloy processed by selective laser melting and casting, Materials Science and Engineering A 724 (2018) 357–367. https://doi.org/10.1016/j.msea.2018.03.073.

[53] E.M. Fayed, M. Saadati, D. Shahriari, V. Brailovski, M. Jahazi, M. Medraj, Effect of homogenization and solution treatments time on the elevated-temperature mechanical behavior of Inconel 718 fabricated by laser powder bed fusion, Sci Rep 11 (2021) 1–17. https://doi.org/10.1038/s41598-021-81618-5.

[54] G.K. Bouse, Eta (η) and Platelet Phases in Investment Cast Superalloys, Superalloys (1996).

[55] L.O. Osoba, A Study on Laser Weldability Improvement of Newly Developed Haynes 282 Superalloy, Ph.D. Thesis, 2012.

[56] F. Sun, J. Zhang, Topologically close-packed phase precipitation in Ni-based superalloys, Adv Mat Res 320 (2011) 26–32. https://doi.org/10.4028/www.scientific.net/AMR.320.26.

[57] F. Stein, A. Leineweber, Laves phases: a review of their functional and structural applications and an improved fundamental understanding of stability and properties, J Mater Sci 56 (2021) 5321–5427. https://doi.org/10.1007/s10853-020-05509-2.

[58] M.T. Boyraz, IN 738 LC Microstructure Optimization with Heat Treatment and Simulation to Improve Mechanical Properties of Turbine Blades, M.Sc. Thesis, 2018.

[59] A.J. Goodfellow, E.I. Galindo-Nava, C. Schwalbe, H.J. Stone, The role of composition on the extent of individual strengthening mechanisms in polycrystalline Ni-based superalloys, Mater Des 173 (2019). https://doi.org/10.1016/j.matdes.2019.107760.

[60] W.D. Callister, D.G. Rethwisch, Materials Science and Engineering an Introduction, 8th ed., WILEY, 2009.

[61] R.W. Kozar, A. Suzuki, W.W. Milligan, J.J. Schirra, M.F. Savage, T.M. Pollock, Strengthening mechanisms in polycrystalline multimodal nickel-base superalloys, Metall Mater Trans A Phys Metall Mater Sci 40 (2009) 1588–1603. https://doi.org/10.1007/s11661-009-9858-5.

[62] T.B. Gibbons, R. Stickler, IN939: Metallurgy, Properties and Performance, High Temperature Alloys for Gas Turbines (1982). https://doi.org/10.1007/978-94-009-7907-9.

[63] S. Banoth, C.W. Li, Y. Hiratsuka, K. Kakehi, The effect of recrystallization on creep properties of alloy in939 fabricated by selective laser melting process, Metals (Basel) 10 (2020) 1–16. https://doi.org/10.3390/met10081016.

[64] S.W.K. Shaw, Response of IN-939 to Process Variations, Superalloys (1980).

[65] K.M. Delargy, G.D.W. Smith, Phase Composition and Phase Stability of a High-Chromium Nickel-Based Superalloy, IN939, Metallurgical Transactions. A, Physical Metallurgy and Materials Science 14 A (1983) 1771–1783. https://doi.org/10.1007/BF02645547.

[66] J. Litz, A. Rahmel, M. Schorr, J. Weisst, Scale Formation on the Ni-Base Superalloys IN 939 and IN 738 LC, Oxidation of Metals 32 (1988) 1989.

[67] Siemens Energy, Material Datasheet Nickel Alloy Inconel 939, (2020). www.siemens-energy.com/am.

[68] EOS, Nickel Alloy IN939 Material Data Sheet Metal Solutions, (2020). https://www.eos.info/en-us/metal-solutions/metal-materials/data-sheets/mds-eos-nickelalloy-in939.

[69] SLM Solutions, Material Data Sheet Ni-Alloy IN939, (2020). https://www.slm-solutions.com/fileadmin/Content/Powder/MDS/MDS_Ni-Alloy_IN939_0219_EN.pdf.

[70] A. Formenti, A. Eliasson, H. Fredriksson, On the dendritic growth and microsegregation in Ni-base superalloys In718, In625 and In939, High Temperature Materials and Processes 24 (2005) 221–238. https://doi.org/https://doi.org/10.1515/HTMP.2005.24.4.221.

[71] F. Arhami, S.E. Mirsalehi, The effect of heat treatment sequence on microstructure and mechanical properties of diffusion brazed IN-939 superalloy, J Mater Process Technol 266 (2019) 351–362. https://doi.org/10.1016/j.jmatprotec.2018.11.020.

[72] Z. Mišković, M. Jovanović, M. Gligić, B. Lukić, Microstructural investigation of IN 939 superalloy, Vacuum 43 (1992) 709–711. https://doi.org/10.1016/0042-207X(92)90115-D.

[73] M.Y. Nazmy, C. Wüthrich, Creep crack growth in IN-738 and IN-939 nickel-base superalloys, Materials Science and Engineering 61 (1983) 119–125. https://doi.org/10.1016/0025-5416(83)90194-5.

[74] W. Philpott, M.A.E. Jepson, R.C. Thomson, Comparison of the effects of a conventional heat treatment between cast and selective laser melted IN939 alloy, in: Advances in Materials Technology for Fossil Power Plants - Proceedings from the 8th International Conference, 2016: pp. 735–746.

[75] A. Formenti, A. Eliasson, A. Mitchell, H. Frediksson, Solidification Sequence and Carbide Precipitation in Ni-Base Superalloys In718, In625 and In939, High Temperature Materials and Processes 24 (2005) 239–258. https://doi.org/https://doi.org/10.1515/HTMP.2005.24.4.239.

[76] M. Okazaki, M. Sakaguchi, O. Sasaki, K. Namba, Degradation in fatigue crack propagation resistance of a gas turbine vane after long term service, Adv Mat Res 278 (2011) 375–380. https://doi.org/10.4028/www.scientific.net/AMR.278.375.

[77] M.R. Jahangiri, H. Arabi, S.M.A. Boutorabi, Comparison of microstructural stability of IN939 superalloy with two different manufacturing routes during long-time aging, Transactions of Nonferrous Metals Society of China (English Edition) 24 (2014) 1717–1729. https://doi.org/10.1016/S1003-6326(14)63245-3.

[78] M. Jahangiri, Influence of Cooling Rate During Solidification on Microstructural Features and γ′ Size and Morphology in Cast IN939 Superalloy, International Journal of Metalcasting (2023). https://doi.org/10.1007/s40962-023-01183-7.

[79] M.R. Jahangiri, H. Arabi, S.M.A. Boutorabi, High-temperature compression behavior of cast and homogenized IN939 superalloy, Metall Mater Trans A Phys Metall Mater Sci 44 (2013) 1827–1841. https://doi.org/10.1007/s11661-012-1538-1.

[80] K.M. Delargy, S.W.K. Shaw, G.D.W. Smith, Effects of heat treatment on mechanical properties of high-chromium nickel-base superalloy IN 939, Materials Science and Technology 2 (1986) 1031–1037.

[81] M.R. Jahangiri, H. Arabi, S.M.A. Boutorabi, Development of wrought precipitation strengthened IN939 superalloy, Materials Science and Technology (United Kingdom) 28 (2012) 1470–1478. https://doi.org/10.1179/1743284712Y.0000000073.

[82] M.N. Doğu, S. Ozer, M.A. Yalçın, K. Davut, G.M. Bilgin, M.A. Obeidi, H. Brodin, H. Gu, D. Brabazon, Effect of Solution Heat Treatment on the Microstructure and Crystallographic Texture of In939 Fabricated by Powder Bed Fusion-Laser Beam, SSRN (2023). https://doi.org/10.2139/ssrn.4365807.

[83] Y. Li, X. Liang, Y. Yu, H. Li, W. Kan, F. Lin, Microstructures and mechanical properties evolution of IN939 alloy during electron beam selective melting process, J Alloys Compd 883 (2021) 160934. https://doi.org/10.1016/j.jallcom.2021.160934.

[84] T. Wimmer, Y. Mick, B. Weigand, Experimental investigation into capabilities of laser powder bed fusion to produce wavy macro-channels from IN939, Addit Manuf 35 (2020) 101345. https://doi.org/10.1016/j.addma.2020.101345.

[85] B. Zhang, H. Ding, A.C. Meng, S. Nemati, S. Guo, W.J. Meng, Crack reduction in Inconel 939 with Si addition processed by laser powder bed fusion additive manufacturing, Addit Manuf 72 (2023). https://doi.org/10.1016/j.addma.2023.103623.

[86] A. Fardan, U. Klement, H. Brodin, E. Hryha, Effect of Part Thickness and Build Angle on the Microstructure, Surface Roughness, and Mechanical Properties of Additively Manufactured IN-939, Metall Mater Trans A Phys Metall Mater Sci 54 (2023) 1792–1807. https://doi.org/10.1007/s11661-022-06940-7.

[87] E. Nandha Kumar, K.S. Athira, S. Chatterjee, D. Srinivasan, Effect of Heat Treatment on Structure and Properties of Laser Powder Bed Fusion Inconel 939, in: IAM2022, 2022. https://doi.org/https://doi.org/10.1115/IAM2022-93945.

[88] A. Bridges, J. Shingledecker, A. Torkaman, L. Houck, Metallurgical Evaluation of an Additively Manufactured Nickel-Base Superalloy for Gas Turbine Guide Vanes, in: Proceedings of ASME Turbo Expo 2020, 2020. http://asmedigitalcollection.asme.org/GT/proceedings-pdf/GT2020/84195/V008T18A005/6616399/v008t18a005-gt2020-14808.pdf.

[89] I. Šulák, T. Babinský, A. Chlupová, A. Milovanović, L. Náhlík, Effect of building direction and heat treatment on mechanical properties of Inconel 939 prepared by additive manufacturing, Journal of Mechanical Science and Technology 37 (2023) 1071–1076. https://doi.org/10.1007/s12206-022-2101-7.

[90] G. Dursun, A. Orhangul, A. Urkmez, G. Akbulut, Understanding the Parameter Effects on Densification and Single Track Formation of Laser Powder Bed Fusion Inconel 939, in: Procedia CIRP, Elsevier B.V., 2022: pp. 258–263. https://doi.org/10.1016/j.procir.2022.03.045.

[91] A.R.P. Singh, Mechanisms of Ordered Gamma Prime Precipitation in Nickel Base Superalloys, Ph.D. Thesis, 2011.

[92] H. Kazempour-Liasi, M. Tajally, H. Abdollah-Pour, Effects of pre- and post-weld heat treatment cycles on the liquation and strain-age cracking of IN939 superalloy,

Engineering Research Express 1 (2019). https://doi.org/10.1088/2631-8695/ab4d6c.

[93] J.F.S. Markanday, Applications of alloy design to cracking resistance of additively manufactured Ni-based alloys, Materials Science and Technology 38 (2022) 1300–1314. https://doi.org/10.1080/02670836.2022.2068759.

[94] DuPont, John N, Lippold, John C, Kiser, Samuel D, Welding Metallurgy and Weldability of Nickel-Base Alloys, 2009.

[95] K. Sindo, Welding Metallurgy, 2002. https://doi.org/https://doi.org/10.1002/0471434027.index.

[96] D. Tomus, P.A. Rometsch, M. Heilmaier, X. Wu, Effect of minor alloying elements on crack-formation characteristics of Hastelloy-X manufactured by selective laser melting, Addit Manuf 16 (2017) 65–72. https://doi.org/10.1016/j.addma.2017.05.006.

[97] N.J. Harrison, I. Todd, K. Mumtaz, Reduction of micro-cracking in nickel superalloys processed by Selective Laser Melting: A fundamental alloy design approach, Acta Mater 94 (2015) 59–68. https://doi.org/10.1016/j.actamat.2015.04.035.

[98] M.C. Lam, S.C.V. Lim, H. Song, Y. Zhu, X. Wu, A. Huang, Scanning strategy induced cracking and anisotropic weakening in grain texture of additively manufactured superalloys, Addit Manuf 52 (2022). https://doi.org/10.1016/j.addma.2022.102660.

[99] S. Griffiths, H. Ghasemi Tabasi, T. Ivas, X. Maeder, A. De Luca, K. Zweiacker, R. Wróbel, J. Jhabvala, R.E. Logé, C. Leinenbach, Combining alloy and process modification for micro-crack mitigation in an additively manufactured Ni-base superalloy, Addit Manuf 36 (2020). https://doi.org/10.1016/j.addma.2020.101443.

[100] A. Basak, Additive Manufacturing of High-Gamma Prime Nickel-Based Superalloys through Selective Laser Melting (SLM), Solid Freeform Fabrication 2019: Proceedings of the 30th Annual International (2019).

[101] J. Xu, H. Gruber, R.L. Peng, J. Moverare, A novel γ′-strengthened nickel-based superalloy for laser powder bed fusion, Materials 13 (2020) 1–12. https://doi.org/10.3390/ma13214930.

[102] Q. Wei, Y. Xie, Q. Teng, M. Shen, S. Sun, C. Cai, Crack Types, Mechanisms, and Suppression Methods during High-energy Beam Additive Manufacturing of Nickel-based Superalloys: A Review, Chinese Journal of Mechanical Engineering: Additive Manufacturing Frontiers 1 (2022) 100055. https://doi.org/10.1016/j.cjmeam.2022.100055.

[103] C. Guo, G. Li, S. Li, X. Hu, H. Lu, X. Li, Z. Xu, Y. Chen, Q. Li, J. Lu, Q. Zhu, Additive manufacturing of Ni-based superalloys: Residual stress, mechanisms of crack formation and strategies for crack inhibition, Nano Materials Science 5 (2023) 53–77. https://doi.org/10.1016/j.nanoms.2022.08.001.

[104] H. Wu, D. Zhang, B. Yang, C. Chen, Y. Li, K. Zhou, L. Jiang, R. Liu, Microstructural evolution and defect formation in a powder metallurgy nickel-based superalloy processed by selective laser melting, J Mater Sci Technol 36 (2020) 7–17. https://doi.org/10.1016/j.jmst.2019.08.007.

[105] E. Chauvet, P. Kontis, E.A. Jägle, B. Gault, D. Raabe, C. Tassin, J.J. Blandin, R. Dendievel, B. Vayre, S. Abed, G. Martin, Hot cracking mechanism affecting a non-weldable Ni-based superalloy produced by selective electron Beam Melting, Acta Mater 142 (2018) 82–94. https://doi.org/10.1016/j.actamat.2017.09.047.

[106] L. Liu, D. Wang, G. Deng, Z. Liu, C. Tan, X. Zhou, C. Han, R. Jiang, Y. Yang, Crack inhibition to enhance strength-ductility of CM247LC alloy fabricated by laser powder bed fusion, Materials Science and Engineering: A 875 (2023). https://doi.org/10.1016/j.msea.2023.145114.

[107] L. Aucott, D. Huang, H.B. Dong, S.W. Wen, J. Marsden, A. Rack, A.C.F. Cocks, A Three-Stage Mechanistic Model for Solidification Cracking During Welding of Steel, Metall Mater Trans A Phys Metall Mater Sci 49 (2018) 1674–1682. https://doi.org/10.1007/s11661-018-4529-z.

[108] M. Cloots, P.J. Uggowitzer, K. Wegener, Investigations on the microstructure and crack formation of IN738LC samples processed by selective laser melting using Gaussian and doughnut profiles, Mater Des 89 (2016) 770–784. https://doi.org/10.1016/j.matdes.2015.10.027.

[109] J.J. Pepe, W.F. Savage, The Weld Heat-Affected Zone of the 18Ni Maraging Steels, Weld J (1970) 545–553.

[110] O.A. Ojo, N.L. Richards, M.C. Chaturvedi, Contribution of constitutional liquation of gamma prime precipitate to weld HAZ cracking of cast Inconel 738 superalloy, Scr Mater 50 (2004) 641–646. https://doi.org/10.1016/j.scriptamat.2003.11.025.

[111] W. Ren, F. Lu, R. Yang, X. Liu, Z. Li, Liquation cracking in fiber laser welded joints of inconel 617, J Mater Process Technol 226 (2015) 214–220. https://doi.org/10.1016/j.jmatprotec.2015.07.004.

[112] X. Zhang, H. Chen, L. Xu, J. Xu, X. Ren, X. Chen, Cracking mechanism and susceptibility of laser melting deposited Inconel 738 superalloy, Mater Des 183 (2019). https://doi.org/10.1016/j.matdes.2019.108105.

[113] Y. Chen, F. Lu, K. Zhang, P. Nie, S.R. Elmi Hosseini, K. Feng, Z. Li, P.K. Chu, Investigation of dendritic growth and liquation cracking in laser melting deposited Inconel 718 at different laser input angles, Mater Des 105 (2016) 133–141. https://doi.org/10.1016/j.matdes.2016.05.034.

[114] M.D. Rowe, Ranking the Resistance of Wrought Superalloys to Strain-Age Cracking., Weld J (2006) 27–34.

[115] J.H. Boswell, D. Clark, W. Li, M.M. Attallah, Cracking during thermal post-processing of laser powder bed fabricated CM247LC Ni-superalloy, Mater Des 174 (2019). https://doi.org/10.1016/j.matdes.2019.107793.

[116] M.G. Collins, J.C. Lippold, An Investigation of Ductility Dip Cracking in Nickel-Based Filler Materials-Part I, Weld J (2003).

[117] H. Kazempour-Liasi, M. Tajally, H. Abdollah-Pour, Liquation cracking in the heat-affected zone of IN939 superalloy tungsten inert gas weldments, International Journal of Minerals, Metallurgy and Materials 27 (2020) 764–773. https://doi.org/10.1007/s12613-019-1954-y.

[118] M.A. González, D.I. Martínez, A. Pérez, H. Guajardo, A. Garza, Microstructural response to heat affected zone cracking of prewelding heat-treated Inconel 939 superalloy, Mater Charact 62 (2011) 1116–1123. https://doi.org/10.1016/j.matchar.2011.09.006.

[119] A. Mashhuriazar, C. Hakan Gur, Z. Sajuri, H. Omidvar, Effects of heat input on metallurgical behavior in HAZ of multi-pass and multi-layer welded IN-939

superalloy, Journal of Materials Research and Technology 15 (2021) 1590–1603. https://doi.org/10.1016/j.jmrt.2021.08.113.

[120] M.N. Doğu, Z. Esen, K. Davut, E. Tan, B. Gümüş, A.F. Dericioglu, Microstructural and texture evolution during thermo-hydrogen processing of Ti6Al4V alloys produced by electron beam melting, Mater Charact 168 (2020). https://doi.org/10.1016/j.matchar.2020.110549.

[121] S.M. Yusuf, S. Cutler, N. Gao, Review: The Impact of Metal Additive Manufacturing on the Aerospace Industry, Metals (Basel) 9 (2019) 1286. https://doi.org/https://doi.org/10.3390/met9121286.

[122] B. Blakey-Milner, P. Gradl, G. Snedden, M. Brooks, J. Pitot, E. Lopez, M. Leary, F. Berto, A. du Plessis, Metal additive manufacturing in aerospace: A review, Mater Des 209 (2021) 110008. https://doi.org/10.1016/j.matdes.2021.110008.

[123] A. Gisario, M. Kazarian, F. Martina, M. Mehrpouya, Metal additive manufacturing in the commercial aviation industry: A review, J Manuf Syst 53 (2019) 124–149. https://doi.org/10.1016/j.jmsy.2019.08.005.

[124] T. DebRoy, H.L. Wei, J.S. Zuback, T. Mukherjee, J.W. Elmer, J.O. Milewski, A.M. Beese, A. Wilson-Heid, A. De, W. Zhang, Additive manufacturing of metallic components – Process, structure and properties, Prog Mater Sci 92 (2018) 112–224. https://doi.org/10.1016/j.pmatsci.2017.10.001.

[125] L. Hitzler, M. Merkel, W. Hall, A. Öchsner, A Review of Metal Fabricated with Laser- and Powder-Bed Based Additive Manufacturing Techniques: Process, Nomenclature, Materials, Achievable Properties, and its Utilization in the Medical Sector, Adv Eng Mater 20 (2018). https://doi.org/10.1002/adem.201700658.

[126] A. Mussatto, R. Groarke, R.K. Vijayaraghavan, C. Hughes, P.J. Mcnally, Y. Delaure, D. Brabazon, Assessing dependency of part properties on the printing location in laser-powder bed fusion metal additive manufacturing, Mater Today Commun 30 (2022). https://doi.org/10.1016/j.mtcomm.2022.103209.

[127] M.A. Obeidi, A. Conway, A. Mussatto, M.N. Dogu, S.P. Sreenilayam, H. Ayub, I.U. Ahad, D. Brabazon, Effects of powder compression and laser re-melting on the microstructure and mechanical properties of additively manufactured parts in laser-

powder bed fusion, Results in Materials 13 (2022) 100264. https://doi.org/10.1016/j.rinma.2022.100264.

[128] M. Srivastava, S. Rathee, Additive manufacturing: recent trends, applications and future outlooks, Progress in Additive Manufacturing 7 (2022) 261–287. https://doi.org/10.1007/s40964-021-00229-8.

[129] W.S.W. Harun, M.S.I.N. Kamariah, N. Muhamad, S.A.C. Ghani, F. Ahmad, Z. Mohamed, A review of powder additive manufacturing processes for metallic biomaterials, Powder Technol 327 (2018) 128–151. https://doi.org/10.1016/j.powtec.2017.12.058.

[130] M.A. Obeidi, Metal additive manufacturing by laser-powder bed fusion: Guidelines for process optimisation, Results in Engineering 15 (2022) 100473. https://doi.org/10.1016/j.rineng.2022.100473.

[131] M. Ahmed Obeidi, A. Mussatto, R. Groarke, R.K. Vijayaraghavan, A. Conway, F. Rossi Kaschel, E. McCarthy, O. Clarkin, R. O'Connor, D. Brabazon, Comprehensive assessment of spatter material generated during selective laser melting of stainless steel, Mater Today Commun 25 (2020) 101294. https://doi.org/10.1016/j.mtcomm.2020.101294.

[132] Fraunhofer IFAM, Laser Powder Bed Fusion (PBF-LB/M), (n.d.). https://www.ifam.fraunhofer.de/en/technologies/laser-beam-melting.html (accessed February 9, 2024).

[133] J.P. Oliveira, A.D. LaLonde, J. Ma, Processing parameters in laser powder bed fusion metal additive manufacturing, Mater Des 193 (2020) 1–12. https://doi.org/10.1016/j.matdes.2020.108762.

[134] O.A. Mohamed, S.H. Masood, W. Xu, Nickel-titanium shape memory alloys made by selective laser melting: a review on process optimisation, Adv Manuf 10 (2022) 24–58. https://doi.org/10.1007/s40436-021-00376-9.

[135] N. Ahmed, I. Barsoum, G. Haidemenopoulos, R.K.A. Al-Rub, Process parameter selection and optimization of laser powder bed fusion for 316L stainless steel: A review, J Manuf Process 75 (2022) 415–434. https://doi.org/10.1016/j.jmapro.2021.12.064.

[136] L. Scime, J. Beuth, Melt pool geometry and morphology variability for the Inconel 718 alloy in a laser powder bed fusion additive manufacturing process, Addit Manuf 29 (2019). https://doi.org/10.1016/j.addma.2019.100830.

[137] P. Kumar, J. Farah, J. Akram, C. Teng, J. Ginn, M. Misra, Influence of laser processing parameters on porosity in Inconel 718 during additive manufacturing, International Journal of Advanced Manufacturing Technology 103 (2019) 1497–1507. https://doi.org/10.1007/s00170-019-03655-9.

[138] N. Perevoshchikova, J. Rigaud, Y. Sha, M. Heilmaier, B. Finnin, E. Labelle, X. Wu, Optimisation of selective laser melting parameters for the Ni-based superalloy IN-738 LC using Doehlert's design, Rapid Prototyp J 23 (2017) 881–892. https://doi.org/10.1108/RPJ-04-2016-0063.

[139] C. Guo, S. Li, S. Shi, X. Li, X. Hu, Q. Zhu, R.M. Ward, Effect of processing parameters on surface roughness, porosity and cracking of as-built IN738LC parts fabricated by laser powder bed fusion, J Mater Process Technol 285 (2020). https://doi.org/10.1016/j.jmatprotec.2020.116788.

[140] Q. Shi, D. Gu, M. Xia, S. Cao, T. Rong, Effects of laser processing parameters on thermal behavior and melting/solidification mechanism during selective laser melting of TiC/Inconel 718 composites, Opt Laser Technol 84 (2016) 9–22. https://doi.org/10.1016/j.optlastec.2016.04.009.

[141] D. Grange, J.D. Bartout, B. Macquaire, C. Colin, Processing a non-weldable nickel-base superalloy by Selective Laser Melting: role of the shape and size of the melt pools on solidification cracking, Materialia (Oxf) 12 (2020). https://doi.org/10.1016/j.mtla.2020.100686.

[142] Y. Li, M. Založnik, J. Zollinger, L. Dembinski, A. Mathieu, Effects of the powder, laser parameters and surface conditions on the molten pool formation in the selective laser melting of IN718, J Mater Process Technol 289 (2021). https://doi.org/10.1016/j.jmatprotec.2020.116930.

[143] D. Grange, A. Queva, G. Guillemot, M. Bellet, J.D. Bartout, C. Colin, Effect of processing parameters during the laser beam melting of Inconel 738: Comparison between simulated and experimental melt pool shape, J Mater Process Technol 289 (2021). https://doi.org/10.1016/j.jmatprotec.2020.116897.

[144] M. Sadowski, L. Ladani, W. Brindley, J. Romano, Optimizing quality of additively manufactured Inconel 718 using powder bed laser melting process, Addit Manuf 11 (2016) 60–70. https://doi.org/10.1016/j.addma.2016.03.006.

[145] H. Yang, L. Meng, S. Luo, Z. Wang, Microstructural evolution and mechanical performances of selective laser melting Inconel 718 from low to high laser power, J Alloys Compd 828 (2020). https://doi.org/10.1016/j.jallcom.2020.154473.

[146] M. Balbaa, S. Mekhiel, M. Elbestawi, J. McIsaac, On selective laser melting of Inconel 718: Densification, surface roughness, and residual stresses, Mater Des 193 (2020) 108818. https://doi.org/10.1016/j.matdes.2020.108818.

[147] A. Mussatto, Re-inforcing nano-particle integration into metal AM and produced part characterisation, Ph.D. Thesis, 2022.

[148] G. Marchese, X. Garmendia Colera, F. Calignano, M. Lorusso, S. Biamino, P. Minetola, D. Manfredi, Characterization and Comparison of Inconel 625 Processed by Selective Laser Melting and Laser Metal Deposition, Adv Eng Mater 19 (2017). https://doi.org/10.1002/adem.201600635.

[149] T. Mukherjee, H.L. Wei, A. De, T. DebRoy, Heat and fluid flow in additive manufacturing – Part II: Powder bed fusion of stainless steel, and titanium, nickel and aluminum base alloys, Comput Mater Sci 150 (2018) 369–380. https://doi.org/10.1016/j.commatsci.2018.04.027.

[150] I. Koutiri, E. Pessard, P. Peyre, O. Amlou, T. De Terris, Influence of SLM process parameters on the surface finish, porosity rate and fatigue behavior of as-built Inconel 625 parts, J Mater Process Technol 255 (2018) 536–546. https://doi.org/10.1016/j.jmatprotec.2017.12.043.

[151] X. Su, Y. Yang, Research on track overlapping during Selective Laser Melting of powders, J Mater Process Technol 212 (2012) 2074–2079. https://doi.org/10.1016/j.jmatprotec.2012.05.012.

[152] M. Ahmed Obeidi, S.M. Uí Mhurchadha, R. Raghavendra, A. Conway, C. Souto, D. Tormey, I.U. Ahad, D. Brabazon, Comparison of the porosity and mechanical performance of 316L stainless steel manufactured on different laser powder bed fusion metal additive manufacturing machines, Journal of Materials Research and Technology 13 (2021) 2361–2374. https://doi.org/10.1016/j.jmrt.2021.06.027.

[153] Q.B. Nguyen, D.N. Luu, S.M.L. Nai, Z. Zhu, Z. Chen, J. Wei, The role of powder layer thickness on the quality of SLM printed parts, Archives of Civil and Mechanical Engineering 18 (2018) 948–955. https://doi.org/10.1016/j.acme.2018.01.015.

[154] J. Ye, S.A. Khairallah, A.M. Rubenchik, M.F. Crumb, G. Guss, J. Belak, M.J. Matthews, Energy Coupling Mechanisms and Scaling Behavior Associated with Laser Powder Bed Fusion Additive Manufacturing, Adv Eng Mater 21 (2019). https://doi.org/10.1002/adem.201900185.

[155] V.S. Sufiiarov, A.A. Popovich, E. V. Borisov, I.A. Polozov, D. V. Masaylo, A. V. Orlov, The Effect of Layer Thickness at Selective Laser Melting, in: Procedia Eng, Elsevier Ltd, 2017: pp. 126–134. https://doi.org/10.1016/j.proeng.2017.01.179.

[156] M. Amirjan, H. Sakiani, Effect of scanning strategy and speed on the microstructure and mechanical properties of selective laser melted IN718 nickel-based superalloy, International Journal of Advanced Manufacturing Technology 103 (2019) 1769–1780. https://doi.org/10.1007/s00170-019-03545-0.

[157] N.T. Aboulkhair, N.M. Everitt, I. Ashcroft, C. Tuck, Reducing porosity in AlSi10Mg parts processed by selective laser melting, Addit Manuf 1 (2014) 77–86. https://doi.org/10.1016/j.addma.2014.08.001.

[158] Y. Lu, S. Wu, Y. Gan, T. Huang, C. Yang, L. Junjie, J. Lin, Study on the microstructure, mechanical property and residual stress of SLM Inconel-718 alloy manufactured by differing island scanning strategy, Opt Laser Technol 75 (2015) 197–206. https://doi.org/10.1016/j.optlastec.2015.07.009.

[159] O.O. Salman, F. Brenne, T. Niendorf, J. Eckert, K.G. Prashanth, T. He, S. Scudino, Impact of the scanning strategy on the mechanical behavior of 316L steel synthesized by selective laser melting, J Manuf Process 45 (2019) 255–261. https://doi.org/10.1016/j.jmapro.2019.07.010.

[160] M. Guo, Y. Ye, X. Jiang, L. Wang, Microstructure, Mechanical Properties and Residual Stress of Selective Laser Melted AlSi10Mg, J Mater Eng Perform 28 (2019) 6753–6760. https://doi.org/10.1007/s11665-019-04423-2.

[161] A. Mussatto, R. Groarke, R.K. Vijayaraghavan, M.A. Obeidi, P.J. McNally, V. Nicolosi, Y. Delaure, D. Brabazon, Laser-powder bed fusion of silicon carbide

reinforced 316L stainless steel using a sinusoidal laser scanning strategy, Journal of Materials Research and Technology 18 (2022) 2672–2698. https://doi.org/10.1016/j.jmrt.2022.03.170.

[162] O. Gokcekaya, T. Ishimoto, S. Hibino, J. Yasutomi, T. Narushima, T. Nakano, Unique crystallographic texture formation in Inconel 718 by laser powder bed fusion and its effect on mechanical anisotropy, Acta Mater 212 (2021) 116876. https://doi.org/10.1016/j.actamat.2021.116876.

[163] N. Nadammal, T. Mishurova, T. Fritsch, I. Serrano-Munoz, A. Kromm, C. Haberland, P.D. Portella, G. Bruno, Critical role of scan strategies on the development of microstructure, texture, and residual stresses during laser powder bed fusion additive manufacturing, Addit Manuf 38 (2021). https://doi.org/10.1016/j.addma.2020.101792.

[164] D.J. Newell, R.P. O'Hara, G.R. Cobb, A.N. Palazotto, M.M. Kirka, L.W. Burggraf, J.A. Hess, Mitigation of scan strategy effects and material anisotropy through supersolvus annealing in LPBF IN718, Materials Science and Engineering: A 764 (2019). https://doi.org/10.1016/j.msea.2019.138230.

[165] J.H. Robinson, I.R.T. Ashton, E. Jones, P. Fox, C. Sutcliffe, The effect of hatch angle rotation on parts manufactured using selective laser melting, Rapid Prototyp J 25 (2019) 289–298. https://doi.org/10.1108/RPJ-06-2017-0111.

[166] B. AlMangour, D. Grzesiak, J.M. Yang, Scanning strategies for texture and anisotropy tailoring during selective laser melting of TiC/316L stainless steel nanocomposites, J Alloys Compd 728 (2017) 424–435. https://doi.org/10.1016/j.jallcom.2017.08.022.

[167] O. Adegoke, J. Andersson, H. Brodin, R. Pederson, Review of laser powder bed fusion of gamma-prime-strengthened nickel-based superalloys, Metals (Basel) 10 (2020) 1–26. https://doi.org/10.3390/met10080996.

[168] V.P. Kumar, A.V. Jebaraj, Comprehensive review on residual stress control strategies in laser-based powder bed fusion process– Challenges and opportunities, Lasers in Manufacturing and Materials Processing 10 (2023) 400–442. https://doi.org/10.1007/s40516-023-00217-6.

[169] A. Mostafaei, C. Zhao, Y. He, S. Reza Ghiaasiaan, B. Shi, S. Shao, N. Shamsaei, Z. Wu, N. Kouraytem, T. Sun, J. Pauza, J. V. Gordon, B. Webler, N.D. Parab, M. Asherloo, Q. Guo, L. Chen, A.D. Rollett, Defects and anomalies in powder bed fusion metal additive manufacturing, Curr Opin Solid State Mater Sci 26 (2022). https://doi.org/10.1016/j.cossms.2021.100974.

[170] M. Tang, P.C. Pistorius, J.L. Beuth, Prediction of lack-of-fusion porosity for powder bed fusion, Addit Manuf 14 (2017) 39–48. https://doi.org/10.1016/j.addma.2016.12.001.

[171] C. Du, Y. Zhao, J. Jiang, Q. Wang, H. Wang, N. Li, J. Sun, Pore defects in Laser Powder Bed Fusion: Formation mechanism, control method, and perspectives, J Alloys Compd 944 (2023). https://doi.org/10.1016/j.jallcom.2023.169215.

[172] J. V. Gordon, S.P. Narra, R.W. Cunningham, H. Liu, H. Chen, R.M. Suter, J.L. Beuth, A.D. Rollett, Defect structure process maps for laser powder bed fusion additive manufacturing, Addit Manuf 36 (2020). https://doi.org/10.1016/j.addma.2020.101552.

[173] M. Laleh, A.E. Hughes, S. Yang, J. Wang, J. Li, A.M. Glenn, W. Xu, M.Y. Tan, A critical insight into lack-of-fusion pore structures in additively manufactured stainless steel, Addit Manuf 38 (2021). https://doi.org/10.1016/j.addma.2020.101762.

[174] A. Martucci, A. Aversa, M. Lombardi, Ongoing Challenges of Laser-Based Powder Bed Fusion Processing of Al Alloys and Potential Solutions from the Literature—A Review, Materials 16 (2023). https://doi.org/10.3390/ma16031084.

[175] P.A. Hooper, Melt pool temperature and cooling rates in laser powder bed fusion, Addit Manuf 22 (2018) 548–559. https://doi.org/10.1016/j.addma.2018.05.032.

[176] B. Song, X. Zhao, S. Li, C. Han, Q. Wei, S. Wen, J. Liu, Y. Shi, Differences in microstructure and properties between selective laser melting and traditional manufacturing for fabrication of metal parts: A review, Frontiers of Mechanical Engineering 10 (2015) 111–125. https://doi.org/10.1007/s11465-015-0341-2.

[177] T. Mukherjee, J.W. Elmer, H.L. Wei, T.J. Lienert, W. Zhang, S. Kou, T. DebRoy, Control of grain structure, phases, and defects in additive manufacturing of high-

performance metallic components, Prog Mater Sci 138 (2023). https://doi.org/10.1016/j.pmatsci.2023.101153.

[178] P. Kanagarajah, F. Brenne, T. Niendorf, H.J. Maier, Inconel 939 processed by selective laser melting: Effect of microstructure and temperature on the mechanical properties under static and cyclic loading, Materials Science and Engineering A 588 (2013) 188–195. https://doi.org/10.1016/j.msea.2013.09.025.

[179] A. Mussatto, R. Groarke, A. O'Neill, M.A. Obeidi, Y. Delaure, D. Brabazon, Influences of powder morphology and spreading parameters on the powder bed topography uniformity in powder bed fusion metal additive manufacturing, Addit Manuf 38 (2021) 101807. https://doi.org/10.1016/j.addma.2020.101807.

[180] M.A. Obeidi, M. Monu, C. Hughes, D. Bourke, M.N. Dogu, J. Francis, M. Zhang, I.U. Ahad, D. Brabazon, Laser beam powder bed fusion of nitinol shape memory alloy (SMA), Journal of Materials Research and Technology 14 (2021). https://doi.org/10.1016/j.jmrt.2021.07.126.

[181] Y. Liu, Y. Yang, S. Mai, D. Wang, C. Song, Investigation into spatter behavior during selective laser melting of AISI 316L stainless steel powder, Mater Des 87 (2015) 797–806. https://doi.org/10.1016/j.matdes.2015.08.086.

[182] D. Wang, S. Wu, F. Fu, S. Mai, Y. Yang, Y. Liu, C. Song, Mechanisms and characteristics of spatter generation in SLM processing and its effect on the properties, Mater Des 117 (2017) 121–130. https://doi.org/10.1016/j.matdes.2016.12.060.

[183] S.A. Khairallah, A.T. Anderson, A. Rubenchik, W.E. King, Laser powder-bed fusion additive manufacturing: Physics of complex melt flow and formation mechanisms of pores, spatter, and denudation zones, Acta Mater 108 (2016) 36–45. https://doi.org/10.1016/j.actamat.2016.02.014.

[184] A. Mussatto, R. Groarke, A. A-Hameed, I.U.I. Ahad, R.K. Vijayaraghavan, A. O'Neill, P. McNally, Y. Delaure, D. Brabazon, Evaluation via powder metallurgy of nano-reinforced iron powders developed for selective laser melting applications, Mater Des 182 (2019) 108046. https://doi.org/10.1016/j.matdes.2019.108046.

[185] R. Groarke, C. Danilenkoff, S. Karam, E. McCarthy, B. Michel, A. Mussatto, J. Sloane, A.O. Neill, R. Raghavendra, D. Brabazon, 316l stainless steel powders for

additive manufacturing: Relationships of powder rheology, size, size distribution to part properties, Materials 13 (2020) 1–19. https://doi.org/10.3390/ma13235537.

[186] P. Li, Effect of Powder Flow Properties on the Process Performance of Loss-in-Weight Feeders, M.Sc. Thesis, 2015.

[187] ASTM International, Standard Test Methods for Density of Compacted or Sintered Powder Metallurgy (PM) Products Using Archimedes' Principle, Astm B962-13 i (2013) 1–7.

[188] H.-J. Bunge, Texture Analysis in Materials Science, 1982. https://doi.org/https://doi.org/10.1016/B978-0-408-10642-9.50006-4.

[189] ASTM International, Standard Test Method for Microindentation Hardness of Materials - ASTM E384 - 17, 2017.

[190] M. Mehrabi, J. Gardy, F.A. Talebi, A. Farshchi, A. Hassanpour, A.E. Bayly, An investigation of the effect of powder flowability on the powder spreading in additive manufacturing, Powder Technol 413 (2023) 117997. https://doi.org/10.1016/j.powtec.2022.117997.

[191] A.N.D. Gasper, B. Szost, X. Wang, D. Johns, S. Sharma, A.T. Clare, I.A. Ashcroft, Spatter and oxide formation in laser powder bed fusion of Inconel 718, Addit Manuf 24 (2018) 446–456. https://doi.org/10.1016/j.addma.2018.09.032.

[192] B.P. Payne, M.C. Biesinger, N.S. McIntyre, Use of oxygen/nickel ratios in the XPS characterisation of oxide phases on nickel metal and nickel alloy surfaces, J Electron Spectros Relat Phenomena 185 (2012) 159–166. https://doi.org/10.1016/j.elspec.2012.06.008.

[193] S. Zhang, X. Lin, L. Wang, X. Yu, Y. Hu, H. Yang, L. Lei, W. Huang, Strengthening mechanisms in selective laser-melted Inconel718 superalloy, Materials Science and Engineering A 812 (2021) 141145. https://doi.org/10.1016/j.msea.2021.141145.

[194] P. Köhnen, M. Létang, M. Voshage, J.H. Schleifenbaum, C. Haase, Understanding the process-microstructure correlations for tailoring the mechanical properties of L-PBF produced austenitic advanced high strength steel, Addit Manuf 30 (2019) 100914. https://doi.org/10.1016/j.addma.2019.100914.

[195] O. Engler, V. Randle, Introduction to texture analysis: macrotexture, microtexture, and orientation mapping, 2008.

[196] Y.N. Zhang, X. Cao, P. Wanjara, M. Medraj, Oxide films in laser additive manufactured Inconel 718, Acta Mater 61 (2013) 6562–6576. https://doi.org/10.1016/j.actamat.2013.07.039.

[197] D. Bergström, J. Powell, A.F.H. Kaplan, The absorptance of steels to Nd:YLF and Nd:YAG laser light at room temperature, Appl Surf Sci 253 (2007) 5017–5028. https://doi.org/10.1016/j.apsusc.2006.11.018.

[198] F. Coste, M. Ridlova, N. Gallienne, J. Quintard, G. Bert, Surface oxidation of nickel base alloys and stainless steel under pure oxygen atmosphere: Application to oxygen safety, J Laser Appl 31 (2019) 022518. https://doi.org/10.2351/1.5096149.

[199] B. Brandau, A. Da Silva, C. Wilsnack, F. Brueckner, A.F.H. Kaplan, Absorbance study of powder conditions for laser additive manufacturing, Mater Des 216 (2022) 110591. https://doi.org/10.1016/j.matdes.2022.110591.

[200] W. Zhou, N. Takase, M. Dong, N. Watanabe, S. Guo, Z. Zhou, N. Nomura, Elucidating the impact of severe oxidation on the powder properties and laser melting behaviors, Mater Des 221 (2022) 110959. https://doi.org/10.1016/j.matdes.2022.110959.

[201] S.N. Naik, S.M. Walley, The Hall–Petch and inverse Hall–Petch relations and the hardness of nanocrystalline metals, J Mater Sci 55 (2020) 2661–2681. https://doi.org/10.1007/s10853-019-04160-w.

[202] Q. Deng, X. Wang, Q. Lan, Z. Chang, Z. Liu, N. Su, Y. Wu, D. Liu, L. Peng, W. Ding, Limitations of linear energy density for laser powder bed fusion of Mg-15Gd-1Zn-0.4Zr alloy, Mater Charact 190 (2022). https://doi.org/10.1016/j.matchar.2022.112071.

[203] J. Wang, R. Zhu, Y. Liu, L. Zhang, Understanding melt pool characteristics in laser powder bed fusion: An overview of single- and multi-track melt pools for process optimization, Advanced Powder Materials 2 (2023). https://doi.org/10.1016/j.apmate.2023.100137.

[204] X. Qi, X. Liang, J. Wang, H. Zhang, X. Wang, Z. Liu, Microstructure tailoring in laser powder bed fusion (L-PBF): Strategies, challenges, and future outlooks, J Alloys Compd 970 (2024). https://doi.org/10.1016/j.jallcom.2023.172564.

[205] M. Malý, K. Nopová, L. Klakurková, O. Adam, L. Pantělejev, D. Koutný, Effect of Preheating on the Residual Stress and Material Properties of Inconel 939 Processed by Laser Powder Bed Fusion, Materials 15 (2022) 6360. https://doi.org/10.3390/ma15186360.

[206] S. Vock, B. Klöden, A. Kirchner, T. Weißgärber, B. Kieback, Powders for powder bed fusion: a review, Progress in Additive Manufacturing 4 (2019) 383–397. https://doi.org/10.1007/s40964-019-00078-6.

[207] M. Zavala-Arredondo, T. London, M. Allen, T. Maccio, S. Ward, D. Griffiths, A. Allison, P. Goodwin, C. Hauser, Use of power factor and specific point energy as design parameters in laser powder-bed-fusion (L-PBF) of AlSi10Mg alloy, Mater Des 182 (2019). https://doi.org/10.1016/j.matdes.2019.108018.

[208] ASTM B311-17, Standard Test Method for Density of Powder Metallurgy (PM) Materials Containing Less Than Two Percent Porosity, (n.d.). https://doi.org/10.1520/B0311-17.

[209] D. Kong, C. Dong, S. Wei, X. Ni, L. Zhang, R. Li, L. Wang, C. Man, X. Li, About metastable cellular structure in additively manufactured austenitic stainless steels, Addit Manuf 38 (2021). https://doi.org/10.1016/j.addma.2020.101804.

[210] M. Hafezi, A. Kermanpur, A. Rezaeian, S. Saeidirad, V. Nikneshan, H. Rabieifar, E. Kamouri Yousefabad, Investigating crack formation in IN738LC Ni-based superalloy fabricated by laser powder-bed fusion process, Journal of Materials Research and Technology 29 (2024) 1983–2002. https://doi.org/10.1016/j.jmrt.2024.01.264.

[211] E. Chlebus, K. Gruber, B. Kuźnicka, J. Kurzac, T. Kurzynowski, Effect of heat treatment on the microstructure and mechanical properties of Inconel 718 processed by selective laser melting, Materials Science and Engineering: A 639 (2015) 647–655. https://doi.org/10.1016/j.msea.2015.05.035.

[212] I. Serrano-Munoz, A. Ulbricht, T. Fritsch, T. Mishurova, A. Kromm, M. Hofmann, R.C. Wimpory, A. Evans, G. Bruno, Scanning Manufacturing Parameters Determining the Residual Stress State in LPBF IN718 Small Parts, Adv Eng Mater 23 (2021). https://doi.org/10.1002/adem.202100158.

[213] P. Pant, F. Salvemini, S. Proper, V. Luzin, K. Simonsson, S. Sjöström, S. Hosseini, R.L. Peng, J. Moverare, A study of the influence of novel scan strategies on residual stress and microstructure of L-shaped LPBF IN718 samples, Mater Des 214 (2022). https://doi.org/10.1016/j.matdes.2022.110386.

[214] A. Paraschiv, G. Matache, N. Constantin, M. Vladut, Investigation of Scanning Strategies and Laser Remelting Effects on Top Surface Deformation of Additively Manufactured IN 625, Materials 15 (2022). https://doi.org/10.3390/ma15093198.

[215] A.J. Dunbar, E.R. Denlinger, J. Heigel, P. Michaleris, P. Guerrier, R. Martukanitz, T.W. Simpson, Development of experimental method for in situ distortion and temperature measurements during the laser powder bed fusion additive manufacturing process, Addit Manuf 12 (2016) 25–30. https://doi.org/10.1016/j.addma.2016.04.007.

[216] A. Paraschiv, G. Matache, M. Vladut, Assessment of Residual Stresses in Laser Powder Bed Fusion Manufactured IN 625, Materials 17 (2024). https://doi.org/10.3390/ma17020413.

[217] Y.M. Arısoy, L.E. Criales, T. Özel, B. Lane, S. Moylan, A. Donmez, Influence of scan strategy and process parameters on microstructure and its optimization in additively manufactured nickel alloy 625 via laser powder bed fusion, International Journal of Advanced Manufacturing Technology 90 (2017) 1393–1417. https://doi.org/10.1007/s00170-016-9429-z.

[218] B. Diepold, M.S. Palm, A. Wimmer, T. Sebald, H.W. Höppel, S. Neumeier, M. Göken, Rotating Scan Strategy Induced Anisotropic Microstructural and Mechanical Behavior of Selective Laser Melted Materials and Their Reduction by Heat Treatments, Adv Eng Mater 23 (2021). https://doi.org/10.1002/adem.202100622.

[219] X. Zhang, H. Xu, Z. Li, A. Dong, D. Du, L. Lei, G. Zhang, D. Wang, G. Zhu, B. Sun, Effect of the scanning strategy on microstructure and mechanical anisotropy of Hastelloy X superalloy produced by Laser Powder Bed Fusion, Mater Charact 173 (2021). https://doi.org/10.1016/j.matchar.2021.110951.

[220] L.N. Carter, C. Martin, P.J. Withers, M.M. Attallah, The influence of the laser scan strategy on grain structure and cracking behaviour in SLM powder-bed fabricated

nickel superalloy, J Alloys Compd 615 (2014) 338–347. https://doi.org/10.1016/j.jallcom.2014.06.172.

[221] Ł. Rakoczy, M. Grudzień-Rakoczy, B. Rutkowski, R. Cygan, A. Zielińska-Lipiec, The role of the microstructural changes during induction preheating on the HAZ liquation cracking susceptibility of Ni-based superalloy, J Mater Sci 59 (2024) 631–649. https://doi.org/10.1007/s10853-023-09184-x.

[222] M.N. Doğu, M.A. Obeidi, H. Gu, C. Teng, D. Brabazon, Powder Bed Fusion–Laser Beam of IN939: The Effect of Process Parameters on the Relative Density, Defect Formation, Surface Roughness and Microstructure, Materials 17 (2024). https://doi.org/10.3390/ma17133324.

[223] G. Çelik, The Influence of Additive Manufacturing Process Parameters on Residual Stress of 17-4 PH Stainless Steel Parts Manufactured by Laser Powder Bed Fusion Additive Manufacturing System, M.Sc. Thesis, 2023.

[224] ASTM International, E915-Standard Test Method for Verifying the Alignment of X-Ray Diffraction Instrumentation for Residual Stress Measurement, (n.d.). https://doi.org/10.1520/E0915-19.

[225] L.S. Aota, P. Bajaj, K.D. Zilnyk, E.A. Jägle, D. Ponge, H.R.Z. Sandim, D. Raabe, Recrystallization kinetics, mechanisms, and topology in alloys processed by laser powder-bed fusion: AISI 316L stainless steel as example, Materialia (Oxf) 20 (2021) 101236. https://doi.org/10.1016/j.mtla.2021.101236.

[226] F.C. Pinto, L.S. Aota, I.R. Souza Filho, D. Raabe, H.R.Z. Sandim, Recrystallization in non-conventional microstructures of 316L stainless steel produced via laser powder-bed fusion: effect of particle coarsening kinetics, J Mater Sci 57 (2022) 9576–9598. https://doi.org/10.1007/s10853-021-06859-1.

[227] E. de Sonis, S. Dépinoy, P.F. Giroux, H. Maskrot, L. Lemarquis, O. Hercher, F. Villaret, A.F. Gourgues-Lorenzon, Dependency of recrystallization kinetics on the solidification microstructure of 316L stainless steel processed by laser powder bed fusion (LPBF), Mater Charact 194 (2022). https://doi.org/10.1016/j.matchar.2022.112370.

[228] R. Buerstmayr, F. Theska, E. Kozeschnik, R.F. Webster, M. Lison-Pick, S. Street, S. Primig, Investigation and Simulation of the Effects of nm-Scale γ′ Precipitates on

the Recrystallization of Ni-based Superalloys, Metall Mater Trans A Phys Metall Mater Sci 54 (2023) 2259–2276. https://doi.org/10.1007/s11661-023-07008-w.

[229] H. Ali, H. Ghadbeigi, K. Mumtaz, Effect of scanning strategies on residual stress and mechanical properties of Selective Laser Melted Ti6Al4V, Materials Science and Engineering: A 712 (2018) 175–187. https://doi.org/10.1016/j.msea.2017.11.103.

[230] P.V. Cobbinah, S. Matsunaga, Y. Yamabe-Mitarai, Controlled Crystallographic Texture Orientation in Structural Materials Using the Laser Powder Bed Fusion Process—A Review, Adv Eng Mater 25 (2023). https://doi.org/10.1002/adem.202300819.

[231] Y. Song, Q. Sun, K. Guo, X. Wang, J. Liu, J. Sun, Effect of scanning strategies on the microstructure and mechanical behavior of 316L stainless steel fabricated by selective laser melting, Materials Science and Engineering: A 793 (2020). https://doi.org/10.1016/j.msea.2020.139879.

[232] N. Kouraytem, J. Varga, B. Amin-Ahmadi, H. Mirmohammad, R.A. Chanut, A.D. Spear, O.T. Kingstedt, A recrystallization heat-treatment to reduce deformation anisotropy of additively manufactured Inconel 718, Mater Des 198 (2021). https://doi.org/10.1016/j.matdes.2020.109228.

[233] K. Huang, R.E. Logé, A review of dynamic recrystallization phenomena in metallic materials, Mater Des 111 (2016) 548–574. https://doi.org/10.1016/j.matdes.2016.09.012.

[234] H.E. Sabzi, X.H. Li, C. Zhang, H. Fu, D. San-Martín, P.E.J. Rivera-Díaz-del-Castillo, Deformation twinning-induced dynamic recrystallization during laser powder bed fusion, Scr Mater 207 (2022). https://doi.org/10.1016/j.scriptamat.2021.114307.

[235] H.E. Sabzi, N.T. Aboulkhair, X. Liang, X.H. Li, M. Simonelli, H. Fu, P.E.J. Rivera-Díaz-del-Castillo, Grain refinement in laser powder bed fusion: The influence of dynamic recrystallization and recovery, Mater Des 196 (2020). https://doi.org/10.1016/j.matdes.2020.109181.

[236] J. Zhao, L. Sun, P. Ji, X. Yu, L. Chen, S. Liu, K. Zheng, F. Yin, The effect of scanning strategies on the microstructure and mechanical properties of M2052 alloy

manufactured by selective laser melting, Journal of Materials Research and Technology 27 (2023) 7084–7093. https://doi.org/10.1016/j.jmrt.2023.11.141.

[237] V.S. Hariharan, R. Kaushik, B.S. Murty, G. Phanikumar, Effect of laser scan rotation on the microstructure and mechanical properties of laser powder bed fused Haynes 282, Materialia (Oxf) 33 (2024). https://doi.org/10.1016/j.mtla.2023.101992.

[238] J.L. Bartlett, X. Li, An overview of residual stresses in metal powder bed fusion, Addit Manuf 27 (2019) 131–149. https://doi.org/10.1016/j.addma.2019.02.020.

[239] W. Zhang, D. Guo, L. Wang, C.M. Davies, W. Mirihanage, M. Tong, N.M. Harrison, X-ray diffraction measurements and computational prediction of residual stress mitigation scanning strategies in powder bed fusion additive manufacturing, Addit Manuf 61 (2023). https://doi.org/10.1016/j.addma.2022.103275.

[240] J. Robinson, I. Ashton, P. Fox, E. Jones, C. Sutcliffe, Determination of the effect of scan strategy on residual stress in laser powder bed fusion additive manufacturing, Addit Manuf 23 (2018) 13–24. https://doi.org/10.1016/j.addma.2018.07.001.

[241] W. Huang, J. Yang, H. Yang, G. Jing, Z. Wang, X. Zeng, Heat treatment of Inconel 718 produced by selective laser melting: Microstructure and mechanical properties, Materials Science and Engineering A 750 (2019) 98–107. https://doi.org/10.1016/j.msea.2019.02.046.

[242] G.E. Bean, D.B. Witkin, T.D. McLouth, D.N. Patel, R.J. Zaldivar, Effect of laser focus shift on surface quality and density of Inconel 718 parts produced via selective laser melting, Addit Manuf 22 (2018) 207–215. https://doi.org/10.1016/j.addma.2018.04.024.

[243] M. Komarasamy, S. Shukla, S. Williams, K. Kandasamy, S. Kelly, R.S. Mishra, Microstructure, fatigue, and impact toughness properties of additively manufactured nickel alloy 718, Addit Manuf 28 (2019) 661–675. https://doi.org/10.1016/j.addma.2019.06.009.

[244] X. Li, J.J. Shi, C.H. Wang, G.H. Cao, A.M. Russell, Z.J. Zhou, C.P. Li, G.F. Chen, Effect of heat treatment on microstructure evolution of Inconel 718 alloy fabricated by selective laser melting, J Alloys Compd 764 (2018) 639–649. https://doi.org/10.1016/j.jallcom.2018.06.112.

[245] J. Li, Z. Zhao, P. Bai, H. Qu, B. Liu, L. Li, L. Wu, R. Guan, H. Liu, Z. Guo, Microstructural evolution and mechanical properties of IN718 alloy fabricated by selective laser melting following different heat treatments, J Alloys Compd 772 (2019) 861–870. https://doi.org/10.1016/j.jallcom.2018.09.200.

[246] M. Ni, S. Liu, C. Chen, R. Li, X. Zhang, K. Zhou, Effect of heat treatment on the microstructural evolution of a precipitation-hardened superalloy produced by selective laser melting, Materials Science and Engineering: A 748 (2019) 275–285. https://doi.org/10.1016/j.msea.2019.01.109.

[247] M.P. Haines, V. V. Rielli, S. Primig, N. Haghdadi, Powder bed fusion additive manufacturing of Ni-based superalloys: a review of the main microstructural constituents and characterization techniques, J Mater Sci 57 (2022) 14135–14187. https://doi.org/10.1007/s10853-022-07501-4.

[248] A. Shaji Karapuzha, D. Fraser, Y. Zhu, X. Wu, A. Huang, Effect of solution heat treatment and hot isostatic pressing on the microstructure and mechanical properties of Hastelloy X manufactured by electron beam powder bed fusion, J Mater Sci Technol 98 (2022) 99–117. https://doi.org/10.1016/j.jmst.2021.04.059.

[249] Z. Wang, K. Guan, M. Gao, X. Li, X. Chen, X. Zeng, The microstructure and mechanical properties of deposited-IN718 by selective laser melting, J Alloys Compd 513 (2012) 518–523. https://doi.org/10.1016/j.jallcom.2011.10.107.

[250] V.A. Popovich, E. V. Borisov, A.A. Popovich, V.S. Sufiiarov, D. V. Masaylo, L. Alzina, Impact of heat treatment on mechanical behaviour of Inconel 718 processed with tailored microstructure by selective laser melting, Mater Des 131 (2017) 12–22. https://doi.org/10.1016/j.matdes.2017.05.065.

[251] B. Zhang, Y. Li, Q. Bai, Defect Formation Mechanisms in Selective Laser Melting: A Review, Chinese Journal of Mechanical Engineering 30 (2017) 515–527. https://doi.org/10.1007/s10033-017-0121-5.

[252] A. Rezaei, A. Kermanpur, A. Rezaeian, M. Badrossamay, E. Foroozmehr, F. Sadeghi, J. Han, T.M. Park, Contribution of hot isostatic pressing on densification, microstructure evolution, and mechanical anisotropy of additively manufactured IN718 Ni-based superalloy, Materials Science and Engineering: A 823 (2021). https://doi.org/10.1016/j.msea.2021.141721.

[253] A. Jena, S.E. Atabay, M. Brochu, Microstructure and mechanical properties of crack-free Inconel 738 fabricated by laser powder bed fusion, Materials Science and Engineering A 850 (2022) 143524. https://doi.org/10.1016/j.msea.2022.143524.

[254] X. Cao, Y.-N. Zhang, P. Wanjara, M. Medraj, Tensile properties of laser additive manufactured Inconel 718 using filler wire, J Mater Res 29 (2014) 2006–2020. https://doi.org/10.1557/jmr.2014.199.

[255] Y. Zhao, K. Guan, Z. Yang, Z. Hu, Z. Qian, H. Wang, Z. Ma, The effect of subsequent heat treatment on the evolution behavior of second phase particles and mechanical properties of the Inconel 718 superalloy manufactured by selective laser melting, Materials Science and Engineering A 794 (2020) 139931. https://doi.org/10.1016/j.msea.2020.139931.

[256] M.R. Jahangiri, M. Abedini, Effect of long time service exposure on microstructure and mechanical properties of gas turbine vanes made of IN939 alloy, Mater Des 64 (2014) 588–600. https://doi.org/10.1016/j.matdes.2014.08.035.

[257] M.R. Jahangiri, H. Arabi, S.M.A. Boutorabi, Investigation on the dissolution of η phase in a cast Ni-based superalloy, International Journal of Minerals, Metallurgy and Materials 20 (2013) 42–48. https://doi.org/10.1007/s12613-013-0691-x.

[258] J.P. Choi, G.H. Shin, S. Yang, D.Y. Yang, J.S. Lee, M. Brochu, J.H. Yu, Densification and microstructural investigation of Inconel 718 parts fabricated by selective laser melting, Powder Technol 310 (2017) 60–66. https://doi.org/10.1016/j.powtec.2017.01.030.

[259] C. Panwisawas, Y.T. Tang, R.C. Reed, Metal 3D printing as a disruptive technology for superalloys, Nat Commun 11 (2020) 1–4. https://doi.org/10.1038/s41467-020-16188-7.

[260] W.M. Tucho, P. Cuvillier, A. Sjolyst-Kverneland, V. Hansen, Microstructure and hardness studies of Inconel 718 manufactured by selective laser melting before and after solution heat treatment, Materials Science and Engineering A 689 (2017) 220–232. https://doi.org/10.1016/j.msea.2017.02.062.

[261] N.C. Ferreri, S.C. Vogel, M. Knezevic, Determining volume fractions of γ, γ′, γ″, δ, and MC-carbide phases in Inconel 718 as a function of its processing history using

an advanced neutron diffraction procedure, Materials Science and Engineering A 781 (2020) 139228. https://doi.org/10.1016/j.msea.2020.139228.

[262] K. Moussaoui, W. Rubio, M. Mousseigne, T. Sultan, F. Rezai, Effects of Selective Laser Melting additive manufacturing parameters of Inconel 718 on porosity, microstructure and mechanical properties, Materials Science and Engineering A 735 (2018) 182–190. https://doi.org/10.1016/j.msea.2018.08.037.

[263] A. Ozsoy, E. Yasa, M. Keles, E.B. Tureyen, Pulsed-mode Selective Laser Melting of 17-4 PH stainless steel: Effect of laser parameters on density and mechanical properties, J Manuf Process 68 (2021) 910–922. https://doi.org/10.1016/j.jmapro.2021.06.017.

[264] E.M. Fayed, D. Shahriari, M. Saadati, V. Brailovski, M. Jahazi, M. Medraj, Influence of homogenization and solution treatments time on the microstructure and hardness of Inconel 718 fabricated by laser powder bed fusion process, Materials 13 (2020). https://doi.org/10.3390/ma13112574.

[265] G.H. Cao, T.Y. Sun, C.H. Wang, X. Li, M. Liu, Z.X. Zhang, P.F. Hu, A.M. Russell, R. Schneider, D. Gerthsen, Z.J. Zhou, C.P. Li, G.F. Chen, Investigations of γ′ γ″ and δ precipitates in heat-treated Inconel 718 alloy fabricated by selective laser melting, Mater Charact 136 (2018) 398–406. https://doi.org/10.1016/j.matchar.2018.01.006.

[266] J.J. Shi, X. Li, Z.X. Zhang, G.H. Cao, A.M. Russell, Z.J. Zhou, C.P. Li, G.F. Chen, Study on the microstructure and creep behavior of Inconel 718 superalloy fabricated by selective laser melting, Materials Science and Engineering A 765 (2019). https://doi.org/10.1016/j.msea.2019.138282.

[267] K. Gruber, R. Dziedzic, B. Kuźnicka, B. Madejski, M. Malicki, Impact of high temperature stress relieving on final properties of Inconel 718 processed by laser powder bed fusion, Materials Science and Engineering A 813 (2021). https://doi.org/10.1016/j.msea.2021.141111.

[268] K. Gruber, W. Stopyra, K. Kobiela, B. Madejski, M. Malicki, T. Kurzynowski, Mechanical properties of Inconel 718 additively manufactured by laser powder bed fusion after industrial high-temperature heat treatment, J Manuf Process 73 (2022) 642–659. https://doi.org/10.1016/j.jmapro.2021.11.053.

[269] ASTM International, F3055-14a, Standard Specification for Additive Manufacturing Nickel Alloy (UNS N06625) with Powder Bed Fusion, 2014.

[270] G.F. Vander Voort, E.P. Manilova, Metallographic techniques for superalloys, Microscopy and Microanalysis 10 (2004) 690–691. https://doi.org/10.1017/S1431927604883442.

[271] D. Deng, R.L. Peng, H. Brodin, J. Moverare, Microstructure and mechanical properties of Inconel 718 produced by selective laser melting: Sample orientation dependence and effects of post heat treatments, Materials Science and Engineering A 713 (2018) 294–306. https://doi.org/10.1016/j.msea.2017.12.043.

[272] S.Y. Liu, H.Q. Li, C.X. Qin, R. Zong, X.Y. Fang, The effect of energy density on texture and mechanical anisotropy in selective laser melted Inconel 718, Mater Des 191 (2020). https://doi.org/10.1016/j.matdes.2020.108642.

[273] S. Suwas, R.K. Ray, Crystallographic Texture of Materials, 2014. https://doi.org/10.1007/978-1-4471-6314-5_5.

[274] R. Jiang, A. Mostafaei, J. Pauza, C. Kantzos, A.D. Rollett, Varied heat treatments and properties of laser powder bed printed Inconel 718, Materials Science and Engineering A 755 (2019) 170–180. https://doi.org/10.1016/j.msea.2019.03.103.

[275] S. Holland, X. Wang, J. Chen, W. Cai, F. Yan, L. Li, Multiscale characterization of microstructures and mechanical properties of Inconel 718 fabricated by selective laser melting, J Alloys Compd 784 (2019) 182–194. https://doi.org/10.1016/j.jallcom.2018.12.380.

[276] L.S. Aota, P. Bajaj, K.D. Zilnyk, D. Ponge, H.R.Z. Sandim, The origin of abnormal grain growth upon thermomechanical processing of laser powder-bed fusion alloys, Materialia (Oxf) 20 (2021) 101243. https://doi.org/10.1016/j.mtla.2021.101243.

[277] S. Holland, X. Wang, X.Y. Fang, Y.B. Guo, F. Yan, L. Li, Grain boundary network evolution in Inconel 718 from selective laser melting to heat treatment, Materials Science and Engineering A 725 (2018) 406–418. https://doi.org/10.1016/j.msea.2018.04.045.

[278] L. Huang, Y. Cao, G. Li, Y. Wang, Microstructure characteristics and mechanical behaviour of a selective laser melted Inconel 718 alloy, Journal of Materials

Research and Technology 9 (2020) 2440–2454. https://doi.org/10.1016/j.jmrt.2019.12.075.

[279] M. Calandri, S. Yin, B. Aldwell, F. Calignano, R. Lupoi, D. Ugues, Texture and microstructural features at different length scales in Inconel 718 produced by selective laser melting, Materials 12 (2019). https://doi.org/10.3390/ma12081293.

[280] Y. Jin, M. Bernacki, A. Agnoli, B. Lin, G.S. Rohrer, A.D. Rollett, N. Bozzolo, Evolution of the annealing twin density during δ-Supersolvus grain growth in the nickel-based superalloy Inconel^{TM} 718, Metals (Basel) 6 (2015) 1–13. https://doi.org/10.3390/met6010005.

[281] S. Mahajan, C.S. Pande, M.A. Imam, B.B. Rath, Formation of annealing twins in f.c.c. crystals, Acta Mater. 45 (1997) 2633–2638.

[282] S. Mahajan, Critique of mechanisms of formation of deformation, annealing and growth twins: Face-centered cubic metals and alloys, Scr Mater 68 (2013) 95–99. https://doi.org/10.1016/j.scriptamat.2012.09.011.

[283] Y. Jin, B. Lin, M. Bernacki, G.S. Rohrer, A.D. Rollett, N. Bozzolo, Annealing twin development during recrystallization and grain growth in pure nickel, Materials Science and Engineering A 597 (2014) 295–303. https://doi.org/10.1016/j.msea.2014.01.018.

[284] A. Mostafa, I.P. Rubio, V. Brailovski, M. Jahazi, M. Medraj, Structure, texture and phases in 3D printed IN718 alloy subjected to homogenization and HIP treatments, Metals (Basel) 7 (2017) 1–23. https://doi.org/10.3390/met7060196.

[285] T.G. Gallmeyer, S. Moorthy, B.B. Kappes, M.J. Mills, B. Amin-Ahmadi, A.P. Stebner, Knowledge of process-structure-property relationships to engineer better heat treatments for laser powder bed fusion additive manufactured Inconel 718, Addit Manuf 31 (2020) 100977. https://doi.org/10.1016/j.addma.2019.100977.

[286] C.K. Yong, G.J. Gibbons, C.C. Wong, G. West, A critical review of the material characteristics of additive manufactured in718 for high-temperature application, Metals (Basel) 10 (2020) 1–22. https://doi.org/10.3390/met10121576.

[287] Y.L. Kuo, S. Horikawa, K. Kakehi, The effect of interdendritic δ phase on the mechanical properties of Alloy 718 built up by additive manufacturing, Mater Des 116 (2017) 411–418. https://doi.org/10.1016/j.matdes.2016.12.026.